INSTABILITIES AND DISTRIBUTION FUNCTIONS ASSOCIATED WITH PHOTOEXCITED CARRIERS IN SEMICONDUCTORS

by

Piotr Andrzej Maksym

A disseration submitted for admission to the degree of Doctor of Philosophy at the University of Warwick, Department of Physics, December 1979.

CONTENTS

LIST OF TABLES

LIST OF FIGURES

Acknowledgments

Firstly I would like to thank Doctor C.J. Hearn and Professor P.N. Butcher for their help and guidance during the course of this work. In addition I am indebted to Drs. J.R. Barker and A. Noguerra for many useful and fruitful discussions. Thanks are also due to Mr. T.B.G. Clark for considerable help with computer graphics. S.R.C. financial support is gratefully acknowledged. Finally I wish to thank Ms. Terri Moss for her skill and patience in typing this thesis.

Declaration

This dissertation is submitted to the University of Warwick in support of my application for admission to the degree of Doctor of Philosophy. It contains an account of my own work performed at the Department of Physics of the University of Warwick, during the period October 1976 to March 1979, under the general supervision of Professor P.N. Butcher and Doctor C.J. Hearn. No part of this dissertation has been used previously in a degree thesis submitted to this or any other university. The work described in this thesis is the result of my own independent research, except where specifically acknowledged in the text.

December 1979

P.A. Maksym.

Abstract

Some aspects of photoexcited carriers in semiconductors are investigated theoretically. Three distinct phenomena are studied namely, photoluminescence, oscillatory photoconductivity and trap modified Gunn domains.

Distribution functions are calculated for photoexcited electrons in gallium arsenide and are discussed within the context of recent photoluminescence experiments. The calculations apply to conditions of continuous, monochromatic photoexcitation and lattice temperatures in the liquid helium range. A Boltzmann equation approach is used to take account of injection of electrons into the conduction band, electron scattering and electron recombination. The effects of inelastic scattering by acoustic phonons, longitudinal optical phonons and other electrons are considered. The equation is solved numerically using an iterative technique. The steady state distribution function and its time evolution from an initial state in which there are no electrons in the band are both computed. Under conditions such that electron-electron scattering has a negligible effect, the steady state distribution function is found to have a non-Maxwellian form. It has a high energy plateau which has some fine structure close to the injection energy (or energies). The origin of the plateau and the fine structure are explained in terms of the phonon scattering events undergone by the photoexcited electrons. Two models for electron-electron scattering are studied. Within a large screening model, distribution functions are computed without recourse to further approximations to the electron-electron scattering rates. Distribution functions applicable to situations in which the screening is not large are computed using a Taylor series approximation to the electron-electron scattering rates. The computations are of a preliminary nature but it is found that at an electron density of $\sim 3 \times 10^{16}$ m^{-3} electron-electron scattering could cause heating of those electrons whose energy is greater than the injection energy. Electron-acceptor luminescence spectra for C doped GaAs, under photoexcitation conditions such that electron-electron scattering has a negligible effect, are derived from the computed distribution functions and are compared with the results of some recent photoluminescence experiments. Fair agreement is obtained.

The theory of oscillatory photoconductivity is studied, with special reference to negative current and instability effects. The theory is used to investigate a one dimensional model for the space-time dependence of the electric field in a semiconductor under conditions such that oscillatory photoconductivity occurs. The semiconductor is taken to be in a resistive circuit. The appropriate equations are solved numerically and thus the stability of the negative current state is investigated. It is shown that this state could be stable with respect to space charge formation if the circuit resistance is sufficiently high. In addition a numerical study is made of the types of domain instability which could otherwise form.

A model for Gunn domain propagation, which includes the effects of the carrier generation recombination process is investigated. The recombination coefficient is taken to be field dependent. Numerical solutions of the equations describing the coupled, space-time dependent electric field and trapped electron density are obtained. The model is found to be qualitatively in accord with many observed features of trap modified Gunn domains.

Publications

Various aspects of the work described in this thesis have been published, or are about to be published in the scientific literature. Two papers have been written jointly with Dr. C.J. Hearn and are entitled as follows:

'Carrier generation-recombination in the Gunn effect'
Solid State Electron. 21 1531 (1978).

'Inhomogenous electric fields in oscillatory photoconductivity'
J. Phys. C. 12 3733 (1979)

A third paper has been accepted for publication in Solid State Communications. It is entitled as follows:

'Electron-acceptor luminescence from a non-Maxwellian distribution of photoexcited electrons in GaAs'.

CHAPTER 1

INTRODUCTION

Non-equilibrium distributions of carriers in semiconductors can be established in two ways: either by electric field induced heating or by photoexcitation. There is an extensive literature devoted to the experimental aspects of both those effects. Studies of electric field induced heating are principally concerned with non-linear effects in high field transport. Such work is of practical importance because of its application to microwave semiconductor devices. Recent work on photoexcited carriers is of equal interest; new developments in laser sources and optical spectroscopy have enabled photoexcited carrier distribution functions to be studied experimentally. The first part of this thesis concerns a theoretical study of some carrier distribution functions appropriate to such experiments. The objective is to show how the distribution function can be characteristic of the scattering events undergone by the photoexcited carriers. The second part of the thesis involves a study of some non-linear effects in photocarrier transport: the stability of the negative current state associated with oscillatory photoconductivity is investigated and the effect of field dependent recombination on Gunn domain propagation is discussed.

One aim of current experimental work on photoexcited carrier distribution functions is to investigate the scattering events undergone by the photoexcited carriers during their lifetime. The energy relaxation of the photoexcited carriers is of particular interest in this respect (Ulbrich, 1978a). A typical experiment involves the use of photoluminescence spectroscopy. In this technique laser illumination is used to establish a non-equilibrium distribution of carriers in a semiconductor. A fraction of the carriers recombine radiatively and spectroscopic observations of the resulting luminescence enable information on the carrier distribution functions to be inferred (Ulbrich 1978b; Bauer 1974). The results of this

type of experiment can yield knowledge of the carrier scattering events only if the carrier distribution functions can be computed according to a specific scattering model. This enables the luminescence spectrum to be calculated and compared with experiment. And thus the theoretical model of carrier scattering used to compute the distribution functions can be tested.

The essential features of the steady state, non-equilibrium distribution function for the photoexcited carriers can be understood with the aid of the following model. (Hearn, 1966; Barker and Hearn, 1973). The photoexcitation process generates carriers in one band of a semiconductor (i.e. causes carriers to be injected into the band). While in the band the carriers are scattered by impurities, phonons and themselves. They recombine at a characteristic rate R. The number of thermally excited carriers is assumed to be negligibly small. Within this model the carrier distribution functions can be classed according to the magnitude of the recombination rate. If R is small compared to the scattering rates the majority of the carriers present in the band at any specific time are those which have undergone many collisions. Hence the carrier distribution function is a quasi-equilibrium one. If, however, the recombination rate greatly exceeds the scattering rates, the majority of the carriers present in the band are those which have undergone no collisions. Therefore the distribution function is representative of the generation and recombination rates. For intermediate values of R the distribution function is characteristic of the competition between the generation, scattering and recombination processes.

In our work on photocarrier distribution functions (Chapter 2) we apply the model described in the previous paragraph to study photoexcited electrons in gallium arsenide. We consider both the steady state distribution function and its time evolution from an initial state in which

there are no electrons in the conduction band. In addition we investigate luminescence spectra due to conduction band to neutral acceptor transitions. Our work is specifically concerned with GaAs under conditions of continuous, monochromatic photoexcitation and lattice temperatures in the liquid helium range. Many experiments on GaAs under these conditions have been described in the literature (See Section 2.2 for a summary). From the results of such experiments it is known that the recombination rate of the photoexcited electrons is intermediate between the two extremes we have previously mentioned. Our studies of the distribution function are therefore primarily concerned with scattering effects. We consider the effects of piezoelectric and deformation potential scattering by acoustic phonons, polar scattering by L.O. phonons and impurity scattering. In addition some account is taken of electron-electron scattering. Calculations are made to show how various features of the distribution functions are characteristic of all these scattering processes. We then compute some electron-acceptor luminescence spectra for carbon doped GaAs and we compare these spectra with some recent experimental results (Ulbrich, 1978b).

Non-linear effects in photocarrier transport are expected to occur at much lower electric fields than those which cause non-linear effects in thermal carrier transport. The reason for this is that the distribution function for photoexcited carriers has a non-equilibrium form even in the absence of electric fields. Non-linearities are, in particular, expected to be associated with oscillatory photoconductivity. This effect occurs in many semiconductors under conditions of monochromatic photoexcitation and lattice temperatures in the liquid helium to nitrogen range. Under such conditions the photoconductive response is found to be an oscillatory function of the energy at which carriers are injected into the appropriate band. And the period of the oscillations is found to be equal to the threshold energy for longitudinal optical phonon emission (Stocker,

Levinstein and Stannard, 1966). The oscillatory photoconductive response has been studied theoretically by a number of authors (Elesin and Manykin, 1965; Stocker and Kaplan, 1966; Barker and Hearn, 1969). In particular Barker and Hearn (1969) have used a Monte Carlo technique to calculate the photoconductive response of indium antimomide and, for most injection energies, the results of these calculations agree well with experiment. However, according to their calculations(and according to all the other theories of oscillatory photoconductivity)the carrier drift velocity should be negative if the injection energy is in a small range of energies just below the optical phonon threshold.For such'sub-threshold'injection energies the carrier drift velocity as a function of electric field is predicted to have ranges of positive and negative velocity and also of positive & negative differential velocity. The latter would be expected to render the electric field unstable against space charge formation. Hence it is uncertain whether a stable, negative current steady state could occur in practice. Only a little theoretical work on this question has been reported, notably by Barker and Hearn (1970) who have applied a Gunn effect model to study the negative current state. A detailed experimental investigation of the same question is still lacking.

Our work on oscillatory photoconductivity (Chapter 3) is concerned with the stability of the negative current state with respect to space charge formation. We use a Gunn effect model to study the space-time dependence of the electric field in a semiconductor under conditions such that the negative current state could occur. This enables us to investigate the conditions under which this state could be stable and also allows us to study the domain instabilities which could otherwise form. Our work differs from previous theoretical work on the negative current state (Barker and Hearn, 1970) because we take the semiconductor to be in a resistive circuit.

Domain instabilities can form in photoexcited semiconductors under conditions totally different to those associated with oscillatory photoconductivity. This can happen provided that the semiconductor contains suitable traps. One example of such a semiconductor is high resistivity GaAs ($\gtrsim 10^3\ \Omega\ cm^{-1}$) in which both fast moving Gunn domains and slow moving, high field domains have been observed under conditions of photoexcitation and temperatures of $\sim 300^oK$. (Ridley, Crisp and Shishiyanu, 1972). Electron trapping has also been found to affect the propagation of Gunn domains in low resistivity GaAs (Teszner and Boccon-Gibod, 1973). The accepted explanation for all these phenomena involves a field dependent recombination mechanism (Ridley and Wisbey, 1967; Sacks and Milnes, 1970). Although this mechanism is well known, numerical studies of the coupled equations describing the space-time dependence of the electric field and trapped electron density have only been reported for the case of field independent recombination (Kroemer, 1972). Our work on trap modified Gunn domains (Chapter 4) involves a similar numerical study but we investigate the effects of field dependent recombination.

We now outline the methods of study we have used in our work and following this we explain how the results of our work are presented. A similar method of study has been used in our work on distribution functions, oscillatory photoconductivity and trap modified Gunn domains. The method is as follows. Firstly, a model problem relevant to the phenomenon under study is devised. Analytic techniques are then used to establish the basic properties of the model and these properties are used as a guide to further investigations using numerical methods. The major part of the knowledge concerning each model is obtained through exhaustive computation: numerical solutions of the model problem are calculated for as wide a range of parameters as possible within the available computer time. All the

computations are performed using a Burroughs B6700 computer.

The results of our work are presented in Chapters 2 to 4. These chapters are relatively independent of each other, however they do form a sequence in the sense that the work described in each is more concerned with macroscopic concepts than is the work described in the preceding one. Each of the chapters has a similar structure and this structure reflects the method of study we have used. Each chapter opens with an introductory section which contains an outline of the work described subsequently. This is followed by a review of previous experimental and theoretical work on the phenomenon under study. Next the model we have used in our work is explained and an account of some of its analytic properties is given. The major part of each chapter is devoted to an explanation of our numerical studies. Emphasis is placed on the physics we have inferred from our numerical results; mathematical details concerning the model problems and the methods we have employed for their solution are given as appendices. Any discussions of computational techniques are kept to a minimum. Each chapter closes with a summary of the conclusions we have reached.

In Chapter 5 we outline the most important results of the work described in the preceding three chapters. Following this we discuss some relations between various aspects of the phenomena we have studied. We conclude by making extensive recommendations for future work on photoexcited carriers.

CHAPTER 2

NON-MAXWELLIAN DISTRIBUTIONS OF PHOTOEXCITED ELECTRONS IN GALLIUM ARSENIDE

2.1. Introduction.

Many experimental results on photoexcited electrons in gallium arsenide have been reported in the literature. A number of these results have been obtained using photoluminescence techniques. The principle of such techniques is quite simple. (Fig. 2.1). Light of sufficient energy to cause band to band or impurity to band transitions is allowed to illuminate part of a semiconductor crystal. This creates a non-equilibrium distribution of carriers within. A fraction of these carriers recombine radiatively and spectroscopic observations of the emitted radiation enable information on the distribution function to be inferred.

Our interest in photoluminescence experiments lies in the results they have yielded on the distribution function for monochromatically photoexcited electrons in GaAs under conditions such that the number of thermally excited carriers is negligibly small (i.e. lattice temperature in the liquid helium range). The first experimental work relevant to GaAs under these conditions is due to Shah and Leite (1969). They have observed the band to band luminescence spectrum of photoexcited electrons and holes in GaAs at a lattice temperature of $2.0^{o}K$. They report that their spectra can be explained if it is assumed that both the electrons and holes have Maxwellian distributions, with a common temperature greater than that of the lattice. Later work on monochromatic photoexcitation has involved observations of electron-acceptor luminescence. (Ulbrich, 1973). The results of this work have confirmed that, provided the excitation intensity is sufficiently high, the photoexcited electron distribution function has a heated Maxwellian form. However the shape of the electron-acceptor line observed under conditions of low intensity excitation (10^{-5} W cm^{-2}) implies that the photoexcited electrons have a non-Maxwellian distribution. This is interpreted

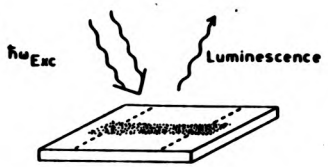

(a)

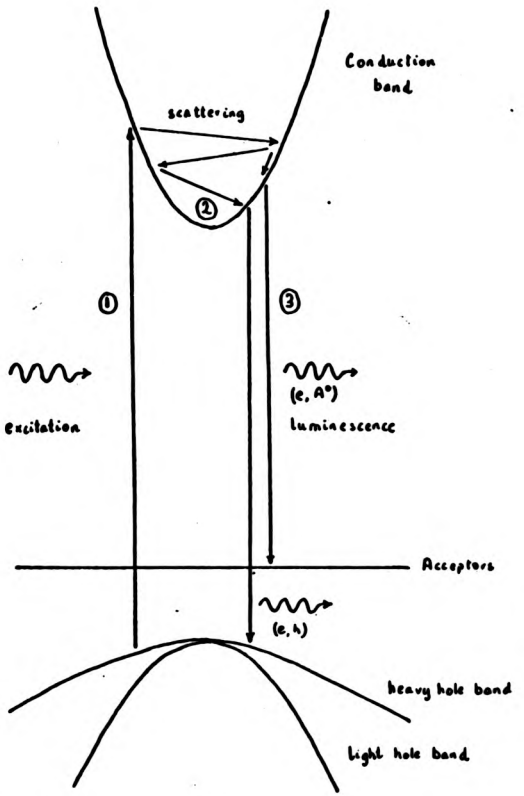

(b)

Fig.2.1. The principle of a typical photoluminescence experiment.

(a) Experimental geometry (from Ulbrich, 1978).

(b) A schematic illustration of the electron transitions involved. For clarity injection from the light hole band has been ignored and only a few scattering transitions are shown.

as meaning that the distribution is unaffected by intercarrier scattering (Ulbrich 1976, 1978b).

The work described in this Chapter involves the use of a one band, Boltzmann equation model to study non-Maxwellian distributions of photo-excited electrons in GaAs. The work is specifically concerned with conditions of continuous, monochromatic photoexcitation and lattice temperatures in the liquid helium range. The aims of the work are threefold. The primary aim is to compute some electron-acceptor luminescence spectra appropriate to low intensity ($\sim 10^{-5}$ W cm^{-2}) photoexcitation of GaAs. A secondary aim is to study how the distribution functions appropriate to low intensity photoexcitation are likely to be characteristic of the phonon scattering events undergone by the photoexcited electrons. The effect of electron-electron scattering is neglected in these two parts of the work. The third aim of the work is to investigate the effect of this scattering mechanism on the photoexcited electron distribution. The results of our work should aid the interpretation of existing photoluminescence data and could help to guide future experiments on photoexcited electrons in GaAs.

We commence the work with a review of some existing experimental results on the photoluminescence properties of GaAs (Section 2.2.1). This is followed by a brief survey of previous theoretical work on photoexcited carriers in general (Section 2.2.2). The one band, Boltzmann equation model for photoexcited electrons in GaAs is described in Section 2.3.1. Most of our work with the model has involved numerical solutions of the Boltzmann equation. Both the steady state distribution function and its time evolution from an initial state in which there are no electrons in the band have been computed. Many of the computed distribution functions correspond to an electron injection spectrum which has the form of a δ function in energy. Section 2.3.2 is concerned with the features of the distribution function which are characteristic of this type of injection spectrum, and with the way in which δ function injection is handled computationally. The material

parameters required to compute the distribution functions are described in Section 2.3.3.

All our distribution functions have been computed using iterative methods. Some knowledge of such methods is essential to understanding these distribution functions. In particular a formal iterative solution of the Boltzmann equation can be used to show how the distribution function is characteristic of the phonon scattering events undergone by the photo-excited electrons (subject to the condition that interelectron collisions have a negligible effect). The iterative methods are described in Section 2.4. Subsections 2.4.1 to 2.4.3 are respectively concerned with the principles of the methods, the formal iterative solution and the implementation of the methods in practice.

In Sections 2.5 to 2.9 we consider the form of the distribution function corresponding to monoenergetic injection of electrons into the band. We present the results of a systematic, compututional study of the distribution functions which would be established if the various electron scattering mechanisms active in GaAs were to operate either collectively, or individually. Our computed distribution functions can be classed into five cases as listed in Table 2.1. Sections 2.5 to 2.9 are concerned separately with each one of these cases. The first two cases involve the distribution functions which would be established as a result of electron-phonon scattering; the effect of electron-electron scattering is neglected. Steady state distribution functions are described in Section 2.5 and their time evolution is explained in Section 2.6. The next two cases involve a large screening model for electron-electron scattering; the effect of electron-phonon scattering is neglected. Steady state distribution functions and their time evolution are described in Sections 2.7 and 2.8 respectively. The final case (Section 2.9) involves electron-electron scattering under conditions such that the electron density is insufficient for the large

Type of Distribution	Injection Spectrum	Scattering Mechanisms taken into account	Recombination Rate	Numerical Procedure	Described in Section
Steady State	δ function	Phonons only	k independent, $R = \frac{A}{(1+Bk^n)^m}$	Matrix Iteration	2.5.
Time dependent	Pulse	Acoustic Phonons only	k independent	Iteration with finite difference approximation to $\frac{\partial f}{\partial t}$	2.6.
Steady State	δ function	Electron-electron (Large Screening Model)	k independent	Iteration	2.7.
Time dependent	Pulse	Electron-electron (Large Screening Model)	k independent	Iteration with finite difference approximation to $\frac{\partial f}{\partial t}$	2.8.
Time dependent	Pulse	Electron-electron (Series Expansion Model). Acoustic phonons	k independent	Iteration with finite difference approximation to $\frac{\partial f}{\partial t}$	2.9.

TABLE 2.1: A classification of the distribution functions described in Sections 2.5 to 2.9.

screening model to be applicable. Both electron-electron and electron-phonon scattering are taken into account. A Taylor series expansion is used to estimate the electron-electron scattering rates.

Our work on electron-acceptor luminescence is described in Section 2.10. Some model distributions functions are computed which are appropriate to interband photoexcitation under conditions such that the carrier density is insufficient for intercarrier scattering to be of importance. Electron-acceptor luminescence spectra for C doped GaAs are derived from these distributions and are compared with some recent experimental results. The chapter closes with a summary of the conclusions we have reached. (Section 2.11).

2.2. Photoexcited carriers in theory and experiment.

2.2.1. Experimental work on monochromatically photoexcited electrons in GaAs at low lattice temperatures.

This subsection is concerned with a review of some experimental work on the photoluminescence properties of GaAs. We start with an explanation of how various luminescence lines can be used to obtain information on the photoexcited electron distribution function. Following this we describe a representative selection of experimental results on photoluminescence in GaAs, under conditions of monochromatic photoexcitation and lattice temperatures in the liquid helium to nitrogen range. We first describe those experimental results which show how the luminescence spectra depend on the excitation intensity and energy. Next we discuss some results on electric field induced heating of photoexcited carriers. Finally we mention some experimental work on transient photoexcitation. The aims, methods and experimental conditions appropriate to the work we review are summarized in Table 2.2.

Two luminescence lines which can provide information on the electron distribution are the electron-hole, (e,h), and electron-acceptor, (e,A^0), lines. (Bauer 1974,1978). If the lattice temperature is in the helium range, the (e,h) line can only be detected if the intensity is sufficiently high

Author	Material	Measured Quantity	Inferred Quantity	Excitation Energy $\hbar\omega_e$ (eV)	Excitation intensity P[Wcm^{-2}]	Lattice temperature ^oK	Refer to Fig.
Ulbrich, 1976,1978	C doped GaAs $N_A \sim 2 \times 10^{20}$ m^{-3}	(e,A^0) lineshape	(e,A^0) lineshape implies a non-Maxwellian distribution of electrons	1.5283, 1.531 1.533	10^{-5}	1.2	2.2a
Ulbrich, 1973	n type N_D=2.8×10^{20} N_A=2.6×10^{20} m^{-3}	dependence of (e,A^0) lineshape on P	T_e as a function of P (Maxwellian distribution)	1.916	2×10^{-4} - 5	4.2	2.2c
Shah and Leite,1969 Shah,1978	n type, p-type $\sim10^{21}$ impurities m^{-3}	dependence of (e,h) lineshape on P	T_e as a function of P (Maxwellian distribution) non-Maxwellian distribution reported for $P > 2 \times 10^5$	2.41	10 - 6×10^6	2.0	2.2b,d
Ulbrich, 1971	n type $N_D = 1.2\times10^{20}$m^{-3} $N_A = 10^{20}$ m^{-3}	dependence of (e,A^0) lineshape on $\hbar\omega_e$	-	1.52 - 2.05	3×10^{-6}	4.2	2.2e
Weissbuch, 1978	p type N_A-$N_D \sim 7\times10^{19}$m^{-3}	dependence of (e,A^0) lineshape on $\hbar\omega_e$	T_e as a function of $\hbar\omega_e$ (Maxwellian distribution)	1.52 - 1.64	10^{-4} - 10^2	1.7	2.2f
Goebel and Hildebrand, 1978	p type N_A-$N_D \sim 1.1\times10^{20}$m^{-3}	dependence of (e,A^0) lineshape on $\hbar\omega_e$	T_e as a function of $\hbar\omega_e$ (Fermi-Dirac distribtuion)	1.52 - 1.646	3×10^{1}	2.0	2.2g
Ulbrich, 1978	N_A,N_D < 10^{20} m^{-3}	Dependence of (e,A^0) lineshape on applied electric field $0\leq E\leq10^3$ Vm^{-1}	-	$\epsilon_G + \frac{3}{2}k_BT_L$	10^{-2}, 10^{-4}	4.2	2.2i
Inoue,1978a	n type	Dependence of (e,A^0) lineshape on applied electric field $0 \leq E \leq 1.05\times10^5$ Vm^{-1}	-	2.814	-	4.2	2.2j
Inoue,1978 a,b,c	n type	Dependence of (e,h) lineshape on electric field $0\leq E\leq1.5\times10^5$ Vm^{-1}	Electron distribution function. Hole distributions assumed to be Maxwellian with a temperature T_L	2.814	-	77	2.2k
Ulbrich, 1973	-	Time dependence of (e,A^0) lineshape following pulse photoexcitation	Time evolution of distribution function	1.916	transient photoexcitation pulse with ≈0.2nS 2×10^{-11} per pulse max. electron density ≈9×10^{18} m^{-3}	4.2	2.2l

Table 2.2: A summary of some photoluminescence experiments on GaAs at low lattice temperatures. Double lines are used within the table to distinguish between different types of experiment. Each type of experiment is discussed in Section 2.2.1.

(Goebel and Hildebrand 1978). The intensity of this line depends on both the electron and hole distributions and some assumptions have to be made if the electron distribution is to be deduced from the (e,h) line shape. If the carrier density is sufficiently low it is assumed that the holes have Maxwellian distributions with a temperature equal to that of the lattice, T_L.(Inoue and co-workers,1978a).Alternatively, if the carrier density is sufficiently high, it is assumed that the electrons and holes are thermalized to a common temperature T_e. (Shah and Leite, 1969).

Interpretation of the (e,A^0) line shape does not involve such assumptions on the nature of the distribution. The intensity of this line has the form (Barry-Bebb and Williams, 1972):

$$I(\omega) \quad \alpha \quad \frac{\omega^2 \, \epsilon_c^{\frac{1}{2}} \, f(\epsilon_c)}{\left[1 + \frac{2m^*}{\hbar^2} \, a^2 \, \epsilon_c\right]^4} \, , \; \epsilon_c = \hbar\omega - \epsilon_G + \epsilon_A \qquad (2.1)$$

where ϵ_c is the energy of an electron in the conduction band, a is the Bohr radius of an acceptor and ϵ_A is the acceptor binding energy. It is evident from equation 2.1 that analysis of the (e,A^0) line shape can yield the distribution function directly.(e,A^0) line shape studies have the additional advantage that the line is not significantly affected by re-absorption effects but have the restriction that well resolved spectra can only be obtained from relatively pure samples (Ulbrich, 1973).

It is implicitly assumed that the distribution function derived from any photoluminescence data is spatially uniform. In general the excitation intensity would be expected to be spatially non-uniform within the sample. As a result the distribution function would be spatially non-uniform due to spatially non-uniform injection of carriers and their subsequent diffusion at different rates. The experimental conditions under which the luminescence spectrum would be well approximated by that from a spatially uniform distribution are uncertain.

One type of photoluminescence experiment involves a study of how the shape of a particular luminescence line depends on the excitation intensity. Ulbrich (1976, 1978b) has made a study of (e,A^0) luminescence from C doped GaAs under conditions of very low intensity photoexcitation (10^{-5} W cm^{-2}) and a lattice temperature of 1.2°K. The excitation energies used in Ulbrich's work have all been sufficiently high to cause interband transitions but sufficiently low for electron injection to occur at an energy below the threshold for longitudinal optical phonon emission. (Our work on (e,A^0) luminescence (Section 2.10) is particularly relevant to these conditions of photoexcitation). Three (e,A^0) spectra which have been recorded by Ulbrich are shown in Fig. 2.2a which illustrates the luminescence intensity as a function of luminescence energy, $\hbar\omega$, ($\hbar\omega = \epsilon_c + \epsilon_G - \epsilon_A$). Distinct shoulders are present in each curve at values of $\hbar\omega$ such that ϵ_c corresponds to injection of electrons from the heavy hole band. Just below the shoulder energy each curve has the form of a flat plateau but each curve is steeper for smaller values of $\hbar\omega$. The presence of the shoulder and plateau implies that the luminescence originates from a non-Maxwellian distribution of electrons, and Ulbrich has interpreted this as meaning that the distribution is unaffected by inter-carrier scattering. He has found that the shoulder and plateau disappear if the excitation intensity is increased. Ulbrich has used this effect to estimate the critical electron density above which the electron energy relaxation rate by inter-electron collisions exceeds the relaxation rate by acoustic phonon collisions. This density is found to be $\sim 5 \times 10^{17}$ m^{-3} (In the experiments leading to the spectra shown in Fig. 2.2a the electron density was 2×10^{16} m^{-3}).

Photoluminescence under conditions of high intensity excitation has been studied by several authors. Ulbrich (1973) has used an excitation energy of 1.916 eV and intensities in the range 2×10^{-4} to 5 W cm^{-2}. The distribution function was inferred from the (e,A^0) line shape and was found to have the form of a heated Maxwellian for all the intensities in the range mentioned. Shah and Leite (1969) and Shah (1974, 1978) performed similar

One type of photoluminescence experiment involves a study of how the shape of a particular luminescence line depends on the excitation intensity. Ulbrich (1976, 1978b) has made a study of (e,A^0) luminescence from C doped GaAs under conditions of very low intensity photoexcitation (10^{-5} W cm^{-2}) and a lattice temperature of 1.2°K. The excitation energies used in Ulbrich's work have all been sufficiently high to cause interband transitions but sufficiently low for electron injection to occur at an energy below the threshold for longitudinal optical phonon emission. (Our work on (e,A^0) luminescence (Section 2.10) is particularly relevant to these conditions of photoexcitation). Three (e,A^0) spectra which have been recorded by Ulbrich are shown in Fig. 2.2a which illustrates the luminescence intensity as a function of luminescence energy, $\hbar\omega$, ($\hbar\omega = \epsilon_c + \epsilon_G - \epsilon_A$). Distinct shoulders are present in each curve at values of $\hbar\omega$ such that ϵ_c corresponds to injection of electrons from the heavy hole band. Just below the shoulder energy each curve has the form of a flat plateau but each curve is steeper for smaller values of $\hbar\omega$. The presence of the shoulder and plateau implies that the luminescence originates from a non-Maxwellian distribution of electrons, and Ulbrich has interpreted this as meaning that the distribution is unaffected by inter-carrier scattering. He has found that the shoulder and plateau disappear if the excitation intensity is increased. Ulbrich has used this effect to estimate the critical electron density above which the electron energy relaxation rate by inter-electron collisions exceeds the relaxation rate by acoustic phonon collisions. This density is found to be $\sim 5 \times 10^{17}$ m^{-3} (In the experiments leading to the spectra shown in Fig. 2.2a the electron density was 2×10^{16} m^{-3}).

Photoluminescence under conditions of high intensity excitation has been studied by several authors. Ulbrich (1973) has used an excitation energy of 1.916 eV and intensities in the range 2×10^{-4} to 5 W cm^{-2}. The distribution function was inferred from the (e,A^0) line shape and was found to have the form of a heated Maxwellian for all the intensities in the range mentioned. Shah and Leite (1969) and Shah (1974, 1978) performed similar

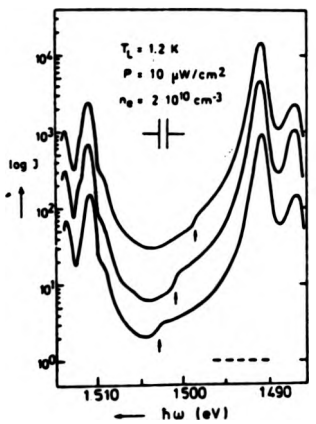

Fig. 9. The short wavelength tail of the (e, A^0) band exhibits kinks which are caused by the optical injection of electrons (excitation wavelengths: 8122, 8108 and 8096 Å). The arrows give the position of the initial electron energy for the transition $hh \rightarrow e$.

(a) (from Ulbrich, 1978b)

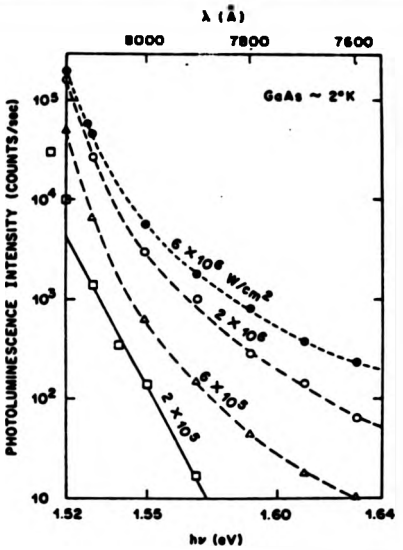

Fig. 5. High Energy Photoluminescence tail in GaAs showing the non-Maxwellian carrier distributions for $I > 2 \times 10^5$ W/cm² (from Shah, Ref. [9]).

(b) (from Shah, 1978)

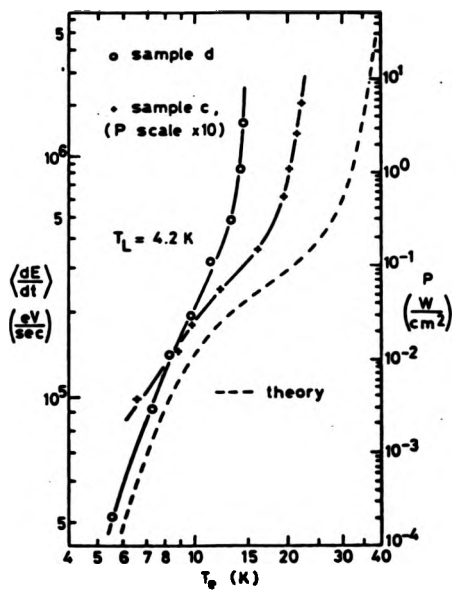

FIG. 4. Electron temperature T_e as a function of absorbed excitation light power P (right-hand ordinate scale), as measured in the cw experiments (solid lines). The left-hand ordinate scale gives the average power per carrier, $\langle dE/dt \rangle$, transferred to the randomized electron distribution. For comparison, the theoretical energy-loss rate is shown for a lattice temperature $T_L = 4.2$ K (dashed line). Note that the relation between $\langle dE/dt \rangle$ and P is not linear, as defined by Eqs. (11)–(13) (see Sec. V B).

(c) (from Ulbrich, 1973)

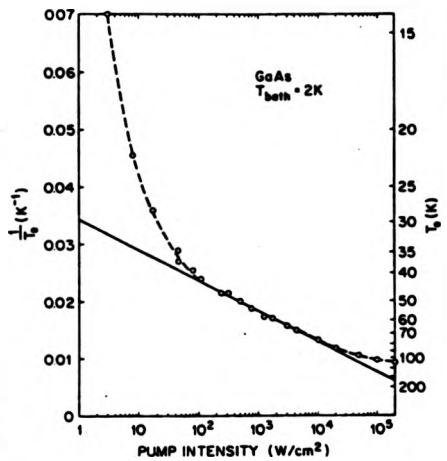

Fig. 3. $(1/T_e)$ vs Excitation Intensity I for GaAs at 2K. The points are experimental data from Refs. [1] and [9]. The solid line corresponds to a slope of $(\hbar\omega_0/k) = 427$K where $\hbar\omega_0 = 36.8$ meV = LO phonon energy.

(d) (from Shah, 1978)

Figs.2.2a to d. Some experimental results on the excitation intensity dependence of photoluminescence spectra (See also Table 2.2)

a,b luminescence due to non-Maxwellian distributions at low and high intensity respectively.

c,d Electron temperature as a function of excitation intensity

Authors captions have been retained for clarity.

(e)
(from
Ulbrich,1978b)

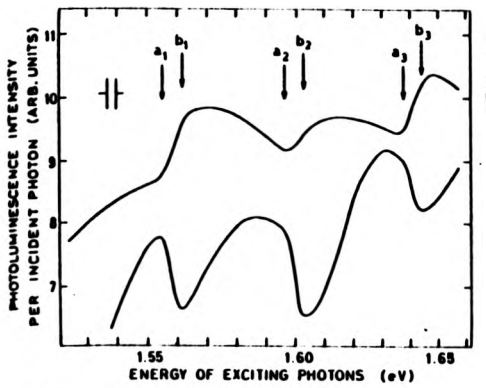

FIG. 2. Excitation spectra of the (D^0, A^0) luminescence (upper curve) and the (e, A^0) luminescence (lower curve). The arrows indicate the theoretical thresholds for relaxation of hot conduction-band electrons into 5.8-meV-deep donor states (a_n) or into the $k = 0$ conduction-band minimum (b_n) by successive emission of n LO phonons.

(f)
(from
Weisbuch,1978)

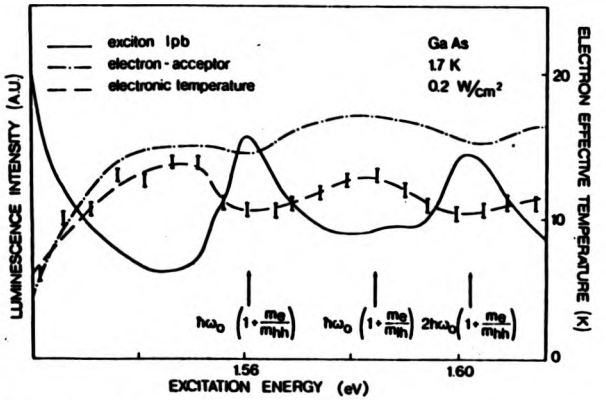

Fig. 2. Excitation spectra of high-purity GaAs ($N_A - N_D \approx 7.10^{13}\,cm^{-3}$). Full line and dashed-dotted line represent respectively the intensity of lower polariton emission at 1.515 eV and electron-acceptor emission at 1.4937 eV (*not* the integrated intensity of these lines). The dashed line is drawn for conveniency to join the experimental points displaying the effective electron temperature deduced from the lineshape analysis of the electron-acceptor line.

(g)
(Results due to
Goebel et al 1978;
figure from Shah,
1978.)

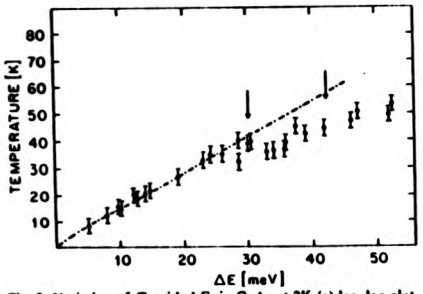

Fig. 9. Variation of T_e with ΔE_e in GaAs at 2K (a) log. log plot, (b) linear plot (from E. Goebel and O. Hilderbrand, to be published).

(h)
(from Komolov
and Yassievich,1974)

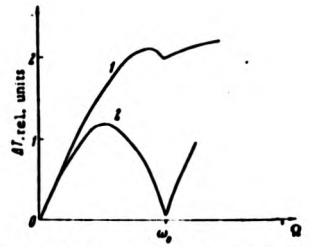

Fig. 3. Dependence of the excess of the electron temperature over the lattice temperature ($\Delta T = T_e - T_0$) on the frequency of incident light: 1) $\nu_{opt}/\nu_{ee} \ll 1$; 2) $\nu_{opt}/\nu_{ee} \sim 1$.

Figs. 2.2e to f.

Some results on the excitation energy dependence of photoluminescence spectra.

a. excitation energy dependence of luminescence at low excitation intensity.

f,g excitation energy dependence of T_e at higher excitation intensities

h theoretical ~~carriers for~~ T_e as a function of excitation energy

Authors captions have been retained for clarity.

(i) part 1
(from
Ulbrich 1978b)

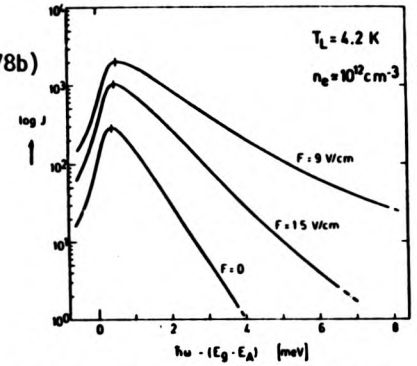

Fig. 11. Measured number densities of a low-density electron plasma for different fields strengths. Note the logarithmic ordinate scale; the curves are shifted by a factor 4 for clarity. There is pronounced heating and a non-Maxwellian high energy tail.

(i) part 2
(from
Ulbrich, 1978)

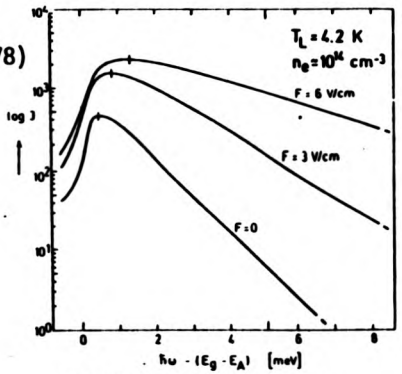

Fig. 12. Electron heating at higher densities.

(j)
(from Inoue
et al, 1978a)

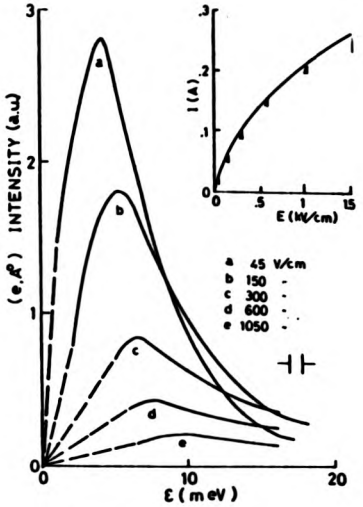

Fig. 3. (e, A^0) luminescence of Zn:GaAs at 4.2K with applied electric fields.

(k)
(from Inoue
et al, 1978b)

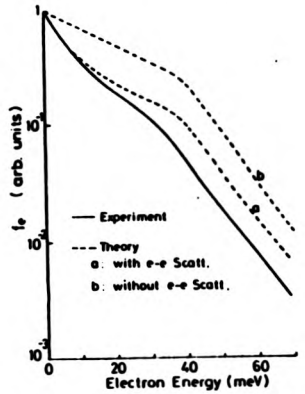

Fig. 5. Comparison of the electron distribution function at 900 V/cm between experiment and theory with and without inter-electron scattering. The concentrations of electrons and impurity are assumed to be $n = N_I = 5 \times 10^{14}$ cm^{-3}.

(l)

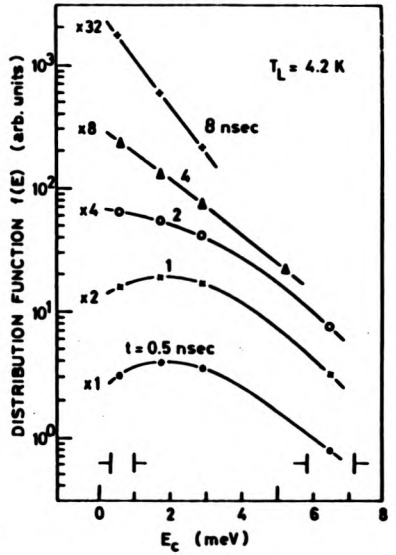

FIG. 2. Electron energy distribution function $f(E)$ at different times t after the photoexcitation of hot electrons at $t = 0$ with a 0.2-nsec light pulse. $f(E)$ was determined from time-resolved measurements of the (e, A^0) emission line shape. For clarity the curves are shifted vertically by the factors indicated at left.

Figs.2.2i to k. Some experimental results on the dependence of luminescence spectra on electric field

Inset in Fig.2.2j shows electric current as a function of field

Fig.2.2l. A distribution function derived from the results of a transient photoexcitation experiment (Ulbrich,1973) Authors captions have been retained for clarity.

experiments, but have analysed the (e,h) line shape. They used an excitation energy of 2.41 ev and excitation intensities >10W cm^{-2}. It was found that if the excitation intensity was in the range 10 to 10^5 W cm^{-2} the distribution function took the form of a heated Maxwellian. However, for excitation intensities greater than 2×10^5 W cm^{-2} the (e,h) spectrum could not be explained on the assumption that the carrier distributions were Maxwellian: the high energy ($\geq$ 1.55 eV) part of the spectrum was found to have a flat, non-Maxwellian tail. (Fig. 2.2b). The reason for this non-Maxwellian behaviour is still uncertain.

Both Shah and Leite and Ulbrich have compared the temperatures of their Maxwellian distributions against theoretical predictions. For this purpose power balance methods are used. The rate at which the electron distribution receives energy from the excitation radiation is equated to the rate at energy is lost to the lattice and thus a fair prediction of the electron temperature is obtained (Figs. 2.2c,d).

A different type of photoluminescence experiment involves a study of how the luminescence spectrum depends on the excitation energy. Various authors have described the results of this type of experiment and some of these results are not in mutual agreement: it appears that the form of the spectrum depends critically on the excitation intensity used. The first work on the dependence of the luminescence spectrum on excitation energy is due to Ulbrich (1971). He has studied electron-acceptor luminescence in GaAs at a lattice temperature of 4.2^{o}K under conditions of very low intensity photoexcitation (3×10^{-6} W cm^{-2}). The intensity of the (e,A^{o}) emission at a function of excitation energy is found to have a periodic structure (Fig. 2.2e). Maxima are present at excitation energies such that electrons injected from the heavy hole band can relax into the bottom of the conduction bandvia longitudinal optical (L.O) phonon emission. Minima are present if the excitation energy is such that electrons injected from the heavy hole band can be captured into donor ground states via L.O. phonon

emission. This periodic structure is coupled to a similar but complementary structure in the donor-acceptor emission. No oscillations corresponding to electrons injected from the light hole band are evident. Ulbrich has shown from an analysis of the (e,A^0) line shape that the electrons had a Maxwellian distribution with a temperature of $5.1 \pm .1^\circ K$. He has interpreted the results of his experiment as providing evidence for direct capture of electrons into donor ground states via L.O. phonon emission.

Weisbuch (1978a) has studied the excitation intensity dependence of the (e,A^0) luminesence spectrum of GaAs at a lattice temperature of $1.7^\circ K$. He has used excitation intensities in the range 10^{-4} to 10^2 W cm^{-2}. From an analysis of his (e,A^0) spectra he has shown that the photoexcited electron distribution function has the form of a heated Maxwellian. The electron temperature as a function of excitation energy is found to have an oscillatory structure (Fig. 2.2f). Minima are present at excitation energies such that electrons injected from the heavy hole band can relax into the conduction band minimum by emitting L.O. phonons. Some subsidiary oscillations characteristic of injection of electrons from the light hole band are also present. The intensities of the (e,A^0) and exciton lines are also found to be oscillatory functions of the excitation energy.

Goebel and Hildebrand (1978; see also Hildebrand, Goebel and co-workers, 1978 and Hildebrand, Goebel and Romanek, 1978) have also reported work on the excitation energy dependence of photoluminescence in GaAs. They have studied the (e,h) line shape at an excitation intensity of 3×10^3 W cm^{-2} and a lattice temperature of $2^\circ K$. They show that the (e,h) line shape can be understood if the electrons and holes are assumed to have Fermi-Dirac distributions. However, they do not find that the electron temperature as a function of excitation energy has a periodic structure. (Fig. 2.2g). Instead the electron temperature curve has a change in slope at an excitation energy such that the energy of electrons injected from the heavy hole band is equal to the threshold energy for L.O. phonon emission.

The response of photoexcited electrons to an applied electric field has been studied by several authors. Ulbrich (1978b) has used resonant excitation (i.e. $\hbar\omega_e = \epsilon_G + \frac{3}{2} K_B T_L$, $T_L = 4.2^oK$) at intensities of 10^{-4} and 10^{-2} W cm^{-2}, to study electron heating by fields in the range 0 to 10^3 Vm^{-1}. The symmetric part of the distribution is inferred from the (e,A^o) line shape, and at the lower intensity is found to have a non-Maxwellian high energy tail (Fig. 2.2i). Similar work has been reported by Inoue and co-workers (1978a,b,c). Photoluminescence in samples of GaAs at lattice temperatures of 4.2^oK and 77^oK has been excited with a He-Cd laser operating at 2.814eV. Electric fields in the range 0 to 1.5×10^5 Vm^{-1} have been used in the experiments. The low temperature experiment has simply involved observations of the (e,A^o) line shape (Fig. 2.2j). The results of the high temperature experiment have been quantitatively analysed. The symmetric part of the electron distribution function has been deduced from the (e,h) line shape and has been compared with the results of Monte Carlo calculations. Fair agreement has been obtained (Fig. 2.2k).

A rather different type of photoluminescence experiment involves *transient* photoexcitation. Ulbrich (1973) has photoexcited a sample of GaAs at a lattice temperature of 4.2^oK with a single light pulse 0.2nS wide and has observed the time evolution of the (e,A^o) luminescence over a period of 12 nS following excitation. The excitation energy was 1.916 eV. He found that the electron distribution function had a heated Maxwellian form at times greater than 2nS following the application of the excitation pulse (Fig. 2.2k).

2.2.2. Theoretical studies of photoexcited carriers.

In contrast to the wealth of experimental results on photoexcited electrons in GaAs (as described in the previous section) there is a paucity of theoretical work on photoexcited electrons in the same material. Indeed only a few theoretical studies of the distribution function for photoexcited

carriers in any material have been reported. Some of these studies are listed in Table 2.3 and are described in this subsection. The first work involving calculations of photocarrier distribution functions is due to Hearn (1966). He considered a one-band model and assumed that the electron-electron interaction was dominant. The electron injection spectrum was supposed to have the form of a narrow pulse and the electron life time was assumed to be energy independent. Numerical calculations were made of the first order departure from a Maxwellian distribution, whose temperature could be determined from a power balance equation. It was found that large deviations from the Maxwellian form occurred if the inter-electron collision rate was significantly less than the recombination rate. In addition it was emphasized that the distribution could only be close to a Maxwellian form if the electron density was high enough for the inter-electron collision rate to exceed the electron phonon transition rate.

A general theory of the steady state distribution and transport properties of photoexcited electrons under conditions of black body excitation from a single donor level at low lattice temperatures, has been given by Barker and Hearn (1973; see also Hearn, 1979). The electron density was assumed to be sufficiently low for the electron-electron collision rate to be negligible and numerical calculations of the steady state distribution function were made. The theory was applied to germanium and silicon. Recently (1978) Noguerra and Hearn have applied a similar theory to study the properties of hot photoexcited holes in copper doped germanium. In addition Noguerra (1978) has investigated the steady state distribution function for monochromatically photoexcited holes in the same material.

The distribution functions calculated by Barker and Hearn are appropriate to conditions when the recombination rate is comparable to or greater than the scattering rates. Ridley and Harris (1976) have investigated the form of the distribution in the opposite extreme i.e. when the recombination rate is small compared with the scattering rates. They consider laser excitation of a model semiconductor; electrons are injected from donors·

Author	Excitation spectrum	Scattering mechanisms	Recombination rate relative to scattering rate	Material and type of carrier
Hearn 1966	Monochromatic	electron-electron	All values	Model calculation
Barker & Hearn 1973	Black Body	acoustic phonon L.O. phonon	$R \gtrsim S$	Si, Ge; electrons, holes
Noguerra and Hearn 1978	Black Body	acoustic phonon L.O. phonon	$R \gtrsim S$	Cu doped Ge, holes
Noguerra 1978	Monochromatic	acoustic phonon	$R \gtrsim S$	Cu doped Ge, holes
Ridley and Harris 1973	Monochromatic	acoustic phonon L.O. phonon	$R << S$	Model calculation electrons
Komolov & Yassievich, 1974	Monochromatic	electron-electron L.O. phonon	$R << S$	Model calculation electrons

Table 2.3: A summary of some theoretical work on distribution functions for photoexcited carriers. A further discussion of the work is given in Section 2.2.2.

into the conduction band. Electron-electron scattering is neglected and recombination is supposed to occur only by stimulated emission of photons. The lattice is taken to be at room temperature. If the excitation spectrum takes the form of a single laser line the distribution function is predicted to have a Maxwellian form with a temperature T_L. Significant departures from the Maxwellian form are expected only if the excitation is due to multiple laser lines.

In a most interesting paper Komolov and Yassievich (1974) have studied a model for the distribution function such that the only relevant scattering mechanisms are electron-electron scattering and optical phonon emission, and the recombination rate is smaller than the scattering rates. Unfortunately a prerequisite for a full understanding of their treatment of the electron-electron interaction is a paper by Landau (1937) for which no English translation appears to be available. Equivalent information has probably been given by Dykman and Tomchuk (1960). It appears that Komolov and Yassievich made use of a Fokker-Planck approach to the electron-electron collision term. The essence of the method, is the use of a Taylor series expansion of the distribution function, which enables the electron-electron collision integral to be approximated by a non-linear differential term. It is to be noted that if the inter-electron collisions are treated classically a rather arbitrary upper cut-off to an integration over impact parameters has to be imposed to avoid divergence of the coefficients in the differential term. Similarly if the golden rule is employed to estimate the collision rate an upper cut-off is involved to an integration over the magnitude of the change in electron wave vector. Komolov and Yassievich solved their differential equation by using a Maxwellian function with an effective temperature T_{eff} to approximate the non-linear terms. The value of the effective temperature was then determined by substituting the resulting solution into a power balance equation. They found that if the electron-electron

collision rate is of the order of the phonon emission rate a minimum in T_{eff} as a function of injection energy is present at the L.O. phonon threshold energy. If the electron density is large enough for inter-electron collisions to be dominant the minimum is less pronounced.(Fig.2.2h) The qualitative agreement between their calculations and the experiments of Weisbuch and Goebel et al, as described in the previous subsection, is remarkable.

2.3. The distribution function for photoexcited electrons in GaAs at low lattice temperatures : a model.

2.3.1. The model

We consider the simplest model situation relevant to low temperature photoluminescence in GaAs. The optical excitation causes injection of electrons into a spherical, parabolic conduction band. They are scattered during their lifetime and then recombine. No thermally excited electrons are present. Exciton and plasmon effects are ignored. The electron distribution function $f(\underline{k},t)$ is assumed to be spatially uniform and hence to obey the Boltzmann transport equation (Ziman, 1960) in the form

$$\frac{\partial f}{\partial t} = \left.\frac{\partial f}{\partial t}\right|_{scat} - R(k)f(\underline{k}) + G(k,t) \qquad (2.2)$$

Some of the assumptions underlying our model are discussed in Chapter 5. For a discussion of the validity of the Boltzmann equation we refer to a review by Barker (1979). In equation 2.2 G and R are generation and recombination rates respectively and $\left.\frac{\partial f}{\partial t}\right|_{scat}$ is the collision term. The photoexcitation is assumed to be suddenly applied at a time $t = 0$ and is supposed to be continuous at all subsequent times. Hence $G(k,t)$ takes the form of the product of a unit step function $\theta(t)$ and a time independent injection rate $G(k)$. Initially no electrons are present in the band therefore equation 2.2 is solved subject to the initial condition:

$$f(\underline{k},0) = 0 \qquad (2.2a)$$

We can immediately make a simplifying assumption, namely that the electron distribution is non-degenerate. This assumption is likely to be a good one. In the case of monoenergetic injection it is justifiable if the photoexcitation process does not fill the states having the injection energy, (or, equivalently the remaining energy of an electron after it has completed any possible L.O. phonon emissions) and if the scattering processes do not fill the states at the bottom of the band. Let us consider first the states with energy ϵ_i. Assume that the injection energy is 10 meV above the conduction band minimum, and that the width $\Delta\epsilon_i/\epsilon_i$ of the injection spectrum is $\sim 10^{-6}$. (The linewidth of a typical laser). Then the total number of states available to the injected electrons is $\frac{1}{3}(2m^*/\hbar^2)^{3/2}\ \epsilon_i^{\frac{1}{2}}\ \Delta\epsilon_i \sim 2 \times 10^{20}\ m^{-3}$. In a typical experiment the injection rate would be no more than $\sim 10^{27}\ m^{-3}\ s^{-1}$ and the phonon scattering out rate* for a 10 meV electron in GaAs is $\sim 10^{9}\ s^{-1}$. Therefore the number of electrons within $\Delta\epsilon_i$ of ϵ_i would be $\sim 10^{18}\ m^{-3}$, which is considerably less than the number of available states. Now consider the states at the band minimum. These states could be filled if the scattering rates were large compared to the recombination rate. But if the scattering rates were of such a magnitude the distribution function would be well approximated by a Fermi-Dirac function. A typical photoluminescence experiment would involve electron densities no more than $\sim 10^{20}\ m^{-3}$ and so the Fermi level would be no more than ~ 0.1 meV above the bottom of the band. The assumption of non-degeneracy is therefore justifiable.

In general the collision term of the Boltzmann equation can be written in terms of a transition rate $S(\underline{k}' \rightarrow \underline{k})$ for scattering of an electron from a state $\underline{k}'$ to a state $\underline{k}$. (Ziman, 1960). Making use of the collision term appropriate to a non-degenerate distribution of electrons

* The scattering in or out rate for an electron in a state $\underline{k}$ is the rate at which it is scattered into or out of that state.

we write equation 2.2 explicitly in terms of S as follows:

$$\frac{\partial f}{\partial t} = \int f(\underline{k}',t)\, S(\underline{k}' \rightarrow \underline{k})d\underline{k}' - f(\underline{k},t) \int S(\underline{k}\rightarrow\underline{k}')d\underline{k}' - R(k)f(\underline{k},t)+G(k)\theta(t) \tag{2.3}$$

And analogously, the steady state distribution function obeys the equation

$$\int f(\underline{k}')S(\underline{k}' \rightarrow \underline{k})d\underline{k}' - f(\underline{k}) \int S(\underline{k}\rightarrow\underline{k}')d\underline{k}' - R(k)f(\underline{k}) + G(k) = 0 \tag{2.4}$$

In the remainder of this subsection we explain the forms of the generation, scattering and recombination terms appropriate to our work on GaAs.

The generationand recombination rates cannot be treated exactly within a one band model because in reality they involve the populations of carriers in impurity levels and in other bands. We therefore choose some empirical forms for G and R. The precise form chosen for G differs according to the purpose for which we are solving the model. In all cases injection into the band is assumed to be isotropic.

In Section 2.10 we compare the predictions of the model with the results of a photoluminescence experiment involving inter-band injection due to monochromatic photoexcitation. The appropriate generation rate is

$$G(k) = Q\{ \frac{X_l}{e(\epsilon_{il})}\ \delta(\epsilon(k) - \epsilon_{il}) + \frac{X_h}{\rho(\epsilon_{ih})}\ \delta(\epsilon(k) - \epsilon_{ih})\} \tag{2.5}$$

ρ is the density of states in the conduction band and Q the total rate at which electrons are injected. ϵ_{il} and ϵ_{ih} are energies corresponding to injection from the light and heavy hole bands respectively. X_l and X_h are the fractions of electrons injected from each of these bands.

In Sections 2.5 to 2.9 we are also concerned with monochromatic photo-excitation but our principal aim is to understand how the steady state distribution function and its time evolution are characteristic of the injection, scattering and recombination processes. Emphasis is placed on

the scattering processes so it is convenient to choose the simplest injection rate consistent with monochromatic photoexcitation: direct computations of the steady state distribution function are made with G(k) in the form of a single δ function at an energy ϵ_1:

$$G(k) = \frac{Q}{\rho(\epsilon_1)} \delta(\epsilon(k) - \epsilon_1). \tag{2.6}$$

However, for computational reasons, calculations of the time evolution of the distribution function are made using a narrow pulse for G(k):

$$\begin{aligned} G(k) &= \frac{Q}{\rho_T} \quad \text{if } k_1 - \Delta k \le k \le k_1 + \Delta k \\ &= 0 \quad \text{otherwise.} \end{aligned} \tag{2.7}$$

K_1 is the magnitude of the wave-vectors corresponding to energies ϵ_1 and ρ_T is the density of states in the conduction band, integrated over the range of energies for which the pulse is non-zero. Δk is taken to be equal to the mesh step used in the calculations. Numerical tests have shown that for wave vectors whose magnitude is other than within Δk of k_1, the steady state distributions computed with pulse and δ function injection spectra agree to within 1%.

In choosing an empirical form for R(k) we would like to make use of experimental data. Unfortunately little appropriate data is available. Weisbuch (1978b) has stated that in his experiments the energy loss rate due to the luminescence is a small fraction of the rate at which energy is supplied by the laser. Hence radiative recombination is unlikely to be the most important recombination process. Ulbrich (1973) has used the decay rate of the luminescence to estimate the electron lifetime to be $\sim 10^{-7}$s. In most of our work we employ an k independent recombination rate of 10^7 s^{-1}. However we have computed a few distribution functions using various empirically chosen k dependent recombination rates. These distribution functions are described in Section 2.5.

The Kernel S of equation 2.3 formally represents all the scattering mechanisms appropriate to the conduction band of GaAs. We consider impurity scattering, phonon scattering and electron-electron scattering. One of the phonon scattering mechanisms in GaAs, piezoelectric scattering by acoustic phonons, is anisotropic (i.e. the piezoelectric scattering rate depends on the orientation of the phonon wave vector with respect to the crystal axes. If piezoelectric scattering was the only scattering mechanism then $f(\underline{k})$ could be anisotropic. However in a real crystal elastic scattering of electrons by ionized and neutral impurities always occurs. These two scattering mechanisms connect states on the constant energy surfaces, which, in our model, are assumed to be spherical. And because the elastic scattering rate is expected to be large compared to the piezoelectric scattering rate it is physically plausible that the isotropic part of $f(\underline{k})$ is large compared to the anisotropic part. Under these conditions the isotropic part of f can be found from equation 2.3 (to a good approximation) if the piezoelectric scattering rates are replaced by their spherical averages. The spherical averaging does not affect the isotropic scattering rates so we can write the Boltzmann equation for the isotropic part offin terms of $S(\underline{k}' \rightarrow \underline{k})$ as follows:

$$\frac{\partial f}{\partial t} = \int f(k',t) \langle S(\underline{k}' \rightarrow \underline{k}) \rangle d\underline{k}' - [\lambda(k)+R(k)]f(k,t) + G(k)\theta(t) = 0 \qquad (2.8)$$

where $f(k,t)$ is the isotropic part of $f(\underline{k},t)$.
And similarly the isotropic part $f(k)$ of the steady state distribution function is given by the equation:

$$\int f(k') \langle S(\underline{k}' \rightarrow \underline{k}) \rangle d\underline{k}' - [\lambda(k) + R(k)]f(k) + G(k) = 0. \qquad (2.9)$$

All the distribution functions described in this chapter have been obtained by solving either equation 2.8 or 2.9. In these equations $\langle S(\underline{k}' \rightarrow \underline{k}) \rangle$ and $\lambda(k)$ are spherically averaged scattering kernels and scattering out rates respectively and are defined as follows:

$$\langle S(\underline{k}' \rightarrow \underline{k}) \rangle = \frac{1}{4\pi} \int S(\underline{k}' \rightarrow \underline{k}) d\Omega \quad \lambda(k) = \frac{1}{4\pi} \int S(\underline{k} \rightarrow \underline{k}') d\underline{k}' \; d\Omega.$$

The spherical averaging procedure is discussed further in Appendix 2.1.

Because f(k,t) and f(k) are isotropic only inelastic scattering processes need be taken into account explicitly in the scattering term of equations 2.8 and 2.9. These processes are electron-phonon (e.p.) scattering and electron-electron (e.e.) scattering. To calculate the e.p. scattering rates we suppose that for each acoustic phonon wave vector there are two degenerate modes of transverse polarization and one mode of longitudinal polarization, and each mode is assumed to have a linear dispersion relation. The longitudinal optical phonon frequency is taken to be independent of wave vector. In addition all the types of phonon are assumed to be in thermal equilibrium. Deformation potential (D.P.) and piezoelectric (L.P.) scattering by longitudinal acoustic phonons,piezoelectric (T.P.) scattering by transverse acoustic phonons and polar scattering by longitudinal optical (L.O.) phonons are taken into account. To calculate the e.e. scattering rates we use one of two models which are explained in Sections 2.7 and 2.9. At present it is sufficient to note that the scattering kernel appropriate to e.e. scattering is functionally dependent on f because it involves an integration of the product of f with a suitable matrix element. Full mathematical details of the e.e. and e.p. scattering rates we have used in our work are given in Appendix 2.3.

Screening of the piezoelectric, polar and electron-electron interactions has been taken into account(within the Debye approximation) in deriving the scattering rates given in Appendix 2.3. Screening of the deformation potential interaction has been ignored. In principle the change in electron density associated with an acoustic phonon does affect the D.P. interaction and this effect should be taken into account.

this could be done if we knew the deformation potential constant at zero electron density, but we are uncertain how to correct the available D.P. constant which is measured in the presence of the conduction band electrons. (The effect of screening on the D.P. interaction has been taken into account in calculations due to Narayaramurti, Logan, Chin and Lax but these authors have not given details of how their calculations were done).

Within the Debye approximation the potential due to a point change, q, screened by an isotropic distribution of electrons, has the form $V(\underline{r}) = (4\pi\varepsilon\varepsilon_0 r)^{-1} q e^{-\mu r}$. And the inverse screening length μ is given by the following equation (See Appendix 2.3):

$$\mu^2 = \frac{1}{\pi^2} \frac{e^2}{\varepsilon\varepsilon_0} \frac{m^*}{\hbar^2} \int_0^\infty f(k)dk \qquad (2.10)$$

An inverse screening length of this kind is present as a parameter in all the scattering rates tabulated in Appendix 2.3 (Except for D.P. scattering which is assumed to be unscreened). The form given by equation 2.10 is appropriate to the screening effect of the electrons on the electron-electron and piezoelectric interactions. The form appropriate to screening of the polar interaction of electrons and L.O. phonons is similar except that the low frequency dielectric constant ε in equation 2.10 is replaced by the high frequency dielectric constant ε_∞. (Note that the replacement of ε by ε_∞ is an agreement with the L.O. phonon scattering rates given by Ehrenreich (1959) but does not agree with the form given by Zawadzki and Szymańska (1971) who use ε in place of ε_∞). In addition to its direct effect on the strength of the polar interaction screening also causes a change in the L.O. phonon frequency. (Ehrenreich 1959, Zawadzki and Szymańska, 1971). However this change is small and we have neglected it.

In order to compute a distribution function it is, in principle, necessary to solve equations 2.10 and 2.8 or 9 self consistently for μ and f. We have attempted to do this but we have been unsuccessful: a

prohibitive amount of computer time is required. An additional problem connected with screening is that we cannot use a one band model to take full account of all screening effects: in a real crystal screening by holes and ionized impurities occurs additionally to screening by electrons. Because of these difficulties we treat μ as a free parameter whose value is specified prior to computation of a distribution function. The computed distribution function is then used to calculate μ according to equation 2.10 and this provides a test of whether the specified value is adequate.

2.3.2. The effect of monoenergetic injection of electrons into a conduction band.

In this subsection we consider the form of the distribution functions corresponding to a δ function injection spectrum. First we show how various features of the distribution function are characteristic of this type of injection and then we explain how δ function injection is handled computationally. Only the monoenergetic injection spectrum given by Equation 2.6 is considered explicitly and emphasis is placed on the physical meaning of the mathematical results used in our subsequent numerical work. Full mathematical details of the quantities introduced here are given in Appendix 2.2.

First we consider the form of the distribution function which would result if the only inelastic scattering mechanism active was scattering by L.O. phonons of energy $\hbar\omega_0$. Because the injection is monoenergetic and because L.O. phonon scattering is the only active inelastic scattering mechanism, the electrons can only occupy states whose energies differ from the injection energy by integral multiples of $\hbar\omega_0$. At low temperatures only emission of L.O. phonons can occur and the injected electrons lose energy by a cascade of such emissions. The solution of the Boltzmann equation appropriate to these conditions has the form of a δ function ladder:

$$f(k,t) = \sum_{n=0}^{N_0} a_n(t)\ \delta(\epsilon(k) - \epsilon_i + n\hbar\omega_0) \qquad (2.10a)$$

ϵ_i is the injection energy and N_0 is the maximum possible number of L.O. phonon emissions. The actual values of the a_n do not concern us at present. They obey a system of equations which results when the form of f given by equation 2.10a, the injection spectrum given by equation 2.6, and the L.O. phonon scattering rates given in Appendix 2.3 are substituted into equation 2.8.

If other inelastic scattering mechanisms are active in addition to L.O. phonon scattering electrons can also be scattered into states other than those connected by the L.O. phonon emissions. Therefore the distribution function consists of the sum of a non-singular function, $\bar{f}$, and a ladder of δ functions

$$f(k,t) = \bar{f}(k,t) + \sum_{n=0}^{N_0} a_n(t)\ \delta(\epsilon(k) - \epsilon_i + n\hbar\omega_0) \qquad (2.11)$$

The singular part of the distribution (i.e. the δ function ladder) is characteristic of those electrons which have either undergone no inelastic scattering events or have emitted one or more L.O. phonons. The non-singular part $\bar{f}$, is characteristic of those electrons which have undergone at least one inelastic collision via a mechanism other than L.O. phonon scattering, and additionally may have emitted one or more L.O. phonons. The distribution function corresponding to an interband injection spectrum (equation 2.5), has a similar form to that given by equation 2.11 except that there is a separate L.O. phonon ladder, for each of the injection energies ϵ_{il} and ϵ_{ih}.

In sections 2.5 to 2.10 of this chapter we describe many computed distribution functions. It is to be understood that for all cases involving δ function injection these distribution functions have been computed by writing f as the sum of its singular and non-singular parts and that the

results presented (in graphical form) refer to $\bar{f}$. In general $\bar{f}$ and the a_n are found from a coupled system of integro-differential equations which we describe fully in Appendix 2.2. Knowledge of the detailed form of these equations is not essential to understanding the results of our computations. However some knowledge of the way in which $\bar{f}$ and the a_n are related is required to follow our discussion of the iterative method (Section 2.4). We summarize the pertinent results from Appendix 2.2 in the remainder of this subsection.

If only e.p. scattering is taken into account the equations for $\bar{f}$ and the a_n are not coupled. The a_n are found from a system of difference equations in (Appendix 2.2) involving the phonon scattering rates. $\bar{f}$ obeys equation 2.9 with the true generation rate G replaced by an effective generation rate $\bar{G}$ which is the rate at which are injected and then enter other states in the band by interacting with an acoustic phonon, either directly or by prior emission of one or more L.O. phonons. If the injection energy is below the L.O. phonon theshold energy all the a_n are vanishing, except a_0 which then has the particularly simple form:

$$a_0 = \frac{1}{\lambda(k_i) + R(k_i)} \quad \frac{Q}{\rho(\epsilon_i)} \tag{2.12}$$

Physically, this form of a_0 represents the number of electrons per state with energy ϵ_i, which have undergone no collisions. The effective generation rate appropriate to injection below the L.O. threshold is as follows :

$$\bar{G}(k) = \frac{Q\pi^2}{\lambda(k_i) + R(k_i)} \int \langle S(\underline{k}' \rightarrow \underline{k}) \rangle \, d\Omega' \Big|_{k'=k_i} \tag{2.13}$$

If e.e. scattering is the sole scattering mechanism taken into account $\bar{f}$ and a_0 are given by the solution to a coupled pair of equations. The form of a_0 is as given by equation 2.12 but λ is functionally dependent on $\bar{f}$. $\bar{f}$ obeys an equation similar to 2.9 with the generation rate G

replaced by an appropriate effective generation rate $\bar{G}$ which describes the rate at which electrons are injected and then scattered out of the states with energy ϵ_1. In addition the scattering rates S and λ must be replaced by effective scattering rates $\bar{S}$ and $\bar{\lambda}$ which are each a sum of contributions describing scattering of the electrons in the non-singular part of f by other electrons in the non-singular part and by electrons in the singular part. This latter rate depends on a_0. The explicit forms of $\bar{S}$, $\bar{\lambda}$ and $\bar{G}$ appropriate to e.e. scattering are best understood by reference to Appendix 2.2.

2.3.3. Some properties of GaAs.

The material parameters used in our computations are listed in Table 2.3. Some comments concerning these parameters are made in this subsection.

Velocities of sound are obtained using spherically averaged elastic constants due to Zook (1964). According to Hutson and White (1962) a piezoelectric stiffening effect should be taken into account in calculating of the velocity of sound. They give a one dimensional model which shows that the velocity of sound should be found from a modified elastic constant given as $C + \frac{e_p^2}{\epsilon\epsilon_0}$ where C is the elastic constant and e_p is a suitable piezoelectric constant. This effect changes the velocity of sound by $\sim$ 0.3% and is neglected in our calculations. As far as possible all the material parameters have been chosen to be appropriate to liquid helium temperatures. One exception is the piezoelectric constant e_{14} for which only values measured at 300°K (0.16 Cm^2; Arlt and Quadflieg, 1968) and 77°K (0.158 Cm^{-2}; Hambleton, 1965) are available. The difference between these two values is smaller than the experimental uncertainty (± 10%) in the measurements so we assume that the temperature change in e_{14} is not

Quantity	Symbol	Value	Unit	Reference
Band Gap	ϵ_G	1.5192	eV	Ulbrich, 1973
Conduction Band Effective mass	m^*/m_o	0.0665	-	Ulbrich, 1973
Heavy hole band Effective mass	m_{hh}/m_o	0.62	-	Lawaetz, 1971
Light hole band Effective mass	m_{lh}/m_o	0.074	-	Lawaetz, 1971
Density	ρ	5.36×10^3	Kgm^{-3}	Quoted by Rode, 1975
Elastic constant	C_{11}	12.26×10^{10}	Nm^{-2}	Garland and Park, 1962
Elastic constant	C_{12}	5.71×10^{10}	Nm^{-2}	Garland and Park, 1962
Elastic constant	C_{44}	6.0×10^{10}	Nm^{-2}	Garland and Park, 1962
Transverse velocity of sound	V_{ST}	$[\frac{1}{5\rho}(3C_{44}-C_{12}+C_{11})]^{\frac{1}{2}} = 3.026\times10^3$	$m\ s^{-1}$	Spherical average due to Zook, 1964
Longitudinal velocity of sound	V_{SL}	$[\frac{1}{5\rho}(3C_{11}+4C_{44}+2C_{12})]^{\frac{1}{2}} = 5.19\times10^3$	$m\ s^{-1}$	Spherical average due to Zook, 1964
Piezoelectric constant	e_{14}	0.16	Cm^{-2}	Arlt and Quadflieg, 1968
Deformation potential	C_D	7.0	eV	Quoted by Ulbrich, 1973
Low frequency Dielectric constant	ϵ	12.59	-	Stillman et al, 1971
High frequency Dielectric constant	ϵ_∞	10.63	-	Stillman et al, 1971
Optical phonon threshold energy	$\hbar\omega_o$	36.74	meV	Mooradian and Wright, 1966
Carbon acceptor ground state energy	ϵ_A	26.9	meV	Ulbrich, 1973

Table 2.4: Material parameters for GaAs.

significant and adopt the 300°K value for use in our calculations.

There is also some uncertainty in the value of the deformation potential. The value of 7 eV given in Table 2.4 was quoted by Ulbrich (1973) as being appropriate to liquid helium temperatures. Ulbrich apparently obtained this figure from a tabulation by Rode (1970).

But in a later tabulation (1975) Rode quotes a figure of 8.6 eV which he assumes to be temperature independent.

2.4. The Iterative Method.

2.4.1. Basic Principles

This and the following two subsections are concerned with the iterative method we have used to compute our distribution functions. Firstly, in the present subsection, we explain the general principles of the method. In the next subsection we describe a formal iterative solution of the Boltzmann equation and discuss its physical meaning. Subsection 2.4.3 is concerned with how the method is implemented in practice, but only features common to all our computations are described. Specific details of the application of the method to the individual cases listed in Table 2.1 are given in the latter parts of this Chapter (Sections 2.5 to 2.10).

We commence this subsection with an explanation of how the iterative method can be used to compute steady state distribution functions corresponding to an arbitrary injection spectrum. We then describe how distributions corresponding to δ function injection are computed. Finally we show how the iterative procedure can be modified to compute time dependent distribution functions.

The steady state distribution function corresponding to an arbitrary injection spectrum is given by the solution to equation 2.9. We recall that in general this equation is non-linear because for e.e. scattering the rates S and λ are functionally dependent on f. Supposing that an

approximation f_m to f, and hence approximations S_m and λ_m to S and λ are known, we assume that an improved approximation f_{m+1} can be found from f_m as follows:

$$f_{m+1}(k) = \frac{1}{\lambda_m(k) + R(k)} \left[\int f_m(k') \langle S_m(\underline{k}' \rightarrow \underline{k}) \rangle \, d\underline{k}' + G(k)\right] \tag{2.14}$$

f_{m+1} is then used to recalculate the scattering and generation rates and the procedure applied recursively until it is felt that the iteration has converged.

One convergence test involves use of the normalization of f. Upon integrating equation 2.9 with respect to $\underline{k}$ we obtain the relation

$$\int G(k) d\underline{k} - \int R(k)\, f(k) d\underline{k} = 0 \tag{2.15}$$

which we call the normalization condition.
Clearly the iteration must be continued at least until f_m satisfies this relation to some previously specified degree of accuracy. $\bar{f}$ obeys the same normalization condition but with G replaced by $\bar{G}$.

Another convergence test involves use of the value of $f_m(0)$. The reason for this is as follows. The scattering in rate for electrons with k = 0 depends on f(k), k > 0 for k ≠ 0 the scattering in rate is independent of f(0) because the density of states is vanishing for k = 0. (The scattering rates for k = 0 are explained in detail in Appendix 2.3). Therefore, at any stage in the iteration, we can calculate $f_m(0)$ from $f_m(k)$, k > 0. We can also estimate $f_m(0)$ by extrapolating $f_m(k)$ to k = 0. If the two values match we can be sure that a reasonable degree of convergence has been obtained. The value of $\bar{f}_m(0)$ can be similarly used to assess the degree of convergence of $\bar{f}_m(k)$.

To initialize the iterative procedure we need to choose the zeroth approximation, $f_o(k)$ to f(k). The optimum form for this function is a matter for some debate: we need to choose f_o such that relatively few iterations

are required to compute a good approximation to f. In the next two subsections we present evidence to suggest that the function $f_0(k) \equiv 0$ is the optimum choice.

Distribution functions corresponding to δ function injection are computed as follows. We first write f as the sum of its singular and non-singular parts (see Section 2.3.2). Then the precise form of the iterative procedure we use depends on the scattering mechanisms we take into account in the calculations. If only e.p. scattering is included the singular parts of f are calculated first and are then used to find the effective generation rate, $\bar{G}$. $\bar{f}$ is then found using the iterative scheme defined by equation 2.14, but with G replaced by $\bar{G}$. If e.e. scattering is included the singular and non-singular parts of f are inter-dependent and so a two stage iterative procedure is employed. First the singular parts of f are calculated from the current approximation to $\bar{f}_\Lambda$ and are then used to find the next approximation to the effective scattering and generation rates, $\bar{S}$, $\bar{\lambda}$ and $\bar{G}$. Finally an improved approximation to $\bar{f}$ is found using the procedure defined by equation 2.14 but with S, λ and G replaced by $\bar{S}$, $\bar{\lambda}$ and $\bar{G}$. (Further details of the calculations involving δ function injection are given in Appendix 2.2).

The time evolution of f appropriate to an arbitrary injection spectrum, is given by equation 2.8. We solve this equation numerically by replacing the time derivative by a forward difference (See Appendix 3 for an explanation of finite difference techniques). Then if the distribution function is known at the mth time step, the distribution function at the (m+1)th time step is found using the following modified iterative procedure:

$$f_{m+1} = \frac{1}{(\Gamma + \lambda_m + R)} \left[\int f_m(k') \langle S_m(\underline{k}' \rightarrow \underline{k}) \rangle d\underline{k}' + \Gamma f_m(k) + G(k)\right] \qquad (2.16)$$

where Γ is the inverse time step ie. $\Gamma = 1/\Delta t$. As mentioned in Section 2.3.1 computations of the time evolution of f are made using a pulse injection spectrum (equation 2.7) in place of the δ function spectrum. The reason

for this replacement is now clear: it obviates the need to compute the time dependence of the singular parts of f.

An alternative modified iterative procedure which enables time dependent distribution functions to be computed has been reported in the literature. It is known as Rees self scattering device (Rees, 1969) and, although we have used it in some trial computations it has not been used to compute the distribution functions described in this chapter. The reason for this is the need to ensure numerical stability. We have found that if the e.e. scattering rates are approximated as described in Section 2.9 then the finite difference method allows numerically stable computations to be performed using a longer time step than would be possible with the self scattering device.

2.4.2. A formal iterative solution of the Boltzmann equation

In this subsection we formally solve equation 2.3 for the steady state distribution function $f(\underline{k})$. Scattering by phonons and impurities is taken into account; electron-electron scattering is neglected. For generality, we include the possibility that the generation, scattering and recombination rates may be anisotropic. We use a formalism originally devised by Rees (1969, 1972) for the solution of a Boltzmann equation appropriate to high field transport problems. Our application of the formalism clearly demonstrates how the steady state distribution function for photoexcited electrons is characteristic of the scattering undergone by these electrons. In addition we use the same formalism to discuss the physical meaning of the iterative method.

We start by writing equation 2.3 in the form

$$\frac{\partial f}{\partial t} + [\lambda(\underline{k}) + R(\underline{k})]f(\underline{k}) = \int f(\underline{k}')S(\underline{k}' \rightarrow \underline{k})d\underline{k}' + G(\underline{k})\theta(t) \qquad (2.17)$$

where $\lambda(\underline{k}) = \int S(\underline{k} \rightarrow \underline{k}')d\underline{k}'$. Equation 2.17 is linear because we have not taken e.e. scattering into account. To solve this equation we use a Green function $P_o(\underline{k}' \rightarrow \underline{k}, t-t')$, (In Rees' terms the propagator) which satisfies the equation:

$$\frac{\partial P_o}{\partial t} + [\lambda(\underline{k}) + R(\underline{k})]P_o = \delta(\underline{k} - \underline{k}')\ \delta(t-t') \qquad (2.18)$$

And the explicit form of P_o is:

$$P_o(\underline{k}' \rightarrow \underline{k},\ t-t') = \theta(t-t')\ \delta(\underline{k}-\underline{k}')\ \exp\{-(\lambda+R)(t-t')\}$$

Physically P_o represents the probability that if an electron is in a state $\underline{k}'$ at a time t' it remains in the same state during a subsequent interval (t-t'), i.e. the probability that it undergoes neither scattering nor recombination events during the interval (t-t'). In terms of P_o the formal solution to equation 2.17 is found to be

$$f(\underline{k},t) = \int_o^t \iint f(\underline{k}',t-\tau)\ S(\underline{k}' \rightarrow \underline{k}")\ P_o(\underline{K}" \rightarrow \underline{k},\tau)d\underline{k}"\ d\underline{k}'\ d\tau$$

$$+ \int_o^t G(\underline{k}")\ P_o(\underline{k}" \rightarrow \underline{k},\tau)\ d\underline{k}"\ d\tau. \qquad (2.19)$$

We are especially interested in the steady state distribution, $f(\underline{k})$, which is given by the limit of $f(\underline{k},t)$ as $t \rightarrow \infty$. Equation 2.19 involves a convolution of f and P_o with respect to τ. Therefore the distribution function in the steady state limit (assuming it exists) is readily found by taking Laplace transforms $f(\underline{k},s)$, $P_o(\underline{k}' \rightarrow \underline{k},s)$ of f and P_o with respect to time and then taking the limit of $s\ f(\underline{k},s)$ as $s \rightarrow 0$. Thus $f(\underline{k})$ is given by the following linear integral equation

$$f(\underline{k}) = \int_o^\infty \iint f(\underline{k}')S(\underline{k}' \rightarrow \underline{k}")\ P_o(\underline{k}" \rightarrow \underline{k},\tau)\ d\underline{k}'\ d\underline{k}"\ d\tau \qquad (2.20)$$

$$+ \int_o^\infty \iint G(k")\ P_o(\underline{k}" \rightarrow \underline{k},\tau)\ d\underline{k}"\ d\tau$$

which we write symbolically as

$$f = f\,S\,\tilde{P}_o + G\,\tilde{P}_o \tag{2.21}$$

In equation 2.21 the integral operators S and $\tilde{P}_o$ act to the left, integrations with respect to $\underline{k}'$ and $\underline{k}''$ are understood, and $\tilde{P}_o$ denotes the integral of P_o with respect to time i.e. $\tilde{P}_o = \int_o^\infty P_o\, d\tau$. Next we use equation 2.21 to generate an iterative procedure:

$$f_m = f_{m-1}\,S\,\tilde{P}_o + G\,\tilde{P}_o \tag{2.22}$$

And applying the procedure recursively, starting from the zeroth approximation $f_o \equiv 0$, we obtain the following explicit solution for f:

$$f = \sum_{m=0}^{\infty} G\,\tilde{P}_o(S\,\tilde{P}_o)^m \tag{2.23}$$

(This solution is in effect the Liouville-Neumann series for the integral equation 2.20). Now we consider the physical meaning of each term in equation 2.23. Following Rees (1969) we introduce a function $P_m(\underline{k}' \to \underline{k},t)$ defined as the probability that an electron initially in a state $\underline{k}'$, is in a state $\underline{k}$ after a time interval t, after having undergone m collisions during that interval. Rees shows that the P_m can be generated by the recurrence relation:

$$P_m(\underline{k}'\to\underline{k},t) = \int_o^t \iint P_{m-1}(\underline{k}'\to\underline{k}'',t-\tau)S(\underline{k}''\to\underline{k}''')P_o(\underline{k}'''\to\underline{k},\tau)d\underline{k}'''\,d\underline{k}''d\tau$$

The Laplace transform with respect to time of P_m therefore obeys the relation

$$P_m(\underline{k}' \to \underline{k},s) = \iint P_{m-1}(\underline{k}' \to \underline{k}'',s)\; S(\underline{k}' \to \underline{k}''')P_o(\underline{k}''' \to \underline{k},s)\,d\underline{k}'''\,d\underline{k}'' \tag{2.24}$$

We now use this relation to explain the physical meaning of equation 2.23.

Putting s = 0 and using the symbolic notation introduced previously we find that equation 2.24 becomes

$$\tilde{P}_m = \tilde{P}_{m-1} S \tilde{P}_o \tag{2.25}$$

where $\tilde{P}_m$ denotes the integral $\int_o^\infty P_m(\underline{k}' \to \underline{k},\tau)d\tau$. And a relation between $\tilde{P}_o(S \tilde{P}_o)^m$ and the mth probability function now follows from a recursive application of equation 2.25

$$\tilde{P}_o(S \tilde{P}_o)^m = \tilde{P}_m = \int_o^\infty P_m(\underline{k}' \to \underline{k},\tau)d\tau \tag{2.26}$$

From equation 2.26 we see that $\tilde{P}_o(S \tilde{P}_o)^m$ represents the probability that an electron initially in a state $\underline{k}'$ enters a state $\underline{k}$ after having undergone m collisions, integrated over all time intervals in which these collisions can occur. Hence the mth term in the sum 2.23 represents the contribution to f of those electrons which are injected, enter a state $\underline{k}$ by undergoing m collisions and survive in the limit $t \to \infty$. The steady state is a sum over collision number, m, of all such contributions.

Having understood the manner in which the steady state is established we now need to show that the iterative method used in our computations is the same as the one defined by equation 2.22. It is a simple matter to evaluate the integrals over τ and $\underline{k}''$ which are involved in that equation. First we integrate P_o with respect to τ

$$\tilde{P}_o = \int_o^\infty P_o\ (\underline{k}' \to \underline{k},\tau)d\tau = \frac{1}{\lambda+R}\ \delta(\underline{k}-\underline{k}')$$

then, upon performing the $\underline{k}''$ integration, equation 2.22 reduces to

$$f_m(\underline{k}) = \frac{1}{\lambda(\underline{k})+R(\underline{k})}\left[\ \int f_{m-1}(\underline{k}')\ S(\underline{k}' \to \underline{k})d\underline{k}' + G(\underline{k})\ \right]$$

which is essentially the defining relation for the iterative procedure used in our computations (equation 2.14).

It is now clear that the iterative procedure adds into f_{m-1} a contribution characteristic of those electrons which have been scattered m times after being injected. The steady state distribution function consists of all such contributions summed over collision number, but the iterative procedure gives this function only in the limit of an infinite number of iterations. In practice only a finite number of iterations, say N, can be employed and the distribution function so obtained is the contribution to f which is characteristic of those electrons which have been scattered N or less times. A similar physical interpretation applies when the iterative method is used to compute the non-singular part of the distribution: $\bar{f}_N$ is the contribution to $\bar{f}$ characteristic of those electrons which have been scattered N or less times after being injected and then leaving the states in the L.O. phonon ladder. This physical interpretation of the iterative method has enabled us to understand our computed distribution functions in terms of the scattering events undergone by the photoexcited electrons.

2.4.3. Implementation

This subsection is concerned with our numerical implementation of the iterative method. In the first part of the subsection we explain the general principles upon which all our computations are based. In the remaining part we discuss two special aspects of the computation of steady state distributions corresponding to δ function excitation, namely the choice of the zeroth approximation used to initialize the procedure and the convergence criteria used to terminate the procedure. The same two aspects of the computation of time dependent distributions require less discussion. f at the zeroth timestep is obtained from the initial condition (equation 2.2a) and the need for accuracy criteria does not arise.

To implement the iterative procedures defined by equations 2.14 and 2.16 we represent the continuous variable $|\underline{k}|$ on a one dimensional mesh having N_p points separated by equal intervals Δk. This allows us to estimate the integrals involved in the procedures numerically. Simpson's rule or the trapezium rule are used, as appropriate, for this purpose. Thus computations according to equations 2.14 or 2.16 are performed.

The iterative procedure is designed to solve an integral equation (equation 2.9). If the integrals involved in this equation are numerically evaluated as mentioned in the previous paragraph, then the integral equation becomes a system of algebraic equations for a set of quantities f_j (or $\bar{f}_j$ if the injection spectrum has the form of a δ function) which approximate the continuous functions $f(k)$ or $\bar{f}(k)$ at the jth mesh point. In general the algebraic equations are non-linear. (However they are linear if only e.p. scattering is taken into account-this case is discussed in Appendix 2.4). The numerical implementation of the iterative procedure yields the mth approximation f^m, ($\bar{f}_j^m$) to the f_j ($\bar{f}_j$), which themselves approximate the function $f(k)$ ($\bar{f}(k)$) which we seek. The computed approximation f_j^m, ($\bar{f}_j^m$) to the f_j ($\bar{f}_j$) is very good when after a sufficient number of iterations but to obtain an improved approximation to $f(k)$ ($\bar{f}(k)$) we normalize the f_j^m ($\bar{f}_j^m$) such that the normalization condition (equation 2.15) is satisfied. This involves multiplication of the f_j^m ($\bar{f}_j^m$) by the following normalization factor, A_N:

$$A_N = \frac{\int G(k)d\underline{k}}{4\pi \sum_{j=1}^{N_p} \gamma_j R(k_j) f_j^m k_j^2} \qquad (2.27)$$

In equation 2.27 the γ_j are the weight coefficients of the rule used for numerical integration. The normalization factor for the $\bar{f}_j^m$ is similar but G and f_j^m are replaced by $\bar{G}$ and $\bar{f}_j^m$ respectively.

The zeroth approximation used to compute all the distribution functions described in this Chapter is a mesh representation of the function $f \equiv 0$. In computations involving e.e. scattering both the singular and non-singular parts of f are initialized to zero; otherwise only $\bar{f}$ needs to be initialized. Trial computations using both a Maxwellian with a temperature T_L and the function $f \equiv 0$ for initialization have shown that the latter function invariably results in faster convergence of the iteration. A useful consequence choosing $f \equiv 0$ as the zeroth approximation is that, if e.e. scattering is neglected, we compute distribution functions in the form of a sum over collision number. And the physical meaning of this form is as described in the previous subsection.

The convergence criteria we use to test the iterated distribution functions are based on the normalization condition and the value of $\bar{f}_m(0)$ (as described in Section 2.4.1). We need to ensure both that the iteration has produced a good approximation to the $\bar{f}_j$ and that the $\bar{f}_j$ well approximate $\bar{f}(k)$. In general the normalization condition does not provide a precise convergence test for the $\bar{f}_j^m$. The reason for this is that, if the collision term of the Boltzmann equation is numerically integrated with respect to $\underline{k}$, the result is non-zero. This point is discussed further in Appendix 2.4, where it is also shown that the normalization condition does provide a precise test for the special case that only scattering by acoustic phonons is included in the calculations. (See also Section 2.5.1.). However, if the mesh step is small and if the $\bar{f}_j^m$ well approximate $\bar{f}(k)$ the normalization factor A_N, defined by equation 2.27, is expected to be close to unity. We can therefore use the value of A_N to compare the degree of convergence of successive iterates. Apart from two exceptions the distribution functions presented in this chapter have normalization factors ≤ 1.2.

The value of $\bar{f}_1^m$ (equivalent to $\bar{f}^m(0)$) is used to judge the convergence of the $\bar{f}_j^m$. From the discussion of Section 2.4.1 it should be clear that whereas the f_j^m, $j > 1$ must be computed iteratively f_1^m can be computed directly from the f_j^m, $j > 1$. f_1^m can also be estimated by extrapolation of the f_j^m, $j > 1$, to $j = 1$. The two values so obtained should closely match if the f_j^m have a sufficient degree of convergence.

Ideally we would continue the iteration until the two criteria mentioned in the previous two paragraphs are satisfied to a preset degree of accuracy. In practice the availability of computer time places constraints on what can be done. We adopt the procedure of first performing as many iterations as thought to be possible within the available computer time. Next the two convergence criteria are applied. We then carry out a few (≤ 5) extra iterations and examine the difference between the successive iterates so obtained to ensure that the iterative procedure has indeed converged.

2.5. Distribution functions corresponding to the absence of electron-electron scattering: the steady state.

We now consider some distribution functions which have been computed with only e.p. scattering taken into account.

This subsection is concerned with some details of how the iterative method is implemented to compute the distribution functions. We start with an explanation of how the phonon scattering rates listed in Appendix 2.3 are calculated. Next we describe some appropriate convergence criteria. Finally we discuss the question of whether the iterative procedure provides the optimum method for computing the distribution functions. In the next subsection we present the computed distribution functions themselves.

Let us first review the essential results of Sections 2.3 and 2.4. The steady state distribution function is in general given by the solution to the

integral equation 2.9. If only e.p. scattering is taken into account the equation is linear. The same equation gives the non-singular part, $\bar{f}$, of the distribution appropriate to a δ function injection spectrum, provided that the generation rate G is replaced by an effective generation rate $\bar{G}$. The equation is solved using an iterative method. In practice the iterative method is implemented by introducing a discrete mesh of steplength Δk and evaluating the scattering rates numerically. The computations actually yield a set of quantities $\bar{f}_j$ which approximate the function $\bar{f}(k)$ at the points $(j-1)\Delta k$. The $\bar{f}_j$ are the exact solution to a system of algebraic equations which are linear if only e.p. scattering is taken into account, because then equation 2.9 is the linear.

Simpson's rule and the trapezium rule are amongst the methods suitable for numerical evaluation of the scattering integrals. Of the two methods Simpson's rule is the more accurate. The integrals involved in the acoustic phonon scattering rates have limits of the form $k, |k \pm 2k_\alpha|$ (where $\hbar k_\alpha = m^* v_s$ and v_s is the appropriate velocity of sound.) We find it convenient to define the mesh such that $k_{\alpha T}$ (the transverse phonon k_α) is an integral multiple of Δk. Then we can use Simpson's rule to calculate the transverse scattering rates. However with the mesh defined in terms of $k_{\alpha T}$, the limits of the integrals involved in the longitudinal scattering rates are incommensurate with the mesh points. So we calculate these rates from the sum of an application of the trapezium rule to the mesh points lying within the limits and an estimate of the remaining parts of the integral.

No numerical integrations are required to calculate the L.O. phonon emission rates for these rates can be expressed simply in terms of $f(k)$ and $f((k^2 + k_o^2)^{\frac{1}{2}})$ premultiplied by suitable k dependent coefficients. (k_o is defined by the relation $\hbar k_o^2 = 2m^* \omega_o$). In the computations we take $\bar{f}((k^2 + k_o^2)^{\frac{1}{2}})$ to be the value of $\bar{f}_j^m$ at the nearest mesh point to $(k^2 + k_o^2)^{\frac{1}{2}}$.

We recall from Section 2.4 that the normalization condition (equation 2.15) does not, in general provide a precise test of accuracy for the $\bar{f}_j^m$. If, however, only acoustic phonon scattering is taken into account the $\bar{f}_j$ obey the following sum rule, which is equivalent to the normalization condition, and which does provide a precise accuracy test for the $\bar{f}_j^m$:

$$\sum_{j=1}^{N_p} k_j^2 R(k_j) \bar{f}_j = \sum_{j=1}^{N_p} k_j^2 \bar{G}(k_j) \quad , \quad k_j = (j-1)\Delta k \qquad (2.28)$$

where N_p is the number of mesh points.

The sum rule is a twin consequence of the acoustic phonon scattering integrals having finite limits and of the manner in which the numerical integrations are performed. It is derived in Appendix 2.4. If L.O. phonon scattering is taken into account the sum rule is not obeyed exactly because the L.O. phonon scattering rates involve $\bar{f}$ at values of k not exactly coincident with the mesh points. To apply the sum rule in practice we calculate a test parameter, A_T, from the $\bar{f}_j^m$.

$$A_T = \frac{\left| \sum_{j=1}^{N_p} k_j^2 R(k_j) \bar{f}_j^m - \sum_{j=1}^{N_p} k_j^2 \bar{G}(k_j) \right|}{\sum_{j=1}^{N_p} k_j^2 \bar{G}(k_j)} \qquad (2.29)$$

If the $\bar{f}_j^m$ were identical to the $\bar{f}_j$ then A_T would be zero. And so we use the smallness of A_T to judge whether the $\bar{f}_j^m$ have a sufficient degree of convergence. For most of the distribution functions described in the present section and in section 2.10, $A_T < 0.2$.

The computation of $\bar{f}$ requires a solution of the linear equations for the $\bar{f}_j$ and we have made some enquiries into the optimum numerical method for this purpose. Since the matrix of coefficients is large

We recall from Section 2.4 that the normalization condition (equation 2.15) does not, in general provide a precise test of accuracy for the $\bar{f}_j^m$. If, however, only acoustic phonon scattering is taken into account the $\bar{f}_j$ obey the following sum rule, which is equivalent to the normalization condition, and which does provide a precise accuracy test for the $\bar{f}_j^m$:

$$\sum_{j=1}^{N_p} k_j^2 R(k_j) \bar{f}_j = \sum_{j=1}^{N_p} k_j^2 \bar{G}(k_j) \ , \ k_j = (j-1)\Delta k \qquad (2.28)$$

where N_p is the number of mesh points.

The sum rule is a twin consequence of the acoustic phonon scattering integrals having finite limits and of the manner in which the numerical integrations are performed. It is derived in Appendix 2.4. If L.O. phonon scattering is taken into account the sum rule is not obeyed exactly because the L.O. phonon scattering rates involve $\bar{f}$ at values of k not exactly coincident with the mesh points. To apply the sum rule in practice we calculate a test parameter, A_T, from the $\bar{f}_j^m$.

$$A_T = \left| \frac{\sum_{j=1}^{N_p} k_j^2 R(k_j) \bar{f}_j^m - \sum_{j=1}^{N_p} k_j^2 \bar{G}(k_j)}{\sum_{j=1}^{N_p} k_j^2 \bar{G}(k_j)} \right| \qquad (2.29)$$

If the $\bar{f}_j^m$ were identical to the $\bar{f}_j$ then A_T would be zero. And so we use the smallness of A_T to judge whether the $\bar{f}_j^m$ have a sufficient degree of convergence. For most of the distribution functions described in the present section and in section 2.10, $A_T < 0.2$.

The computation of $\bar{f}$ requires a solution of the linear equations for the $\bar{f}_j$ and we have made some enquiries into the optimum numerical method for this purpose. Since the matrix of coefficients is large

and sparse an iterative technique is in fact the most suitable method. Such techniques are fairly well understood (Young, 1971; Isaacson and Keller, 1966; See also Appendix 2.4). The matrix equivalent of equation 2.14 is known as the Jacobi iteration method. It is not usually recommended for the solution of large linear systems, on account of its slow convergence. Two other procedures, the forward and backward Gauss-Seidel methods converge more rapidly than the Jacobi method (in the sense that fewer iterations are required for the difference between successive iterates to become less in magnitude than a given small number). We have found them to be unsuitable for our purposes. Test computations have shown that although the Gauss-Seidel methods offer more rapid convergence, they yield solutions which do not obey the sum rule 2.28.

In the program we use to compute distribution functions the iterative method is implemented in the manner described in subsection 2.4.3 and the present subsection. All quantities used repetitively are tabulated prior to commencing the iteration. Initialization and termination of the iterative procedure are as described in subsection 2.4.3, except that the test parameter A_T is used, whenever applicable, to assess convergence. The program has been tested in two ways. Firstly by ensuring that the iteration converges to a Maxwellian function with a temperature T_L if the generation and recombination terms are both set to zero. Secondly by ensuring that if a positive function is used for the zeroth approximation, and the generation term is set to zero, then the iteration converges to the function $f \equiv 0$.

2.5.2. Distribution functions.

In this subsection we study some distribution functions which would be established as a result of monoenergetic injection of electrons, their scattering by phonons and their recombination. Electron-electron scattering is not taken into account. We describe three sets of such distribution

functions, each set computed according to the methods explained in the previous two subsections. The individual distributions in the first set are each computed with different types of phonon scattering taken into account, but a k independent recombination rate of $10^7 s^{-1}$ is common to them all (Figs. 2.3, 2.5). All three acoustic phonon scattering mechanisms are taken into account in computing the distribution functions in the second set but a different form of recombination rate is chosen to compute each individual distribution in this set (Figs. 2.7, 2.8). The final set of distribution functions is calculated to test the sensitivity of the form of $\bar{f}$ to the value of the inverse screening length.

To enable comparison of the distribution functions, the electron injection rate, the lattice temperature and the inverse screening length are chosen to be common to as many of the calculations as possible. In all the computations involving an energy independent recombination rate, the injection rate is chosen such that the electron density is 10^{20} m^{-3}. The lattice temperature and inverse screening length μ are taken as $1.7^{o}K$ and 1.56×10^7 m^{-1} respectively. (The value of μ is the inverse Debye length for a Maxwellian distribution of electrons of density 10^{20} m^{-3} and temperature $10^{o}K$). For all the distributions in the first two sets the value of μ computed from f is found to be within a factor of 5 of the input value. All the physical and computational parameters associated with the distribution functions described in this and subsequent sections are summarized in Tables 2.5 and 2.6.

Two of the parameters listed in Table 2.5 the mean energy and the fraction of electrons contributing to $\bar{f}$, usually do not enter into our subsequent discussions. We give these parameters for reference purposes only. The 'mean energy' is the electron energy averaged over the non-singular part of f. This quantity provides some indication of how far the distributions deviate from thermal ones. All the distribution functions

functions, each set computed according to the methods explained in the previous two subsections. The individual distributions in the first set are each computed with different types of phonon scattering taken into account, but a k independent recombination rate of $10^7 s^{-1}$ is common to them all (Figs. 2.3, 2.5). All three acoustic phonon scattering mechanisms are taken into account in computing the distribution functions in the second set but a different form of recombination rate is chosen to compute each individual distribution in this set (Figs. 2.7, 2.8). The final set of distribution functions is calculated to test the sensitivity of the form of $\bar{f}$ to the value of the inverse screening length.

To enable comparison of the distribution functions, the electron injection rate, the lattice temperature and the inverse screening length are chosen to be common to as many of the calculations as possible. In all the computations involving an energy independent recombination rate, the injection rate is chosen such that the electron density is 10^{20} m^{-3}. The lattice temperature and inverse screening length μ are taken as $1.7^{o}K$ and 1.56×10^7 m^{-1} respectively. (The value of μ is the inverse Debye length for a Maxwellian distribution of electrons of density 10^{20} m^{-3} and temperature $10^{o}K$). For all the distributions in the first two sets the value of μ computed from f is found to be within a factor of 5 of the input value. All the physical and computational parameters associated with the distribution functions described in this and subsequent sections are summarized in Tables 2.5 and 2.6.

Two of the parameters listed in Table 2.5 the mean energy and the fraction of electrons contributing to $\bar{f}$, usually do not enter into our subsequent discussions. We give these parameters for reference purposes only. The 'mean energy' is the electron energy averaged over the non-singular part of f. This quantity provides some indication of how far the distributions deviate from thermal ones. All the distribution functions

Injection Spectrum	Injection Energy (meV)	Injection rate Q	Scattering Mechanisms	Recombination Rate s^{-1}	Steady State electron density m^{-3}	% of electrons contributing to $\bar{f}$.	Mean energy of electrons contributing to $\bar{f}$. (meV)	Distrib. function shown in figure.
Monoenergetic	3.989	10^{27}	T.P.	10^{7}	10^{20}	99.59	0.7845	2.3a
		10^{27}	L.P.	10^{7}	10^{20}	99.57	0.8406	2.3b
		10^{27}	D.P.	10^{7}	10^{20}	97.53	1.206	2.3c
		10^{27}	T.P,L.P,D.P.	10^{7}	10^{20}	99.72	0.5185	2.3d,2.7a
Monoenergetic	40.4	10^{27}	T.P,L.P,D.P	10^{7}	10^{20}	99.8	5.191	2.5a
		10^{27}	T.P,L.P,D.P,	10^{7}	10^{20}	99.72	0.5582	2.5b
		10^{27}	D.P.	10^{7}	10^{20}	99.72	4.999	2.5c
		10^{27}	D.P.,L.O.	10^{7}	10^{20}	97.3	1.137	2.5d
Monoenergetic	3.989	10^{28}	T.P,L.P,D.P.	10^{8}	10^{20}	97.24	1.756	2.7b
		5×10^{28}	T.P,L.P,D.P.	5×10^{8}	10^{20}	87.5	3.110	2.7c
		10^{29}	T.P,L.P,D.P.	10^{9}	10^{20}	77.9	3.444	2.7d
Monoenergetic	3.989	10^{27}	T.P,L.P,D.P.	$A(1+Bk)^{-3}$	4.146×10^{20}	99.32	0.3391	2.8a
		10^{27}	T.P,L.P,D.P.	$A(1+Bk^{2})^{-4}$	9.751×10^{19}	99.71	0.4233	2.8b
Monoenergetic	0.997	7.5×10^{23}	large screening e.e.$\mu=5\times10^{9}m^{-1}$	10^{7}	7.5×10^{16}	1.45×10^{-7}	0.9958	2.13a
		7.5×10^{23}	large screening e.e.$\mu=5\times10^{8}$ m^{-1}	10^{7}	7.5×10^{16}	1.45×10^{-3}	0.9958	2.13b
		7.5×10^{23}	large screening e.e.$\mu=10^{8}$ m^{-1}	10^{7}	7.5×10^{16}	47.65	0.9965	2.13c
		7.5×10^{23}	large screening e.e.$\mu=5\times10^{7}$ m^{-1}	10^{7}	7.5×10^{16}	92.65	0.9569	2.13d
Interband	See Table 2.8.	2.5×10^{23}	T.P,L.P,D.P.	2.5×10^{7}	2×10^{16}	99.25	1.323	2.19a
		2.5×10^{23}	T.P,L.P,D.P.	2.5×10^{7}	2×10^{16}	99.25	1.713	2.20a
		2.5×10^{23}	T.P,L.P,D.P.	2.5×10^{7}	2×10^{16}	99.25	2.048	2.21a

Table 2.5a: Some physical parameters associated with the steady state distribution functions described in Sections 2.5 to 2.10. The terms 'monoenergetic' and 'interband' as used in the table are defined in Section 2.3. The parameter A and B are defined in Section 2.5.2.

Injection Spectrum	Injection Energy (meV)	Injection Rate Q (m^{-3} s^{-1})	Scattering Mechanisms	Recombination Rate	Period over which time evolution was followed T(nS)	Electron density at time T	Mean energy at time T	Distri. function shown in figure
Pulse	3.989	10^{27}	D.P.	10^{7}	5	3.74×10^{18}	3.707	2.9
		10^{27}	D.P.	10^{7}	50	3.01×10^{19}	2.33	2.10
Pulse	3.989	10^{27}	T.P,L.P,D.P.	10^{7}	5	2.82×10^{18}	3.26	2.11
		10^{27}	T.P,L.P,D.P.	10^{7}	50	2.42×10^{19}	1.021	2.12
Pulse	0.997	7.5×10^{23}	e.e.large screening model $\mu=5\times10^{7}\,m^{-1}$	10^{7}	500	6.36×10^{16}	0.9649	2.14
Pulse	0.997	10^{24}	e.e. series expansion model	10^{7}	5	4.47×10^{15}	1.049	2.15
		10^{24}	e.e. series expansion	10^{7}	50	2.38×10^{16}	1.351	2.16
Pulse	3.989	10^{21}	e.e. series expansion T.P,L.P,D.P.	10^{7}	50	7.31×10^{12}	2.37	2.17a
		10^{22}	e.e. series expansion T.P,L.P,D.P.	10^{7}	50	7.37×10^{13}	2.365	2.17b
		10^{23}	e.e. series expansion T.P,L.P,D.P.	10^{7}	50	6.94×10^{14}	2.322	2.17c
		5×10^{23}	e.e.series expansion T.P,L.P,D.P.	10^{7}	50	3.19×10^{15}	2.255	2.17d
		10^{24}	e.e.series expansion T.P,L.P,D.P.	10^{7}	50	6.16×10^{15}	2.184	2.17e
		5×10^{24}	e.e.series expansion T.P,L.P,D.P.	10^{7}	50	3.17×10^{16}	2.569	2.17f
Pulse	3.989	10^{21}	e.e.series expansion T.P,L.P,D.P.	10^{7}	5×10^{4}	2.68×10^{13}	0.9247	2.18a
		10^{22}	e.e.series expansion T.P,L.P,D.P.	10^{7}	500	2.50×10^{14}	0.9609	2.18b
		10^{23}	e.e.series expansion T.P,L.P,D.P.	10^{7}	50	2.18×10^{15}	1.005	2.18c

Table 2.5b: Some physical parameters associated with the time dependent distribution functions described in Sections 2.6, 2.8 and 2.9. The term 'pulse' as used in the table is defined in Section 2.3.

Mesh Length (m^{-1})	Mesh Step (m^{-1})	No. of iterations	Normalization Factor A_N	Test Parameter A_T	Distribution function shown in figure
10^8	$\frac{1}{3} k_{\alpha T}$	500	1.16	0.13	2.2a
			0.98	2.7×10^{-4}	2.3b
			0.96	1.3×10^{-8}	2.3c
			1.25	0.2	2.3d,2.7a
2.83×10^8	$\frac{1}{2} k_{\alpha T}$	300	1.83	0.41	2.5a
			1.68	-	2.5b
2.83×10^8	$\frac{1}{3} k_{\alpha T}$	200	0.947	1.7×10^{-9}	2.5c
			0.953	-	2.5d
10^8	$\frac{1}{3} k_{\alpha T}$	500	0.99	3.7×10^{-7}	2.7b
			0.99	3.0×10^{-8}	2.7c
			0.99	4.6×10^{-3}	2.7d
10^8	$\frac{1}{3} k_{\alpha T}$	500	0.997	4.7×10^{-3}	2.8a
			1.232	0.195	2.8b
10^8	$k_{\alpha T}$	38	1.001	-	2.13a
			1.001	-	2.13b
			1.015	-	2.13c
			1.177	-	2.13c
1.6×10^8	$\frac{1}{3} k_{\alpha T}$	1,000	1.2	0.17	2.19a
			1.19	0.16	2.20a
			1.17	0.16	2.21a

Table 2.6a: Some computational parameters associated with the steady state distribution functions described in Sections 2.5 to 2.10. The wave vector $k_{\alpha T}$ and the test parameter A_T are defined in Section 2.5. The normalization factor A_T is defined in Section 2.4.

Mesh length (m^{-1})	Mesh step (m^{-1})	Time step (s)	Distribution function shown in Figure
10^8	$\frac{1}{3}k_{\alpha T}$	10^{-10}	2.9
		10^{-10}	2.10
10^8	$\frac{1}{3}k_{\alpha T}$	10^{-10}	2.11
		10^{-10}	2.12
10^8	$k_{\alpha T}$	5×10^{-9}	2.14
1.414×10^8	$k_{\alpha T}$	2.5×10^{-11}	2.15
		2.5×10^{-11}	2.16
10^8	$k_{\alpha T}$	2.5×10^{-11}	2.17a
		2.5×10^{-11}	2.17b
		2.5×10^{-11}	2.17c
1.414×10^8	$k_{\alpha T}$	2.5×10^{-11}	2.17d
		2.5×10^{-11}	2.17e
		2.5×10^{-11}	2.17f
10^8	$k_{\alpha T}$	10^{-7}	2.18a
		10^{-9}	2.18b
		5×10^{-11}	2.18c

Table 2.6b. Some computational parameters associated with the time dependent distribution functions described in Sections 2.6, 2.8 and 2.9. The wave vector $k_{\alpha T}$ is defined in Section 2.5.

described in this section have a mean energy > 0.5 meV and this figure should be compared with the mean energy of a 1.7°K Maxwellian (0.22 meV). Reference to Table 2.5 shows that in most of the distributions we have computed the majority of the electrons (> 98%) contribute to the non-singular part of f. The fraction of electrons contributing to the singular part is significant only if the recombination rate is chosen to be comparable to the scattering rates.

All the distribution functions listed in Tables 2.5 and 2.6 are presented in Figs. 2.3, 2.5 and 2.7 to 2.20. Each figure shows f or $\bar{f}$, as appropriate, as a function of energy, ϵ, relative to the conduction band minimum. Arrows are used to indicate the injection energy or energies. In the figures showing distributions computed using a pulse injection spectrum the arrow is positioned at the centre of the pulse.

We now describe the distribution functions in the first of the three sets previously mentioned. Four distribution functions which have been computed with the injection energy taken to be below the L.O. phonon threshold energy are illustrated in Fig. 2.3. In each case the actual value of the injection energy is 3.989 meV. Parts a to c of the figure show distribution functions computed with each acoustic phonon scattering mechanism taken into account separately and part d shows a distribution function obtained with these three mechanisms taken into account together. If either T.P. or L.P. scattering are the sole scattering mechanisms the distribution functions which result are very similar in shape. (Figs. 2.3a and b). At low energies ($\lesssim$ 1 meV) $\bar{f}$ is well approximated by a Maxwellian with a temperature T_L (= 1.7°K) but has a non-Maxwellian plateau at higher energies. A pronounced shoulder is present at an energy just below ϵ_1 and the form of $\bar{f}$ above this energy is again Maxwellian. If D.P. scattering is the sole scattering mechanism the Maxwellian form at low energies is replaced by a

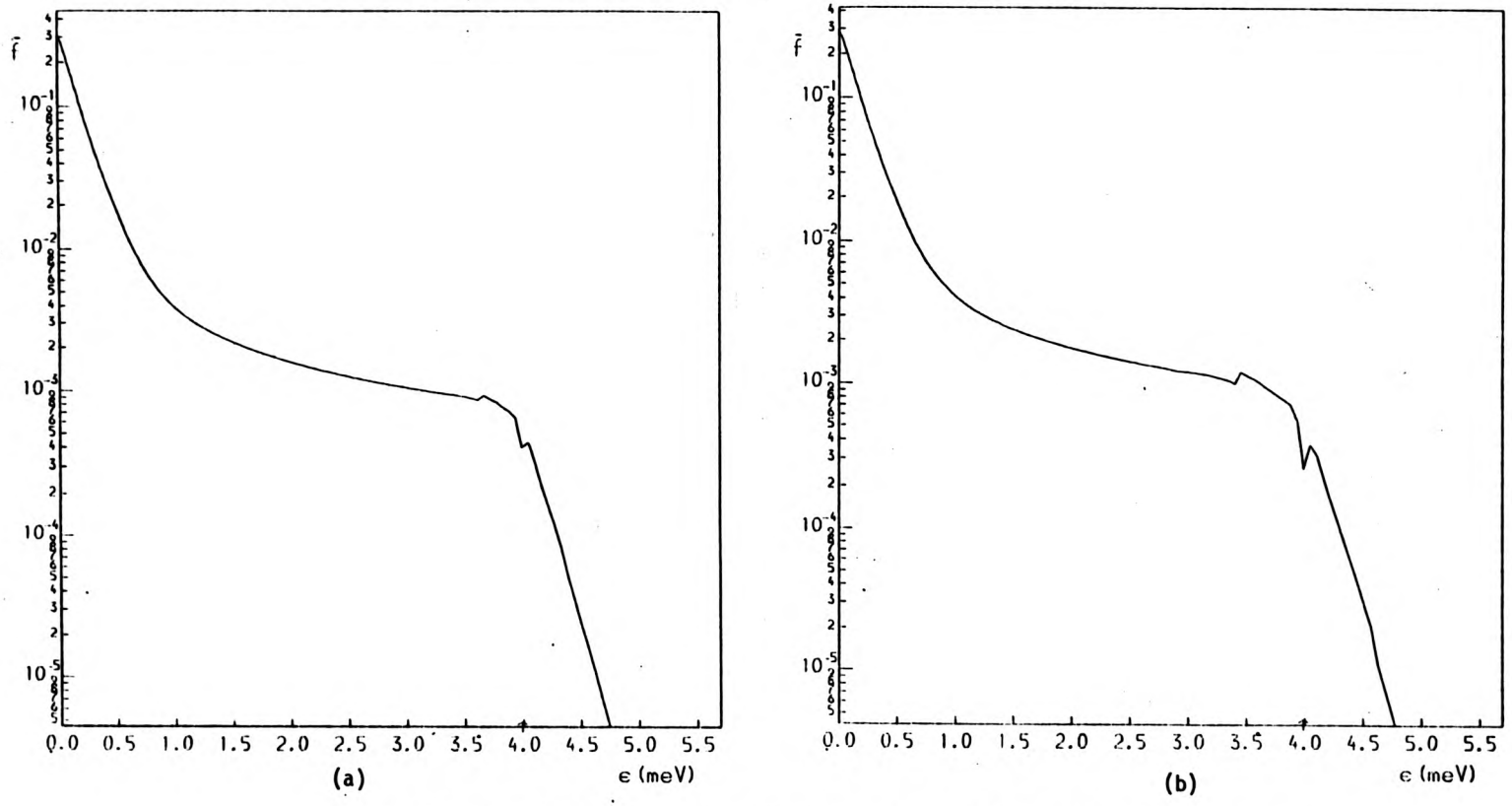

Figs. 2.3a and b distribution functions computed taking ϵ_i to be less than $\hbar\omega_o$.

(a) Only T.P. scattering taken into account

(b) Only L.P. scattering taken into account

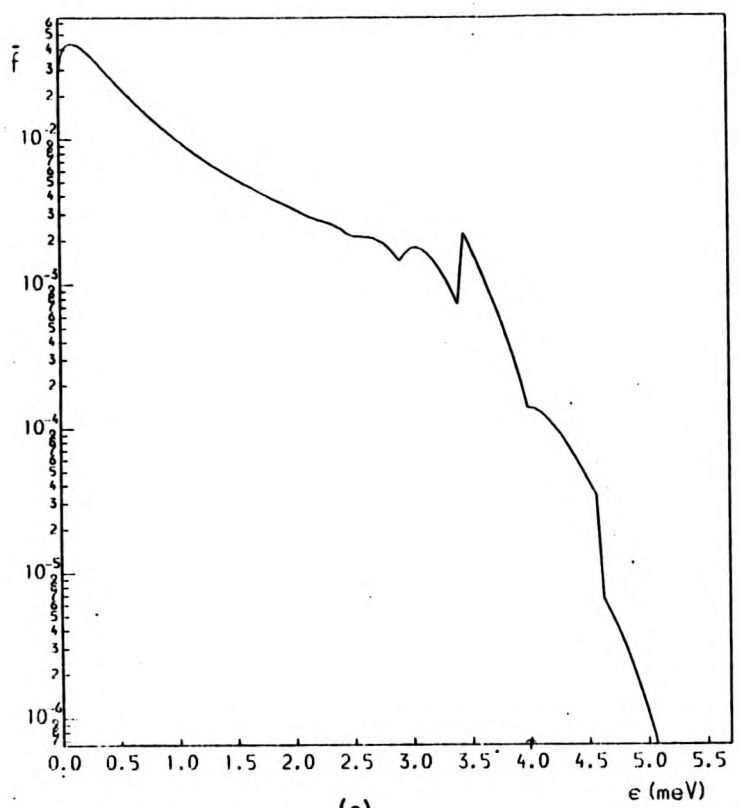

(c)

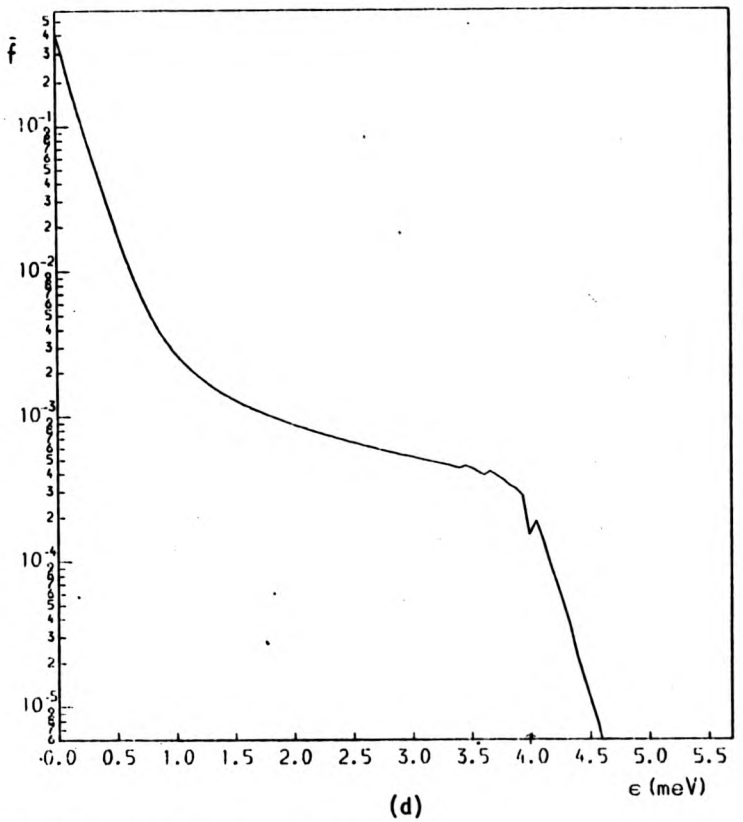

(d)

Figs.2.3c and d . Distribution functions computed taking ϵ_i to be less than $\hbar\omega_o$.

(c) Only D.P. scattering taken into account

(d) T.P., L.P. and D.P. scattering taken into account

turnover (Fig. 2.3c). All the distribution functions have some fine structure in the form of a series of modulations at energies $\sim \epsilon_1$. The origin of the structure is discussed later in this subsection.

The overall form of the distribution functions shown in Figs. 2.3a to c can be understood in terms of the scattering processes as follows. The Maxwellian form above ϵ_1 is attributable to phonon absorption by a minority of the injected electrons. The majority of the injected electrons undergo a cascade of spontaneous acoustic phonon emissions and the plateau is characteristic of this process. The cascade process continues either until the injected electrons recombine or until they have a wave vector of so small a magnitude that they interact only with low energy phonons. (An electron with a wavevector of magnitude k can exchange an energy of at most $2\hbar^2 k_\alpha k/m^*$ in an acoustic phonon collision. Thus small wave vector electrons can only interact with low energy acoustic phonons). Even at low lattice temperatures phonon states of sufficiently low energy are highly populated. Therefore the small wave vector electrons can undergo stimulated absorption and emission of phonons and hence thermalize to the lattice.

The T.P. and L.P. scattering rates are large compared to the recombination rate of 10^7 s^{-1} (See Fig. 2.4 which shows $\lambda(k)$ as a function of k for all three types of acoustic phonon scattering - the T.P. scattering rate is largest for small k) Consequently piezoelectric scattering causes a fraction of the electrons to enter states of sufficiently low energy to enable those electrons to thermalize to the lattice (by interacting with low energy phonons). The low energy form of $\bar{f}$ is therefore Maxwellian. However, the D.P. scattering rate differs from the recombination rate only by about an order of magnitude so if only this mechanism is taken into account the Maxwellian form at low energies is replaced by a turnover.

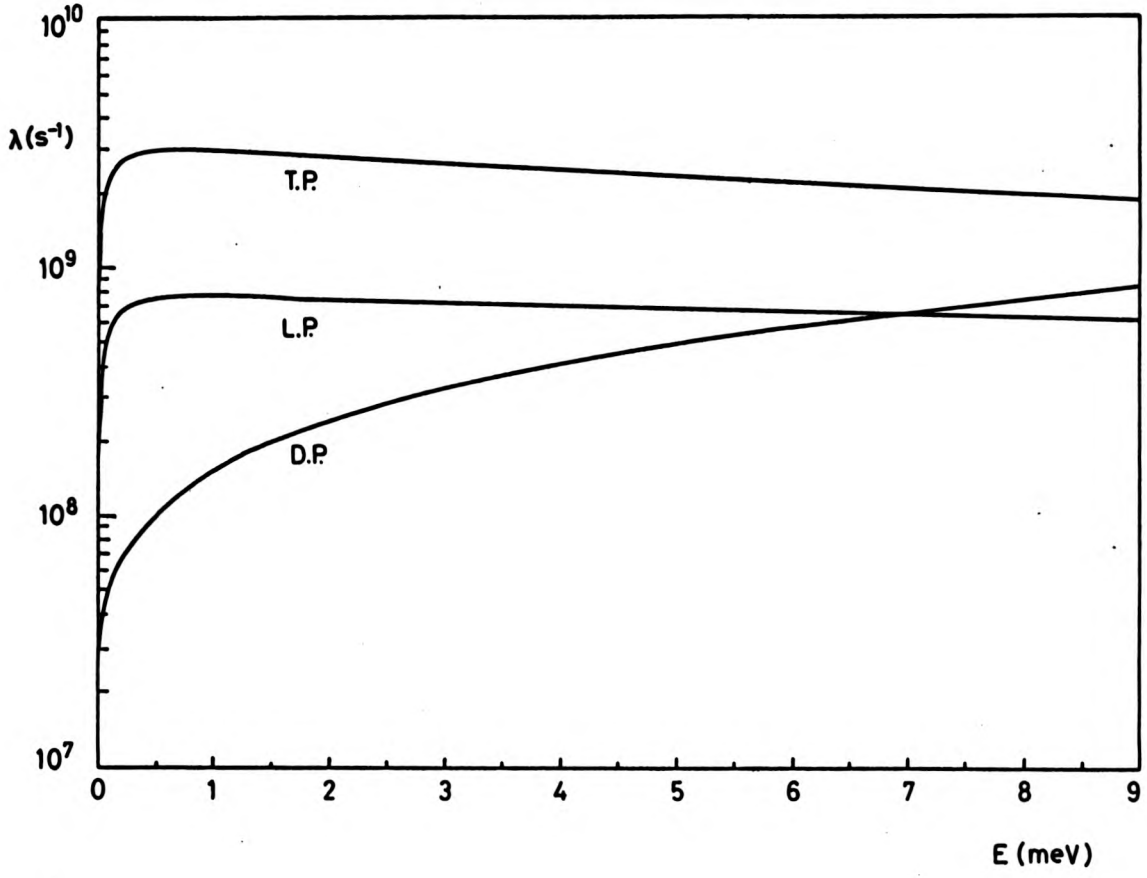

Fig.2.4 The acoustic phonon scattering out rates, λ, as a function of energy.

The distribution function shown in Fig. 2.3d, (all three acoustic phonon processes taken into account) is similar to those shown in Figs. 2.3a and 2.3b. This indicates that D.P. scattering does not play a significant role in thermalizing the low energy electrons. However, if the injection energy was sufficiently high D.P. phonon emission would be an important energy loss process for the photoexcited electrons because the asymptotic forms of $\lambda(k)$ for D.P. and piezoelectric scattering are $\sim k^3$ and $\sim$ constant respectively.

Next we describe the form of the distribution functions corresponding to an injection energy above the L.O. phonon theshold energy. Some distribution functions, computed with ϵ_i chosen as 40.4 meV, are shown in Fig. 2.5. All three acoustic phonon scattering mechanisms have been taken into account in the calculations leading to Figs. 2.5a and b. In addition L.O. phonon emission has been included in the calculations leading to Fig.2.5b. D.P. scattering is the only acoustic phonon mechanism which has been taken into account in computing the distribution functions shown in Fig. 2.5c (L.O. phonon emission not included) and Fig.2.5d (L.O. phonon emission included). Both parts a and b and parts c and d of Fig. 2.5. clearly illustrate how L.O. phonon emission effectively reinjects electrons from an injection energy above threshold to an energy lower by $\hbar\omega_0$.

The distribution function shown in Fig.2.5c has some beautiful fine structure in the form of a series of maxima at energies just below ϵ_i. Fine structure is evident to some extent in all the distribution functions we have computed but is most apparent if only D.P. scattering is taken into account. The fine structure is present in distribution functions computed using only a few iterations (~1 or 2) and therefore represents the contribution to $\bar{f}$ characteristic of those electrons which are scattered only a few times. (See Fig.2.6). The twin constraints of energy and momentum conservation restrict the states that electrons injected at $k=k_i$, can enter via one acoustic phonon scattering event,

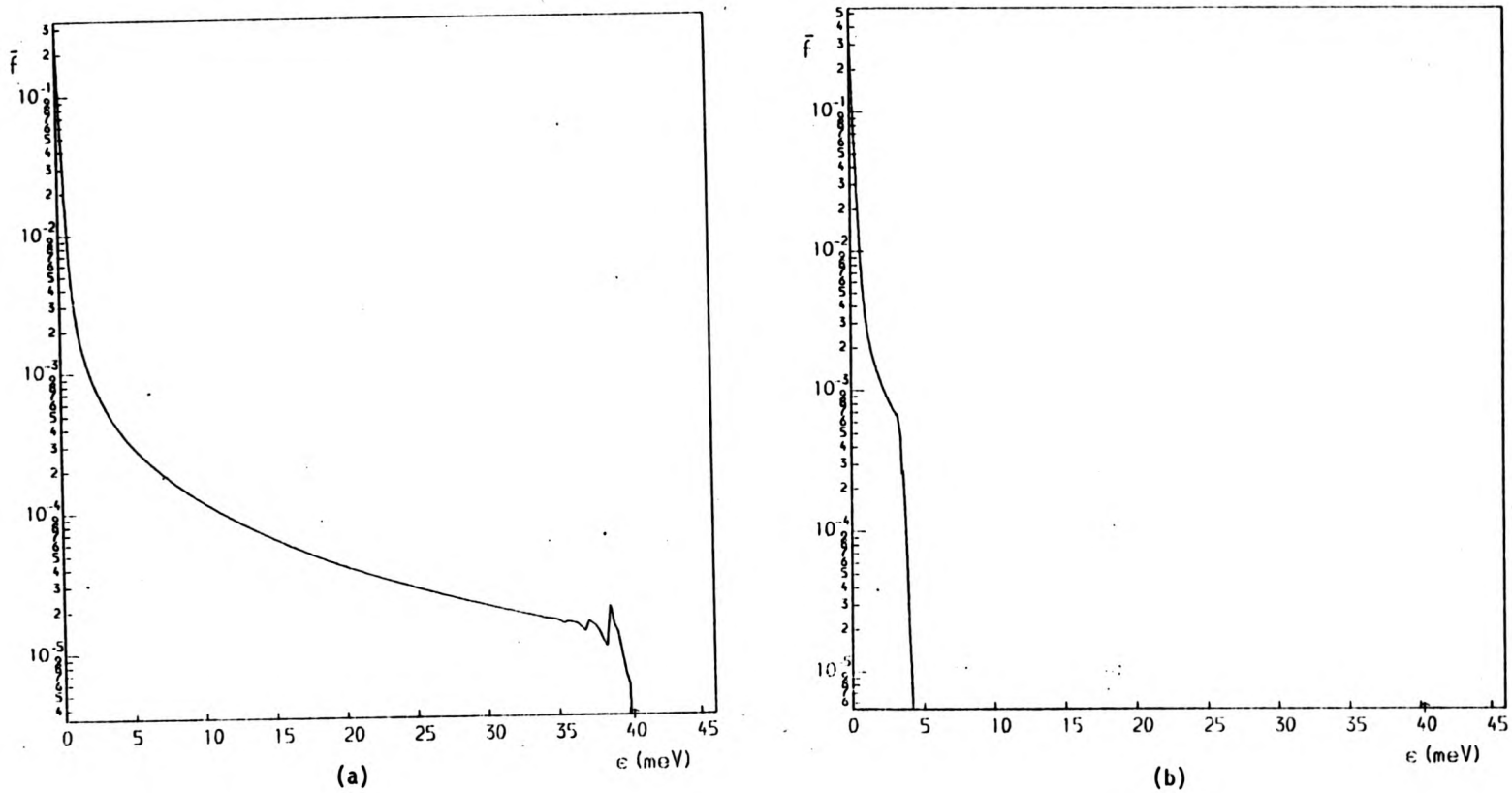

Figs 2.5a and b Distribution functions computed taking ϵ_i to be greater than $\hbar\omega_0$

(a) T.P., L.P, and D.P. scattering taken into account; L.O. scattering ignored

(b) T.P., L.P, D.P. and L.O. scattering taken into account.

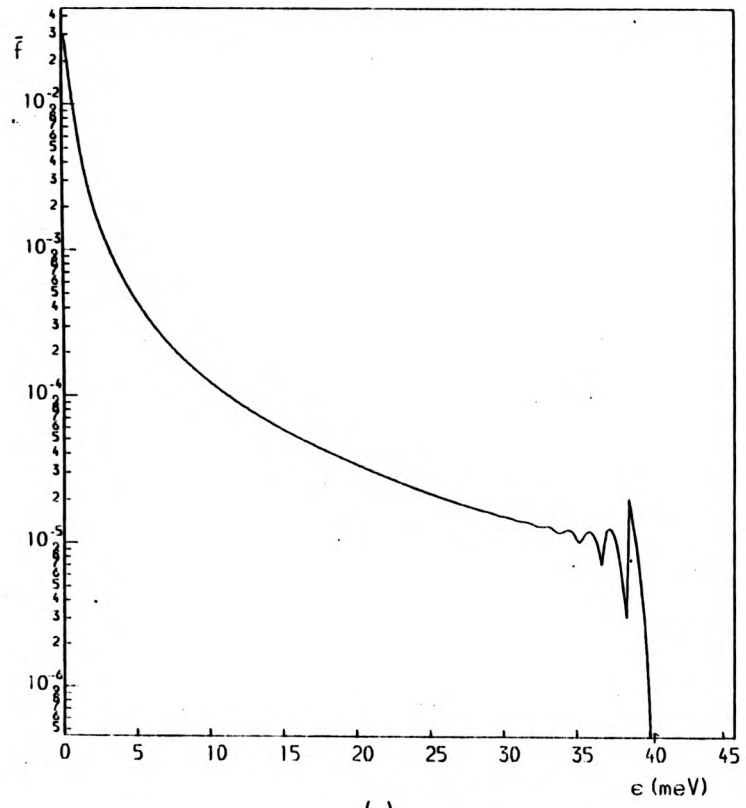

(c)

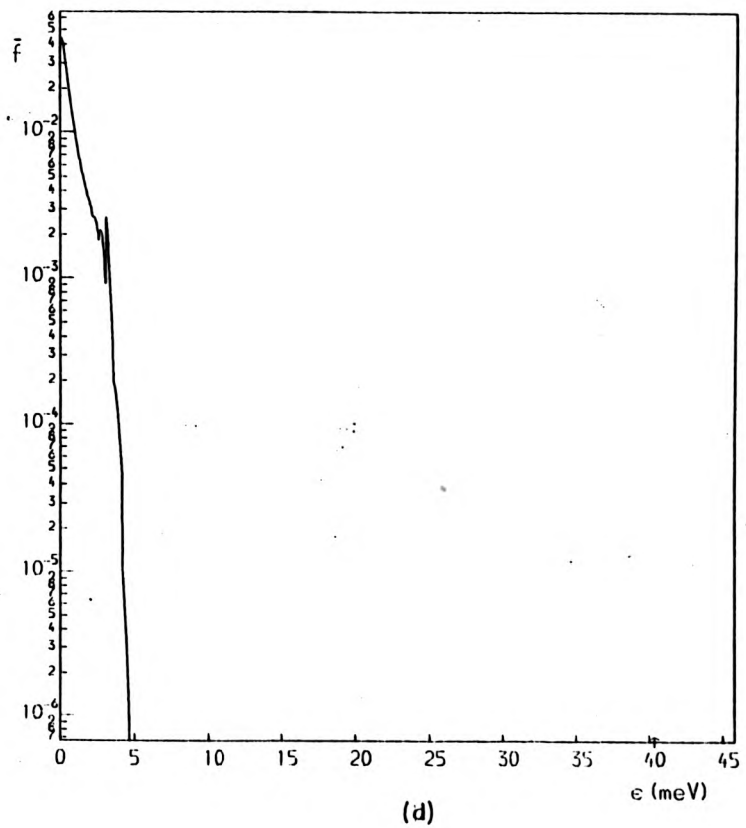

(d)

Figs 2.5c and d Distribution functions computed taking ϵ_i to be greater than $\hbar\omega_0$.

(c) D.P. scattering taken into account; L.O. scattering ignored

(d) D.P. and L.O. scattering taken into account.

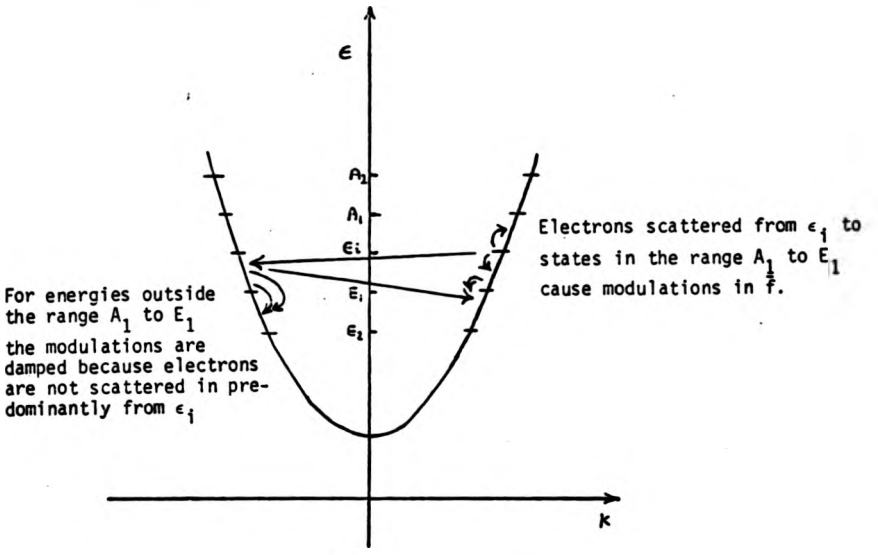

Fig. 2.6. A schematic illustration of the origin of the fine structure in $\bar{f}$. Electrons are injected at any energy ϵ_i. After one acoustic phonon emission events they can enter states having energies in the range A_i to E_1 ($A_i = \hbar^2(k_i + 2k_\alpha)^2/2m^*$, $E_1 = \hbar^2(k_i^2 - 2k_\alpha)^2/2m^*$). The modulations in $\bar{f}$ at energies within the range A_i to E_1 are characteristic of these events. For electrons to enter states having energies in the range A_2 to A_1 and E_1 to E_2 at least two acoustic phonon absorption or emission events are required. Electrons enter these states from a wide range of states instead of predominantly from ϵ_i. So the fine structure is damped for energies outside the range A_1 to E_1. For clarity only a few of the possible scattering transitions are illustrated in the diagram above.

to those having wave vectors in the range

$$|k_i - 2k_\alpha| \leq k \leq k_i + 2\,k_\alpha \qquad (2.30)$$

Therefore we expect that the modulations in $\bar{f}$ as a function of k would have a period of $\sim 2k_\alpha$. And $2k_\alpha$ is indeed the approximate period found for the fine structure if the energy scale of the figures is converted to wave vector.

The detailed form of the fine structure can be understood in terms of the k dependence of the scattering rates listed in Appendix 2.3. For D.P. scattering at low temperatures, the phonon emission rate is largest if the change in electron wave vector is of magnitude $2k_i$-$2k_\alpha$ and the absorption rate largest for very small changes in wave vector. A peak in $\bar{f}$, characteristic of D.P. phonon emission, therefore occurs at $k = |k_i - 2k_\alpha|$ (Figs. 2.5c, 2.3c). A similar peak, characteristic of phonon absorption should occur at a value of k just greater than k_i, but apparently has not been resolved in our calculations. For T.P. and L.P. scattering the screening factor broadens and displaces the maxima in the scattering rates. As a result the fine structure characteristic of these mechanisms is less evident and has a different form. The position of the peak in $\bar{f}$, characteristic of phonon emission, does not coincide with $k = k_i - 2k_\alpha$ and a subsidiary peak, attributable to phonon absorption is present at a wave vector just greater than k_i (Figs. 2.3a and b).

The structure in $\bar{f}$ is damped for wave vectors with magnitudes outside the range given by inequality 2.30 (See especially Fig. 2.5c). This is because electrons enter states having those wave vectors, from a wide range of other states instead of predominantly from states having wave vectors of magnitude k_i. The fine structure is not expected to be unique to GaAs. Similar structure is present in calculated distribution functions for monoenergetically injected holes in the valence band of Cu doped Ge,

at low lattice temperatures (Noguerra, 1978).

Although the fine structure is a genuine feature of the model distribution functions we have computed, it is uncertain whether it could exist in a typical experimental situation. Laser excitation is monochromatic, but in an experiment involving interband excitation, the injection spectrum would be broadened by valence band warping. Fine structure would be less evident if the injection spectrum were broader than $\sim 2\hbar^2 k_\alpha^2/m^*$. And in practice all three acoustic phonon processes are active simultaneously. As a result any fine structure would be confused, but still evident (Fig. 2.3d shows fine structure associated with all three processes). Also it is likely that the fine structure would be broadened by e.e. scattering and, masked by effects due to the electric fields expected to be associated with spatially non-uniform photoexcitation.

The second of our three sets of distribution functions is computed to determine how the form of the distribution depends on the form of the recombination rate. For this purpose all the distribution functions in the set are computed with all three acoustic phonon scattering mechanisms taken into account and with the injection energy taken as 3.989 meV, but a different form of R is used for each individual computation.

In Figs. 2.7a to d we illustrate some distribution functions which have been computed using various k independent recombination rates in the range $10^7 \leq R \leq 10^9\ s^{-1}$. With increasing R the form of the distribution changes in two ways. Firstly the fraction of electrons contributing to $\bar{f}$ decreases and secondly fewer of the electrons contributing to $\bar{f}$ thermalize at the band minimum. These effects are most extreme in the distribution function shown in Fig. 2.7d ($R = 10^9\ s^{-1}$). Only 77.9% of the electrons contribute to $\bar{f}$. And $\bar{f}$ as a function of energy takes the form of a broad pulse which has a maximum at energy $\sim \epsilon_1$.

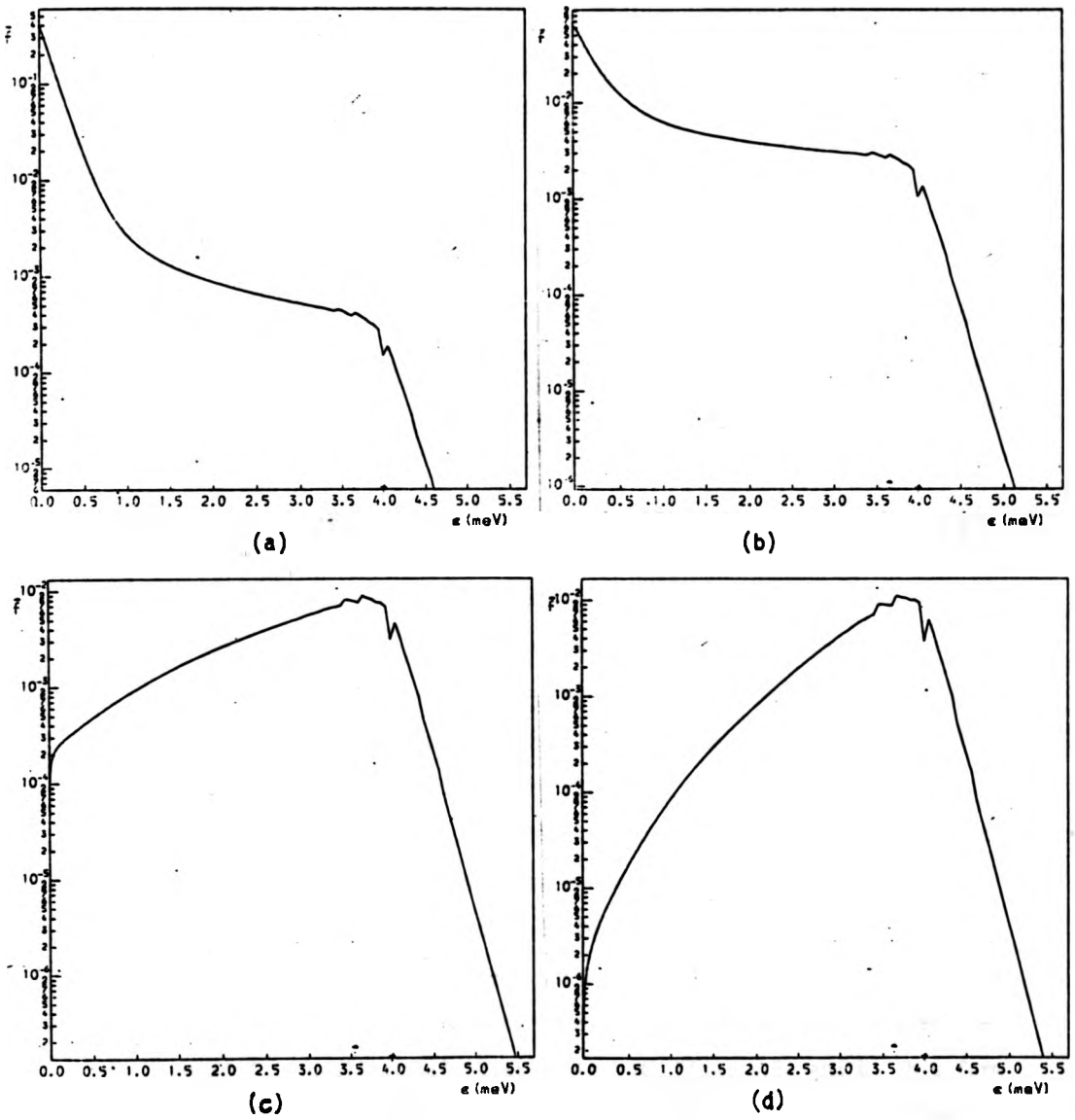

Fig.2.7. The dependence of the distribution function on the magnitude of the recombination rate

(a) $R = 10^7\ s^{-1}$; (b) $R = 10^8\ s^{-1}$

(c) $R = 5\times10^8 s^{-1}$; (d) $R = 10^9\ s^{-1}$

The other distribution functions in the second set are computed using various k dependent recombination rates. The following empirical form is used for R(k):

$$R(k) = \frac{A}{(1+B\ k^n)^m}$$

With n = 1, m = 3 this form models the Lax cascade mechanism (Lax, 1960) and with n = 2, m = 4 it represents (e,A^0) radiative recombination. Lax suggests, that $B^{-1} \sim \sqrt{6}\ k_\alpha$ and we take B as $10^7\ m^{-1}$. For (e,A^0) radiative recombination B is the square of the Bohr radius of an acceptor. We take a as 2.126×10^{-9}m which is a value appropriate to the C doped GaAs used in many photoluminescence experiments (Ulbrich, 1973). The normalization constant A is chosen such that the empirical form of R would give a mean recombination rate of $10^7\ s^{-1}$ if the distribution were a Maxwellian with a temperature of 10^0K. Distribution functions computed using the Lax and radiative forms for R(k) are shown in Figs. 2.8a and b respectively. These distribution functions cannot be quantitatively compared with each other or with those shown in Figs. 2.3, 2.5 and 2.7, because their electron densities differ from the value of $10^{20}\ m^{-3}$ common to all the distributions we have previously described. However this difference in electron density affects only the normalization of f. The distribution function shown in Fig. 2.8a (Lax recombination) has a slight turnover at the band minimum. Otherwise the form of $\bar{f}$ is qualitatively similar in both Figs. 2.8a and b. This form also has a close resemblance to the form of $\bar{f}$ shown in Fig. 2.3d. (The calculations leading to Figs. 2.8 and 2.3d differ only in the form of the recombination rate used). From a study of other computed distribution functions (which are not illustrated) we find that if the empirical form (as above) is used for R(k) then $\bar{f}$ deviates qualitatively from the form shown in Fig.2.3d only if the constant B is arbitrarily made so large that the recombination and scattering rates are comparable at the band minimum. Then the lattice temperature Maxwellian

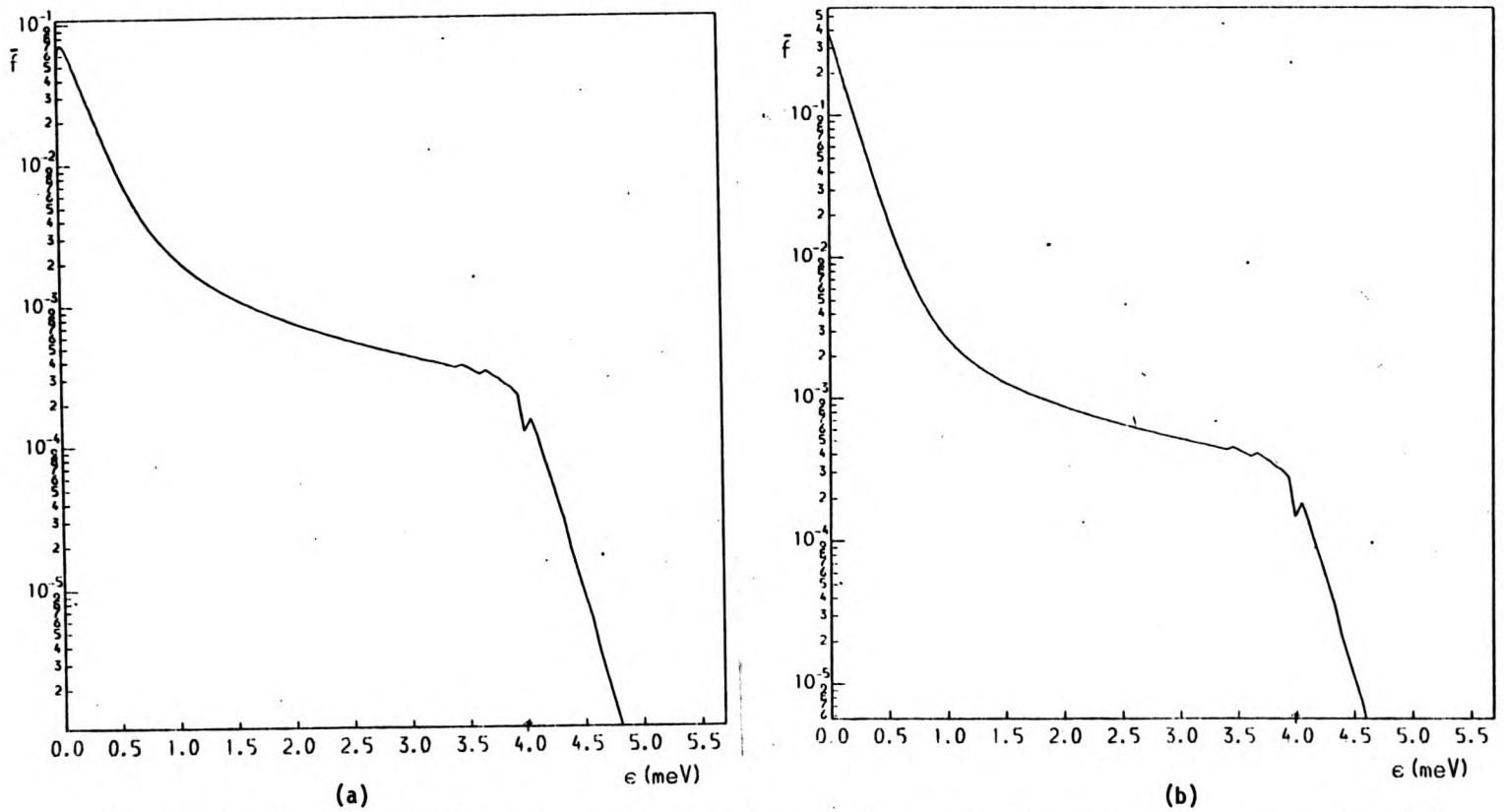

Figs. 2.8a and b. **Distribution functions computed taking the recombination rate to have the form $A(1+Bk^n)^{-m}$**

(a) n = 1 , m = 3

(b) n = 2 , m = 4

form at the band minimum is replaced by a turnover so $\bar{f}$ qualitatively resembles the form shown in Fig. 2.3c.

Our final set of distribution functions is computed to assess the sensitivity of the form of the distribution to the value of the inverse screening length. We repeat some of the calculations that lead to Fig.2.3. Values of μ other than the value of 1.56×10^7 m^{-1} used in those calculations are employed. If μ is reduced the piezoelectric scattering rates increase and so $\bar{f}$ has a lattice temperature Maxwellian form at the band minimum. Conversely increased screening reduces the piezoelectric scattering rates and so $\bar{f}$ has a turnover at low energies, which is similar to the one shown in Fig. 2.3. The turnover is present only if μ takes values $\gtrsim 4.79 \times 10^7$ m^{-1} but these values are greater than expected for many experimental situations.

In summary, the main results of this subsection are as follows. Firstly model distribution functions corresponding to the effects of electron injection, e.p. scattering and electron recombination have been computed and their various features have been interpreted as characteristic of the scattering events which the injected electrons can undergo. Secondly the qualitative form of the distributions has been shown to be insensitive to the k dependence of the recombination rate and to small changes in screening of the phonon interactions. The latter result indicates that we do not require a detailed knowledge of recombination or screening before we can attempt to compare the predictions of our model with experiment. But we do need some knowledge of the effects that e.e. scattering would have and the conditions under which it is important. We investigate some problems concerning e.e. scattering in Sections 2.7 to 2.9. Prior to doing so we study the time evolution of two of the distributions described in this subsection. This is done to further our understanding of how the form of these distributions is characteristic of the phonon scattering events undergone by the injected electrons.

2.6. Distribution functions corresponding to the absence of electron-electron scattering: time evolution.

This section is concerned with the time evolution of two distribution functions equivalent in all respects but the injection spectrum, to those shown in Figs. 2.3 c and d. The time evolution is computed using the iterative procedure defined by equation 2.16 and the computations are appropriate to a pulse injection spectrum (equation 2.7).

In Fig. 2.9 we show the evolution of f, computed with only D.P. scattering taken into account. The figure consists of a series of 'snapshots' showing the evolution of f over a period of 5n$, following application of the photoexcitation. The 'snapshots' are taken at 1n$ intervals. Fig. 2.10 is similar but the period is 50n$ and the interval 10n$. The equivalent steady state distribution is shown in Fig. 2.3c. It is clear from Fig. 2.9 that the initial phonon emission events generate some structure in f. (in the form of 'replicas' of the injection pulse). At later times (Fig. 2.10) this structure is less evident, presumably because a large number of scattering events have taken place. At a time of 50nS the distribution function resembles the steady state form shown in Fig. 2.3c but there are fewer electrons in states close to the band minimum.

The evolution of f, computed with all the acoustic phonon scattering mechanisms are taken into account, is illustrated in Figs. 2.11 and 2.12. These figures show f over similar periods and at similar intervals to those applying to Figs. 2.9 and 2.10 respectively. The equivalent steady state distribution is shown in Fig. 2.3d. The early phase of the evolution (Fig. 2.11) proceeds by a cascade of spontaneous phonon emissions. However, the structure associated with these emissions is less clear in Fig. 2.11 than in Fig. 2.9. This is because all three acoustic phonon scattering mechanisms have been taken into account in the calculations leading to

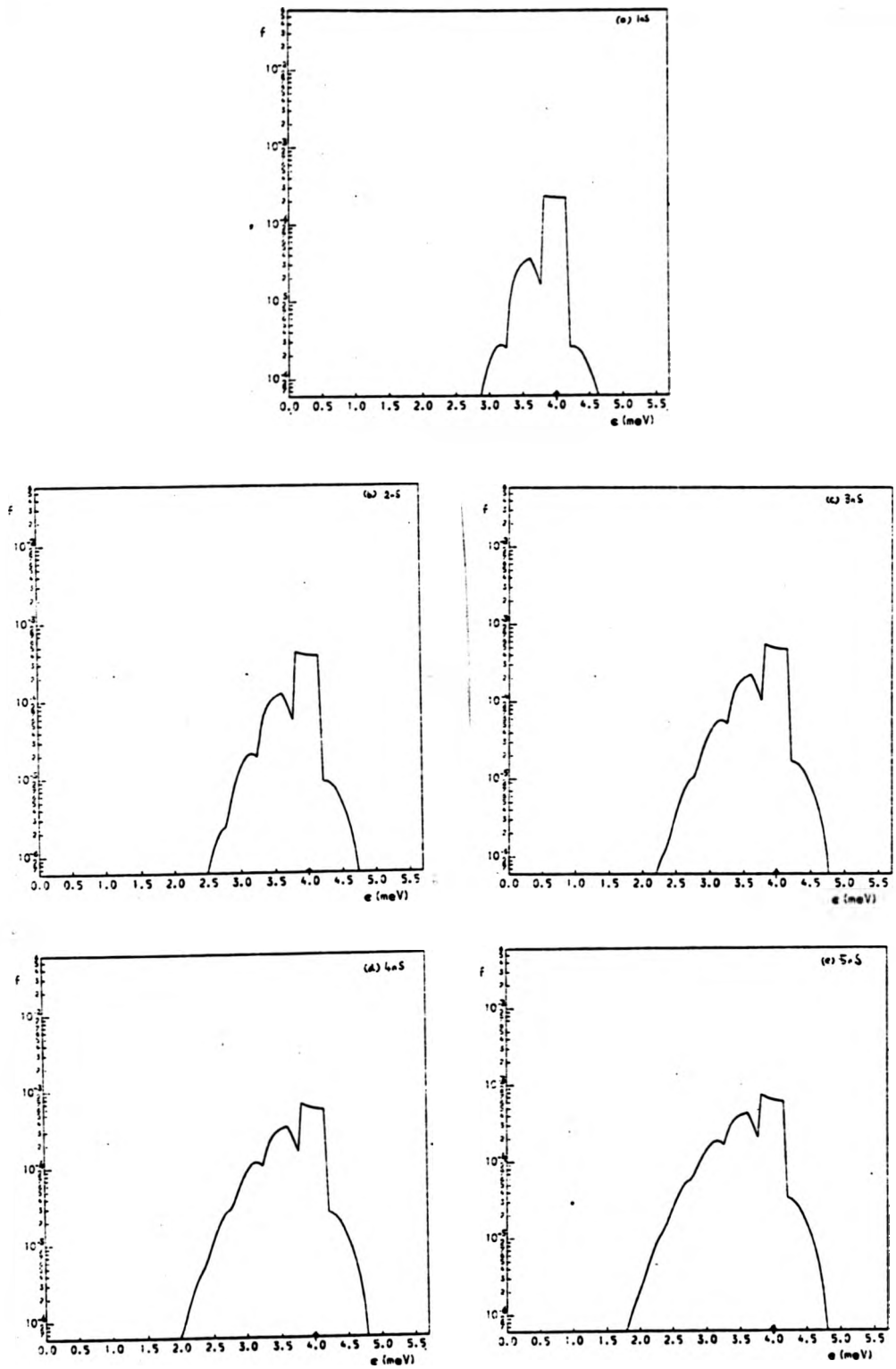

Fig.2.9. The time evolution of a distribution function equivalent to the one shown in Fig. 2.3c. Period = 5nS, interval = 1nS

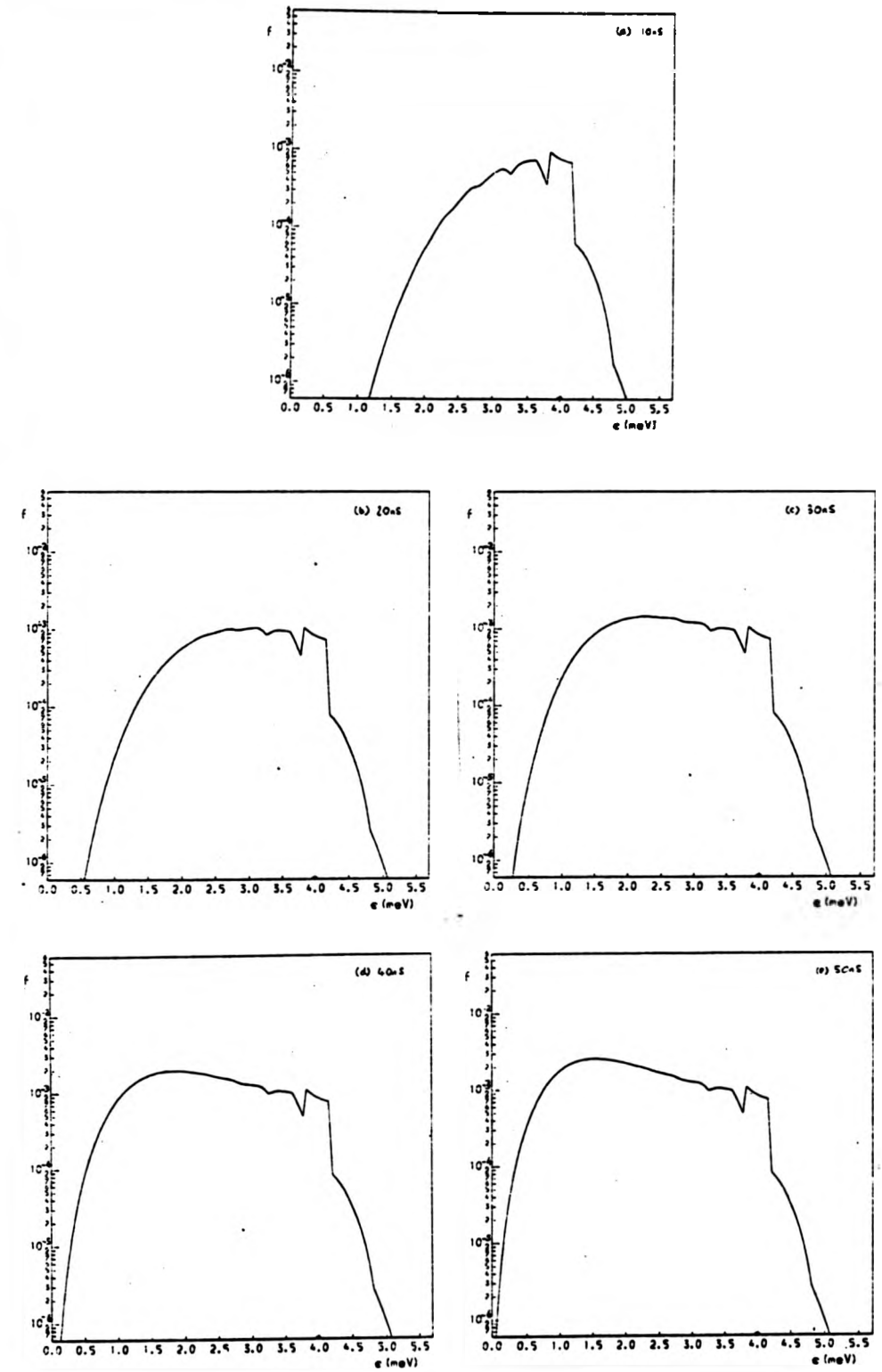

Fig.2.10. The time evolution of a distribution function equivalent to the one shown in Fig. 2.3c. Period = 50nS, interval 10nS.

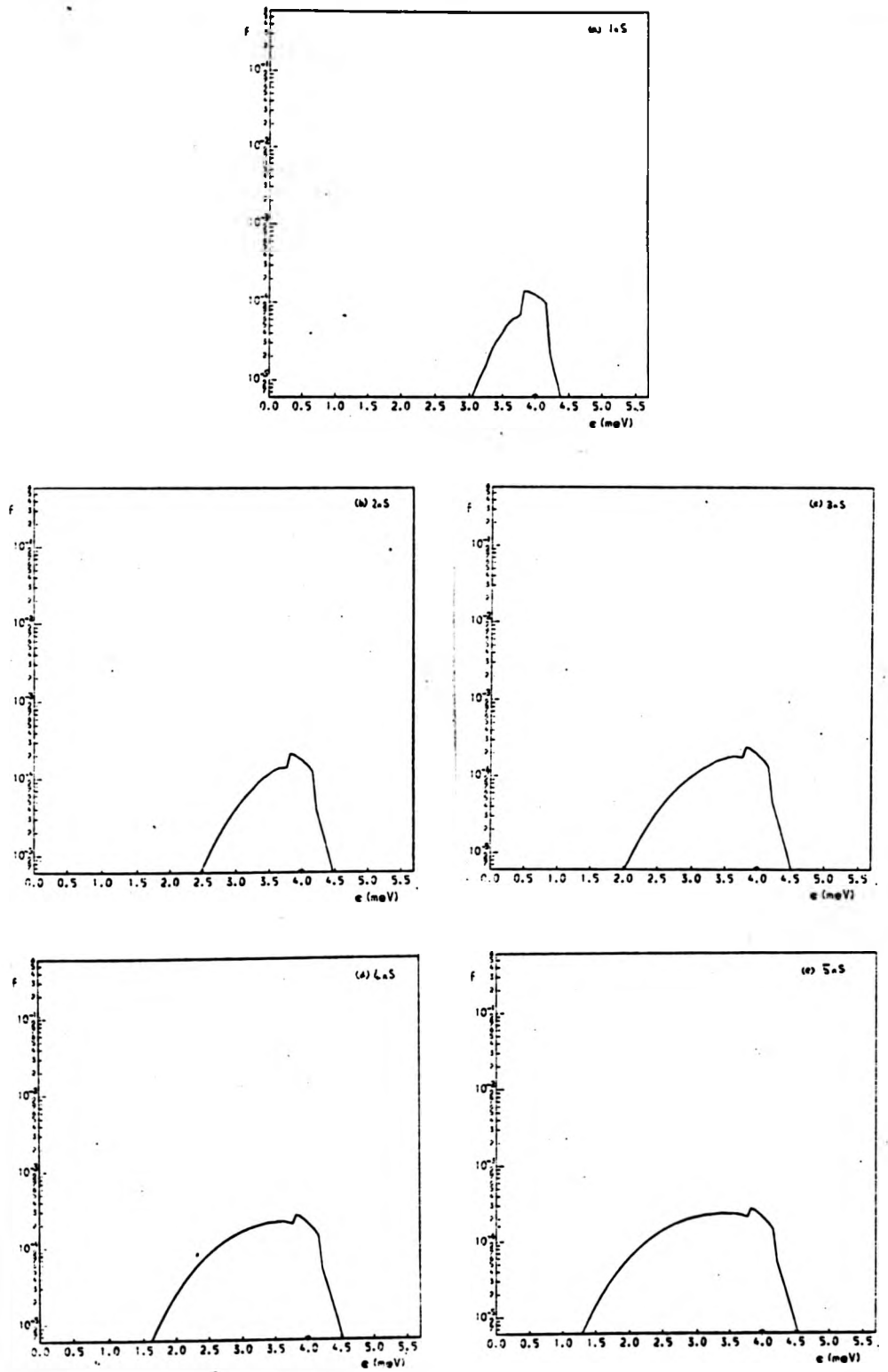

Fig.2.11. The time evolution of a distribution function equivalent to the one shown in Fig. 2.3d. Period = 5nS, interval = 1nS.

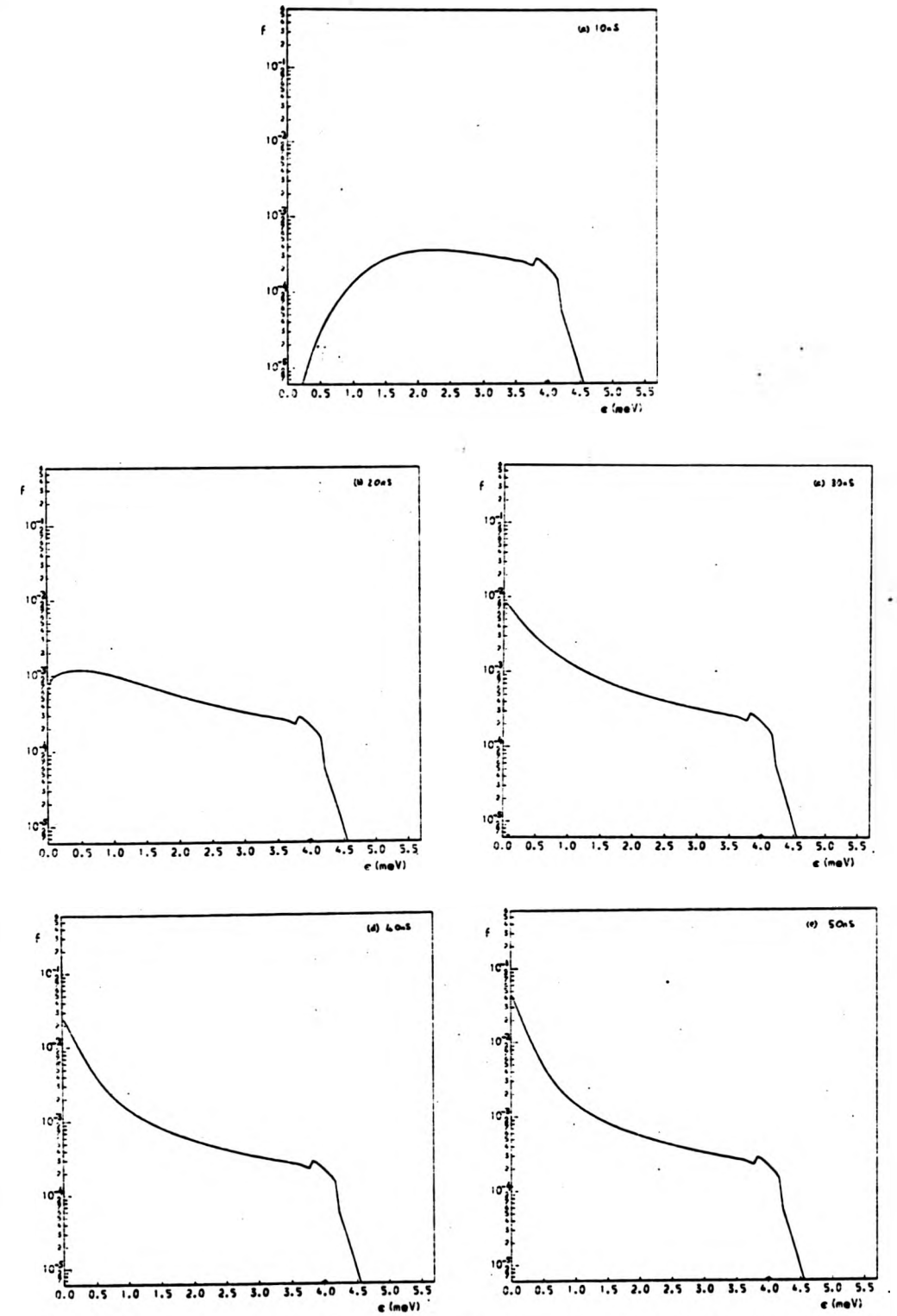

Fig. 2.12. The time evolution of a distribution function equivalent to the one shown in Fig. 2.3d. Period = 50nS, interval = 10nS.

Fig. 2.11. At a time of 50nS the distribution at the band minimum has a distinctly Maxwellian form (Fig. 2.11e). This is to be contrasted with the form of the distribution function shown in Fig. 2.9e. The difference in the two forms reflects the magnitude of the T.P. and L.P. scattering rates compared to the D.P. scattering rate.

2.7. A large screening model for electron-electron scattering: steady state distribution functions.

2.7.1. Electron-electron scattering

This section and sections 2.8 and 2.9 are concerned with the effect of electron-electron scattering on photoexcited electron distributions in GaAs. In principle the effect of this scattering mechanism can readily be taken into account using the iterative procedure described in section 2.4. However in practice, a 5 dimensional integral must be performed to compute the e.e. scattering rates and this type of integration has to be done repetitively during iterative computations of the distribution function. Such repetitive calculations of multidimensional integrals are not feasable using the computing facilities available to us. Therefore we use simplified models to study the effect of e.e. scattering on the photoexcited electron distribution. In section 2.9 we discuss a 'series expansion model' which we use to estimate the electron density at which e.e. scattering has a significant effect on the electron distribution. The model involves an approximation to f which allows the e.e. scattering rates to be estimated using integrals of only one dimension. In subsection 2.7.2 we describe a 'large screening model' which enables us to compute distribution functions exactly (in the sense that no approximations need to be made to f to obtain computationally tractable integrals). The large screening model is applicable to situations involving electron densities greater than those encountered in typical photoluminesce

experiments. Our work with the model is intended to illustrate the physics of e.e. scattering but is not intended to provide distribution function which can be quantitatively tested against experiment. Subsection 2.7.2 is concerned with steady state distribution functions which have been computed within the large screening model and the time evolution of one of these distribution functions is described in section 2.8. In the remainder of this subsection we first describe the exact form of the e.e. scattering rates and then discuss the nature of the approximations we have made to obtain these rates in a computationally tractable form

To derive the e.e. scattering rates we assume that the electron interact via a screened Coulomb potential and that they make transition between Bloch states. Then we estimate the e.e. transition rate using the golden rule. The integrals of the overlap between the modulating functions of Bloch states are assumed to be unity and thus, for a distribution function of arbitrary $\underline{k}$ dependence, the e.e. scattering in and scattering out rates are found to be given by the following equations (See Appendix 2.3; See also Hearn 1966; Landsberg 1966):

$$\left.\frac{\partial f}{\partial t}\right|_{in} = \left(\frac{V}{8\pi^3}\right)^2 \frac{2\pi}{\hbar}\iint[M^2(\underline{k}-\underline{k}_b)+M^2(\underline{k}_a-\underline{k})+\{M(\underline{k}-\underline{k}_b)-M(\underline{k}_a-\underline{k})\}^2]f(\underline{k}_a)f(\underline{k}_b) \tag{2.31a}$$

$$\times\ \delta(\epsilon(\underline{k}_a+\underline{k}_b-\underline{k})+\epsilon(\underline{k})-\epsilon(\underline{k}_a)+\epsilon(\underline{k}_b))\,d\underline{k}_b\,d\underline{k}_a$$

$$\left.\frac{\partial f}{\partial t}\right|_{out} = f(\underline{k})\left(\frac{V}{8\pi^3}\right)^2 \frac{2\pi}{\hbar}\iint[M^2(\underline{k}_a-\underline{k}_b)+M^2(\underline{k}-\underline{k}_a)+\{M(\underline{k}_a-\underline{k}_b)-M(\underline{k}-\underline{k}_a)\}^2]f(\underline{k}_b)$$

$$\times\ \delta(\epsilon(\underline{k}+\underline{k}_b-\underline{k}_a)+\epsilon(\underline{k}_a)-\epsilon(\underline{k})-\epsilon(\underline{k}_b))\,d\underline{k}_b\,d\underline{k}_a \tag{2.31b}$$

where M is defined as

$$M(\underline{k}-\underline{k}_b) = \frac{e^2}{\varepsilon\varepsilon_o V} \frac{1}{\mu^2 + |\underline{k}-\underline{k}_b|^2} \tag{2.32}$$

and μ is the inverse screening length. Physically, the integrand of the scattering in rate (equation 2.31a) represents the transition rate for a collision in which the initial wave vectors of the two electrons are $\underline{k}_a$ and $\underline{k}_b$ and the final wave vectors are $\underline{k}$ and $\underline{k}_a + \underline{k}_b - \underline{k}$. The squared matrix element for this transition rate consists of the sum of the three terms within the square brackets of the integrand. The terms $M^2(\underline{k}-\underline{k}_b)$ and $M^2(\underline{k}_a-\underline{k})$ are squared matrix elements for direct and exchange collisions respectively between electrons of unlike spin. The term $\{M(\underline{k}-\underline{k}_b) - M(\underline{k}_a-\underline{k})\}^2$ is the squared matrix element for collisions between electrons of like spin. (See Appendix 2.3). The integrand of the scattering out rate (equation 2.31b) has a similar physical meaning to the integrand of the scattering in rate except that the initial wave vectors are $\underline{k}$ and $\underline{k}_b$ and the final wave vectors are $\underline{k}_a$ and $\underline{k} + \underline{k}_b - \underline{k}_a$.

The integrals involving the matrix element for collisions between electrons of like spin are less tractable than those involving the other two matrix elements. And so we use a procedure due to Landsberg (1966) to simplify the evaluation of the e.e. scattering rates. The procedure is as follows. The terms within the square brackets of equation 2.31a satisfy the inequality:

$$\{M^2(\underline{k}-\underline{k}_b) - M^2(\underline{k}_a-\underline{k})\}^2 < M^2(\underline{k}-\underline{k}_b) + M^2(\underline{k}_a-\underline{k})$$

Therefore the total scattering in rate is known to be within a factor of 2 of the scattering in rate due to collisions between electrons of unlike spin. And the total scattering in rate can be estimated from equation 2.31a by replacing the terms within square brackets by the simpler term:

$$p_s [M^2(\underline{k}-\underline{k}_b) + M^2(\underline{k}_a-\underline{k})]$$

where p_s is a 'spin uncertainty factor' which is assumed to be independent of wave vector and takes a value in the range $1 \leq p_s \leq 2$. A similar replacement can be made to estimate the scattering out rate given by equation 2.31b.

A further simplification to the form of the scattering rates is possible because in both equations 2.31a and b the direct and exchange terms make identical contributions to the total transition rate. (See Appendix 2.3). Therefore, to estimate the e.e. scattering rates, we replace the three terms in the square brackets of equations 2.31a and b by the single terms $2p_s M^2(\underline{k}-\underline{k}_b)$ and $2p_s M^2(\underline{k}_a-\underline{k}_b)$ respectively. Taking this simplification into account we define an e.e. scattering kernel S_e:

$$S_e(f:\underline{k}_a \rightarrow \underline{k}) = \left(\frac{V}{8\pi^3}\right)^2 \frac{4\pi}{\hbar} p_s \int M^2(\underline{k}-\underline{k}_b) f(\underline{k}_b) \delta(\epsilon(\underline{k}_a+\underline{k}_b-\underline{k})+\epsilon(\underline{k})-\epsilon(\underline{k}_a)-\epsilon(\underline{k}_b)) d\underline{k}_b \tag{2.33}$$

This enables us to write the e.e. scattering rates in a form similar to the collision term of equation 2.3:

$$\left.\frac{\partial f}{\partial t}\right|_{e.e.} = \int f(\underline{k}_a) S_e(f:\underline{k}_a \rightarrow \underline{k}) d\underline{k}_a - f(\underline{k}) \int S_e(f:\underline{k} \rightarrow \underline{k}_a) d\underline{k}_a$$

The symbol f: within the brackets of $S_e(f:\underline{k}_a \rightarrow \underline{k})$ is used to denote that S_e is functionally dependent on f (in the sense that it involves an integration over f).

If the iterative procedure defined by equation 2.14 is used to take account of e.e. scattering then the kernel S_e must be recomputed at each iteration. This task would consume a large amount of computer time. Therefore to take account of e.e. scattering in computations of any distribution function we need to approximate S_e in such a way that this quantity can be computed rapidly. Because we compute spherically symmetric

distribution functions we are especially interested in approximations to $\int S_e(f: \underline{k}_a \rightarrow \underline{k}) d\Omega_a$ (rather than in approximations to S_e.). Two such approximations are provided by the large screening model described in the next subsection and the series expansion model described in Section 2.9.

2.7.2. Steady state distribution functions in the large screening model

To obtain the large screening model we consider the matrix element defined by equation 2.32. We assume that the inverse screening length μ is so large that this matrix element is, to a good approximation, independent of $|\underline{k}-\underline{k}_b|$ over the range of $\underline{k}_b$ over which f is expected to be significant. Thus M can be taken as $e^2(\varepsilon\varepsilon_o \mu^2 V)^{-1}$. Physically this wave vector independence of M means that the electrons behave as point scatterers having the potential $e^2(\varepsilon\varepsilon_o \mu^2)^{-1} \delta(\underline{r})$. For such a potential the k dependence of the scattering rates is dictated solely by the requirements of energy and wave vector conservation. And the form of the distribution functions corresponding to these conditions are expected to provide a simple illustration of the physics of e.e. scattering. These distribution functions are easily computed for in the large screening model the e.e. scattering rates have a particularly simple form:the scattering rate due to collisions between electrons of like spin is vanishing so that $p_s = 1$ and the kernel S_e is found in terms of the following one dimensional integrals (See Appendix 2.3):

$$\int S_e(f: \underline{k}_a \rightarrow \underline{k}) d\Omega_a$$

$$= \frac{B_{1ee}}{k_a} \int_k^\infty f(z) z\, dz + \frac{B_{1ee}}{k_a k} \int_o^k f(z) z^2 dz \quad \text{for } k_a \geq k$$

$$= \frac{B_{1ee}}{k} \int_k^\infty f(z) z\, dz + \frac{B_{1ee}}{k_a k} \int_{(k^2-k_a^2)^{1/2}}^k f(z) z (k_a^2 - k^2 + z^2)^{1/2} dz \quad \text{for } k_a \leq k \qquad (2.34)$$

where $B_{1ee} = \frac{1}{4\pi^3} \frac{2m^*}{\hbar^2} \left(\frac{e^2}{\varepsilon\varepsilon_0}\right)^2 \frac{1}{\mu^4}$

Note that a large screening model similar to ours has previously been studied by Hearn (1966; See also Landsberg 1966). However, this work differs from ours in that the distribution function was assumed to have only a small deviation from a Maxwellian form and the deviation was computed from a linearized version of the Boltzmann equation.

In the remainder of this subsection we discuss some distribution functions which have been computed within the large screening model. These distribution functions serve to illustrate the physics of e.e. scattering but for the following two reasons they are not directly applicable to any real situations. Firstly the large screening model is only applicable to situations involving densities $\geq 10^{24}$ m^{-3}. Typical photoluminescence experiments involve lower electron densities (See, however, Leheney and coworkers, 1979). Secondly a particular one dimensional integral involved in the kernel S_e (See above) has $k \to \infty$ as its upper limit. Truncation errors arising in evaluating this integral numerically have restricted the distribution functions we could compute to those appropriate to low electron densities (7.5×10^{16} m^{-2}) and low injection energies (≤ 1 meV). Low electron densities are inconsistent with large screening and so we treat the electron density and the screening length as independent parameters. The latter parameter serves as a measure of the strength of the e.e. interaction because the magnitude of the δ potential (See previous paragraph) is $\sim \mu^{-2}$. Our computations illustrate how the form of the distribution function depends on the magnitude of μ.

All the distribution functions we have computed within the large screening model correspond to an injection spectrum in the form of a δ function at an energy of 0.997 meV. (Equation 2.6). The electron injection rate is chosen to be such that the electron density is

7.5×10^{16} m^{-3}. Electron-phonon scattering is not taken into account. The recombination rate is supposed to be k independent and taken to be 10^7 s^{-1}. The inverse screening lengths and various other parameters associated with the distribution functions are given in Tables 2.5 and 2.6. The distribution functions have been calculated by approximating the scattering integrals using the trapezium rule and iterating according to equation 2.14. (For this particular task the trapezium rule allows more efficient computation than does Simpson's rule). A mesh step equal to k_α for the transverse phonons has been used in the calculations. In all cases the iteration has converged rapidly; after 40 iterations the normalization factors have been found to be ≤ 1.18. As a check the calculations have been repeated using a pulse injection spectrum, and the distribution functions so obtained are in good agreement with those corresponding to δ function injection. As a further test the mean energy of an electron in the distribution has been computed. This energy should be ϵ_i because e.p. scattering has not been taken into account. All the mean energies are indeed within 4% of ϵ_i.

Our computed distribution functions are shown in Fig. 2.13. The distribution functions shown in parts a to d of this figure are arranged in decreasing order of inverse screening length. The distribution function shown in Fig. 2.13a ($\mu = 5 \times 10^9$ m^{-1}) corresponds to an e.e. interaction so weak that only $\sim 10^{-4}$% of the electrons contribute to the non-singular part of the distribution. This part has the form of a flat plateau at low energies and has a sharp cut off at an energy of $2\epsilon_i$. The physical origin of this form of $\bar{f}$ is thought to be as follows. Because the e.e. interaction is weak the electrons are unlikely to survive sufficiently long to undergo more than one scattering event. The non-singular part of f is thus predominantly characteristic of those electrons which have been injected and scattered off each other but have under gone no further

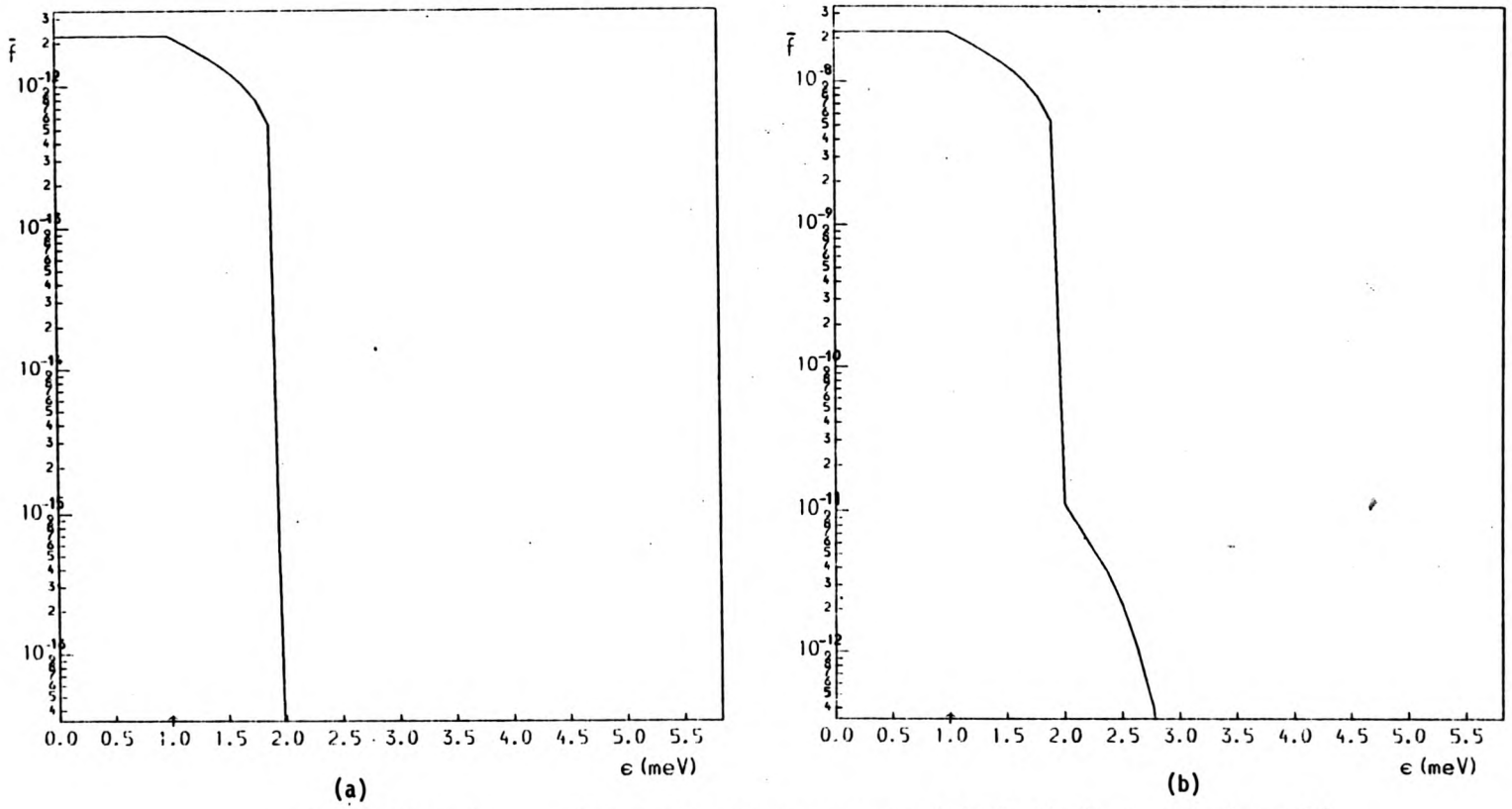

Figs. 2.13a and b. Distribution functions computed within the large screening model. Phonon scattering has been ignored.
(a) $\mu = 5 \times 10^{9}\ m^{-1}$ (b) $\mu = 5 \times 10^{8}\ m^{-1}$

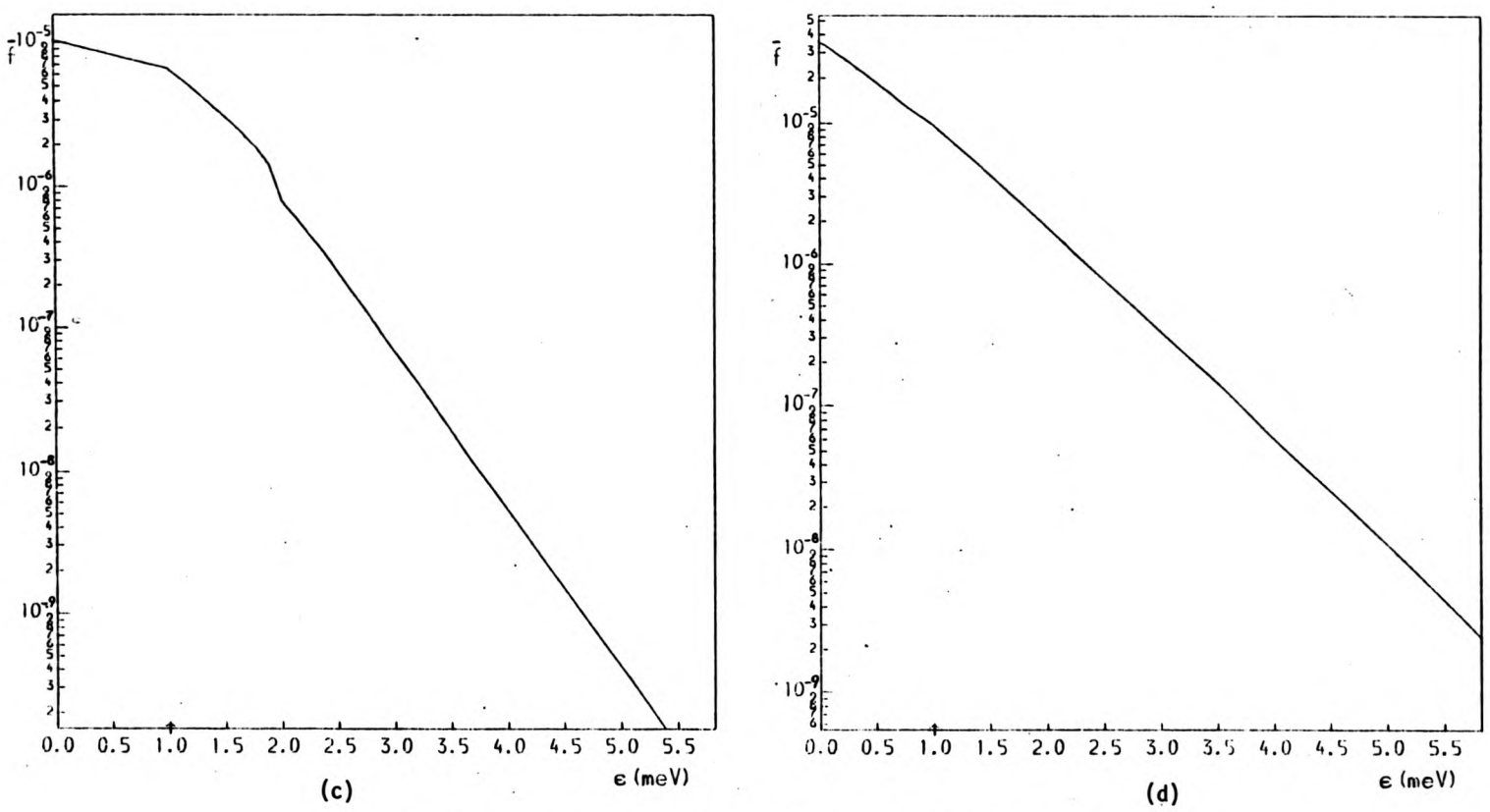

Figs 2.13c and d. Distribution functions computed within the large screening model Phonon scattering has been ignored.

(c) $\mu = 10^8\ m^{-1}$ (d) $\mu = 5 \times 10^7\ m^{-1}$

collisions. In a collision between two electrons of energy ϵ_i one electron can gain at most an energy of ϵ_i, and emerge with an energy $2\epsilon_i$ at the expense of total energy loss by the other. This energy conservation in scattering of electrons having an energy ϵ_i is reflected as the sharp cut off which is present at $\epsilon = 2\epsilon_i$ in the distribution function shown in Fig. 2.13a.

Figs. 2.13b and c show distribution functions which correspond to intermediate values of the e.e. interaction strength. ($\mu = 5 \times 10^8$ and 10^8 m^{-1} respectively). By comparing these distribution functions with the one in Fig.2.13a it can be seen that the primary effect of an increased interaction strength is to scatter some of the electrons into a Maxwellian tail. However, the distribution functions shown in Figs.2.13b and c also have discontinuities at ϵ_i and $2\epsilon_i$. These discontinuities are respectively characteristic of electron injection and of energy conservation in the initial scattering event undergone by the injected electrons.

A distribution function corresponding to an e.e. interaction sufficiently strong to smooth out the discontinuity at $2\epsilon_i$ is shown in Fig. 2.13d ($\mu = 5 \times 10^2$ m^{-1}). 93% of the electrons contribute to the non-singular part of this distribution. For energies $< \epsilon_i$ $\bar{f}$ is well approximated by a Maxwellian function having a temperature of $9.23^{\circ}K$. For energies $> \epsilon_i$ $\bar{f}$ is also well approximated by a Maxwellian, the appropriate temperature being $6.8^{\circ}K$. These two temperatures are reasonably close to the value of $7.73^{\circ}K$ expected for a Maxwellian distribution of electrons, whose mean energy is ϵ_i ($\equiv$ 0.997 meV).

In the next section we describe the time evolution of the distribution function shown in Fig. 2.13d. This is done to provide a further illustration of how the distribution functions described in this section are characteristic of electron-electron scattering.

collisions. In a collision between two electrons of energy ϵ_1 one electron can gain at most an energy of ϵ_1, and emerge with an energy $2\epsilon_1$ at the expense of total energy loss by the other. This energy conservation in scattering of electrons having an energy ϵ_1 is reflected as the sharp cut off which is present at $\epsilon = 2\epsilon_1$ in the distribution function shown in Fig. 2.13a.

Figs. 2.13b and c show distribution functions which correspond to intermediate values of the e.e. interaction strength. ($\mu = 5 \times 10^8$ and 10^8 m^{-1} respectively). By comparing these distribution functions with the one in Fig.2.13a it can be seen that the primary effect of an increased interaction strength is to scatter some of the electrons into a Maxwellian tail. However, the distribution functions shown in Figs.2.13b and c also have discontinuities at ϵ_1 and $2\epsilon_1$. These discontinuities are respectively characteristic of electron injection and of energy conservation in the initial scattering event undergone by the injected electrons.

A distribution function corresponding to an e.e. interaction sufficiently strong to smooth out the discontinuity at $2\epsilon_1$ is shown in Fig. 2.13d ($\mu = 5 \times 10^2$ m^{-1}). 93% of the electrons contribute to the non-singular part of this distribution. For energies $< \epsilon_1$ $\bar{f}$ is well approximated by a Maxwellian function having a temperature of $9.23^{\circ}K$. For energies $> \epsilon_1$ $\bar{f}$ is also well approximated by a Maxwellian, the appropriate temperature being $6.8^{\circ}K$. These two temperatures are reasonably close to the value of $7.73^{\circ}K$ expected for a Maxwellian distribution of electrons, whose mean energy is $\epsilon_1 (\equiv 0.997$ meV).

In the next section we describe the time evolution of the distribution function shown in Fig. 2.13d. This is done to provide a further illustration of how the distribution functions described in this section are characteristic of electron-electron scattering.

2.8. A large screening model for electron-electron scattering: the time evolution of the distribution function.

This section contains an account of the time evolution of the distribution function shown in Fig. 2.13d. (large screening model, inverse screening length = 5×10^7 m^{-1}). The time evolution is computed in the way described in Section 2.6.1.e.the parameters used to compute the time evolution are exactly the same as those used to compute the steady state distribution function, a pulse injection spectrum is used in place of the δ function and the time dependence is calculated according to equation 2.16.

The computed time evolution of the distribution function is illustrated in Fig. 2.14. This figure consists of a sequence of 'snapshots' which show f at various times after application of the photoexcitation. Part a of the figure refers to a time of 10nS. At this time the distribution function has two distinct parts. One part is in the form of a pulse which is characteristic of those electrons which have been injected but have undergone no collisions. The other part is in the form of a smooth function. For energies $\leq \epsilon_1$ this function is about 3 orders of magnitude smaller than the pulse and the same function is very small for energies $\geq 2\epsilon_1$. The form of the smooth function qualitatively resembles that of the steady state distribution function shown in Fig. 2.13a (which was computed to be appropriate to a weak e.e. interaction: $\mu = 5 \times 10^9$). This is because the smooth function and the distribution function shown in Fig. 2.13a are both characteristic of those electrons which have undergone few collisions.

Figs. 2.14b to f show the distribution function at 20nS intervals at times in the range 20nS to 100nS. From these diagrams it is clear that as time progresses the magnitude of both parts of f increases: this is attributable to an increasing number of electrons in the band. In addition

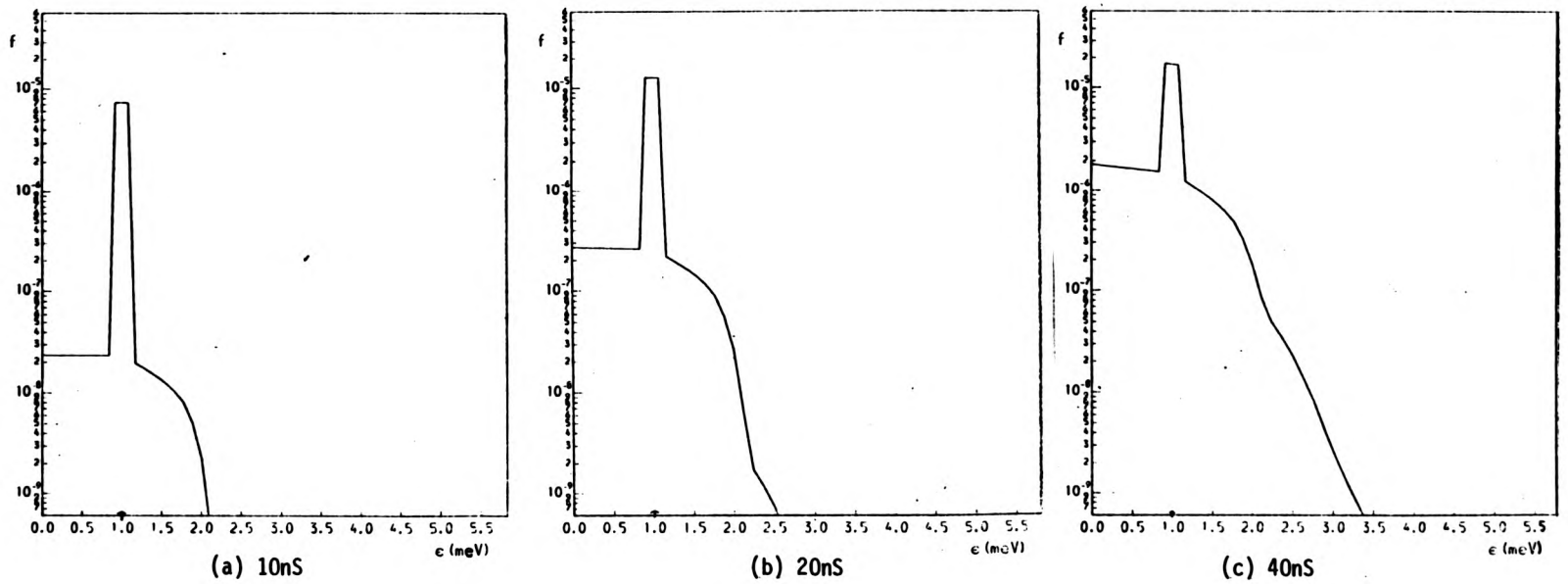

(a) 10nS (b) 20nS (c) 40nS

Figs. 2.14 a to c. The time evolution of a distribution function computed within the large screening model. Phonon scattering has been ignored; $\mu = 5\times10^{7}\ m^{-1}$. The equivalent steady state distribution function is shown in Fig. 2.13d.

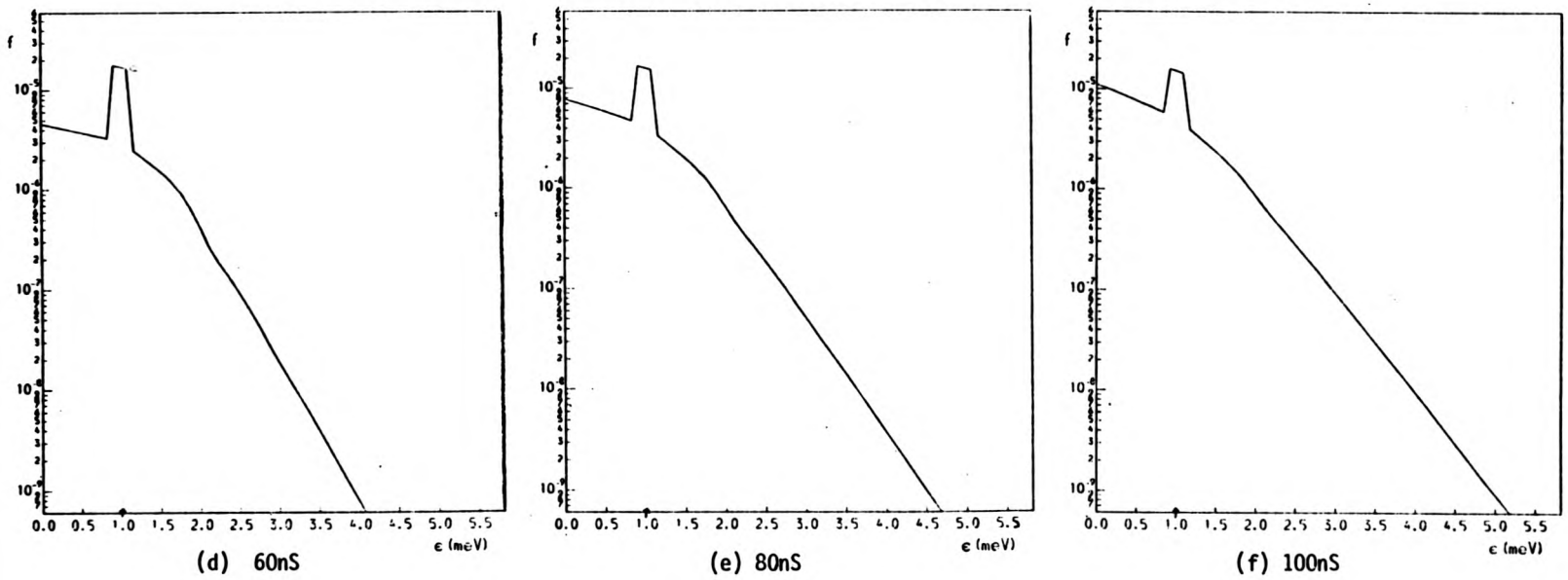

Figs. 2.14d to f. The time evolution of a distribution function computed within the large screening model. Phonon scattering has been ignored. $\mu = 5 \times 10^7\ m^{-1}$. The equivalent steady state distribution function is shown in Fig. 2.13.

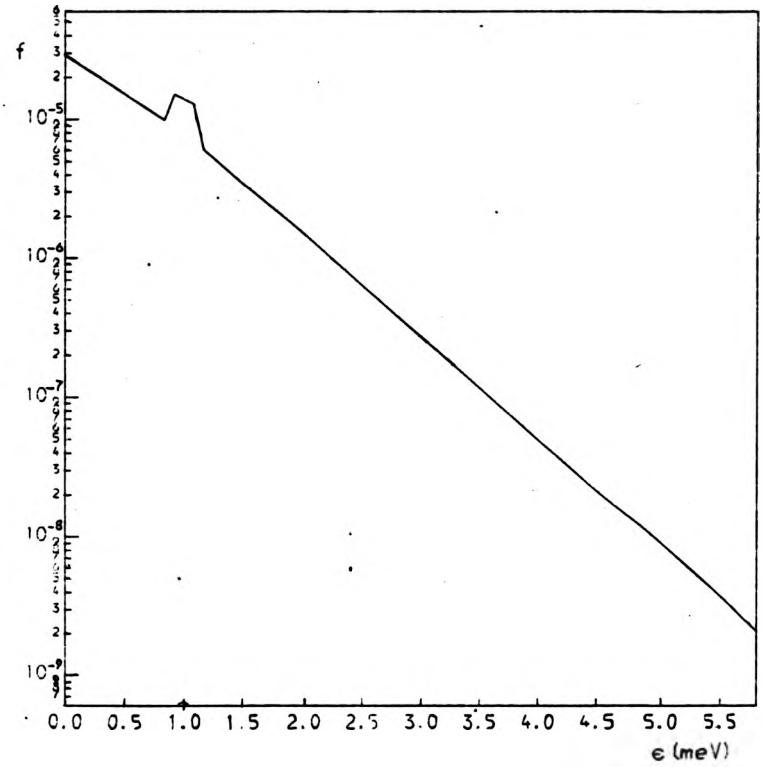

Fig.2.14g. The time evolution of a distribution function computed within the large screening model. Phonon scattering has been ignored.
$\mu = 5 \times 10^{7} m^{-1}$; time = 500nS
The equivalent steady state distribution function is shown in Fig. 2.13d.

the magnitude of the smooth part relative to the pulse increases: this is because the fraction of electrons which have been scattered increases. Figs. 2.14b to f also illustrate how the distribution function develops a Maxwellian tail. At times ≤ 60n$s (Figs. 2.14b to d) a discontinuity is present in f at an energy $\sim 2\epsilon_1$. (Compare with the steady state distribution functions shown in Figs 2.13 b and c). At later times (≥ 80n$s; Figs. 2.14e and f) the distribution function has a Maxwellian tail.

In the final stages of the evolution the only essential difference between the smooth part of the distribution function and its steady state equivalent (Fig. 2.13d) is one of normalization. Fig. 2.14g shows the distribution function corresponding to a time of 500n$s. At this time the normalization factor is 1.18 and at energies $\sim \epsilon_1$ the magnitude of the smooth part is comparable to that of the pulse.

2.9. A series expansion model for electron-electron scattering

2.9.1. The model and its numerical implementation

The electron density dependence of the photoexcited electron distribution in GaAs at low lattice temperatures is known from the result of photoluminescence experiments (See Section 2.2.1). The distribution function has a non-Maxwellian form if the electron density is either high ($\sim 10^{24}$ m^{-3}) or low ($\sim 10^{16}$ m^{-3}) and the distribution function corresponding to intermediate electron densities has a Maxwellian form. In this section we describe an attempt to compute distribution functions corresponding to the low to intermediate density range. The aim of the work is to estimate the minimum electron density at which e.e. scattering has a significant effect on the photoexcited electron distribution and the work involves the use of a Taylor series approximation to the e.e. scattering rates. The approximation allows distribution functions to be computed whilst retaining the non-linear character of the e.e. scattering rates. It is expected to be valid provided that the distribution function does not deviate grossly

from a Maxwellian function and provided that the inverse screening length is sufficiently small. Unfortunately a numerical implementation of the approximation involves some computational difficulties (See later in this subsection). As a result of these difficulties we have only been able to compute distribution functions which correspond to electron densities $\gtrsim 3 \times 10^{16}$ m^{-3} and the deviation of these distribution functions from a Maxwellian form may be too great for the Taylor series approximation to be valid. In addition the accuracy of the computed distribution functions may be suspect. Nevertheless the computations have yielded results for the electron thermalization time and electron density at which e.e. scattering would have a significant effect on the distribution, which agree promisingly well with experiment. These results are described in the next subsection. This subsection continues with a description of the approximate form of the e.e. scattering rates and an explanation of the numerical problems associated with the approximation.

The repetitive evaluation of multi-dimensional integrals required to take exact account of e.e. scattering would consume a prohibitive amount of computer time. Hence we approximate the e.e. scattering kernel $S_e(\underline{k}_a \rightarrow \underline{k})$ (See equation 2.33) in such a way that only integrals of one dimension need be computed to estimate the e.e. scattering rates. To do this we write f as the product of a Maxwellian function (with an effective temperature T_{eff}) and a modulation function g(k): $f = e^{-\gamma k^2} g(k)$, $\gamma = \hbar^2/2m^* k_B T_{eff}$. The e.e. scattering rates appropriate to this form of f are discussed in Appendix 2.3. There it is shown that if a suitable polynomial approximation to g(k) is available then only integrals of one dimension need be computed to calculate the e.e. scattering rates. Next we consider how to approximate g(k).

One method for approximating g suggests itself if we notice that, provided that the inverse screening length μ is sufficiently small, the matrix element defined by equation 2.3.2 is large for $|\underline{k}_b - \underline{k}| \sim 0$. We

make use of this behaviour of the matrix element to obtain an approximation to g by means of a Taylor series expansion of this function about $\underline{k} = \underline{k}_b$. The series is taken to second order and thus we obtain the following approximation to $\int S_e(f:\underline{k}_a \rightarrow \underline{k})d\Omega_a$:

$$\int S_e(f: \underline{k}_a \rightarrow \underline{k})d\Omega$$

$$\sim B_{2ee}\, g(k)\, e^{-\gamma k^2} \sum_{r=0}^{\infty} \frac{w_r}{k} (\gamma k_a)^2$$

$$+ B_{2ee}\, e^{-\gamma k^2} \sum_{r=1}^{\infty} \frac{w_r}{k} \left[\{g''(k) - \frac{g'(k)}{k}\} \frac{r(2r-1)}{4\gamma^2 k^2} + \frac{g'}{k} \frac{r(2r+1)}{4\gamma^2 k_a^2} - \frac{rg'(k)}{\gamma k}\right](\gamma k_a)^{2r}$$

for $k_a \leq k$

$$= B_{2ee}\, g(k) e^{-\gamma k^2} \sum_{r=0}^{\infty} \frac{w_r}{k_a} (\gamma k)^{2r} \qquad (2.35)$$

$$+ B_{2ee}\, e^{-\gamma k^2} \sum_{r=1}^{\infty} \frac{w_r}{k_a} \left[\{g''(k) - \frac{g'(k)}{k}\} \frac{r(2r-1)}{4\gamma^2 k^2} + \frac{g'(k)}{k} \frac{r(2r+1)}{4\gamma^2 k^2} - \frac{rg'(k)}{\gamma k}\right](\gamma k)^{2r}$$

for $k_a \geq k$

where $B_{2ee} = \frac{1}{8\pi^4} \frac{m^*}{\hbar^3} (\frac{e^2}{\varepsilon\varepsilon_o})^2 P_s$ and for $r \geq 1$ the coefficients w_r are defined as:

$$w_r = \frac{1}{(2r)!} \frac{2^{2r}}{(r+\frac{1}{2})} (r\, c_{r-1} - \gamma\, c_r)$$

For $r \geq 1$ the coefficients c_r obey the recurrence relation:

$$c_r = \frac{\pi(r-1)!}{\gamma^r} - \mu\, c_{r-1}$$

and $c_o = \pi e^{\gamma\mu^2} E_1(\gamma\mu^2)$ where E_1 is the exponential integral:

$$E_1(\gamma\mu^2) = \int_{\gamma\mu^2}^{\infty} \frac{e^{-t}}{t}\, dt.$$

The coefficient w_0 is defined as $a_0 = 2(\pi\mu^{-2} - \gamma c_0)$. Equation 2.35 gives the scattering kernel in the form of a sum of two infinite series. The first of these series arises from the zero order term of the Taylor expansion of g and involves a sum from r=0 to ∞. This series gives identical contributions to the e.e. scattering in and out rates and hence gives no net contribution to the total e.e. scattering rate. The second of the two series arises from the first and second order terms of the Taylor expansion and involves a sum from r = 1 to ∞. The results of numerical tests have shown that the sum is highly convergent: the scattering kernel can be adequately computed if the sum is taken to 5 terms.

Doubtless, it is possible to approximate g(k) using methods other than the Taylor series. The optimum form for the approximation to g(k) is uncertain. We have adopted the Taylor series method because it provides the e.e. scattering rates in a form which is relatively tractable computationally. An alternative approximation procedure, which we consider to be especially promising, would be to expand g(k) in Hermite polynomials. However, a numerical implementation of this approach would require the coefficients of the polynomial expansion to be recomputed at each iteration. We judge that this would consume more computer time than does recalculation of the derivatives involved in the Taylor series.

The validity of the Taylor series approximation to g(k) requires some discussion. The physical interpretation of the near divergence of the matrix element for small values of $|\underline{k}_b - \underline{k}|$ is that the transition probability for small angle scattering of electrons is large. It follows that if the screening is weak then the small angle collision rate is large. However, although they are less frequent, large angle collisions are also expected to be of importance because they involve larger exchanges of energy. The Taylor series expansion is likely to give a good approximation to the small angle part of the scattering but it is uncertain how well it

approximates the total scattering rate.

In making use of a Taylor series our method for approximating the e.e. scattering rates is similar to that used by Komolov and Yassievich (see Section 2.2.2). However, we expand g rather than f. This means that an upper cut-off of the form they used in their approximate form of $S_e(f:\underline{k}_a \rightarrow \underline{k})$ is not involved in our scattering rates. But our approximation to S_e does involve another parameter in the form of the effective temperature T_{eff}. It is necessary to choose the optimum value for this parameter if a good approximation to S_e is to be obtained using only a few terms in the Taylor series. The ideal way in which to estimate T_{eff} would be to derive a temperature from equation 2.9 using an energy balance method. However this approach is not really justified in view of the computational problems we have encountered in obtaining our distribution functions. (These problems are discussed later in this section). We therefore estimate T_{eff} as follows. To compute a distribution function, taking into account e.e. scattering and a particular set of parameters (injection energy, lattice temperature etc.) we first compute the steady state distribution function which would correspond to the same set of parameters, but without taking e.e. scattering into account. T_{eff} is then derived from the mean energy $\langle\epsilon\rangle$ of this distribution i.e. $T_{eff} = 2\langle\epsilon\rangle/3k_B$.

From trial computations we have found that if the approximate form for S_e is used in the iterative scheme defined by equation 2.14 then the iteration is susceptible to numerical instabilities. This difficulty is thought to be associated with the finite difference representation which must necessarily be used to compute the derivatives occuring in the Taylor series. Fortunately the instabilities can be controlled if the time evolution of f is computed according to equation 2.16. Then, provided

approximates the total scattering rate.

In making use of a Taylor series our method for approximating the e.e. scattering rates is similar to that used by Komolov and Yassievich (see Section 2.2.2). However, we expand g rather than f. This means that an upper cut-off of the form they used in their approximate form of $S_e(f:\underline{k}_a \rightarrow \underline{k})$ is not involved in our scattering rates. But our approximation to S_e does involve another parameter in the form of the effective temperature T_{eff}. It is necessary to choose the optimum value for this parameter if a good approximation to S_e is to be obtained using only a few terms in the Taylor series. The ideal way in which to estimate T_{eff} would be to derive a temperature from equation 2.9 using an energy balance method. However this approach is not really justified in view of the computational problems we have encountered in obtaining our distribution functions. (These problems are discussed later in this section). We therefore estimate T_{eff} as follows. To compute a distribution function, taking into account e.e. scattering and a particular set of parameters (injection energy, lattice temperature etc.) we first compute the steady state distribution function which would correspond to the same set of parameters, but without taking e.e. scattering into account. T_{eff} is then derived from the mean energy $\langle\epsilon\rangle$ of this distribution i.e. $T_{eff} = 2\langle\epsilon\rangle/3k_B$.

From trial computations we have found that if the approximate form for S_e is used in the iterative scheme defined by equation 2.14 then the iteration is susceptible to numerical instabilities. This difficulty is thought to be associated with the finite difference representation which must necessarily be used to compute the derivatives occuring in the Taylor series. Fortunately the instabilities can be controlled if the time evolution of f is computed according to equation 2.16. Then, provided

that the time step is chosen to be suitably small, the instabilities do not occur. In this respect the behaviour of the iterative procedure defined by equation 2.16 is similar to that of the finite difference scheme we use in our study of oscillatory photoconductivity (Chapter 3 and Appendix 3). The maximum time step compatible with numerical stability increases with the magnitude of the k step. Thus a large k step must be employed in the computations if the time step is to be kept reasonably large. Most of our distribution functions been computed using a k steps of $k_{\alpha T}$ or $K_{\alpha T}/2$.These values of Δk are too large to permit the e.p. scattering rates to be accurately computed but such large values must be employed if the calculations are to be performed within the available computer time. Even with $\Delta k = k_{\alpha T}$ up to 3000 iterations are required to follow the evolution of f over a period of 50nS. The maximum usable time step decreases with electron density and for this reason we have only been able to compute distribution functions corresponding to steady state electron densities $< 3 \times 10^{16}$ m^{-3}.

We have examined the sensitivity of the Taylor series approximation to the parameter T_{eff}, by performing some test computations in the manner outlined in the preceeding paragraphs. Electron-phonon scattering was not taken into account in these computations. A distribution function corresponding to the following parameters was computed: injection energy, $\epsilon_1 = 0.997$ meV; injection rate, $Q = 10^{21}$ m^{-3} s^{-1}; recombination rate, $R = 10^7$ s^{-1}; inverse screening length, $\mu = 10^6$ m^{-1}. T_{eff} was derived from $<\epsilon>$ (as mentioned previously in this section) and, because e.p. scattering was not taken into account, $<\epsilon>$ was known to be equal to ϵ_1. The parameters used to compute the test distribution functions were chosen to allow rapid compution (a large time step was used) and we were able to follow the evolution of f over a period of 1.25 μS. At this time f took the form of a broad, asymmetric pulse centred on ϵ_1.When the same distribution

function was recomputed with T_{eff} twice the value used previously the overall form of f was unaltered. In addition there was little change in some of the mean quantities derived from f - the normalization factor decreased by $\sim$ 6%, the mean energy decreased by $\sim$ 0.2% and the inverse screening length computed from f increased by $\sim$ 2%. There were, however, some greater changes in the actual values of f. At specific points the following changes occurred: f increase by $\sim$ 30% at ϵ_i, decreased by $\sim$ 10% at energies of 0.76 and 1.17 meV and decreased by about an order of magnitude at energies of 0.44 and 2.5 meV. We emphasize that these changes are for a distribution which differs grossly from a Maxwellian form.

2.9.2. Distribution functions

We now use the Taylor series approximation described in the previous subsection to discuss the effect of e.e. scattering on the photoexcited electron distribution. To do this we consider the time evolution of the distribution function in two cases. In the first case the effect of e.p. scattering is neglected; distribution functions are computed and are qualitatively compared with some distribution functions computed within the large screening model. In the second case both e.e. and e.p. scattering are taken into account; distribution functions are computed and are used to estimate the minimum electron density at which e.e. scattering has a significant effect on the photoexcited electrons. In both cases the recombination rate is supposed to be k independent and to have a value of $10^7 s^{-1}$. The exchange uncertainty factor, p_s, (see Section 2.7.1) is set equal to 1.5. All other parameters are taken to have values as discussed in Section 2.5 or listed in Tables 2.5 and 2.6. The distribution functions are computed using the modified iterative procedure defined by equation 2.16.

The time evolution of f in the first case (no e.p. scattering) is illustrated in Figures 2.15 and 2.16. The distribution functions shown in these figures have been computed taking the injection pulse to be centred at 0.997 meV and the injection rate, Q to be 10^{24} $m^{-3}S^{-1}$. Figure 2.15 depicts how f develops over a period of 5nS following photoexcitation and consists of a series of 'snapshots' taken at 1nS intervals. Figure 2.16 is similar but the period is 50nS and the interval is 10nS. From Figures 2.15 a and b it can be seen that at times ≤ 2nS the distribution function has the form of a narrow pulse centred on ϵ_i. During the interval from 2 to 5nS the pulse slowly broadens and becomes asymmetric (Figures 2.15c to e). This slow broadening is in contrast with the time evolution of f in the large screening model (Section 2.8, Figure 2.13) and the contrast presumably indicates that the distribution functions shown in Figure 2.15 are characteristic of small angle e.e. scattering. During the interval from 5 to 50nS (Figures 2.15e, 2.16) the evolution of f for energies > ϵ_i differs from the evolution for energies < ϵ_i. For energies > ϵ_i f develops a high energy tail (Compare Figures 2.15e and 2.16a). The tail is approximately Maxwellian, but in the tail region the slope of ln f exhibits a slight energy dependence. At a time of 50nS (Figure 2.16e) the slope of the tail at ϵ = 3meV corresponds to a temperature of 6.17°K. And the mean energy equivalent to this temperature is 0.798 meV (Compare with the injection energy of 0.997meV). For energies < ϵ_i f is pulse like at all times. At times in the range 20nS to 40nS the pulse has an energy independent plateau (Figures 2.16b to d). At a time of 50nS the plateau has a slight energy dependence (Figure 2.16e). Note that, except for the low energy cut off (∼ 0.25meV) the distribution function shown in Figure 2.16e(50nS) is qualitatively similar to one of the distribution functions we have computed within the large screening model (Figure 2.14d).

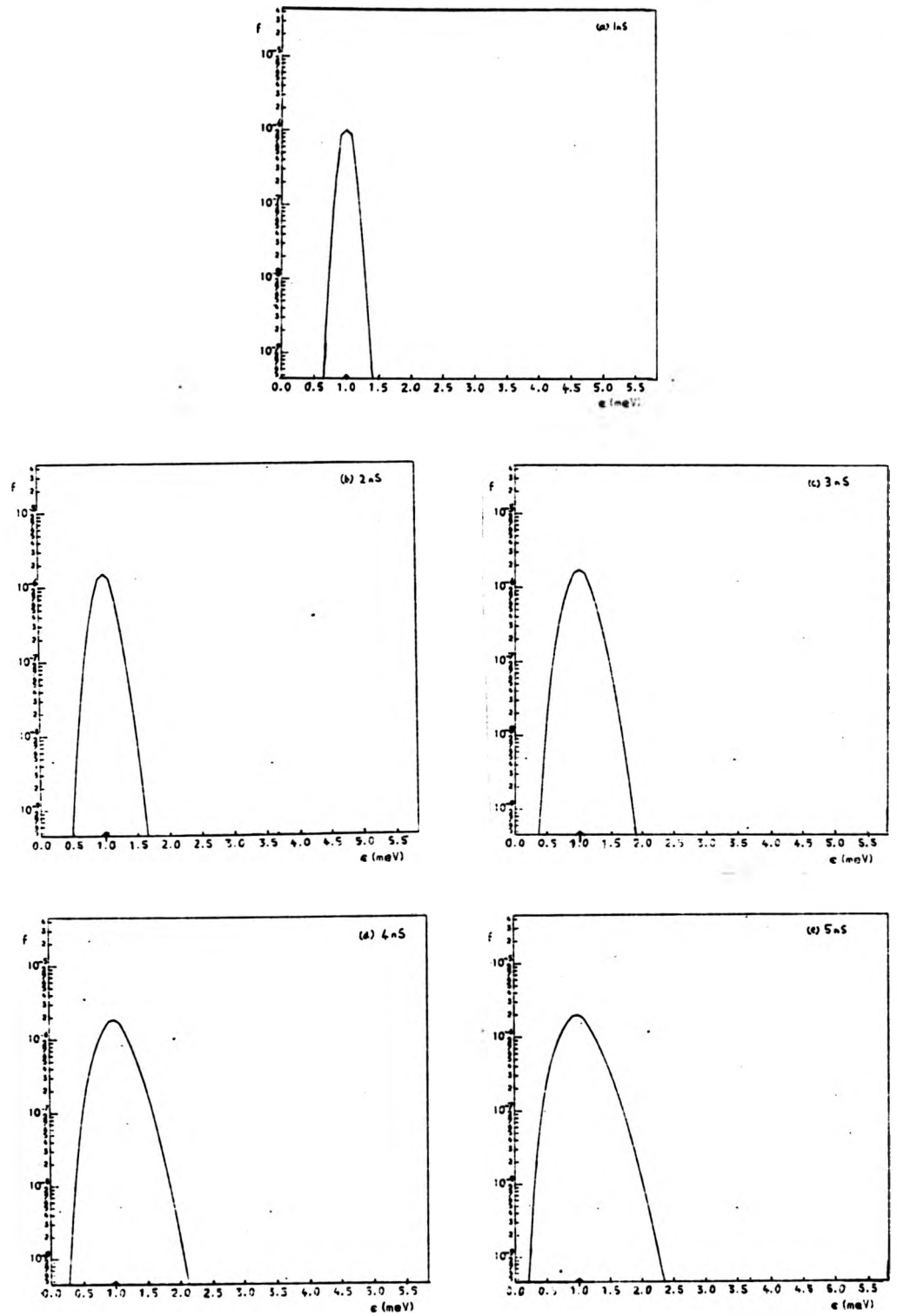

Fig.2.15. The time evolution of a distribution function computed within the series expansion model. Phonon scattering has been ignored; period = 5nS; interval = 1nS.

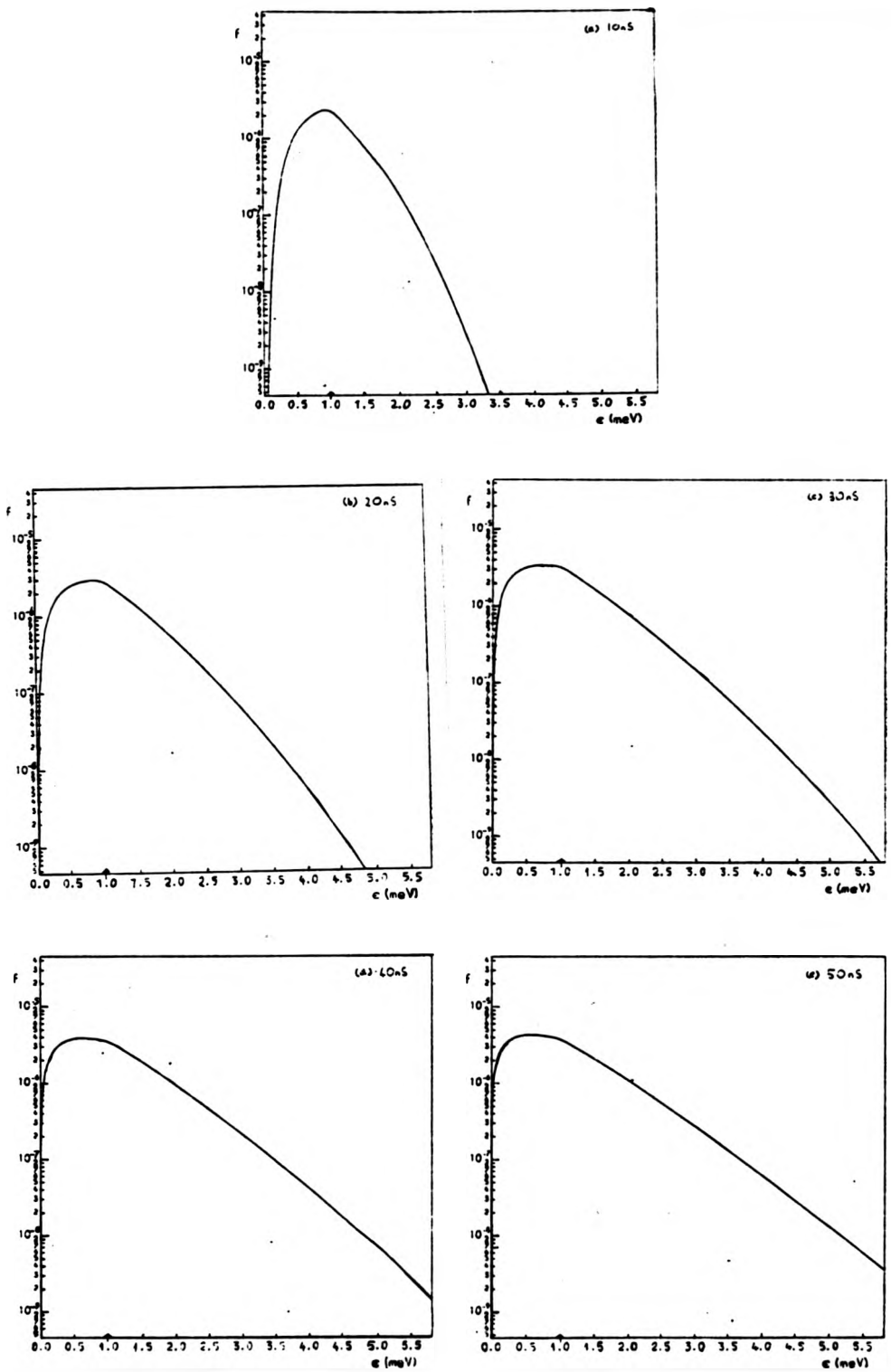

Fig.2.16. The time evolution of a distribution computed within the series expansion model. Phonon scattering has been ignored; period = 50nS; interval = 10nS.

According to the computations described in the previous paragraph the time taken for the distribution function to develop a 'Maxwellian' tail is 5-10nS (See Figures 2.15e, 2.16a). It is of interest to compare this time with a thermalization time measured by Ulbrich (1973). We recall from Section 2.2.1 that Ulbrich has performed an experiment in which a short (0.2nS) pulse of light is used to inject some electrons into the conduction band of GaAs and the subsequent evolution of f followed via observations of (e,A^0) luminescence. Ulbrich finds that the distribution function has a heated Maxwellian form at times greater than 2nS following application of the pulse. Although the distribution functions shown in Figures 2.15 and 2.16 correspond to conditions of continuous photoexcitation and no e.p. scattering it is encouraging that the time of 5-10nS mentioned above is within an order of magnitude of Ulbrich's measured thermalization time

Distribution functions corresponding to the second case (both e.e. and e.p. scattering taken into account) are shown in Figures 2.17 and 2.18. In the calculations leading to these figures the injection pulse was chosen to be centred at 3.989meV, all three acoustic phonon scattering mechanisms were taken into account and the lattice temperature was taken to be $1.7^{o}K$. The phonon scattering integrals were numerically evaluated as described in Section 2.5.1. The mesh steps used in the calculation leading to Figures 2.17 and 2.18 were $K_{\alpha T}$ and $K_{\alpha T}/2$ respectively. Both figures 2.17 and 2.18 consist of a series of distribution functions, each member of which corresponds to a higher injection rate (and hence electron density) than the preceding one. The distribution functions shown in Figure 2.17 all refer to a time of 50nS but are normalised to the electron density which would occur in the steady state. The value of T_{eff} used to compute each member of the series (except the first, Figure 2.17a) has been derived from the mean energy of the preceding one.

From Figure 2.17 it is clear that, provided the electron density is sufficiently high, e.e. scattering can cause heating of the electrons

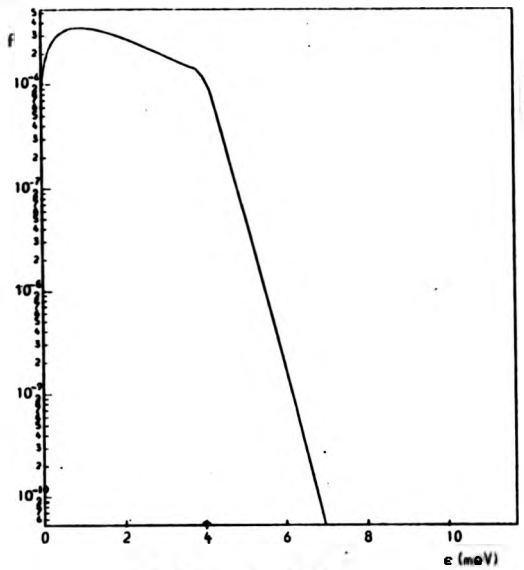

(d) time = 50nS
electron density = $3.19\times10^{13}m^{-3}$
tail temperature = $3.45^{o}K$

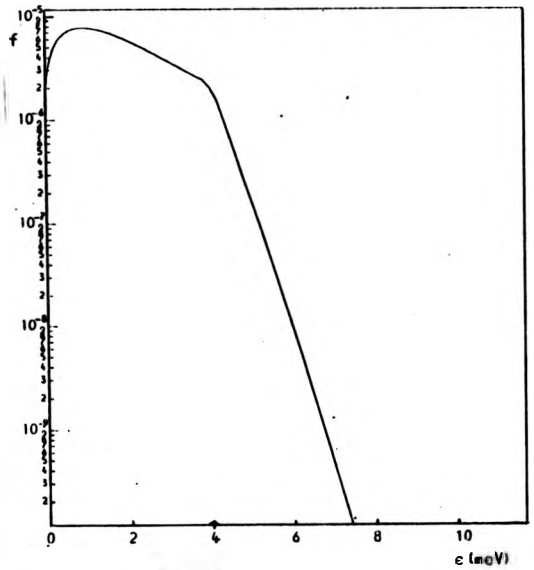

(e) time = 50nS
electron density = $6.16\times10^{13}m^{-3}$
tail temperature = $4.10^{o}K$

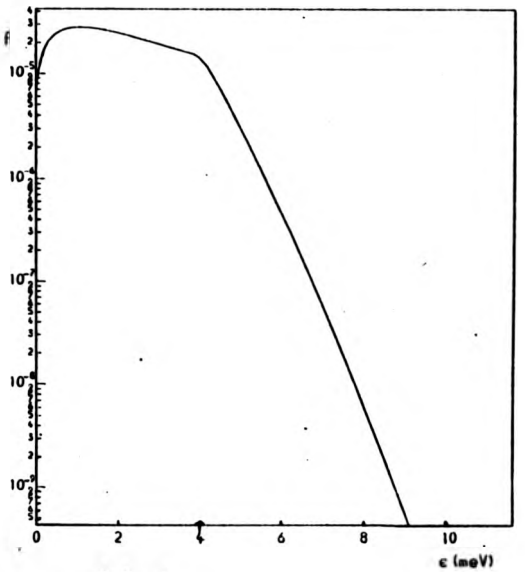

(f) time = 50nS
electron density = $3.17\times10^{16}m^{-3}$
tail temperature = $6.27^{o}K$

Figs 2.17d to c. A series of distribution functions computed within the series expansion model. Phonon scattering has been taken into account. The distribution functions illustrate how e.e. scattering can cause heating of the electrons contributing to the tail of the distribution. The 'tail temperature' is defined in Section 2.9.2.

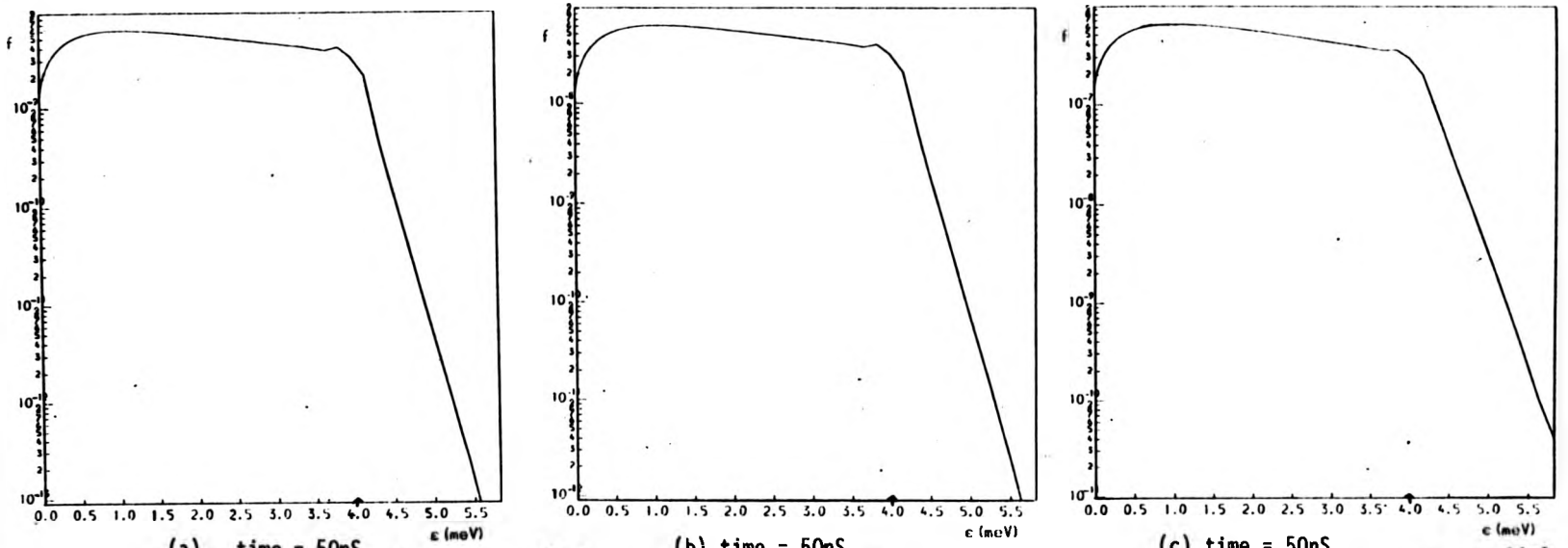

(a) time = 50nS
electron density = $7.31\times10^{12}m^{-3}$
tail temperature = $1.66^{o}K$

(b) time = 50nS
electron density = $7.37\times10^{13}m^{-3}$
tail temperature = $1.71^{o}K$

(c) time = 50nS
electron density = $6.94\times10^{14}m^{-3}$
tail temperature = $2.37^{o}K$

Figs.2.17a to c. A series of distribution functions computed with the series expansion model. Phonon scattering has been taken into account. The distribution functions illustrate how e.e. scattering can cause heating of the electrons contributing to the tail of the distribution. The 'tail temperature' is defined in Section 2.9.2.

contributing to the tail region of f ($\epsilon > \epsilon_i$). This effect can best be seen by comparing the tails of the distribution functions shown in figures 2.17 c to f with the tail of the distribution function shown in Figure 2.17a (electron density at 50nS = 7.37×10^{12} m^{-3}). The latter distribution function has a lattice temperature Maxwellian tail. The distribution functions shown in Figures 2.16c to f each have tails which correspond to heating of the electrons with energies > ϵ_i. The form of f in the tail region is approximately Maxwellian.The heating effect is just in evidence in the distribution function in Figure 2.17c (electron density at 50nS = 6.94×10^{14} m^{-3}; temperature derived from slope of tail at 5meV = 2.37^{o}K) and is significant in the distribution function shown in Figure 2.16f (electron density at 50nS = 3.17×10^{16} m^{-3}; tail temperature = 6.27^{o}K). An additional difference between the distribution functions shown in Figures 2.17a and f is that in the structure at energies $\sim \epsilon_i$ is smoother in the latter than in the former. The heating effect evident from the tails of the distribution functions shown in Figures 2.17c to f is thought to be a consequence of the relative magnitudes of the e.e. and e.p. scattering rates at energies > ϵ_i. For such energies the e.p. scattering in rate is dominated by the phonon absorption rate and the phonon absorption rate is small. For energies < ϵ_i the e.p. scattering in rate is larger. Therefore a small e.e. scattering in rate can effect the distribution function for energies > ϵ_i but has little effect on the distribution function for energies < ϵ_i.

The form of distribution function shown in Figure 2.17a differs significantly from the form of the distribution function shown in Figure 2.12e - the former distribution function does not have a Maxwellian form at the band minimum. Yet in the calculations leading to both distribution functions the injection energy has been taken as 3.984meV and all three acoustic phonon scattering mechanisms have been taken into account. Both distribution functions refer to a time of 50nS and it is unlikely that the

e.e. scattering rate was significant in the calculations leading to Figure 2.17a. It is thought that the difference in the forms of the two distribution functions is a result of numerical errors caused by the use of a large k step ($\Delta k = k_{\alpha T}$) in the calculations leading to Figure 2.17a. Therefore, to test our prediction that e.e. scattering can cause heating of the electrons contributing to the tail of f we have recomputed the distribution functions shown in Figures 2.17a to c, using a smaller k step ($\Delta k = k_{\alpha T}/2$). The recomputed distribution functions are shown in Figures 2.18a to c. They correspond to times of 50μS, 500nS and 50nS respectively but are all normalised to the steady state electron density. The distribution functions shown in parts c of Figures 2.17 and 2.18 (which both refer to a time of 50nS) have similar tails and the slopes of these tails differ by at most 5%. This indicates that the heating effect is not on artefact of the computations leading to Figure 2.17. However, in recomputing the distribution function shown in Figure 2.17a the electron density was found to increase by a factor of 3.15. This reflects the degree of numerical error in the former calculations.

We conclude that because our calculations involve uncertainties associated with the size of the mesh step and the choice of T_{eff} they cannot be regarded as sufficiently accurate to give a quantitative prediction of the electron density at which e.e. scattering has a significant affect on photoexcited electrons in GaAs. However, computations involving e.e. scattering are difficult and calculations of greater precision will require substantial computing resources. Qualitatively, the best conclusion we can draw from our results is that if the electron density is sufficiently high e.e. scattering can cause heating of the electrons contributing to the tail of the distribution function. Quantitatively it is probable that this effect would be significant if the electron density was $\sim 3 \times 10^{16}$ m^{-3} (Figure 2.17f). The density of 3×10^{16} m^{-3} can be

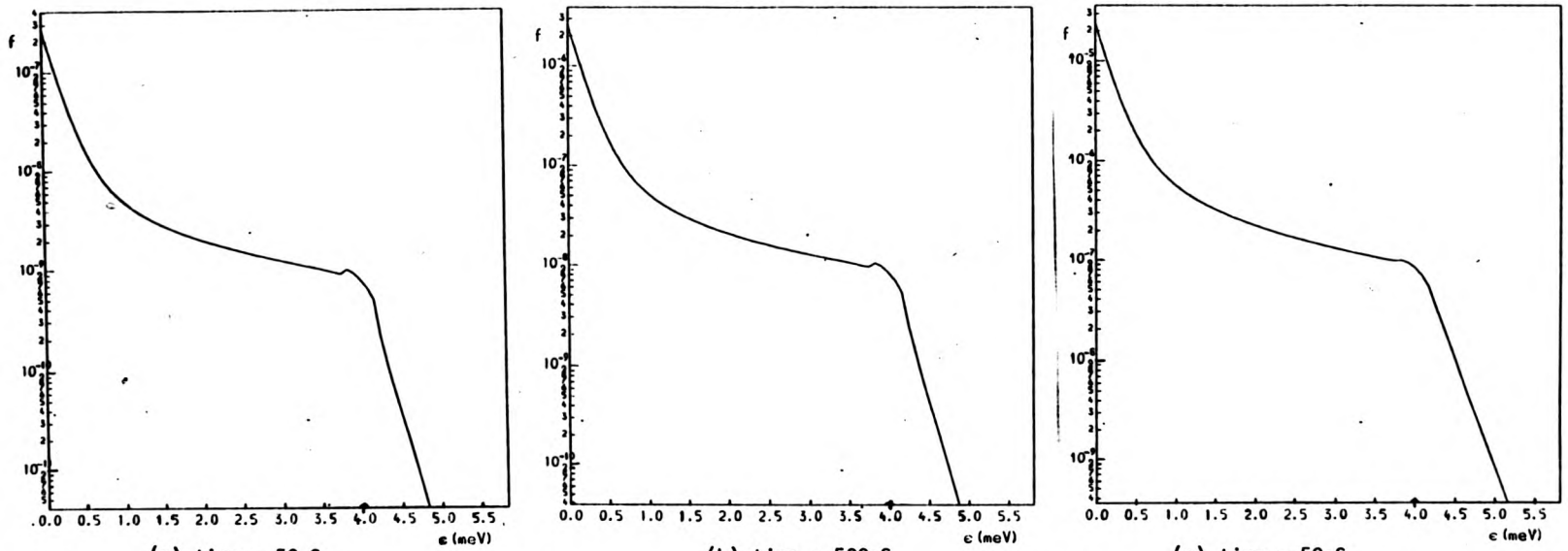

(a) time = 50μS
electron density = $2.68\times10^{13}m^{-3}$
tail temperature = $1.73^{o}K$

(b) time = 500nS
electron density = $2.5\times10^{14}m^{-3}$
tail temperature = $1.76^{o}K$

(c) time = 50nS
electron density = $2.18\times10^{15}m^{-3}$
tail temperature = $2.29^{o}K$

Figs.2.18a to c. The results of repeating the computations leading to Figs. 2.17a to c, using a mesh step of $\frac{1}{2} k_{\alpha T}$ in place of $k_{\alpha T}$.

compared some experimental results due to Ulbrich (1978, See also Section 2.2.1), who has studied the excitation intensity dependence of (e,A^0) luminescence in GaAs at a lattice temperature of 1.2^oK. From the results of this study he concludes that the photoexcited electron energy relaxation rate due to e.e. scattering is comparable to the energy relaxation rate due to acoustic phonon scattering if the electron density is $\sim 5 \times 10^{17}$ m^{-3}. This figure is not too far removed from our estimate of the electron density of which e.e. scattering is significant.

We now summarize the main results of Sections 2.5 to 2.9 and then we briefly explain how these results are relevant to (e,A^0) luminescence in GaAs.

The distribution functions we have described in Sections 2.5.2 and 2.6. illustrate the effect of e.p. scattering on the photoexcited electrons (e.e. scattering has not been taken into account in computing these distribution functions). It has been shown that the overall form of these distribution functions is relatively insensitive to the k dependence of the recombination rate and to the value of the inverse screening length. The results of the calculations described in this subsection indicate that e.e. scattering would have little effect on the photoexcited electrons unless the electron density exceeds $\sim 3 \times 10^{16}$ m^{-3}, and that at a density of 3×10^{16} m^{-3} only the tail of the distribution function would be affected. According to experiment e.e. scattering only has a significant effect if the electron density is $\gtrsim 5 \times 10^{17}$ m^{-3}. These results mean that we do not require a detailed knowledge of recombination, screening and e.e. scattering in order to compute (e,A^0) luminescence spectra which can usefully be compared with the results of photoluminescence experiments on GaAs, under conditions of low intensity photoexcitation. In the next section we describe how the one band, Boltzmann equation model (Section 2.3) can be used to compute (e,A^0) spectra appropriate to GaAs under these conditions.

compared some experimental results due to Ulbrich (1978, See also Section 2.2.1), who has studied the excitation intensity dependence of (e,A^0) luminescence in GaAs at a lattice temperature of 1.2^oK. From the results of this study he concludes that the photoexcited electron energy relaxation rate due to e.e. scattering is comparable to the energy relaxation rate due to acoustic phonon scattering if the electron density is $\sim 5 \times 10^{17}$ m^{-3}. This figure is not too far removed from our estimate of the electron density of which e.e. scattering is significant.

We now summarize the main results of Sections 2.5 to 2.9 and then we briefly explain how these results are relevant to (e,A^0) luminescence in GaAs.

The distribution functions we have described in Sections 2.5.2 and 2.6. illustrate the effect of e.p. scattering on the photoexcited electrons (e.e. scattering has not been taken into account in computing these distribution functions). It has been shown that the overall form of these distribution functions is relatively insensitive to the k dependence of the recombination rate and to the value of the inverse screening length. The results of the calculations described in this subsection indicate that e.e. scattering would have little effect on the photoexcited electrons unless the electron density exceeds $\sim 3 \times 10^{16}$ m^{-3}, and that at a density of 3×10^{16} m^{-3} only the tail of the distribution function would be affected. According to experiment e.e. scattering only has a significant effect if the electron density is $\gtrsim 5 \times 10^{17}$ m^{-3}. These results mean that we do not require a detailed knowledge of recombination, screening and e.e. scattering in order to compute (e,A^0) luminescence spectra which can usefully be compared with the results of photoluminescence experiments on GaAs, under conditions of low intensity photoexcitation. In the next section we describe how the one band, Boltzmann equation model (Section 2.3) can be used to compute (e,A^0) spectra appropriate to GaAs under these conditions.

2.10. Electron-acceptor luminescence

This section is concerned with (e,A^0) luminescence from GaAs under conditions of continuous, monochromatic, interband photoexcitation. Attention is restricted to excitation energies such that the electron injection energy is below the threshold energy for L.O. phonon emission and excitation intensities such that the density of photoexcited carriers is insufficient for intercarrier scattering to affect the electron distribution. First we compute some model distribution functions which are appropriate to GaAs under these conditions. Next we use the model distribution functions to derive some (e,A^0) spectra for C doped GaAs and compare thse spectra with the results of recent photoluminescence experiments on the same material (Ulbrich, 1978). Finally we discuss some ways in which features not included in the model may affect the computed spectra.

The distribution functions we use to derive (e,A^0) spectra are all calculated according to the model explained in Section 2.3. For the generation rate G the interband injection spectrum given by equation 2.6 is used. All three acoustic phonon scattering mechanisms are taken into account using the methods described in Section 2.5.1. The recombination rate is assumed to be energy independent and is taken to have a value of $2.5 \times 10^7\ S^{-1}$. As explained subsequently this value is thought to be more realistic than the value of $10^7\ S^{-1}$ used in the calculations described in Sections 2.5 to 2.9.

The interband injection spectrum given by equation 2.6 has the form

$$G(k) = Q\{\frac{\chi_l}{\rho(\epsilon_{il})}\ \delta(\epsilon(k) - \epsilon_{il}) + \frac{\chi_h}{\rho(\epsilon_{ih})}\ \delta(\epsilon(k) - \epsilon_{ih})\} \qquad (2.6)$$

In this form χ_l and χ_h are the functions of electrons injected from the light and heavy hole bands respectively. The values of these quantities are imprecisely known: various different theoretical estimates of χ_l and

χ_h are possible and experimental photoluminescence spectra do not always have features attributable to injection of electrons from the light hole band (See Figure 2.2a and contrast with work due to Ulbrich, 1976). In view of this uncertainty in the values of χ_l and χ_h we compute three sets of distribution functions and one of three different estimates of χ_l and χ_h is used to compute each set. All other parameters used to compute each set are identical. The actual values of χ_l and χ_h we use are listed in Table 2.7. These values have been calculated from α_l and α_h the coefficients for optical absorption by transitions from the light and heavy hole bands. χ_l and χ_h are related to α_l and α_h as follows:

$$\chi_l = (1 + \alpha_h/\alpha_l)^{-1} \qquad \chi_h = 1 - \chi_l \ .$$

A different estimate of α_l/α_h is used to obtain two of the three sets of values for χ_l and χ_h. The first estimate of α_l/α_h (giving $\chi_l = 0.44$, $\chi_h = 0.50$) is obtained as follows. We assume that the matrix elements for transitions from the light and heavy hole bands are equal. Then we estimate α_l and α_h, taking exciton corrections into account in the manner described by Dimmock (1967). Thus α_l/α_h is found to be given by the equation:

$$\frac{\alpha_l}{\alpha_h} = \left(\frac{\mu_l}{\mu_h}\right)^{\frac{1}{2}} \frac{1-e^{-2\pi\gamma_h}}{1-e^{-2\pi\gamma_l}} \quad , \quad \gamma^2 = \frac{e^2}{4\pi\epsilon\epsilon_0} \frac{\mu}{2\hbar^2} \frac{1}{\hbar\omega_e \epsilon_G} \qquad (2.36)$$

where μ_l is a reduced mass defined by $\mu_l^{-1} = m^{*-1} + m_{lh}^{-1}$, μ_h is similarly defined and $\hbar\omega_e$ is the excitation energy. The ratio α_l/α_h as given by equation 2.36 is, to a good approximation, independent of excitation energy in the range of excitation energies with which we are concerned. The second estimate of α_l/α_h (giving $\chi_l = 0.31$ and $\chi_h = 0.69$) is obtained similarly to the first except that exciton corrections to the absorption are neglected. Then α_l/α_h is simply related to the reduced masses μ_l and μ_h (Dimmock, 1967):

X_l	X_h	Estimated from Equation	Distribution function shown in Figure
0.44	0.56	2.37	2.19a
0.31	0.69	2.38	2.20a
0.0	1.0	-	2.21a

Table 2.7: Some estimates of the fractions of electrons injected from the light and heavy hole bands of GaAs.

$$\frac{\alpha_l}{\alpha_h} = \left(\frac{\mu_l}{\mu_h}\right)^{3/2} \quad . \tag{2.38}$$

For comparative purposes the third set of distribution functions is computed under the assumption that no electrons are injected from the light hole band. We feel that the first set of values of χ_l and χ_h (0.44, 0.56 respectively) are the most realistic of our three estimates.

Each of our sets of distribution functions contains three such fuctions which are appropriate to excitation energies of 1.5383, 1.5310 and 1.5330 eV. The injection energies corresponding to these excitation energies are given in Table 2.8. The distribution functions in all three sets have the following parameters in common: electron injection rate (5×10^{23} m^{-3} S^{-1}), inverse screening length (3.5×10^{5} m^{-1}) and lattice temperature ($1.2^{o}K$). Various other parameters used in the computations leading to the distribution functions are summarized in Tables 2.5 and 2.6.

Each individual distribution function is calculated iteratively. To do this f is first written as the sum of its singular and non-singular parts (see Section 2.3.2 and Appendix 2.2) and then the non-singular part is computed using the iterative procedure defined by equation 2.14. 1,000 iterations are used to compute each distribution function. All the distribution functions have normalization factors < 1.2 and the inverse screening lengths derived from each distribution function are within 5% of 3.5×10^{5} m^{-1}. (the value specified at the start of the computation).

The non-singular part of one distribution function from each set is shown in parts a of Figures 2.18, 219 and 2.20. The excitation energy is 1.533eV and the arrows (labelled l and h) in the figures indicate the corresponding energies for injection from the light and heavy hole bands. For each of the distribution functions shown the electron density

Excitation Energy (eV)	Energy for injection from the light hole band (meV)	Energy for injection from the heavy hole band (meV)	Excitation Wavelength (Å)	Figure
1.5283	4.8175	8.2607	8122	2.19
1.5310	6.2024	10.6441	8108	2.20
1.5330	7.4027	12.6936	8096	2.21

Table 2.8: The values of excitation energy used for the computations leading to Figures 2.19 to 2.21. The injection energies have been estimated using a spherical, parabolic band model.

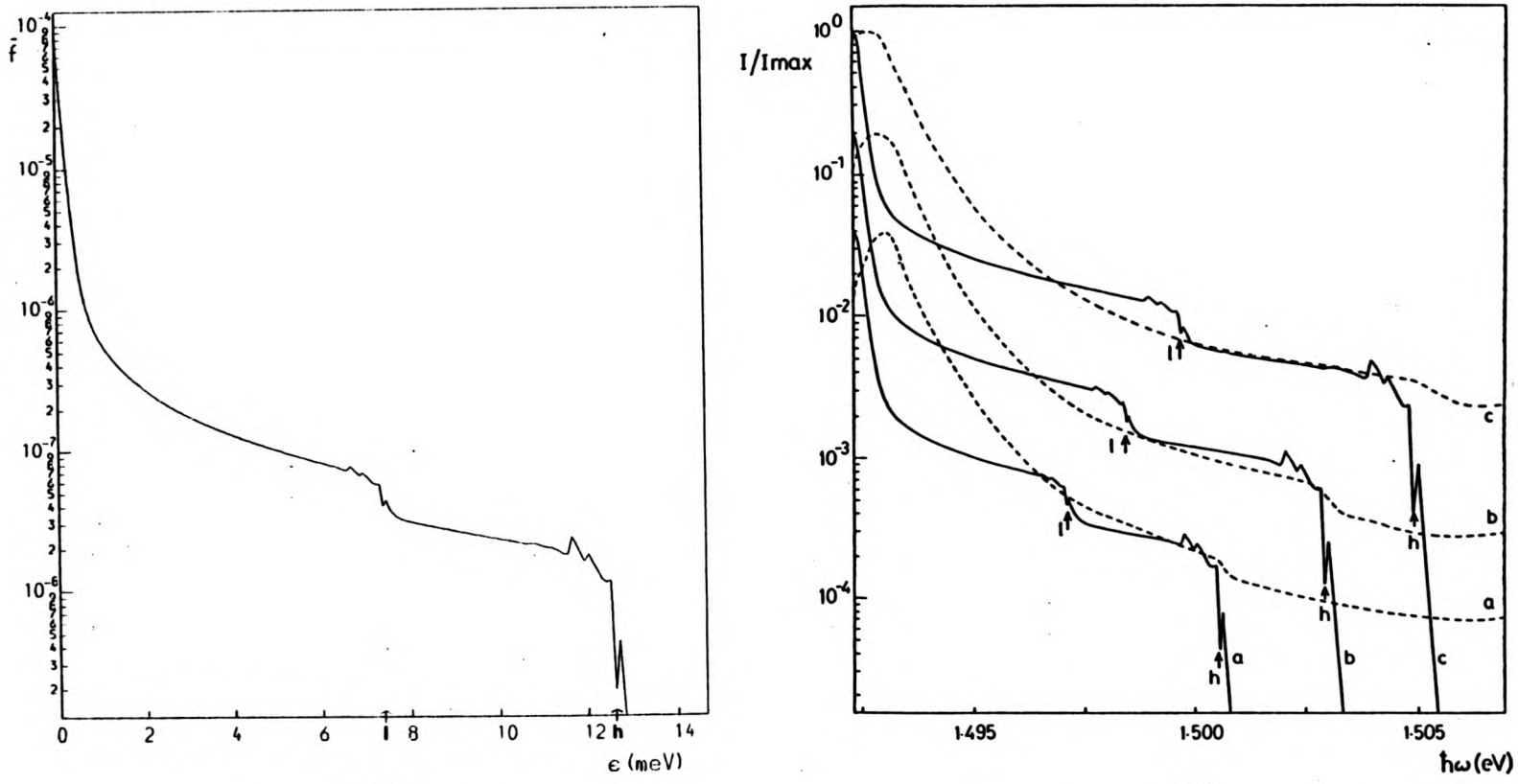

(a) (b)

Figs.2.19a and b. A distribution function and some (e,A^0) spectra corresponding to interband photoexcitation $\chi_l = 0.44$; $\chi_h = 0.56$.

(a) distribution function ; excitation energy = 1.5330eV.

(b) (e,A^0) spectra; curves a to c refer to excitation energies of 1.5283, 1.5310 and 1.5330 eV respectively. Experimental spectra (Ulbrich, 1978b) are shown as broken lines.

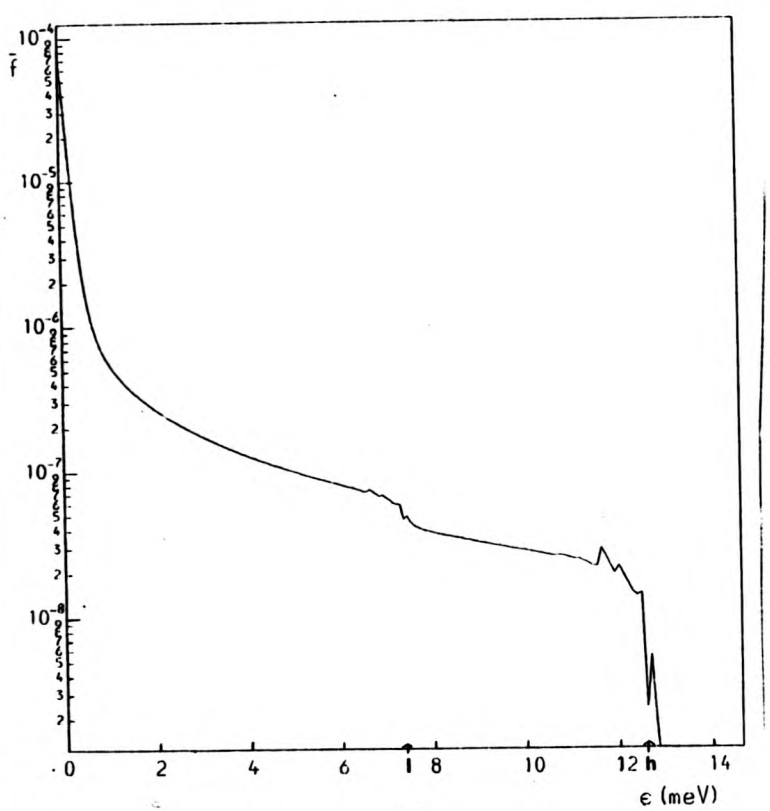

(a)

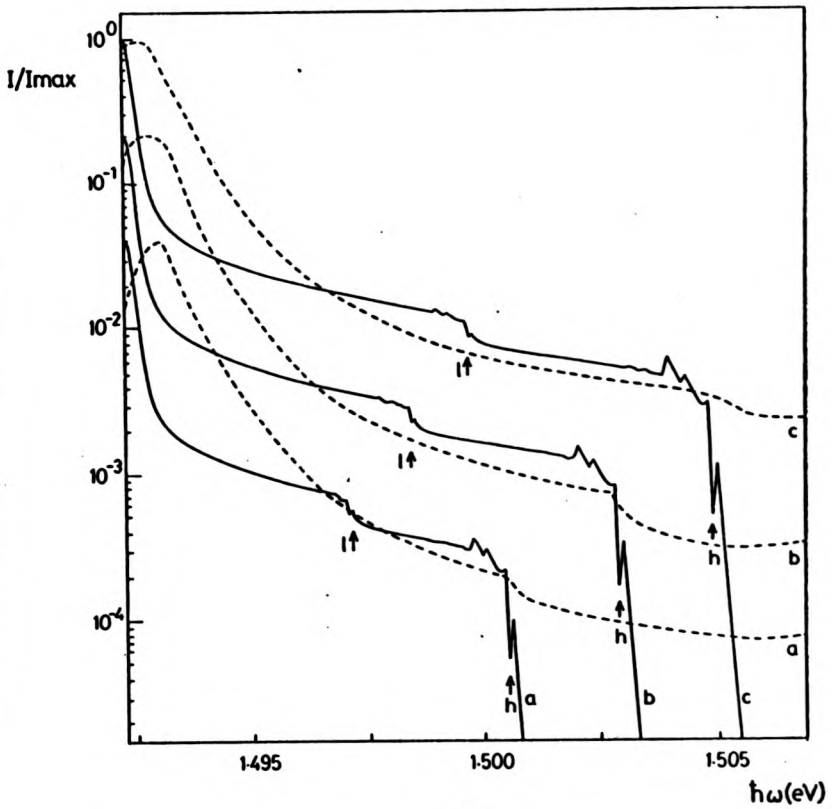

(b)

Figs. 2.20 a and b. A distribution function and some (e,A^0) spectra corresponding to interband photoexcitation $\chi_l = 0.31$; $\chi_h = 0.69$

(a) distribution function ; excitation energy = 1.5330eV.

(b) (e,A^0) spectra; curves a to c refer to excitation energies of 1.5283, 1.5310 and 1.5330eV respectively. Experimental spectra (Ulbrich, 1978b) are shown as broken lines.

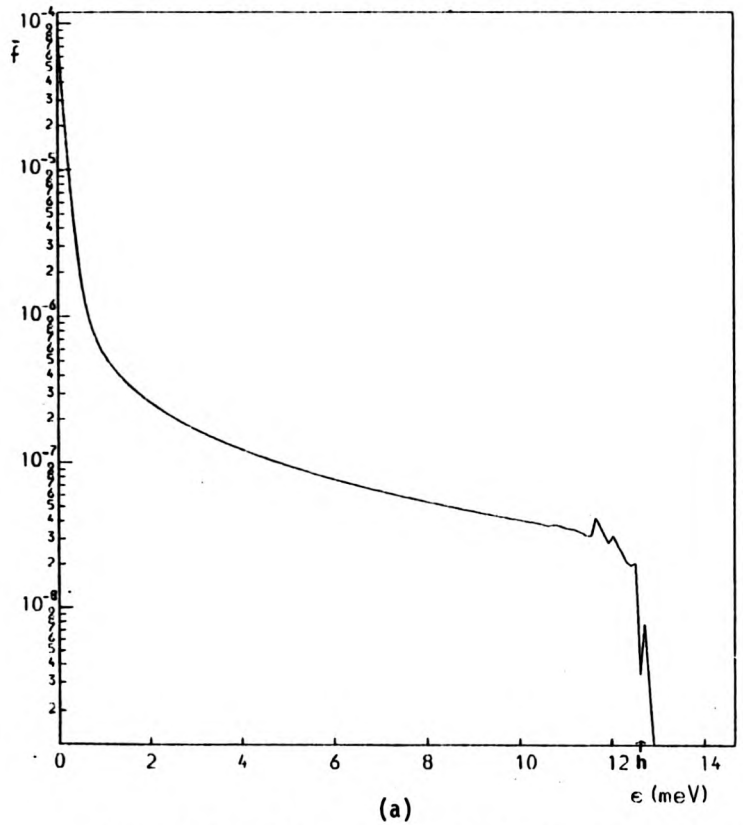

(a)

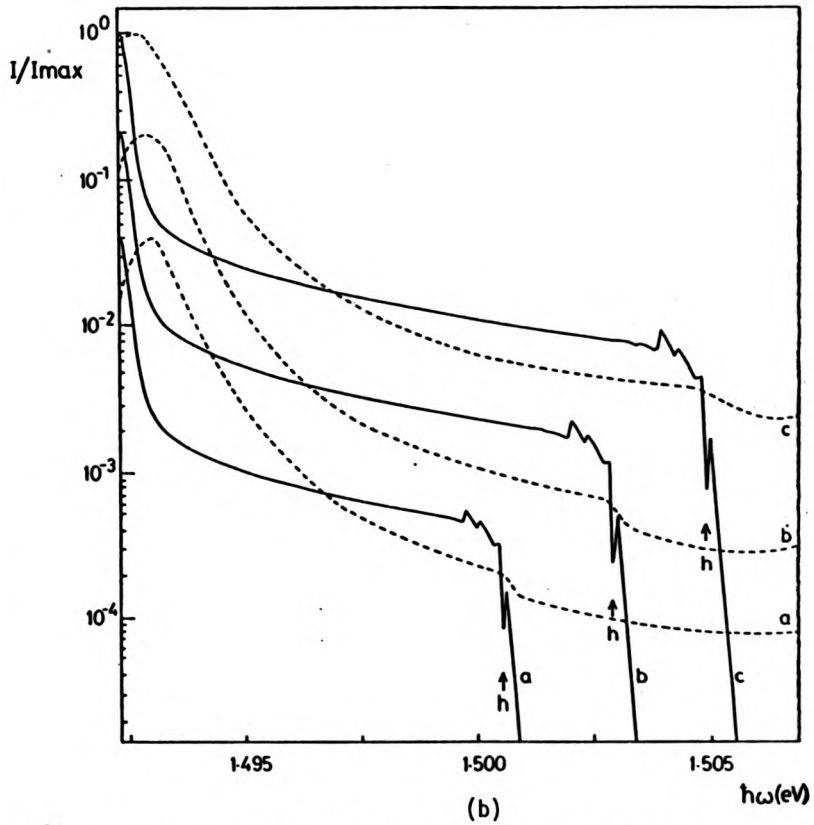

(b)

Figs. 2.21 a and b. A distribution function and some (e,A^0) spectra corresponding to interband photoexcitation $\chi_l = 0$; $\chi_h = 1.0$.

(a) distribution function; excitation energy = 1.5330 eV

(b) (e,A^0) spectra ; curves, a to c refer to excitation energies of 1.5283, 1.5310 and 1.5330 eV respectively. Experimental spectra (Ulbrich, 1978b) are shown as broken lines.

is 2×10^{16} m^{-3} and the majority (> 99%) of the electrons contribute to the non-singular part of the distribution (The other two distribution functions from each set, which are not shown, also correspond to an electron density of 2×10^{16} m^{-3}, with > 99% of the electrons contributing to $\bar{f}$). The overall form of the distribution functions shown in Figures 2.19a to 2.21a is similar to that of the one we have previously described for the case of monoenergetic injection withall the acoustic phonon scattering mechanisms taken into account(Figure 2.3d, Section 2.5.2). Each of the distribution functions has a lattice temperature Maxwellian form at the band minimum and a non-Maxwellian plateau at higher energies. Shoulders are present energies $\sim \epsilon_{ih}$ and at higher energies the distribution functions again have a lattice temperature in Maxwellian form. The distribution functions shown in Figures 2.19a and 2.20 a have a subsidiary shoulder at energies $\sim \epsilon_{il}$. In addition each distribution function has some fine structure at energies $\sim \epsilon_{ih}$ and ϵ_{il}. Both the overall form of $\bar{f}$ and the details of the fine structure can be understood as explained in Section 2.5.2.

In order to compute (e,A^0) spectra we assume that the acceptors are hydrogenic and that the final state for all (e,A^0) transitions is the acceptor ground state. In addition we neglect proximity broadening of the acceptor states and this is probably justified in view of the low acceptor density ($\sim 10^{20}$ m^{-3}; Ulbrich, 1973) commonly employed in photoluminescence experiments. We also suppose the (e,A^0) radiative recombination rate to be small compared with the recombination rate R used to compute the distribution functions. These assumptions allow us to derive the intensity of the (e,A^0) emission, relative to its maximum, $I(\omega)/I_{max}$, from our computed distributions simply by using equation 2.1.

We have used our three sets of distribution functions to derive some (e,A^0) luminescence spectra for C doped GaAs at a lattice temperature of 1.2^oK. (in the manner explained in the preceeding paragraph). These spectra

are shown as solid lines in parts b of Figures 2.19, 2.20 and 2.21. Curves a to c in each figure refer to excitation energies of 1.5283, 1.5310 and 1.5330 eV respectively. The arrows labelled l and h denote energies corresponding to (e,A^0) transitions made by those electrons which are injected but undergo no inelastic collisions. For comparison we show as broken lines some recently published (Ulbrich, 1978; see also Section 2.2.1 and Figure 2.2a) (e,A^0) spectra for C doped GaAs. These spectra have been transcribed onto Figures 2.19 to 2.21 using an energy scale relative to the luminescence energies corresponding to electron injection from the heavy hole band (represented by arrows on Ulbrich's spectra: Figure 2.2a) and absolute values for ϵ_{ih} as given in Table 2.8.

We believe that the parameters we have used in our calculations are appropriate to the conditions under which Ulbrich's spectra have been obtained. In particular our values of the injection rate Q (5×10^{23} $m^{-3}s^{-1}$) and the recombination rate (2.5×10^{7} s^{-1}) are consistent with the electron density measured by Ulbrich (2×10^{16} m^{-3}). Our value of Q is also consistent with the excitation intensity quoted by Ulbrich (10^{-5} W cm^{-2}) provided that this intensity is assumed to be the optical power flux absorbed by the sample and provided that the absorption coefficient is taken to be $\sim 10^{6}$ m^{-1}. (Similar values for the absorption coefficient of GaAs have been measured by Sturge (1962)). Note, however, that we do not require an exact value for Q in order to compute the relative intensity of the (e,A^0) spectra. (The relative intensity is independent of Q). We only need to estimate Q in order to ensure that the injection and recombination rates are consistent with the electron density. An additional parameter which we have obtained from Ulbrich's data is the Bohr radius of a carbon acceptor in GaAs. Ulbrich's (1973) value for the binding energy of such an acceptor has been used to estimate this radius.

The overall comparison between the computed and experimental spectra can only be described as fair. Both types of spectra are qualitatively similar in so far as both exhibit a high energy plateau and a shoulder characteristic of injection of electrons from the heavy hole band. In addition, if χ_1 is calculated with exciton corrections taken into account, the relative intensities of the calculated plateaux agree well with experiment (Figure 2.19b). There are, however, some discrepancies. At low energies ($\lesssim$ 1.4975 eV) the experimental spectra are broader than those we have computed. This indicates that in Ulbrich's experiment the electrons in states close to the band minimum may have been heated. Also the maximum intensity of the computed spectra occurs at an energy $\sim$ 1.4924meV whereas the experimental have intensity maxima an energy $\sim$ 0.5meV greater than this. The experimental spectra have shoulders characteristic of injection from the heavy hole band which are less pronounced than those we have computed. One possible explanation of this is that in the experiment the shoulders have been partly obscured by the background luminescence due to other lines, neighbouring the (e,A^0) line. The experimental spectra have no shoulders characteristic of injection from the light hole band, however, observations of such features in the (e,A^0) spectra of C doped GaAs at 1.2^oK have been reported in the literature (Ulbrich, 1976). It is possible that in the particular experimental spectra shown in Figures 2.19 to 2.20 the subsidiary shoulders we predict have been masked by the same mechanism that is responsible for the low energy broadening of the (e,A^0) line. A final discrepancy is that no fine structure is present in the experimental spectra.

The qualitative resemblance between the observed and calculated spectra provides some indication that the observed spectra are characteristic of a distribution of electrons unaffected by intercarrier scattering, and this interpretation is in accord with a previous discussion by Ulbrich (1978). However it is clear that further experimental and theoretical work must be

carried out to find an explanation for the discrepancies mentioned in the previous paragraph. Some particular outstanding questions are whether injection from the light hole band occurs, whether the fine structure exists in practice and, whether the electrons in states close to the band minimum are thermalized to the lattice. As a guide to future theoretical studies of (e,A^0) luminescence we close this section by listing some of the assumptions we have made and some of the features we have not included in our model. We also comment on the possible significance of both of these aspects of our work.

A. General.

1. We assumed a spherical, parabolic conduction band. This assumption is likely to be valid because we have computed distribution functions corresponding to low injection energies.

2. We assumed a non-degenerate distribution of electrons. The arguments of Section 2.3 show that this is probably justifiable.

3. We assumed the luminescence to originate from a spatially uniform distribution of electrons. This is unlikely to be true in practice.

B. Generation.

1. A δ function injection spectrum was assumed. In an experiment involving interband photoexcitation the injection spectrum would be broader due to warping of the valence bands.

2. The matrix elements for transitions from the light and heavy hole bands were assumed to be equal and this may not be so.

3. Free carrier and impurity absorption were neglected. These processes would cause injection of electrons at higher conduction band energies than does interband absorption. As a result some background luminescence would occur due to electrons making radiative transitions from states with high conduction band energies ($>>\epsilon_1$).

C. Scattering.

1. Intercarrier scattering was neglected. e.e. scattering could broaden the shoulders and there may be transfer of energy from the electrons to the holes. To investigate the latter effect it would be necessary to compute the electron and hole distributions simultaneously.

2. The simple models adopted for the acoustic phonon dispersion relations (linear) and polarizations (two degenerate transverse modes and one longitudinal) may be inadequate. This is especially true of the assumptions we have made concerning the polarizations.

3. Two phonon and multi-phonon processes were neglected. It has been suggested that two phonon processes may be of importance in determining the energy relaxation of photoexcited electrons in GaAs (Ulbrich, 1978b).

4. There is some uncertainty concerning the values of the deformation potential and piezoelectric constants (See Section 2.3.3).

5. The phonons were assumed to be in thermal equilibrium. If phonon heating occurred the low energy electrons could have a heated Maxwellian distribution resulting in some broadening of the spectra at low energies.

6. Screening effects were only crudely taken into account: the Debye approximation was used and the D.P. interaction was assumed to be unscreened. A further investigation of screening effects is desirable.

D. Recombination.

1. We assumed the recombination rate to be energy independent. This is certainly untrue. For some processes such as radiative recombination to acceptors and the Lax cascade mechanism, the recombination rate increases at the band minimum and this may explain the difference in the positions of the experimental and predicted maxima.

2. A full description of the carrier generation-recombination processes will require the electron and hole distributions and impurity level occupancies to be simultaneously computed.

E. Luminescence.

1. In our calculations of the line shape we assumed simple, hydrogenic acceptors. In fact, the situation is more complicated because of the presence of the degenerate light and heavy hole bands.

2. The effect of proximity broadening of the acceptor levels on the luminescence spectra was neglected, and may need to be taken into account in more accurate calculations of the spectra.

3. Within our model we were only able to calculate the (e,A^0) emission intensity. This means that we have no estimate of the contributions of the neighbouring donor-acceptor and bound exciton emission lines to the background luminescence intensity.

2.11. Conclusion.

Distribution functions for photoexcited electrons in GaAs, at lattice temperatures in the liquid helium range, have been studied within a one band, Boltzmann equation model. The distribution functions are expected to be isotropic (in $\vec{k}$ space) if the electron generation and recombination rates are isotropic because frequent elastic scattering events would not allow piezolectric scattering to cause anisotropies. If the electron injection spectrum is represented by a δ function (in energy), the distribution function is composed of the sum of a singular part, which is characteristic of those electrons which have either undergone no inelastic collisions or have interacted solely with L.O. phonons, and a non-singular part, $\bar{f}$, which is characteristic of those electrons which have been scattered by acoustic phonons or other electrons.

If the injection energy is taken to be above the L.O. phonon threshold energy it is found that L.O.phonon emission causes reinjection of the electrons at an energy below the L.O. phonon threshold. If the injection energy is taken to be below the L.O. phonon threshold and both piezoelectric and deformation potential scattering are taken into account it is found that $\bar{f}$

as a function of energy has the form of a lattice temperature Maxwellian at sufficiently low energies ($\lesssim$ 1 meV if the injection energy is 3.989 meV and the lattice temperature 1.7°K but has a non-Maxwellian plateau at higher energies. A characteristic shoulder is present at the injection (or reinjection) energy and above this energy the distribution function again has a lattice temperature Maxwellian form. From the form of model distribution functions, it is inferred that, of the three types of acoustic phonon interaction, transverse piezoelectric scattering plays the most important part in establishing the form of the electron distribution (if the injection energy is 3.989 meV).However, for higher injection energies ($\gtrsim$ 20 meV) deformation potential scattering is expected to be significant because the deformation potential scattering rate then exceeds the piezoelectric scattering rates. The non-singular parts of all the model distribution functions exhibit some fine structure, in the form of a series of modulations of energies close to the injection energy. This structure is characteristic of those electrons which have undergone only a few ($\sim$ 1 or 2) acoustic phonon interactions. Although it is a genuine feature of the computed distribution functions it has not yet been observed in experimental photoluminescence spectra and further work is necessary to establish whether it occurs in practice. The overall form of the distribution functions is insensitive to small changes in the screening of the phonon interactions. It is also insensitive to the k dependence of the recombination rate, unless for some range of energies, this quantity becomes comparable to or exceeds the phonon scattering rates.

The effect of electron-electron scattering on the photoexcited electron distribution has been investigated in a preliminary manner. Two different models for electron-electron scattering have been used. Within a large screening model the Boltzmann equation has been numerically solved without any approximations being made to the collision integrals. The solutions

obtained illustrate some of the physics of electron-electron scattering but are not applicable to the lower inverse screening lengths likely to occur in practice. To compute distribution corresponding to these screening lengths, an approximation to the electron-electron collision integral (based on the use of a Taylor series) had to be employed. Even so, accurate calculations of the distribution function for the range of electron densities of practical interest could not be made using the available computing resources. The few results obtained indicate that if the injection energy is 3.989 meV and the lattice temperature 1.7^{o}K then the minimum electron density at which electron-electron scattering would have an effect on photoexcited electrons in GaAs is in the range $\sim 10^{15}$ to 10^{16} m^{-3}. This effect would be evident as heating of electrons contributing to the tail of the distribution function ($\epsilon > \epsilon_1$). It could be significant at electron densities $\sim 3 \times 10^{16}$ m^{-3}.

Electron-acceptor luminescence spectra, for C doped GaAs under conditions of continuous, monochromatic, interband photoexcitation, (at an excitation intensity such that the effects of inter-carrier scattering are neglible) have been computed within the one band, Boltzmann equation model. Good, qualitative agreement with experimental (e,A^{o}) spectra has been obtained and this indicates that the model can account, in general, for the physical properties of photoexcited electrons in GaAs. However, the quantitative agreement between the computed and experimental spectra is only fair and further experimental and theoretical work is necessary before the model can account, in detail, for the properties of the photo-excited electrons. Some aspects of the model which require further theoretical work have been identified.

CHAPTER 3

INHOMOGENOUS ELECTRIC FIELDS IN OSCILLATORY PHOTOCONDUCTIVITY

3.1. Introduction.

In a wide variety of semiconductors (Eg InSb, CdTe, GaAs, Ge) it has been found that at temperatures in the liquid helium to liquid nitrogen range, the photoconductivity due to monochromatic excitation is a periodic function of the optical excitation energy - the so called 'oscillatory photoconductivity' (Stocker - Levinstein and Stannard, 1966). The effect is due to the rapid emission of longitudinal optical (L.O) phonons by the photo excited carriers which have acquired sufficient energy. Under these conditions it is theoretically possible for a spatially uniform, negative drift velocity state to occur if the injection energy is just below an integral multiple of the threshold energy for L.O. phonon emission ('sub-threshold' injection). This type of state has the interesting property that a fraction of the optical excitation energy is continuously transferred to the electric field via the photo excited carriers. For sub-threshold injection energies the drift velocity as a function of electric field (see Fig. 3.1) exhibits, in addition to the region of negative velocity, a region of negative differential velocity. This renders the system intrinsically unstable against space charge formation. Neither steady negative currents, nor instabilities have yet been observed when oscillatory photoconductivity occurs. However the increasing amount of experimental work being carried out with tunable lasers could provide some evidence as to the existence of these effects and the aim of our work is to provide a theoretical model to guide such experiments.

In having a region of negative differential velocity the oscillatory photoconductivity velocity field characteristic closely resembles the Gunn effect (Butcher, 1967) characteristic. The microscopic origin of both characteristics is also similar since the mechanism underlying both

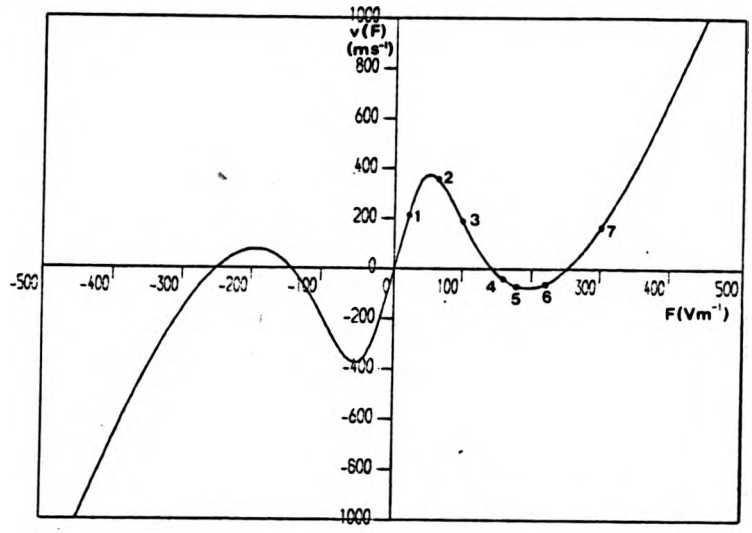

(a)

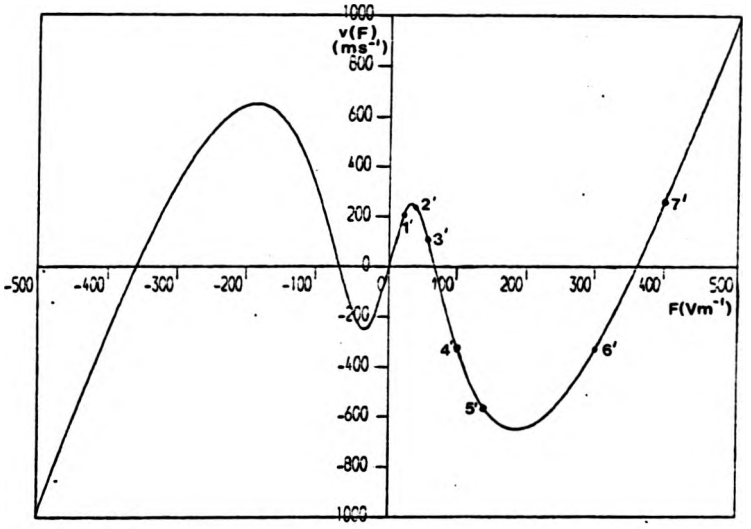

(b)

Fig.3.1. Oscillatory photoconductivity velocity field characteristic calculated according to the Barker-Hearn one dimensional model.
(a) positive area characteristic; injection energy=0.954$\hbar\omega_o$
(b) negative area characteristic; injection energy=0.96$\hbar\omega_o$
The numbered points show the initial fields used in the numerical study described in section 3.6. The terms 'positive area' and negative area are defi-

is a phonon assisted transfer of electrons in K-space. Thus it is plausible that, as in the Gunn effect, the electric field in a semiconductor exhibiting oscillatory photoconductivity may become unstable with respect to space change formation (Jones and Beaudet, 1967). It follows that Gunn-like instabilities may then result. (Barker and Hearn, 1969, 1970; Barker, 1969). In this chapter we investigate the conditions under which either instabilities or steady negative currents are to be expected in the bulk of a semiconductor exhibiting oscillatory photoconductivity (under conditions of sub-threshold injection). We do this by means of a numerical study of the space time dependence of the electric field in such a semiconductor. A model which exploits the analogy between oscillatory photoconductivity and the Gunn effect is used for this purpose.

In section 3.2 we commence our work with a detailed account of the mechanism responsible for oscillatory photoconductivity. The same section contains a review of some theoretical studies of the velocity field characteristic. Emphasis is placed on those studies which specifically discuss sub-threshold injection of carriers. A more complete review of oscillatory photoconductivity and other phenomena associated with the interaction of electrons with L.O. phonons has been given by Harper, Hodby and Stradling (1973).

The Gunn effect model we use for our studies of oscillatory photoconductivity is explained in section 3.3. As the model leads to a non-linear equation it has not been possible to obtain an analytic solution for the electric field. However it is possible to use phase plane analysis in order to deduce some of the properties of possible steady state fields and uniformly propagating instabilities. This is done in section 3.4.

We devote the remainder of the chapter to a numerical study of the non-linear equation describing the electric field. Boundary and initial conditions required for the study are discussed in section 3.5, whilst in section 3.6 we present the numerical solutions themselves. Finally we

summarize our conclusions in section 3.7.

3.2. Oscillatory Photoconductivity: The Underlying Mechanism.

As mentioned in the previous section monochromatic photo-excitation of a semiconductor can produce a photoconductive response which is a periodic function of the optical excitation energy. According to the accepted theory (Stocker and Kaplan, 1966; Elesin and Manykin, 1965; Folland 1970) the effect is due to the dominant interaction of the photo-excited carriers with L.O. phonons. (At the low temperatures involved the number of thermally excited carriers is negligibly small). A carrier excited into a conduction band rapidly emits a number of L.O. phonons, each of energy $\hbar\omega_0$, until its energy lies in the range 0 to $\hbar\omega_0$ relative to the bottom of the band. Thus the steady state non-equilibrium distribution function, which determines the magnitude of the photoconductivity, for an excitation energy $\epsilon + m\hbar\omega_0$ is essentially the same as for an excitation energy ϵ. The period of the oscillation is thus equal to the energy of the appropriate L.O. phonon. (The effect of L.O. phonon emission on photo-carrier distributions is described in Chapter 2). The photoconductivity is also a function of electric field. And according to the accepted theory of oscillatory photoconductivity the photocurrent can be negative for a certain range of electric fields provided that the injection energy is just below an integral multiple of the threshold energy for L.O. phonon emission. This effect can readily be understood in terms of the following sequence of events,(as illustrated in Fig. 3.2.) After any initial phonon emission has occurred all carriers lie just below the first L.O. phonon threshold. Consider these as divided equally between two groups. Group A has carriers with a negative component of velocity parallel to the electric field and group B has carriers with a positive component. For electrons group A gains energy from the field whilst group B loses energy to the field. If the field is strong enough group A electrons cross the threshold early in their lifetime emit a phonon and hence have a mean velocity

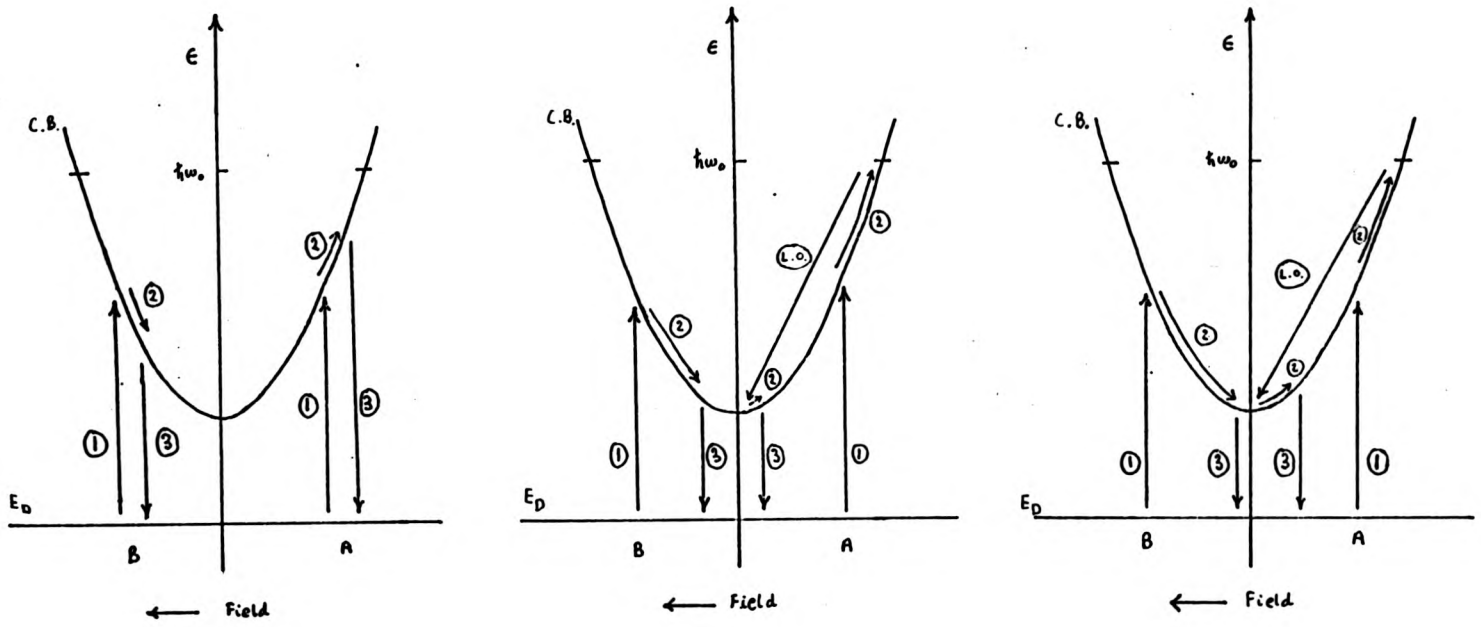

Fig.3.2 A schematic illustration of the mechanism underlying the negative current state associated with oscillatory photoconductivity. Each diagram shows typical life histories of the group A and B electrons.
(a) $F < F_c$; positive velocity (b) $F_c < F < F_r$; negative velocity (c) $F > F_r$; positive velocity
Only L.O. phonon scattering illustrated. ① injection ② acceleration ③ recombination
(L.O.) L.O. phonon emission.

component which is small (and negative). No such process occurs for group B so their mean velocity is large (and positive). Thus the net *conventional* current is negative. If the field is too strong the conventional current is positive because group A electrons are able, during their lifetime, to gain an appreciable negative velocity component after the phonon emission has occurred and group B electrons suffer a considerable reduction in velocity. If the field is too weak the majority of the group A electrons recombine before reaching the L.O. phonon threshold so the conventional current is also positive.

Barker and Hearn (1969) have used a Monte Carlo technique to study the Stocker-Kaplan model of oscillatory photoconductivity. Their work is appropriate to InSb at a lattice temperature of $10^{o}K$ and an electron injection energy equal 0.978 of the L.O. phonon threshold energy and they have predicted a velocity field characteristic which exhibits a range of electric fields for which the drift velocity is negative. Additionally Barker and Hearn have described a simple model for oscillatory photoconductivity which considers electrons excited into a one dimensional conduction band. It predicts a velocity field characteristic qualitatively in accord with Monte Carlo and has the advantage of an analytic solution. A Boltzmann transport equation approach is used with k independent recombination and momentum relaxation times τ and λ respectively. Electrons are injected below the L.O. phonon threshold. Subsequently a fraction of them are accelerated to the threshold and instantaneously emit an L.O. phonon to enter states of the bottom of the band (as outlined above). For all injection energies the zero field slope of the model velocity field characteristic is positive. If the injection energy is just below the L.O. phonon threshold there is a region of negative slope at slightly higher fields and at sufficiently high fields the slope is again positive. If the injection energy is sufficiently close to the threshold there is a region of negative velocity in addition to the region of negative slope.

Upon solving the Barker-HearnlD model, as described in the previous paragraph, the drift velocity can be found as:

$$v(F) = \frac{eF\tau_1}{m^*}\left[1 - \frac{\omega^2 L \cosh \omega k_o}{(\alpha+\beta)(\cosh \omega L - 1) + \omega \sinh \omega L}\right]$$

where α, β and ω are reciprocal wave numbers defined by

$$\alpha = \frac{\hbar}{eF}\left\{\frac{1}{\lambda} + \frac{1}{\tau}\right\} \quad \beta = \frac{\hbar}{eF\lambda} \quad \omega^2 = \alpha^2 - \beta^2$$

and τ_1 is the effective momentum relaxation time given by

$$\frac{1}{\tau_1} = \frac{2}{\lambda} + \frac{1}{\tau}.$$

The L.O. threshold and injection energies are $\frac{\hbar^2 L^2}{2m^*}$ and $\frac{\hbar^2 k_o^2}{2m^*}$ respectively. The above form the velocity field characteristic is in agreement with Barker (1969) but Barker and Hearn give an approximation for sub-threshold injection i.e. $k_o \sim L$. For the threshold energy and lifetimes appropriate to InSb $\omega L \sim 10^3$. Hence the drift velocity can be approximated by the equation:

$$v(F) = \frac{eF\tau_1}{m^*}\left[1 - \frac{\hbar L}{eF\tau}\,\frac{A}{1+A}\exp\left\{-\frac{\hbar A}{eF}(L-k_o)\right\}\right], A^2 = 1+\frac{2\tau}{\lambda} \qquad (3.1)$$

Although not in exact agreement with the result given by Barker and Hearn, equation 3.1 approximates their velocity field characteristic quite well.

Fig. 3.1 shows two velocity field characteristics which have been calculated using equation 3.1. The excitation energies are as shown in the caption to the figure and the following parameters, which are thought to be applicable to electrons in InSb at 10^oK, have been used in the calculations: $\tau = 10^{-10}S$, effective mass $= 0.012m_o$, L.O. phonon theshold $= 0.024$ eV. λ has been taken as 1.38×10^{-12}. This value is chosen to

give the model characteristics a low field mobility of 10 $m^2 V^{-1}s^{-1}$ which is a figure we find convenient for use in our subsequent numerical studies. However our choice of λ makes the model drift velocities artificially low - the Monte Carlo calculations mentioned previously have predicted drift velocities two orders of magnitude higher.

For any model of the velocity-field characteristic there,is for specific scattering conditions and recombination lifetimes, a critical band of energies just below the optical phonon emission thresholds, into which carriers must be excited in order for there to be a range of electric field strengths in which the velocity is negative. The velocity field characteristic for non-monochromatic excitation can readily be synthesized from the monochromatic characteristics and the presence of a negative velocity range is clearly dependent on the fraction of carriers excited into this critical band of energies. Stocker (1967) has computed the velocity field characteristic for a model in which the injection spectrum is assumed to have a Gaussian form with a half-width equal to 0.03 of the phonon threshold energy. He has found that the velocity field characteristic has a negative velocity region if the injection energy ϵ_i is in the range $0.94 \leq \epsilon_i/\hbar\omega_0 \leq 1.0$ and greater than 0.94 of the threshold energy.

In addition to the basic mechanism of dominant L.O. phonon emission, various related mechanisms have been proposed, which may also cause negative drift velocities. Harper, Hodby and Stradling (1973) have argued that capture of electrons into impurities, via L.O. phonon emission can take place from a narrow zone of energies in the conduction band. Should injection into the conduction band occur below this zone those electrons which are subsequently accelerated would recombine rapidly and a net negative current would result. However, if the injection was above this zone, recombination of those electrons which are decelerated would occur and a positive current of enhanced magnitude would result.

Holzhütter and Mocker (1976) have considered the effect of impact ionization of neutral donors. They suggest that electrons could be accelerated to the threshold energy for impact ionization, which would then occur rapidly causing both electron to enter states in the bottom of the band. They calculate that there would be a sharp dip in the photoconductive response if the injection energy was just below the threshold for impact ionization. However, they have not predicted the current to be negative.

In their review Harper, Hodby and Stradling mention two experiments which give indirect evidence to support the existence of negative currents in oscillatory photoconductivity. One of these experiments involved a Fourier transform spectroscopy technique, and the derived photoconductive response was found to be negative for sub-threshold injection energies (Chamberlain et. al. 1971). However Eaves (1979) has warned us that infrared Fourier transform spectra, in general, may be inaccurate at energies close to the L.O. phonon energy. Chamberlain and co-workers do not give precise details of their experiment so we cannot judge whether their experiment has unambiguously detected negative photoconductivity. The other experiment mentioned in the review was performed to determine the photoconductive response of Cadmium Telluride at $4.2^{o}K$. The measured current-voltage characteristic proved to be highly non-linear for injection energies close to the L.O. threshold but no negative currents were detected.

3.3. A Gunn effect model applied to oscillatory photoconductivity.

We now describe the Gunn effect model we employ in our studies of oscillatory photoconductivity. The model is one in which it is assumed that the carrier drift velocity is a local and quasi-static function of electric field. (Butcher, 1967; Bonch-Bruevich, Zvyagin and Mironov, 1972). By this it is meant that the local drift velocity in the presence of a space-time dependent electric field is taken to be that which would occur if the local electric field were uniform and time independent. This model has been

extensively used during early studies of hot electron devices and has allowed a semi-quantitative understanding of the behaviour of such devices. Similarly, we use the same model to obtain a preliminary understanding of the instability phenomena expected to be associated with oscillatory photoconductivity.

We consider a semiconductor connected in a circuit in series with a resistance R and a battery of e.m.f. V_0, (as shown in Fig. 3.3). Electrons are supposed to be excited from donors into a conduction band under conditions such that oscillatory photoconductivity occurs. The spatial variation of all quantities is assumed to be one dimensional. A sign convention is adopted in which the electric field measured in the negative direction is denoted by F, and all other quantities are measured in the positive direction. The cathode of the semiconductor is taken to be at a position x = 0. Then the electric field, electron density n(x,t) and the ionized donor density $n^+(x,t)$ are related by the following system of equations:

$$\frac{\partial n}{\partial t} - \frac{\partial n^+}{\partial t} + \frac{\partial j}{\partial x} = 0 \qquad (3.2)$$

$$j = - D \frac{\partial n}{\partial x} + n\, v(F(x,t)) \qquad (3.3)$$

$$\frac{\partial F}{\partial x} = \frac{e}{\epsilon\epsilon} (n - n^+) \qquad (3.4)$$

Equation 3.2 is the continuity equation for the electron current j, and equation 3.4 is Poisson's equation. Equation 3.3 gives the electron current as the sum of a diffusion term and a drift term. In writing this equation we have assumed that the diffusion coefficient is field independent. This assumption is necessary because of our lack of knowledge of the diffusion process. In addition it enables us to use phase plane analysis to deduce some properties of the instabilities.

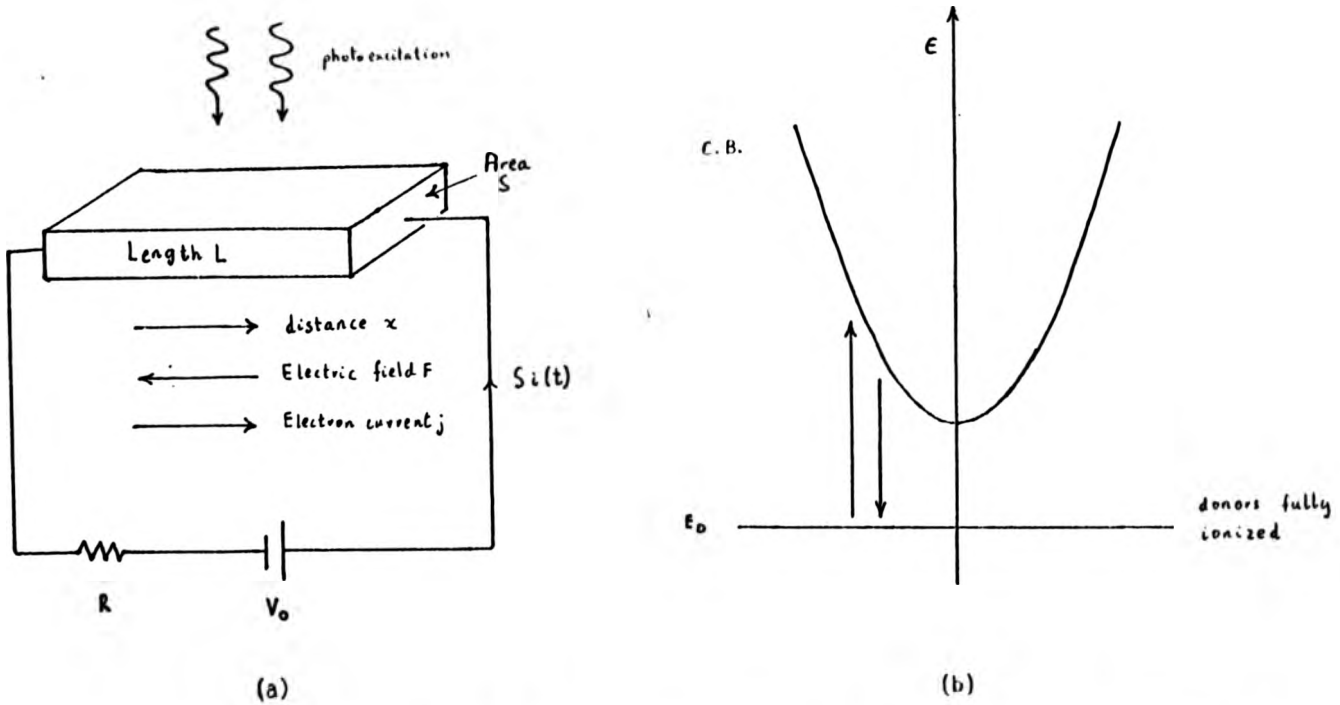

Fig. 3.3. An illustration of the Gunn effect model used to study oscillatory photoconductivity.

(a) The circuit arrangement and a definition of the symbols used

(b) The photoconductive transitions involved.

Next we eliminate n from equations 3.2 to 3.4 to obtain one equation which relates F and n^+. To do this we first use Poisson's equation to find a continuity equation for the total electric current. Upon differentiating Poisson's equation with respect to time and making use of equation 3.2 to substitute for $\frac{\partial}{\partial t}(n-n^+)$ we obtain the equation:

$$\frac{-\partial}{\partial x}\{\varepsilon\varepsilon_o \frac{\partial F}{\partial t} + ej\} = 0$$

From which it follows that

$$\varepsilon\varepsilon_o \frac{\partial F}{\partial t} + ej = -i(t) \tag{3.5}$$

where the function i(t) can be identified as the total current density,(i.e.the sum of the displacement and electron currents). Together equations 3.2, 3.3 and 3.5 give the desired relation between F and n^+:

$$\frac{\partial F}{\partial t} - D\frac{\partial^2 F}{\partial x^2} + v(F)\frac{\partial F}{\partial x} + \frac{e}{\varepsilon\varepsilon_o}\{n^+ v(F) - D\frac{\partial n^+}{\partial x}\} = \frac{-i(t)}{\varepsilon\varepsilon_o} \tag{3.6}$$

And for a semiconductor of length L and cross sectional area S the total electric current density is simply given as

$$i = \{\int_0^L F\,dx - V_o\}/RS \tag{3.7}$$

In general an ionization rate equation is required to determine n^+. However if we take into account spatially non-uniform donor ionization, then we find that the recombination and scattering rates and hence the velocity field characteristic are all spatially non-uniform. This greatly complicates our study and we avoid such complications by restricting ourselves to the case of an excitation intensity which is sufficiently high to keep the donors fully ionized so that n^+ becomes equal to the donor desnity n_o, which we take to be spatially uniform (except for a doping notch used as a perturbation in the numerical study).

The properties of equations 3.6 and 3.7 (under the assumption of spatially uniform donor ionization) are well known from studies of the Gunn Effect (Butcher 1967; Bonch-Bruevich, Zvyagin and Mironov, 1972).

One possible solution is a uniform field, F_u, given by the intersection of a load line with the velocity field characteristic, (see Fig. 3.4).

$$en_o v(F_u) = \frac{V_o - F_u L}{RS} \tag{3.8}$$

If the resistance is sufficiently small this solution is unique but otherwise there may be up to five solutions. Small signal analysis shows that the uniform field can be unstable with respect to space change formation. This happens if the differential velocity corresponding to F_u is negative and the differential dielectric relaxation time τ_d defined by

$$\tau_d^{-1} = \frac{en_o}{\epsilon\epsilon_o} \left.\frac{dv}{dF}\right|_{F=F_u},$$

which is then negative satisfies the inequality

$$\frac{1}{|\tau_d|} > \frac{4\pi^2}{L^2} D \tag{3.9}$$

Small perturbations to a uniform, unstable field may develop into either uniformly propagating solutions or inhomogenous steady states. Uniformly propagating solutions are those for which the field is only a function of the single variable x-ct and the current density remains constant at $en_o\bar{v}$ while the instability propagates. Inhomogenous steady states are characterized by a time independent current density, $en_o\bar{v}$, and a spatially non-uniform electric field. Some qualitative properties of both types of solution are easily deduced using phase plane analysis. Such an analysis forms a useful complement to a numerical study of equations 3.6 and 3.7 and is described in the next section. The phase plane method itself is explained in detail in many texts e.g. Minorsky 1962, 1964.

3.4. A Phase Plane Analysis of the Model.

We commence this section with a brief review of the phase plane properties of the equations describing uniformly propagating solutions. The velocity field characteristic is taken to be arbitrary. We then identify possible closed trajectories in the phase plane, for the case that the velocity field characteristic is appropriate to oscillatory photoconductivity and $c = \bar{v}$. (Physically such trajectories correspond

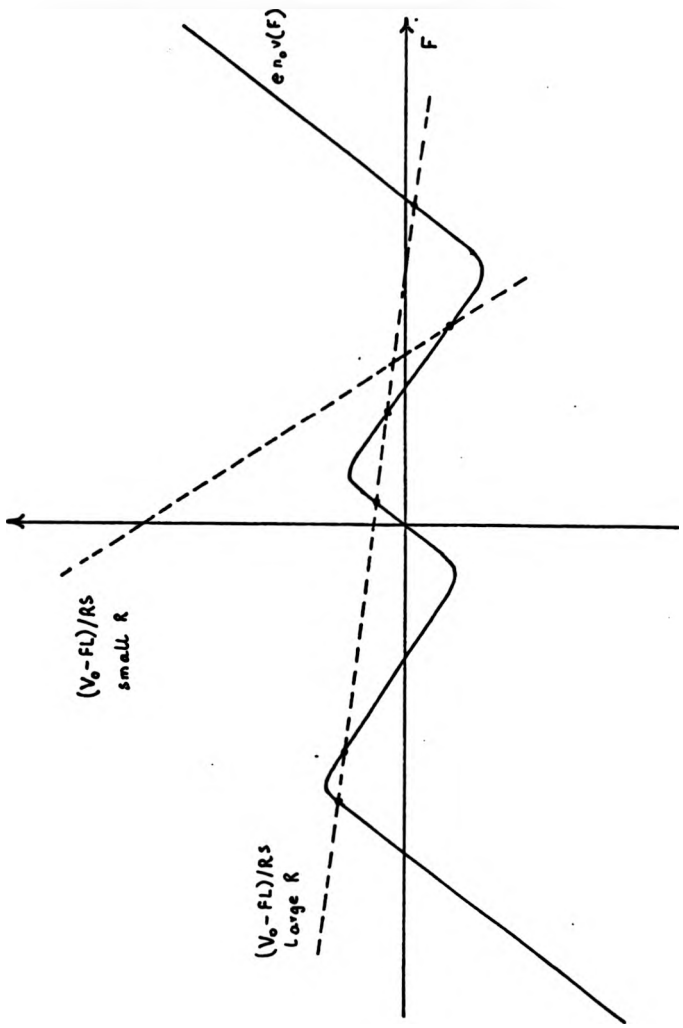

Fig. 3.4. The possible uniform, steady state fields associated with oscillatory photoconductivity under conditions of 'sub-threshold' injection. Depending on the magnitude of R there can be up to 5 possible uniform fields for a particular set of values of V_0, L and A.

to high or low field dipole domains.) Following this we consider how the type of domain formed is likely to depend on the sign and magnitude of $\bar{v}$. Attention is restricted to those domains which propagate in a sample connected as shown in Fig. 3.3 i.e. with the cathode at x = 0. Finally we describe some phase plane properties of inhomogenous steady states.

Setting $i = en_o\bar{v}$ in equation 3.7 and assuming a solution of the form $F \equiv F(y)$, $y = x-ct$ we obtain the following pair of ordinary differential equations.

$$\frac{dF}{dy} = p \tag{3.10}$$

$$\frac{dp}{dy} = \frac{1}{D}\{[v(F)-c]p + \frac{en_o}{\varepsilon\varepsilon_o}[v(F) - \bar{v}]\} \tag{3.11}$$

Solutions to these equations can be plotted in the phase plane $(F,\frac{dF}{dy})$. The singular points occur at $(F_s,0)$ where the F_s are defined by the equation $v(F_s) = \bar{v}$. The singularities saddles if τ_d is positive. Otherwise they are in general nodes or foci, which are stable if $v(F_s) - c < 0$ and unstable if $v(F_s) - c > 0$. They reduce to vortices if $c = \bar{v}$. In this case dipole domains are amongst the possible solutions.

Domains can exist only if the velocity field characteristic has a region of negative differential velocity. They are represented on the phase plane by trajectories which leave a saddle, encircle a vortex and return. High or low field domains can occur and these involve depletion and accumulation layers in the appropriate spatial order, which move at a velocity $\bar{v}$. Single layers moving at velocity $\bar{v}$ are also possible and they are represented as trajectories which link two saddles. If $c=\bar{v}$ all trajectories which leave the F axis at a field F_2 and return at F_1 obey an 'equal area rule' (Butcher, 1967).

$$\int_{F_2}^{F_1} [v(F) - \bar{v}]\, dF = 0 \tag{3.12}$$

For a high field domain F_1 is the peak domain field and F_2 is the outside field and vice versa for a low field domain.

In oscillatory photoconductivity we can distinguish between two types of velocity field characteristic shown as (a) and (b) in Fig. 3.1. In both characteristics the drift velocity is positive for small positive electric fields. With increasing field the velocity first increases, reaches a maximum at the threshold field F_T, then becomes negative above a critical field F_c and returns to positive values again above a restoring field F_r. The two characteristics differ in that the sign of the area $\int_0^{F_r} v(F)dF$ is positive for (a) but negative for (b) in Fig. 3.1. Of the two characteristics the negative area characteristic is likely to occur for injection energies closest to the threshold energy.

In Fig. 3.5 we indicate schematically the form of the phase plane for the case where v(F) is appropriate to oscillatory photoconductivity and $c = \bar{v}$. $\bar{v}$ has been taken to be positive and of such a magnitude that five singular points exist. Use of the equal areas rule (3.12) enables us to identify some possible closed trajectories in the phase plane. To illustrate the procedure for doing so, we show that with the negative area characteristic no trajectory can leave the right hand saddle and return to the F axis whereas a closed trajectory containing the left hand saddle may exist. Let us label the singular points from left to right by the index i : i = 1,5 and let theith point be located at the position $(F_i,0)$ in the phase plane. (Fig. 3.5). We consider first the trajectory emanating from the right hand saddle in the 'north west' direction and suppose that it returns to the F axis at some point $(F_x,0)$. Then according to equal areas rule F_x must satisfy the equation $\int_{F_x}^{F_5} [v(F) - \bar{v}]dF = 0$.

Considering the possible paths our trajectory can take to avoid crossing trajectories entering or leaving the centre and left hand saddles, and

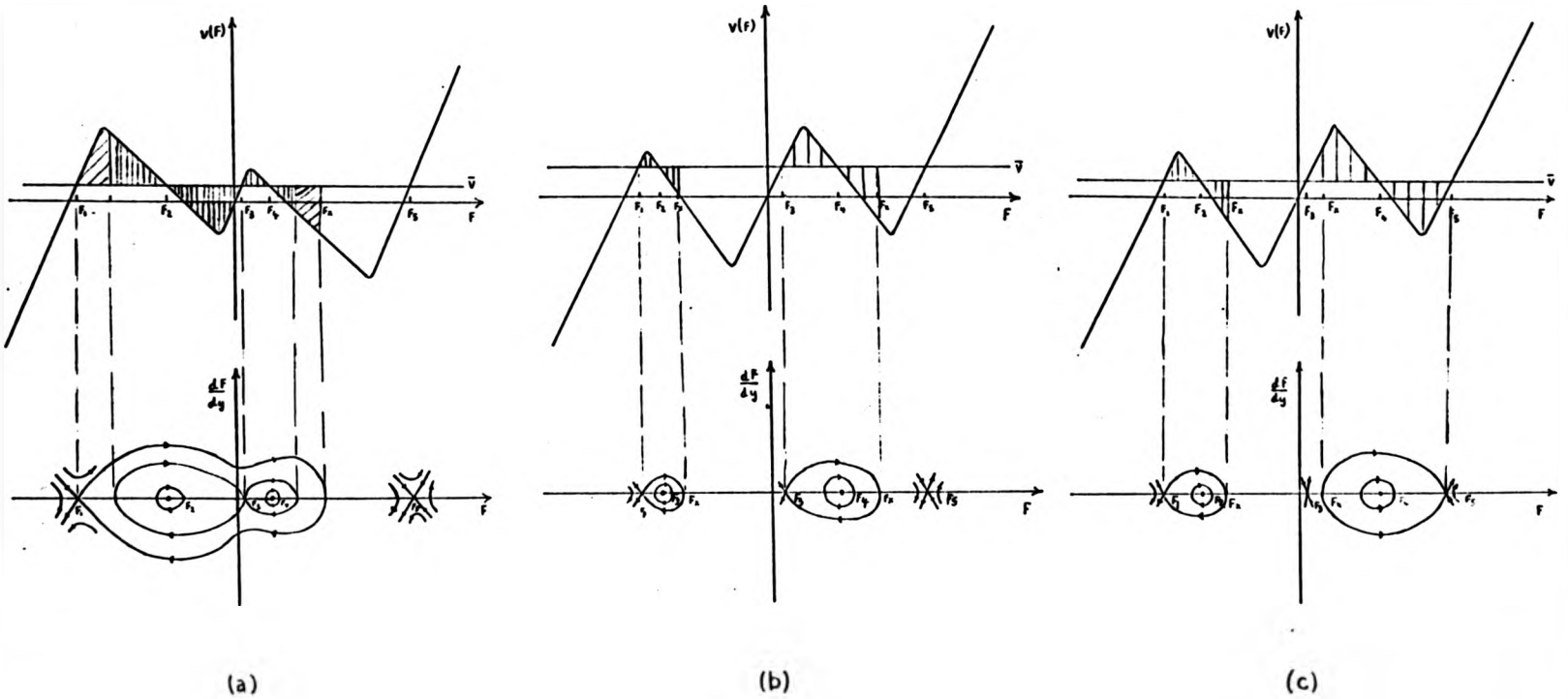

Fig. 3.5. Some possible closed trajectories in the phase planes for $c = \bar{v}$, $0 \leq \bar{v} < v(F_T)$. These trajectories correspond to domain type solutions. The equal area rules for each trajectory are also shown (a) negative area characteristic (b),(c) positive area characteristic.

taking into account the form of the isoclines of $\frac{dp}{dF} = 0$ in the phase plane, we find that F_x must obey one of the inequalities $F_3 \leq F_x < F_4$ or $F_1 \leq F_x < F_2$. For either case with $\bar{v} > 0$ and a negative area characteristic the inequality $\int_{F_x}^{F_5} [v(F) - \bar{v}]dF < 0$ is satisfied. This clearly contradicts our assumption that the equal areas rule holds and therefore our supposed trajectory cannot exist. Next we consider a trajectory entering the left hand saddle from a 'north east' direction and we suppose that it crosses the F axis at a point $(F_x,0)$. As with the previous trajectory we assume that the equal areas rule is satisfied, and considering the possible paths of this trajectory we find that F_x must obey one of the inequalities $F_2 < F_x \leq F_3$ or $F_4 < F_x \leq F_5$. Depending on the magnitude of $\bar{v}$ one or other of these inequalities can be satisfied simultaneously with the equal area rule provided that the velocity field characteristic is of negative area. By an analogous argument we see that the trajectory leaving the left hand saddle in a 'south east' direction could return to the F axis at the same position $(F_x,0)$. Therefore a closed trajectory containing the left hand saddle may exist. The negative area characteristic shown in Fig. 3.1b has the property that $\int_{F_1^T}^{F_T} [v(F) - v(F_T)]dF > 0$, where $(F_1^T,0)$ is the position of the left hand saddle when $\bar{v} = v(F_T)$. It follows that for this particular characteristic and for $\bar{v}$ such that $0 \leq \bar{v} < v(F_T)$, the equal area rule can only be satisfied if F_x satisfies the second of our two inequalities i.e. $F_4 < F_x \leq F_5$. Fig. 3.5a shows a possible closed trajectory containing the left hand saddle and possible closed trajectories within. The equal area rule for these trajectories is also illustrated.

We can apply similar reasoning to identify possible closed trajectories for a positive area characteristic. In this case one possible trajectory contains the left hand saddle and encircles the left hand

vortex. A trajectory encircling the right hand vortex can contain either the right hand or centre saddles. Physically this trajectory corresponds to a low field domain if it contains the former vortex, and a high field domain if it contains the latter. The two cases, together with the corresponding equal area rules are illustrated in Figs. 3.5b and 3.5c.

Next we consider the domains which are likely to be formed from a perturbation to a uniform, unstable and positive field. Such domains correspond to trajectories which encircle the right hand vortex on the phase plane. An application of the equal areas rule together with phase plane analysis, as described in the preceeding paragraphs enables us to deduce how the nature of the domains depends on the sign and magnitude of $\bar{v}$. (Fig.3.6) We find that with a positive area characteristic both high and low field domains can occur at appropriate positive $\bar{v}$ but only low field domains at negative $\bar{v}$. For the negative area characteristic the allowed types of domain are different:only high field domains can occur for positive $\bar{v}$ but both types at appropriate negative $\bar{v}$. For each characteristic there is a critical velocity, v_c, corresponding to a change in the allowed type of domain. Moving layers could propagate at this velocity.

Inhomogenous steady states can also be classified on a phase plane and the relevant equations involve c = 0 in equations 3.10 and 3.11. The position of the singular points is as for c=0 and they are saddles if $\tau_d > 0$. If $\tau_d < 0$ they are nodes if $\{\frac{\bar{v}}{D}\}^2 + \frac{4}{D\tau_d} > 0$, foci if $\{\frac{\bar{v}}{D}\}^2 + \frac{4}{D\tau_d} < 0$ and vortices if $\bar{v} = 0$. The nodes or foci are stable if $\bar{v} < 0$ and unstable if $\bar{v} > 0$. We have depicted the nature of the relevant phase planes in Fig. 3.7.

In order to select possible solutions from the steady state phase planes or carry out a numerical solution of equations 3.10 and 3.11 we must impose some boundary conditions. Choice of boundary conditions for a circuit model involving oscillatory photoconductivity presents more subtle problems than does choice of boundary conditions for a Gunn Effect model. These problems are described at length in the next section. The

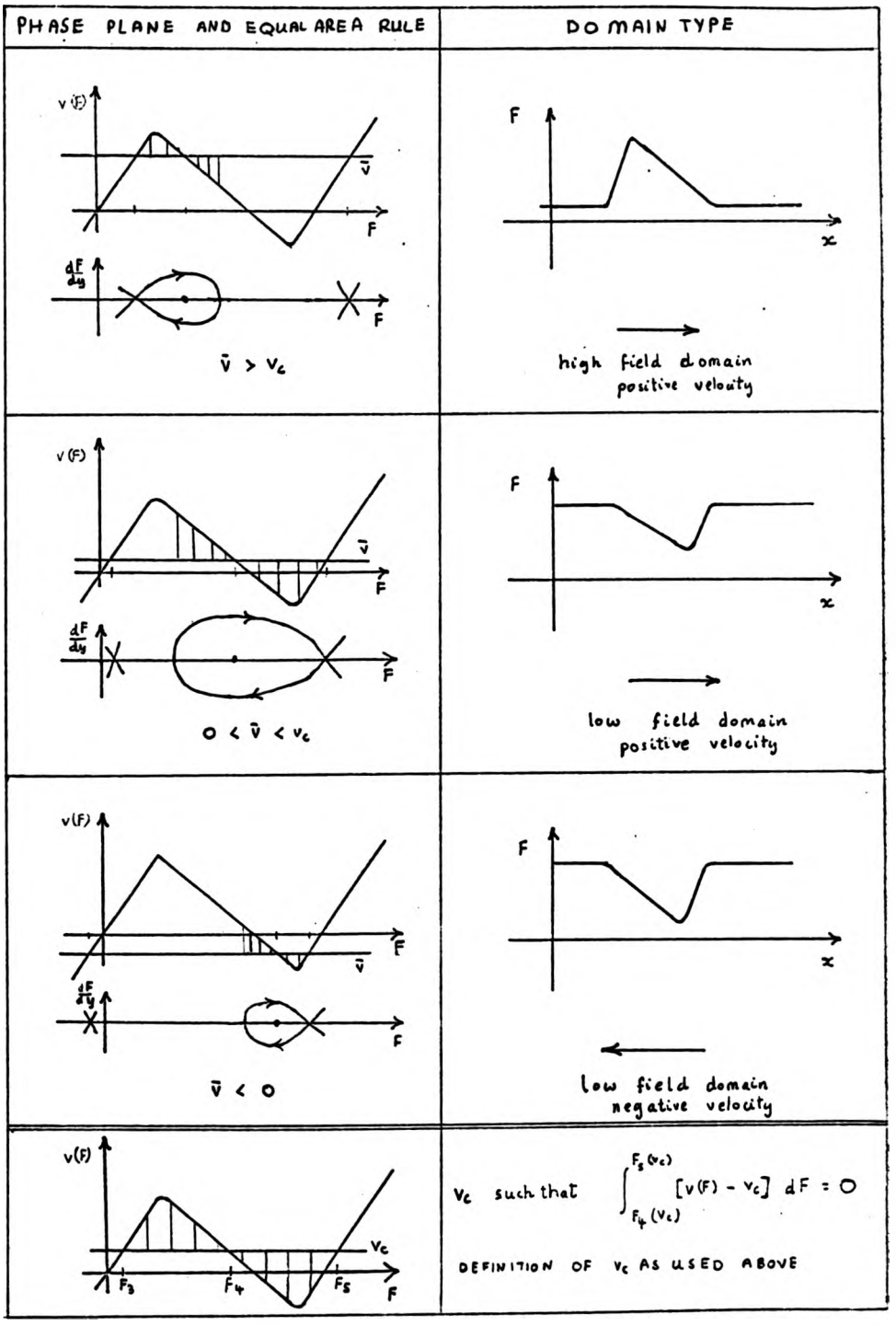

Fig.3.6a. An illustration of how the type of domain which could form fro a perturbation to a uniform, unstable and positive field, depends on the sign and magnitude of v. The phase plane s and equal area rules corresponding to these domains are shown. A sketch of the domain shape is also given. Positive area characteristic.

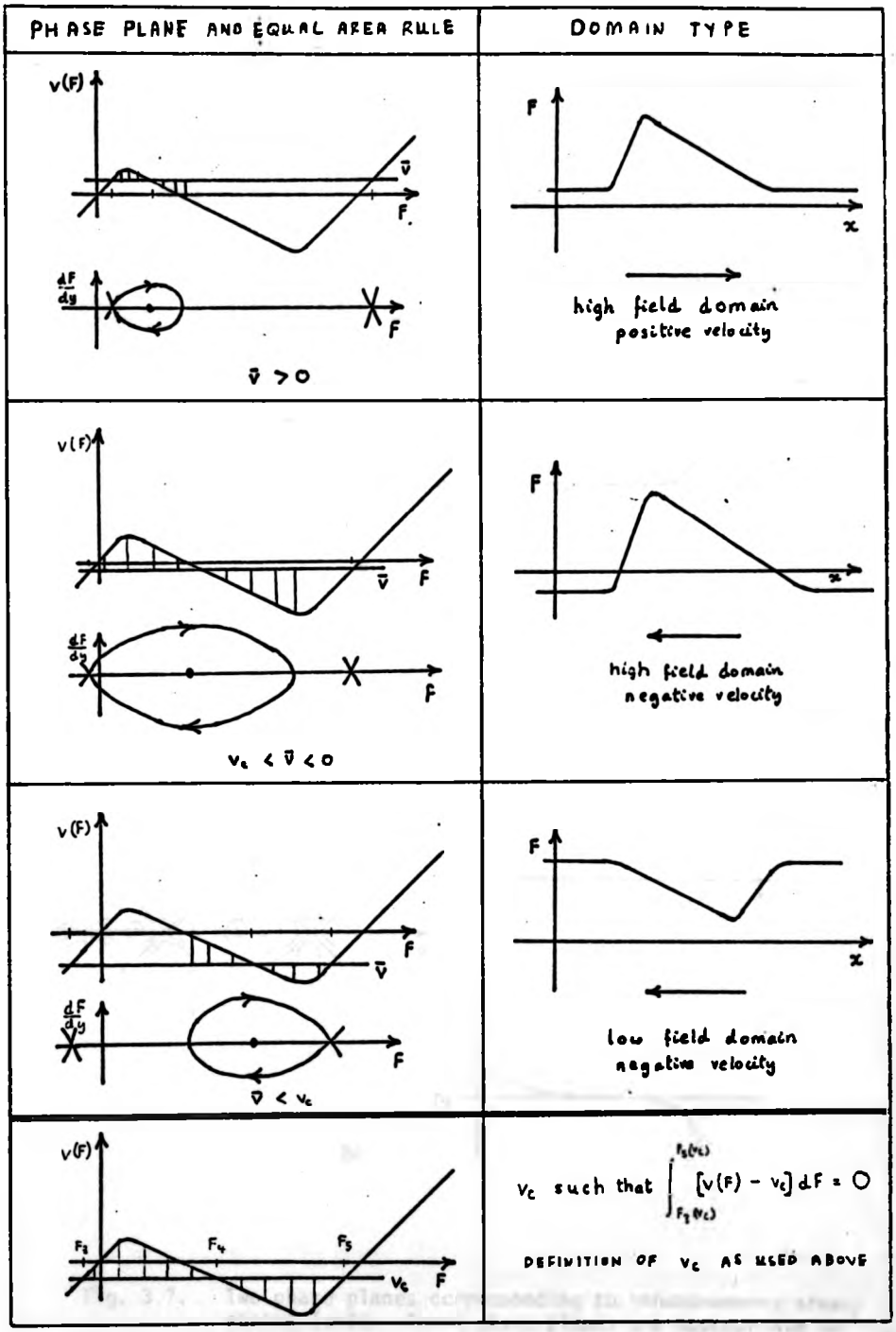

Fig.3.6b. An illustration of how the type of domain which could form from a perturbation to a uniform, unstable and positive field, depends on the sign and magnitude of $\bar{v}$. The phase planes and equal area rules corresponding to these domains are shown. A sketch of the domain shapes is also given. Negative area characteristic.

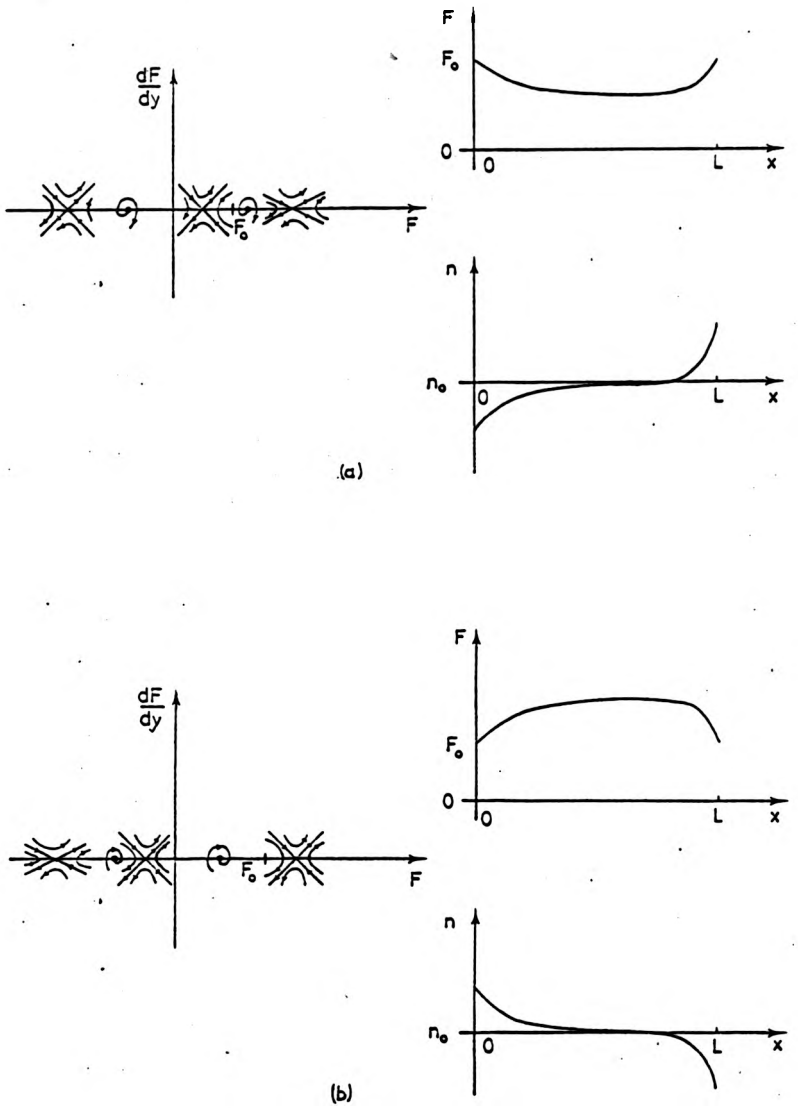

Fig. 3.7. Two phase planes corresponding to inhomogeneous steady states (c=0). These phase planes are appropriate to both types of velocity field characteristic.
(a) $\bar{v} > 0$ (b) $\bar{v} < 0$.
Some steady state electric fields and electron densities possible for field boundary conditions are imposed are also shown (See Section 3.5).

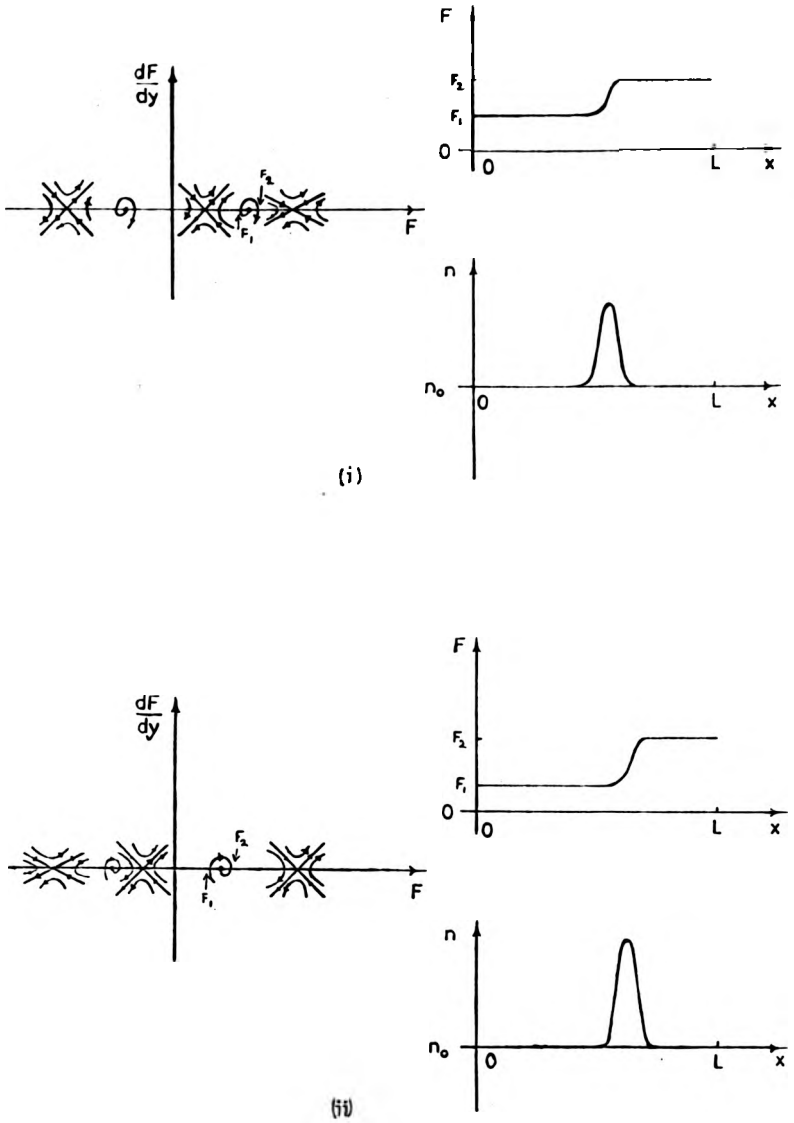

Fig. 3.7b. Two phase planes corresponding to inhomogeneous steady states. These phase planes are appropriate to both types of velocity field characteristic.
(i) $\bar{v} > 0$ (ii) $\bar{v} < 0$.
Some possible steady state electric fields and electron densities for slope boundary conditions imposed are also shown (See Section 3.5).

same section includes a discussion of the initial condition required for our numerical study.

3.5. Initial and boundary conditions for the model.

First we consider the initial condition. We assume that the circuit has been made for a considerably long time before the sample is illuminated and we note that in the dark the sample is totally insulating. Thus the system acts as an RC circuit in which the capacitor is initially fully charged and is suddenly made to conduct at $t = 0$. This gives the initial condition $F(x,0) = V_0/L$.

However the correct form of the boundary conditions is rather uncertain. Barker and Hearn (1969) have given the steady state phase plane for the case when the current is positive and five singular points exist, and we reproduce this from their paper as Fig. 3.8. In addition to the structure in the vicinity of the singularities their phase plane shows trajectories which originate in the physical region for which $n \geq 0$ and enter the non-physical region for which $n < 0$. All trajectories in the phase plane represent steady state solutions, mathematically allowed, for appropriate boundary conditions but physics demands that we select boundary conditions that rule out trajectories for which $n < 0$. In principle the way to do this is clear. We must extend our system of equations to describe not only the bulk semiconductor, but also the entire circuit. In the simulation of Gunn domain phenomena this is sometimes done by assuming the semiconductor to have heavily doped contact regions. The high electron density in these regions forces the drift velocity there to be so low that the contacts behave ohmically for all current densities likely to occur in the bulk i.e. in the contact regions both v and F are small so that $v \propto F$. No space charge is expected to form in

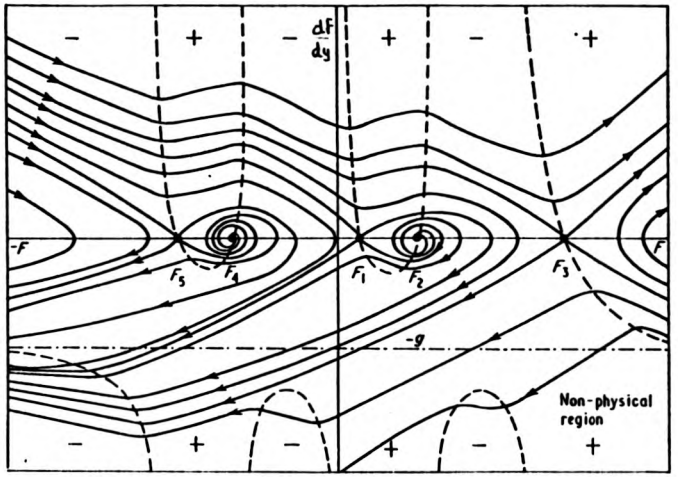

Fig. 3.8. A phase plane showing trajectories in the non-physical region i.e. $n < 0$. (from Barker and Hearn; 1969)

the heavily doped regions so the boundary conditions for the simulation are chosen such that the condition of space charge neutrality is satisfied at the interface between the semiconductor and external circuit.

Let us consider how we could perform such a circuit simulation for a semiconductor exhibiting oscillatory photoconductivity. Suppose that an experiment were conducted in which the junction between the metallic circuit and the bulk of the semiconductor was achieved by means of heavily doped contact regions, and that the entire semiconductor was illuminated. Furthermore suppose that we could take into account the resulting spatially non-uniform recombination and scattering rates by introducing a spatially non-uniform velocity field characteristic into our equations. Within the contact regions the drift velocity would remain small because of the high electron density, but with the oscillatory photoconductivity characteristic there are five possible fields which give rise to a low velocity. It is then uncertain which field would occur at the metallic conductor/contact interface. Since one of the objectives of our simulation is to determine whether uniform fields could be present in the bulk and if so which ones, the need to solve the same problem for the contacts comes as an unwelcome complication. To simulate the experiment, using our model, we would need some phenomenological equationsto describe electron transport between the metallic conductors and the photoconducting contact regions. No such equations appear to be available.

An alternative experimental arrangement would involve spot illumination of a long crystal, with the current to the illuminated region being supplied by thermally excited carriers. Modelling this situation would be an ambitious undertaking. It would be necessary to take into account not only the transport properties of the photoexcited carriers within the illuminated region but also the transport properties of the thermally excited carriers and the diffusion of photoexcited carriers out of the illuminated zone.

Since we are uncertain precisely how an experiment would be carried out and have no phenomenological equations describing electron transport at a metal photoconductor interface we feel that any attempt to construct a detailed circuit model would be premature. Instead we will try to account for the bulk behaviour of the semiconductor simply by assuming that at its boundaries with the metallic circuit the total current density, i, is equal to the electron current density -ej. Use of the current continuity equation (Equation 3.5) then shows that the field at the boundaries always remains at its initial value. This gives the boundary conditions,

$$F(L,t) = F(0,t) = V_0/L \tag{3.13}$$

which we will refer to as field boundary conditions. Analogous boundary conditions appear to have been used by Lebwohl and Price (1971) in a Monte Carlo simulation of Gunn domains.

In many cases field boundary conditions allow physically sensible solutions for F. In Fig. 3.7a we have identified some steady state fields from the phase plane. Similar fields are possible with both types of velocity field characteristic. The field tends towards a saddle in the bulk and a transition from the bulk field to the boundary field is achieved by means of accumulation and depletion layers in the surface regions. If the current is negative the field increases to above the boundary value which implies that the energy stored in the field has increased to above its initial value. This is fully consistent with the capacitor analogy. If the dielectric of a capacitor was able to supply energy we would expect some to flow into the field until a steady state was reached in which the dissipation in the circuit was equal to the rate of supply.

Since we are uncertain precisely how an experiment would be carried out and have no phenomenological equations describing electron transport at a metal photoconductor interface we feel that any attempt to construct a detailed circuit model would be premature. Instead we will try to account for the bulk behaviour of the semiconductor simply by assuming that at its boundaries with the metallic circuit the total current density, i, is equal to the electron current density -ej. Use of the current continuity equation (Equation 3.5) then shows that the field at the boundaries always remains at its initial value. This gives the boundary conditions,

$$F(L,t) = F(0,t) = V_0/L \tag{3.13}$$

which we will refer to as field boundary conditions. Analogous boundary conditions appear to have been used by Lebwohl and Price (1971) in a Monte Carlo simulation of Gunn domains.

In many cases field boundary conditions allow physically sensible solutions for F. In Fig. 3.7a we have identified some steady state fields from the phase plane. Similar fields are possible with both types of velocity field characteristic. The field tends towards a saddle in the bulk and a transition from the bulk field to the boundary field is achieved by means of accumulation and depletion layers in the surface regions. If the current is negative the field increases to above the boundary value which implies that the energy stored in the field has increased to above its initial value. This is fully consistent with the capacitor analogy. If the dielectric of a capacitor was able to supply energy we would expect some to flow into the field until a steady state was reached in which the dissipation in the circuit was equal to the rate of supply.

Although field boundary conditions are intuitively appealing they will fail to predict the behaviour of the field in some cases, for example, when a domain with a fully depleted layer attempts to exit. In this case if the total charge in any stationary layers present close to the boundaries is small a large displacement current could flow at the boundary itself. This is clearly inconsistent with our assumption that the total current at the boundaries is due to particles. However, this problem with the boundary conditions is likely to be irrelevant to any conclusions we may make about the nature of the instabilities in the bulk. To test these conditions we use the condition of space charge neutrality (as mentioned earlier in this section) as an alternative boundary condition.

Poisson's equation, which for our fully ionized donor model takes the form

$$\frac{\partial F}{\partial x} = e(n-n_o)$$

then shows that the boundary field satisfies the equation:

$$\frac{\partial F}{\partial x}_{x=0} = \frac{\partial F}{\partial x}\Big|_{x=L} = 0 \qquad (3.14)$$

We refer to these conditions as slope boundary conditions. Fig. 3.7b shows some steady state fields which are possible when slope boundary conditions are imposed.These fields are represented in the phase plane by trajectories which originate on and return to the dF/dx axis. Physically such trajectories correspond to space charge layers.

A useful feature of slope boundary conditions is that they exclude trajectories which cross into the non-physical region of the steady phase plane. From equations 3.9 and 3.10 and 3.4 we find that for n = 0

$$\frac{dp}{dF} = \frac{(c-\bar{v})}{D}$$

Therefore for all the phase planes considered in the previous section all trajectories crossing the line $p = \frac{-en_o}{\varepsilon\varepsilon_o}$ (which separates the physical and non-physical regions) have the same slope. For the domain type phase planes $(c = \bar{v})$ this slope is zero so it follows that no domain trajectory can enter the non-physical region. For all other phase planes, trajectories which enter the non-physical region are allowed. Suppose now that a trajectory crosses the line $p = -\frac{en_o}{\varepsilon\varepsilon_o}$ twice, first at a field F_1 then at a field F_2, $F_1 < F_2$. All trajectories crossing the same line at fields F in the range $F_1 < F < F_2$ must also cross at least twice and must do so at the same slope. This is impossible unless a singularity is located on the line $p = -\frac{en_o}{\varepsilon\varepsilon_o}$ at some field F^1, $F_1 < F^1 < F_2$ and there are no such singularities. Hence no trajectory can cross into and out of the non-physical region. If slope boundary conditions are imposed the allowed trajectories must have both their origin and destination in the physical region, therefore cannot pass through the non-physical region. This result can also be inferred by considering the possible trajectories in relation to the isoclines of zero slope on the phase plane shown in Fig. 3.8.

3.6. A numerical study of the model.

We now describe a numerical study of equations 3.6 and 3.7, subject to the initial and boundary conditions mentioned in the previous section. First we outline the essential features of the numerical method and its application to our problem. Following this we explain the various parameters involved in the numerical study and present the numerical

solutions themselves. Next we make some comments concerning the boundary conditions and then compare our numerical results with previous work by Barker and Hearn (1970). Finally we investigate some instabilities which could occur in an n^+n junction exhibiting the oscillatory photoconductivity velocity field characteristic.

To obtain our numerical solutions we employ an explicit finite difference scheme. The equations are solved in a dimensionless form using the system of units shown in Table 3.1. The scalesof all curves in Figures 3.10 to 3.14 are presented in these units; note that $x = 1$ represents the length of the sample. The numerical method is based on the use of a discrete mesh of space step Δx and time step Δt to convert the partial differential equation for the field into a partial difference equation. This equation is recursively applied to generate approximate solutions to the differential equation. We give the field equation in dimensionless form and explain the numerical method in detail in Appendix 3. The mesh size we use in the numerical study is restricted by the condition that the solution to the difference equation converges to the solution of the differential equation in the limit $\Delta x \to 0$, $\Delta t \to 0$. In Appendix 3 we show that this condition holds if,for all mesh points,mj,the mesh steps are restricted by the inequalities:

$$\Delta x \leq \frac{D}{2|V_{mj}|}$$

$$1 - \frac{2D\Delta t}{\Delta x^2} - \frac{\Delta t}{\tau'_{dmj}} \geq 0. \qquad (3.15)$$

The quantities τ'_{dmj} and v_{mj} are analogous to a differential dielectric relation time and a drift velocity respectively. They are precisely defined in Appendix 3. Their value at some time depends on the solution

Quantity	Symbol	Unit
Electric field	F	$20 Vm^{-1}$
Distance	x	$10^{-3} m$
Current	i	4.268 nA
Time	t	0.75 μS

Table 3.1: The system of units used to present the results of the computational study of oscillatory photoconductivity (Figs. 3.10 to 3.14).

of the field equation at that time and our program guarantees stability by testing the mesh size as the solution progresses. In calculating our solutions we take a space step equal to be $L \times 10^{-2}$ and choose Δt according to inequalities 3.15. Then the time interval over which we can obtain a solution is set by the available computer time.

It is of the utmost importance to include in the numerical solution some form of perturbation which generates both positive and negative space charge otherwise the system will not recognise unstable situations. For example Gunn domains would not occur in GaAs biased into the region of negative differential velocity if no space charge ever occurred in the semiconductor to perturb the uniform field. Of course, space-charge generation occurs naturally in a variety of ways in a real sample but in a numerical simulation we need to provide this artificially. Since we are interested in the evolution of propagating instabilities we try to initiate the field perturbation as far as possible away from the contact towards which such an instability would move. The simplest artefact is to employ a doping notch in the appropriate region(Fig.3.9). This simulates the effect of fluctuations in donor density which are always present in real samples. Within the notch the donor density falls to 90% of its otherwise uniform value over a distance equal to 0.1 of the sample length. We neglect any effect of the notch on the velocity field characteristic. (In principle the notch would affect v(F) via the donor density dependence of τ & λ)

Since we have no experimental data concerning instabilities we have felt free to solve the field equations with parameters chosen for numerical convenience. In particular we chose the dielectric constant ε to be 18.1 compared with the accepted value for InSb of 17.64 (Rode, 1975) and the relaxation time for the model velocity field characteristic was selected to give a zero field mobility of 10 $m^2 V^{-1} s^{-1}$. An exhaustive

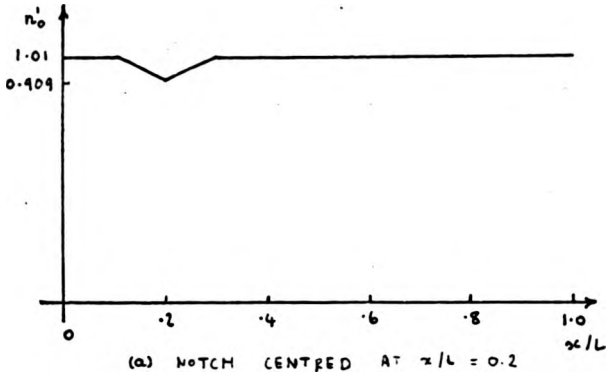

(a) NOTCH CENTRED AT $x/L = 0.2$

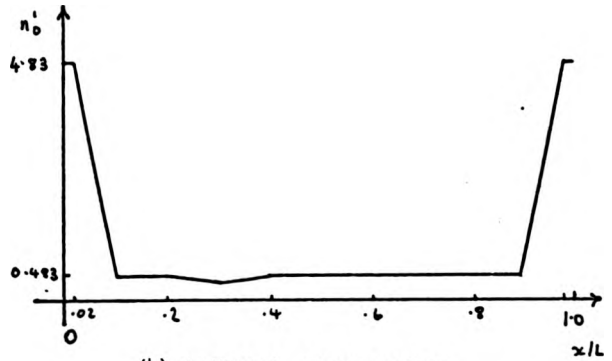

(b) CONTACTS WITH NOTCH

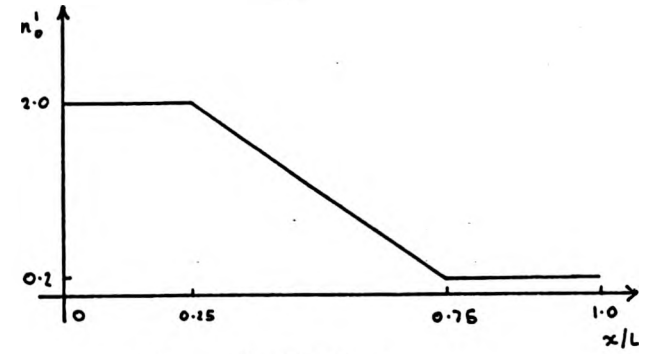

(c) n^+n JUNCTION

Fig. 3.9. The doping profiles used in the computations discussed in Section 3.6. Each curve shows the donor density as a function of distance.

series of computer runs then enabled us to identify those parameters most relevant to the behaviour of the system. The actual parameters used in the solutions of equations 3.6 and 3.7 are shown in Table 3.2. The diffusion coefficient D in equation 3.6 was arbitrarily set at 6×10^{-3} m^2 s^{-1} which corresponds to a temperature of $\sim 7^{o}K$ if the zero field mobility of the characteristics is substituted into the Einstein relation. The quantity N which is listed in the table is the unit in which the donor densities shown in Fig. 3.9 are measured.

We used a piecewise linear form of the 1D model velocity which we derived by approximating v(F) by 100 straight line segments for fields in the range $0 \leq F \leq 500$ m^{-1}, and by a single straight line for fields greater than 500 m^{-1}. This form of v(F) was chosen to allow economical use of computer time.

Our program was tested by using it to solve a linear partial differential equation, for which an analytic solution was known. In addition we let the mesh steps exceed the limits given by the inequalities 3.15 and found that the solutions took the form of rapidly growing spatial and temporal oscillations.

We have computed the time evolution of the field for both positive and negative area velocity field characteristics. The values of initial field, F(x,0), used in the computations are marked on Fig. 3.1 and are listed in Table 3.3, together with the sign of the initial velocity and τ_d. Field boundary conditions were used. Although these conditions permit trajectories to enter the non-physical region of the phase plane this does not occur for any of the solutions obtained in 3.10 to 3.13. In Fig. 3.10 we show the steady states obtained if τ_d is initially positive, and if v(F) is of a positive area (fields 1,6). The centre of the notch is at $x = 0.2$, and the resistance is 1.722×10^5 Ω which values corresponds to a unique intersection of the load line with v(F). With the exception of a

Quantity	Symbol	Value	Unit
Donor density Scaling factor	N	4.9×10^{14} (a,b) 6×10^{16} (c)	m^{-3}
Dielectric constant	ε	18.1	-
Diffusion coefficient	D	6×10^{-3}	$m^2\ s^{-1}$
Sample length	L	10^{-3}	m
Sample Area	S	10^{-6}	m^2
Resistance	R	1.17×10^5 and 2.345×10^7 (a) 1.172×10^3 (b) 9.259×10^5 (c)	Ω

Table 3.2: The parameters used in the computational study of oscillatory photoconductivity.
The donor density scaling factor N is defined such that the donor density is $N\ n_o'(x)$ where $n_o'(x)$ is one of the doping profiles shown in Fig. 3.9. (See also Appendix 3). The letters a, b or c associated with the values of N and R mean that these values were used in computations appropriate to the doping profiles shown in Figs. 3.9a, b and c respectively.

	Field Number	F_o Vm^{-1}	Sign of $v(F_o)$	Sign of $\tau_d(F_o)$	Results shown in Figure
Positive area characteristic (Fig. 3.1a)	1	20	+	+	3.10
	2	65	+	+	3.11 & 3.13
	3	100	+	-	3.11 & 3.13
	4	160	-	-	3.11 & 3.13
	5	180	-	-	3.11 & 3.13
	6	220	-	-	3.10
	7	300	+	+	3.10
Negative area characteristic (Fig. 3.1b)	1'	20	+	+	Not shown
	2'	36.5	+	-	3.12
	3'	50	+	-	3.12
	4'	100	-	-	3.12
	5'	140	-	-	3.12
	6'	300	-	+	Not shown
	7'	400	+	+	Not shown

Table 3.3: The initial fields used in the computations leading to Figs. 3.10 to 3.13. The 'field numbers' refer to the fields marked on the velocity field characteristics shown in Fig. 3.1.

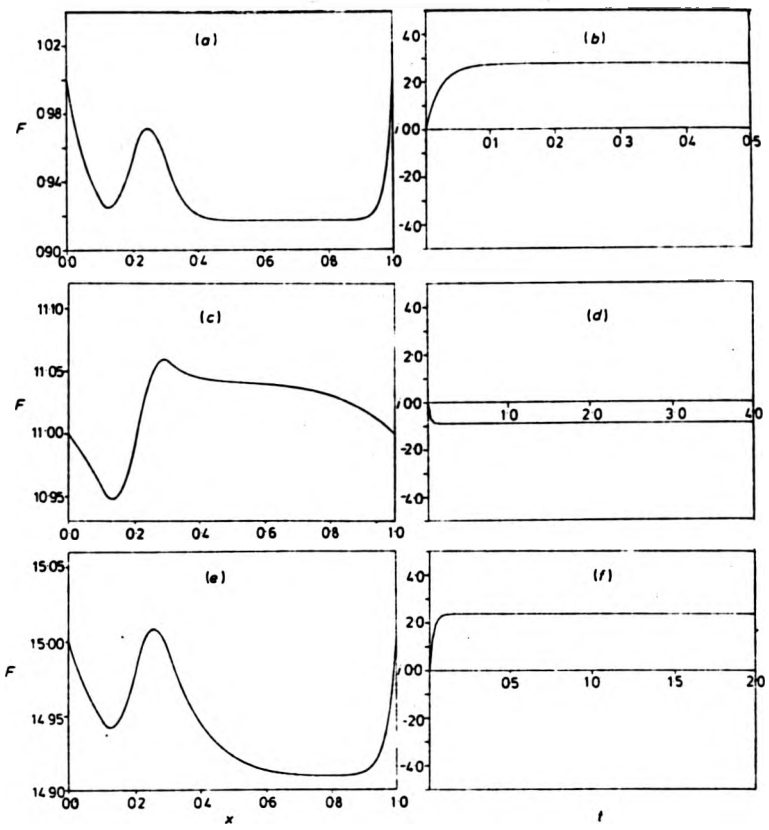

Fig. 3.10. Final electric fields and the time evolution of the current for the positive area characteristic (Fig. 3.1a) and initial field, F_o, such that $\tau_d(F_o)$ is positive. Each pair of curves show F(x) and i(t) for a particular value of F_o as labelled on Fig. 3.1a and given in Table 3.3. The units of F, x, i and t are given in Table 3.1.

(a), (b) field 1, t = 0.5

(c), (d) field 6, t = 4.0

(e), (f) field 7, t = 2.0

distortion at the notch the field as a function of distance conforms to the predictions of the phase plane. The current as a function of time is similar to the form associated with an RC circuit and we note that a steady negative current occurs if the initial drift velocity is negative. The numerical solutions corresponding to the positive τ_d region of the negative area chracteristic (fields 1',6',7') are similar to those shown in Fig. 3.10.

If the initial field is such that τ_d is initially negative the distortion at the notch is unstable. In Fig. 3.11 we illustrate the time development of the current together with a 'snapshot' of the developing instability at a specific time, for increasing values of initial field in the negative τ_d region, and for the positive area characteristic. If the initial field is just in the negative τ_d region (field 2) the instability grows into a high field domain which moves across the sample and is absorbed in the accumulation layer at the right hand boundary. Repetition of this process causes positive current oscillations. If the initial field is higher (field 3) the domain grows more rapidly and field boundary conditions fail to predict cycling because there is insufficient charge in the surface layers to allow the domain to be absorbed.

To study the time evolution from an initial field such that the initial velocity is negative we find it convenient to place the centre of the notch at x = 0.8. If the initial field lies just inside the negative velocity, negative τ_d region, $|\tau_d|$ is small and the instability takes the form of a low field domain which grows rapidly. (field 3). From Fig. 3.11 we see that this growth is accompanied by a sign change in the current. The developing domain initially moves in the negative direction. As it grows the outside field rises and eventually the current changes sign. At the same time the domain changes direction and moves back towards the notch. As for field 3 the boundary charge layers are insufficient to enable proper cycling. At a higher initial field (field 5) $|\tau_d|$ is larger and so smaller low field domains are nucleated which cycle in a manner akin to that of the

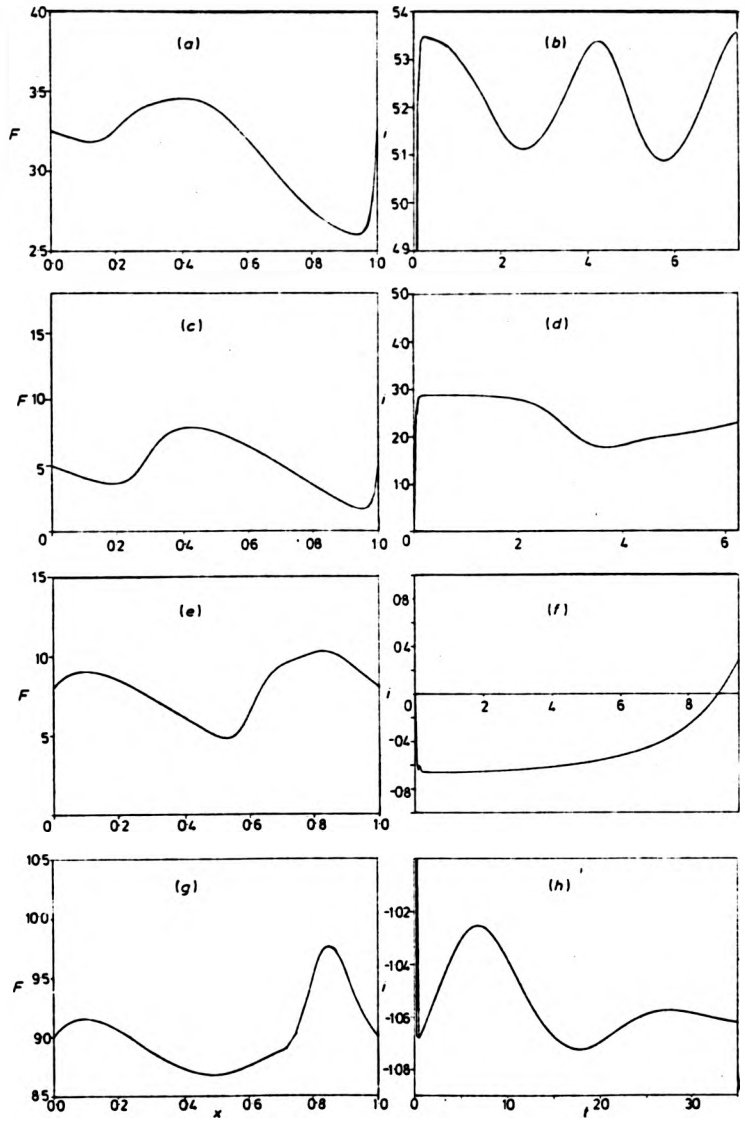

Fig. 3.11. Electric fields and the time evolution of the current for the positive area characteristic and initial fields, F_o, such that $\tau_d(F_o)$ is negative. Here domains occur and F(x) is a 'snapshot' of a domain at the time listed below.

(a), (b) field 2, domain at t = 2.0

(c), (d) field 3, domain at t = 3.75

(e), (f) field 4, domain at t = 9.0

(g), (h) field 5, domain at t = 7.0

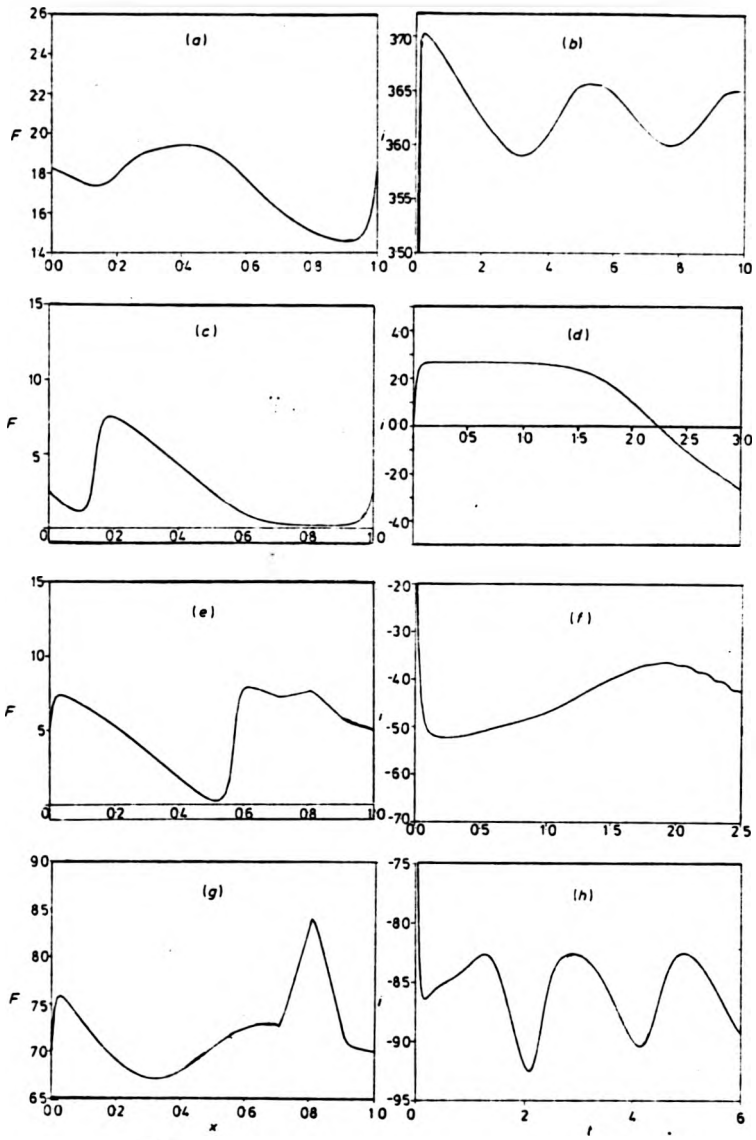

Fig. 3.12. Electric fields and the time evolution of the current for the negative area characteristic (Fig. 3.1b), and initial field, F_0, such that $\tau_d(F_0)$ is negative. Here domains occur and F(x) is a 'snapshot' of a domain at the time listed below:

(a), (b) field 2', domain at t = 3.0.

(c), (d) field 3', domain at t= 2.5.

(e), (f) field 4', domain at t = 1.8

(g), (h) field 5', domain at t = 5.25

small high field domains, causing negative current oscillations.

The numerical solutions obtained with the negative area characteristic and field points 2' to 5' are similar to those shown in Fig. 3.11. However in this case it is the high field domain, nucleated from an initially positive velocity, negative τ_d, state which reverses direction. This observation is fully consistent with the phase plane analysis which shows that only high field domains are possible at positive current with a negative area characteristic and only low field domains are possible at negative current with a positive characteristic. Example solutions are given in Fig. 312

The current as a function of time shown in Fig. 3.12f exhibits small parasitic oscillations at times greater than 1.8 time units. Similar oscillations have been observed during several runs of the program and, when they occur, appear to be associated with the presence of an accumulation layer in the sample. Within such a layer the field changes rapidly with distance and it is likely that these oscillations are the result of a small numerical error, caused by use of too large a space step.

We have found from our computational study that the field can be stabilized by increasing the resistance to 2.345×10^7 Ω (which corresponds to 3 intersection points of the load line, and v(F); if v(F) is of positive area). Steady states obtained using initial fields in the negative τ_d region and the positive area characteristic are shown in Fig. 3.13 (fields 2 to 5). A marked resemblance to the steady states obtained from the positive τ_d region is immediately apparent. The steady states obtained using initial fields 2' to 5' and the negative area characteristic are similar.

We tested the sensitivity of our solutions to the boundary conditions by repeating the calculations just described using slope boundary conditions. The types of domain nucleated in the bulk remained unaltered and their nucleation was suppressed by the same values of resistance. However, as explained in Section 3.5, no charge layers occur in the vicinity of the

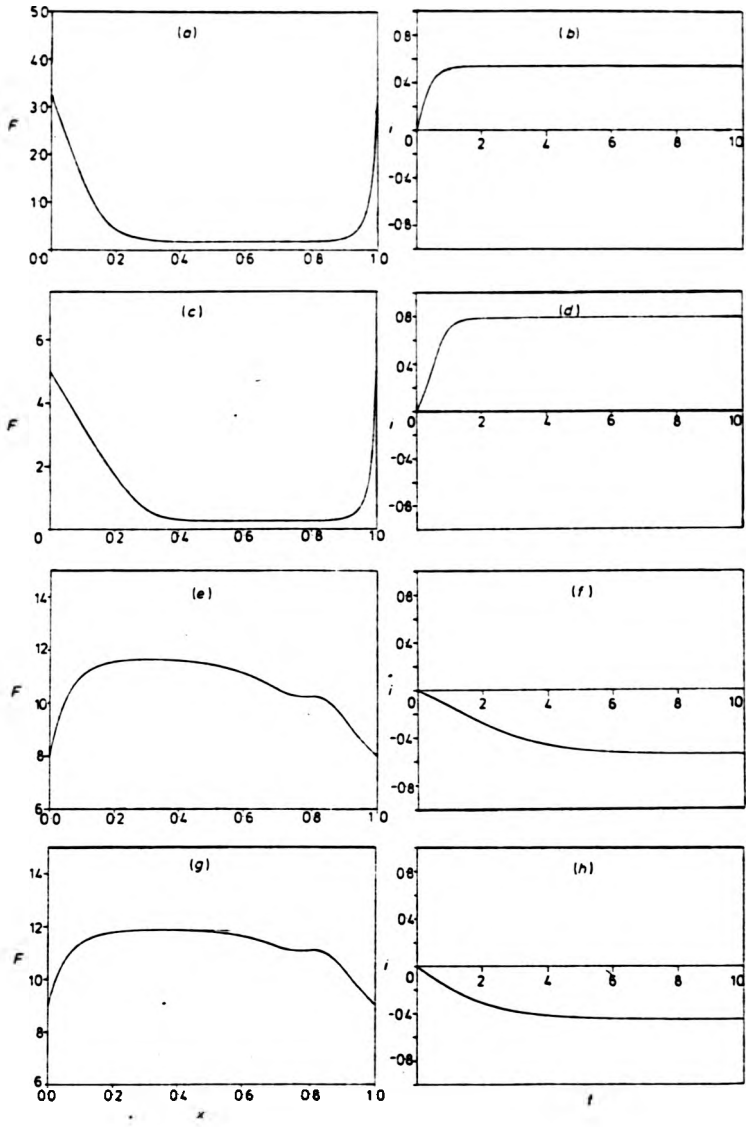

Fig 3.13. An illustration of how a high resistance stabilizes the electric field. The curves show the final electric field, F(x), and the time evolution of the current i(t), for the positive area characteristic and initial fields, F_0, such that $\tau_d(F_0)$ is negative

(a), (b) field 2, t = 10.0

(c), (d) field 3, t = 10.0

(e), (f) field 4, t = 10.0

(g), (h) field 5, t = 10.0

boundaries if slope boundary conditions are imposed. As a result domains generated with these boundary conditions imposed developed into stationary layers on reaching the boundary (instead of cycling).

An interesting feature associated with use of field boundary conditions is that domains can be nucleated even in the absence of a notch. This is because the change layers at the boundary can become unstable if τ_d is negative there. A similar effect seems to occur in the Monte Carlo study of Gunn domains reported by Lebwohl and Price (1971).

It is of interest to compare the results of the present calculations with those of Barker and Hearn (1970) who considered a sample with heavily doped contacts and placed in a constant voltage circuit. The field equation was solved with slope boundary conditions imposed and v(F) was taken to be of positive area. With an initial field in the negative velocity, positive τ_d region a positive current steady state was obtained whereas the present work predicts a negative current steady state. With an initial field in the negative velocity, negative τ_d region, they predicted positive current oscillations in contrast to the domains of the present work (which would be expected to cause negative or alternating current oscillations). It is thought that the difference between their predictions and our study is due to the heavily doped contacts. To test this idea we have computed the time evolution of the field, with the sample taken to have contacts as shown in Fig. 3.9b. A positive current state similar to that predicted by Barker and Hearn was found to develop from an initial field in the negative velocity, positive τ_d, region of the positive area characteristic. The negative area characteristic gave a negative current steady state. The current reversal observed with a positive area characteristic appears to be caused by a high initial diffusion current at the left hand contact which causes the field to decrease rapidly until τ_d becomes negative; whereupon an accumulation layer peels off the contact and moves across the sample. Finally the system settles into a positive current steady state.

Our numerical studies show that the same mechanism can generate moving layers in an n^+n junction, even if there is no e.m.f. in the circuit. In particular we consider the junction shown in Fig.3.9c. Field boundary conditions are used. The velocity field characteristic is assumed to be spatially uniform. Although this assumption is questionable because of the non-uniform donor ionization in the junction, we feel that the results of the numerical studies are of sufficient interest to warrant description here. The sequence of events which is predicted to occur is illustrated in Fig. 3.14. Essentially what happens is that an electric field is generated as a result of diffusion of photoexcited electrons across the junction. If the velocity field characteristic was linear the magnitude of this field would increase until the junction field settled into a stable steady state. Because the oscillatory photoconductivity velocity field characteristic has a region of negative differential velocity the junction field becomes unstable when its magnitude exceeds F_T. (0.05 time units in Fig. 3.14). The field continues to rise and at some time its magnitude exceeds F_c. Then the instability is enhanced because the drift and diffusion currents are in the same direction (0.1 time units). Eventually two moving layers are indicated (0.15 time units) and the junction field stabilize when they reach the boundaries (0.4 time units). If slope boundary conditions are imposed a similar sequence of events is predicted to occur.

3.7. Conclusion.

Our numerical study of the equations which we believe to provide information concerning the time dependent, non-uniform electric field in a semiconductor exhibiting oscillatory photoconductivity has shown that steady positive and negative currents, stable with respect to fluctuations in the bulk donor density may be expected, when the optical excitation energy is such that carriers are injected just below an integral multiple of the L.O. phonon threshold energy. In addition domain instabilities can

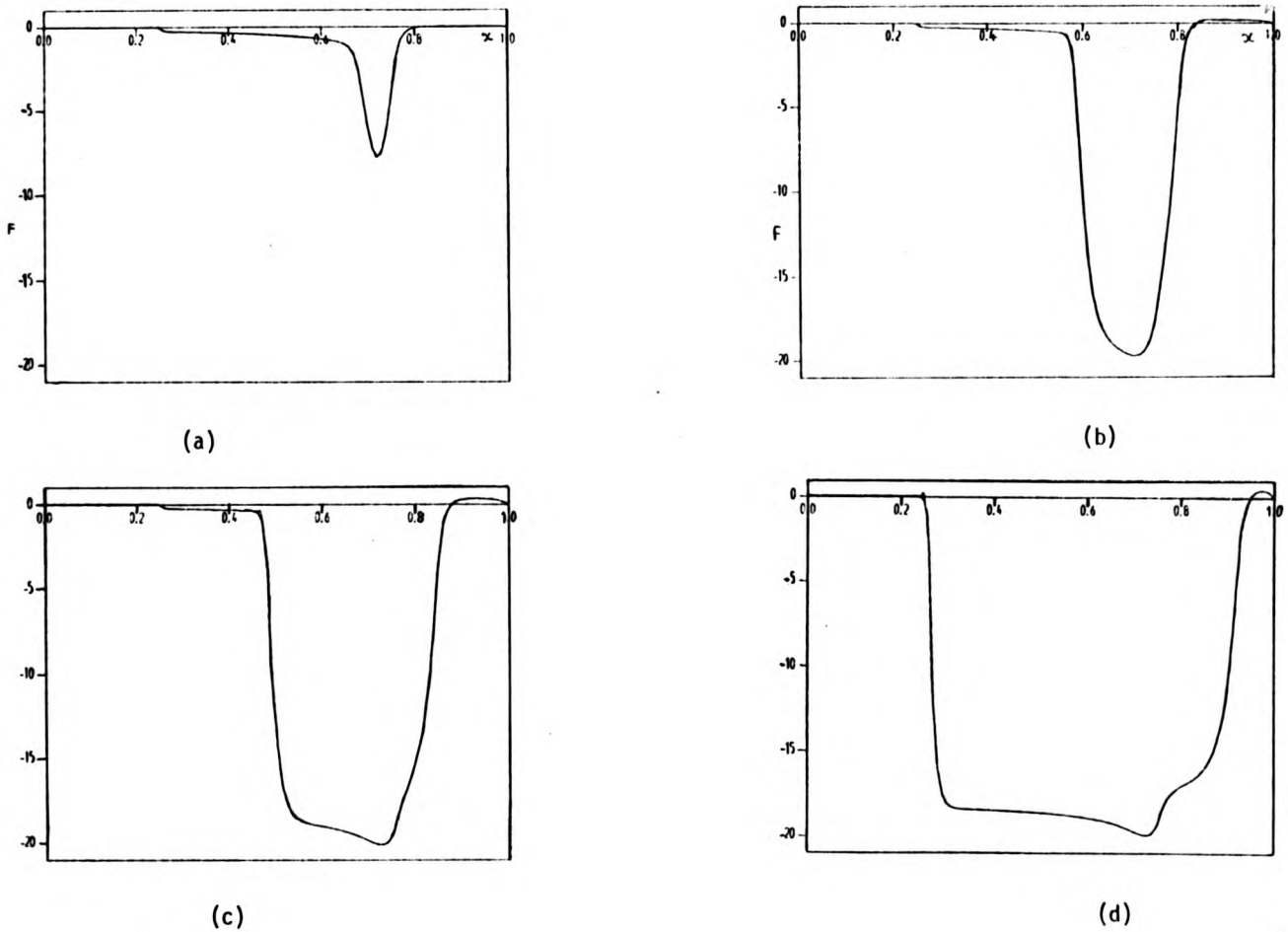

Figs. 3.14a to d. A sequence of figures showing the evolution of an instability associated with an n^+n junction. The initial field is zero. Each figure is a 'snapshot' of F(x) at time s as follows: (a) t = 0.05; (b) t = 0.1. (c) t = 0.15; (d) t = 0.25.

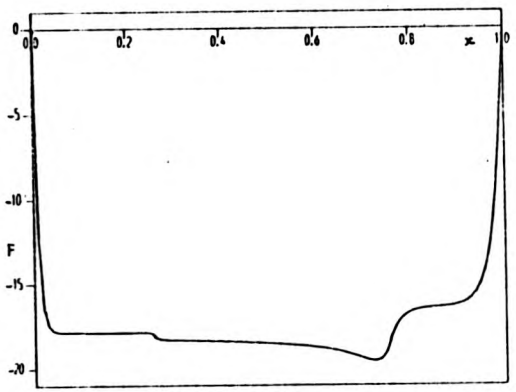

(e)

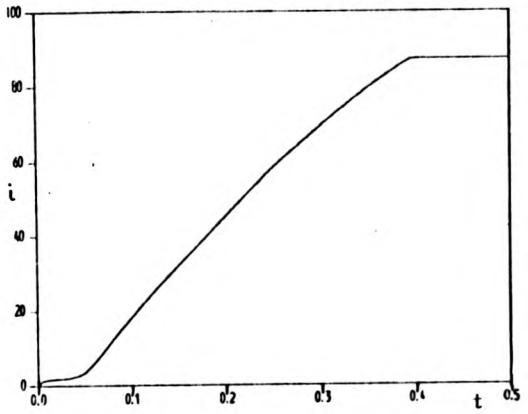

(f)

Figs. 3.14 e and f. The stable field confiouration and time evolution of the current associated with the junction instability shown in Figs. 3.14a to d.

(e) F(x) at t = 0.4

(f) i(t).

form which may lead to positive, negative or alternating current oscillations. These conclusions are largely consistent with a simple phase plane analysis of the equations. None of the features we predict have yet been observed experimentally so we end our study by attempting to scale our model results to real systems.

Experiments are likely to be carried out with donor densities $\sim 10^{20}\ m^{-3}$. Also from the Monte Carlo characteristic due to Barker and Hearn (1969) we see that the drift velocity is likely to be ~ 100 times the model direct velocity. It is impractical to obtain numerical solutions for such high velocities and donor densities because a small mesh is required to satisfy inequalities 3.15, and this causes the program to consume excessive computer time. However it is possible to use the program to deduce some of the conditions under which instabilities would form, in a typical experiment. Specifically we can estimate values for the circuit resistance which would allow propagating instabilities to form and values of the resistance with which the nucleation of such instabilities could be suppressed. This is done with the aid of an empirical rule which we deduce from the results of a set of computations similar to those leading to Figs. 3.10 to 3.13. The donor density is taken to have various values in the range $4 \times 10^{14}\ n_o' \leq n_o \leq 2 \times 10^{17}\ n_o'$. For all donor densities in this range, and for both types of velocity field characteristic we find empircally that propagating instabilities are nucleated if the resistance R is chosen according to the equation:

$$R^{-1} = 12.57\ \frac{eSn_o}{L}\ \left|\frac{dv}{dF}\right|_{max}$$

where $\left|\frac{dv}{dF}\right|_{max}$ is the maximum absolute value of the 1D model negative differential velocity. (With this value of R equation 3.8 has only one solution). We also find empircally that the nucleation of propagating instabilities is suppressed if R satisfies the inequality

$$R^{-1} \leq 0.557 \frac{eSn_o}{L} \quad \frac{v(F_{min})}{F_{min}+F_r}$$

F_{min} is the positive field at which the 1D model velocity has its minimum. (Equation 3.8 has multiple solutions if R obeys this inequality and V_o is sufficiently small).

If we assume that the empirical rule holds for velocities a hundred-fold higher than the 1D model velocity and for donor densities $\sim 10^{20}$ m^{-3} we can predict the conditions under which instabilities could or could not occur, in a typical experiment. Supposing that the donors are kept fully ionized to a depth of 0.1 mm in a sample 1 mm long, and that an area of 1^2 mm is exposed to the exciting radiation, we find that the resistances corresponding to the formation of instabilities and to their suppression are $\sim 0.05\Omega$ and $\sim 10\Omega$ respectively.

Next we estimate the incident power required to keep the donors fully ionized. If we assume that this power is such that ionization occurs much more rapidly than recombination we can do this simply by calculating the photon flux required to replenish the electrons leaving the band at a rate $n_o \tau^{-1}$. Supposing an absorption coefficient 10^5 m^{-1} and a donor density of 10^{20} m^{-3} we find that at an injection energy of 5 $\hbar\omega_o$ ($\equiv$ 0.12 eV for InSb)the power incident on a sample of area 1 mm^2 required to maintain full donor ionization to a depth of 0.1 mm is $\sim$ 100W. In fact this may be an underestimate because the impurity absorption coefficient is likely to be lower than 10^5 m^{-1} (Johnson and Fan, 1965). Fixed frequency carbon dioxide lasers have been made to operate at 10.6 μm ($\equiv$ 0.118 eV) at powers of a few hundred watts, so full donor ionization may be attainable in practice.

We should stress, however, that the model velocity field characteristics are independent of the light intensity so that negative currents are not likely to be restricted to the fully ionized donor regime which was chosen for theoretical convenience.

CHAPTER 4

TRAP MODIFIED GUNN DOMAINS IN GALLIUM ARSENIDE

4.1. Introduction

Slow moving ($v \lesssim 10^3$ m s^{-1}), high field domains have been observed in high resistivity Gallium Arsenide (Northrop et. al., 1964; Ridley et.al., 1972) and gold doped Germanium (Ridley and Pratt, 1965), usually under conditions of photoexcitation. Similar instabilities occur in Cadmium Sulphide, but contain sub-domains which have an even higher field than the primary domain, and which move in the opposite direction (Böer and Ward, 1967; Gilbert and Hoffmann 1975). Most authors (Ridley and Wisbey, 1967; Bonch-Bruevich, Zvyagin and Mironov, 1972) attribute the properties of such types of domain to field dependent recombination. However, the results of a numerical simulation due to Kroemer (1972) have shown that domains of reduced velocity could occur in GaAs even if the recombination is field independent.

Trapping effects can also be of significance for domain propagation in low resistivity GaAs. These effects have been studied by Teszner and Boccon-Gibod (1973) who have found that the motion of the fast domains observed in the Gunn effect is modified, leading to damping of the usual high frequency oscillations.

Kroemer's simulation is the first and probably the only work to date in which the effect of trapping is included in a calculation of the space-time dependent electric field in GaAs using an otherwise standard Gunn-effect model. (Although an essentially similar study had previously been carried out by Barker (1969), this was concerned with oscillatory photo-conductivity). In addition to assuming field independent recombination, Kroemer used a linear rate equation for the population of trapped electrons. In our study, which is described in section 4.5, we perform a similar calculation but we include field dependent recombination and a non-linear

equation for the trapping. An unusual feature of our work is that some of our numerical solutions have been obtained in the form of a computer generated film, which vividly illustrates the nucleation and propagation of trap-modified Gunn domains. The details of the physical model we have employed are explained in Section 4.3 and its small signal properties discussed in Section 4.4. We start in Section 4.2 with a review of previous experimental and theoretical work on slow domains in GaAs and the effects of trapping on Gunn domain propagation.

4.2. Slow Domains and Related Phenomena in GaAs.

Although slow domains in high resistivity ($\gtrsim 10^3\ \Omega\ cm^{-1}$) GaAs have been studied less intensively than Gunn domains, an extensive body of literature concerning their properties exists. Much of the experimental work carried out prior to 1970 has been summarized by Sacks and Milnes (1970). Some more recent work has been described by Ridley, Crisp and Shishiyanu (1972) and also by Leach and Ridley (1978). Slow domains are considerably broader than Gunn domains and lower threshold fields are required for their nucleation (Typical values of the domain velocity, domain width and threshold field for slow and Gunn domains are contrasted in Table 4.1). The outside field during propagation of a mature slow domain can be as low as 10 Vm^{-1} (Leach and Ridley, 1978) - a field remarkably small compared with the threshold field for the Gunn effect. Slow domains usually occur only in the presence of photoexcitation and their velocity is an increasing function of the excitation intensity (Sacks and Milnes, 1970). However Ridley and co-workers (1972) mention that such domains have been observed in samples exposed at most to room temperature thermal radiation. There is an incubation time τ_i associated with the nucleation of slow domains - if the field applied to a sample suddenly exceeds threshold slow domains commence to propagate only after

Property	Slow domain	Gunn domain
Domain velocity	10^{-2}-10^{-3} ms^{-1}	10^{5}-2×10^{5} ms^{-1}
Domain width	3.2×10^{-4}m	10^{-5}m
Threshold field	2×10^{4}-10^{5} Vm^{-1}	$\sim 3\times10^{5}$ Vm^{-1}

Table 4.1: Some typical properties of slow and Gunn domains. Slow domain properties after Leach and Ridley (1978). Gunn domain properties after Butcher (1967).

a time τ_1. This is illustrated schematically in Fig. 4.1a which shows the current, during nucleation of a slow domain, as a function of time.

With the exception of the work by Kroemer, as mentioned in section 4.1, most theoretical studies of slow domains have involved the assumption that, the coupled partial differential equations, for the electric field and the density of trapped electrons, have solutions which are functions of the single variable x-ct. This assumption enables the field and trapped electron density to be predicted from a coupled pair of ordinary differential equations, which are solved either with the aid of a suitable approximation or numerically.

The first work of this kind is due to Ridley and Wisbey (1967) who applied their theory to domains in gold doped germanium. The field dependence of the recombination rate was taken from experimental data and a linear rate equation was used to describe the trapping.(ie the field induced change in the density of trapped electrons was assumed to be small, allowing the recombination rate to be calculated using the density of unoccupied traps at zerofield). Solutions to the equations were obtained in several approximations but the theory predicted domain velocities an order of magnitude higher than those observed. Bonch-Bruevich, Zvyagin and Mironov (1972) have constructed a similar theory but used a non-linear equation for the trapping. They too, predicted domain velocities one or two orders of magnitude higher than those found experimentally in Au doped Ge.

Sacks and Milnes (1970) have considered a model in which the field dependence of the recombination coefficient arises from capture at negatively charged impurities. A potential barrier is associated with such impurities and an electron can be captured either by surmounting the barrier or by tunnelling through it. In either case capture is more probable at high fields. Sacks and Milnes have solved their equations numerically and have been able to calculate domain velocities and widths, within a factor of 2 of some of those observed in high resistivity GaAs.

a time τ_1. This is illustrated schematically in Fig. 4.1a which shows the current, during nucleation of a slow domain, as a function of time.

With the exception of the work by Kroemer, as mentioned in section 4.1, most theoretical studies of slow domains have involved the assumption that, the coupled partial differential equations, for the electric field and the density of trapped electrons, have solutions which are functions of the single variable x-ct. This assumption enables the field and trapped electron density to be predicted from a coupled pair of ordinary differential equations, which are solved either with the aid of a suitable approximation or numerically.

The first work of this kind is due to Ridley and Wisbey (1967) who applied their theory to domains in gold doped germanium. The field dependence of the recombination rate was taken from experimental data and a linear rate equation was used to describe the trapping.(ie the field induced change in the density of trapped electrons was assumed to be small, allowing the recombination rate to be calculated using the density of unoccupied traps at zerofield). Solutions to the equations were obtained in several approximations but the theory predicted domain velocities an order of magnitude higher than those observed. Bonch-Bruevich, Zvyagin and Mironov (1972) have constructed a similar theory but used a non-linear equation for the trapping. They too, predicted domain velocities one or two orders of magnitude higher than those found experimentally in Au doped Ge.

Sacks and Milnes (1970) have considered a model in which the field dependence of the recombination coefficient arises from capture at negatively charged impurities. A potential barrier is associated with such impurities and an electron can be captured either by surmounting the barrier or by tunnelling through it. In either case capture is more probable at high fields. Sacks and Milnes have solved their equations numerically and have been able to calculate domain velocities and widths, within a factor of 2 of some of those observed in high resistivity GaAs.

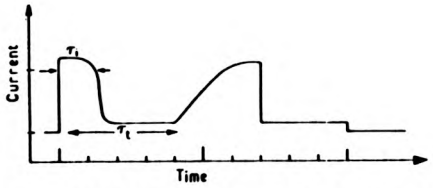

Figure 1. Schematic diagram of current against time during incubation and transit of a slow domain.

(a) The current associated with a slow domain (from Ridley et al, 1972)

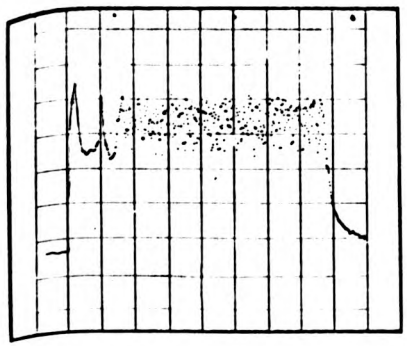

FIG. 3. Evolution towards incoherence in a β sample. Current vs time: horizontal scale = 5 nsec/div; β sample: $R = 2000\ \Omega$, vertical scale = 20 mA/div.

(b) The evolution of current oscillations into noise (from Teszner and Boccon-Gibod, 1973)

Fig. 4.1. The current i(t) associated with slow and damped domains in GaAs. Authors captions have been retained for clarity

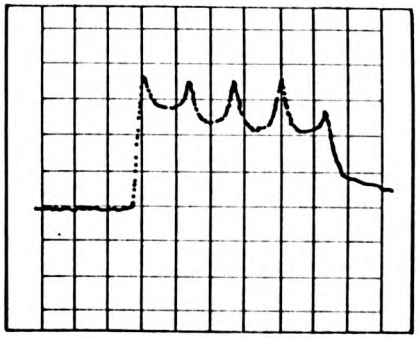

(a)

(b)

FIG. 4. Coherent Gunn oscillations in β samples: current vs time. (a) The valley current remains constant during each transit. β sample: $R = 1800\ \Omega$, horizontal scale = 4 nsec/div, vertical scale = 30 mA/div. (b) The valley current decreases continuously during each transit. β sample: $R = 1500\ \Omega$, horizontal scale = 5 nsec/div, vertical scale = 20 mA/div.

(c),(d) The current i(t) associated with damped domains (from Teszner and Boccon-Gibod,1973)

In 1972 Ridley, Crisp and Shishiyanu proposed that the field dependence of the recombination coefficient in high resistivity GaAs is due to enhanced capture of electrons from the upper valleys. This idea was adopted by Harutunian and Varosian (1977), who also included some field dependence of the coefficient for capture from the lower valley. They obtained approximate solutions of the coupled equations for the electric field and density of trapped electrons, but did not compare their theory with experiment.

Very recently (1978) Leach and Ridley have presented evidence which indicates that the occurence of slow domains in oxygen doped GaAs is associated with capture at an impurity having a potential barrier. However, the measured activation energy of 0.077 eV requires the impurity to have a negative charge, with the rather high magnitude of 1Oe, if the barrier is to be explained in terms of a Coulomb potential.

The influence of trapping on Gunn domains in low resistivity GaAs has been studied by Teszner and Boccon-Gibod (1973). They placed samples of Cr doped GaAs, consisting of epitaxial layers 11 μm thick, in a resistive circuit and observed the current as a function of time during application of a constant voltage pulse. Some of their results are reproduced in Fig. 4.1. When the resistance was 2 kΩ the oscillations in current turned into noise after the passage of one or two domains. With the lower resistances of 1.8 kΩ and 1.5 kΩ the oscillations were damped. (Figs. 4.1c,d). In each of the three curves in Figs. 4.1b to d the period of the first cycle is noticeably longer than that of the others, showing that the first domain has a greater transit time than the subsequent ones.

Our summary of previous work on trapping effects in the propagation of domain instabilities is now complete. In the next section we explain the model we use to study these effects.

4.3. A model for trap modified Gunn domains.

In essence, the model we use to study trap modified Gunn domains is similar to the model we have used to study instabilities in oscillatory photoconductivity (section 3.3). We consider a semiconductor connected in a resistive circuit as shown in Fig. 4.2a. Electrons are excited into a conduction band from impurity levels. The spatial variation of all quantities is assumed to be one dimensional. We adopt a sign convention in which the electric field F is measured in the negative direction and all other quantities are measured in the positive direction. Then the electric field and density of positive background changes n^+ are related by equations 3.6 and 3.7 of section 3.3:

$$\frac{\partial F}{\partial t} - D\frac{\partial^2 F}{\partial x^2} + v(F)\frac{\partial F}{\partial x} + \frac{e}{\varepsilon\varepsilon_o}\{n^+(x,t)v(F) - D\frac{\partial}{\partial x}n^+(x,t)\} = \frac{-i(t)}{\varepsilon\varepsilon_o} \qquad (4.1)$$

$$i = \frac{1}{RS}\left(\int_o^L F dx - V_o\right) \qquad (4.2)$$

To determine n^+ we suppose that the electrons in the conduction band can communicate with two sets of impurities. (Fig.4.2b). One is a set of shallow donors whose ionization density $N_D(x)$ is time independent. The other is a set of deeper compensating acceptors.The total density of acceptors (both ionized and neutral) is $N_A(x)$ and the neutral acceptor density $p(x,t)$ obeys the following rate equation:

$$\frac{\partial p}{\partial t} = A(N_A - p) - B(F)np \qquad (4.3)$$

where A is a constant ionization rate coefficient, n the electron density and B a field dependent capture coefficient. It has been assumed that B is a local and quasi-static function of electric field. The density of positive background charges is simply related to N_D, N_A and p:

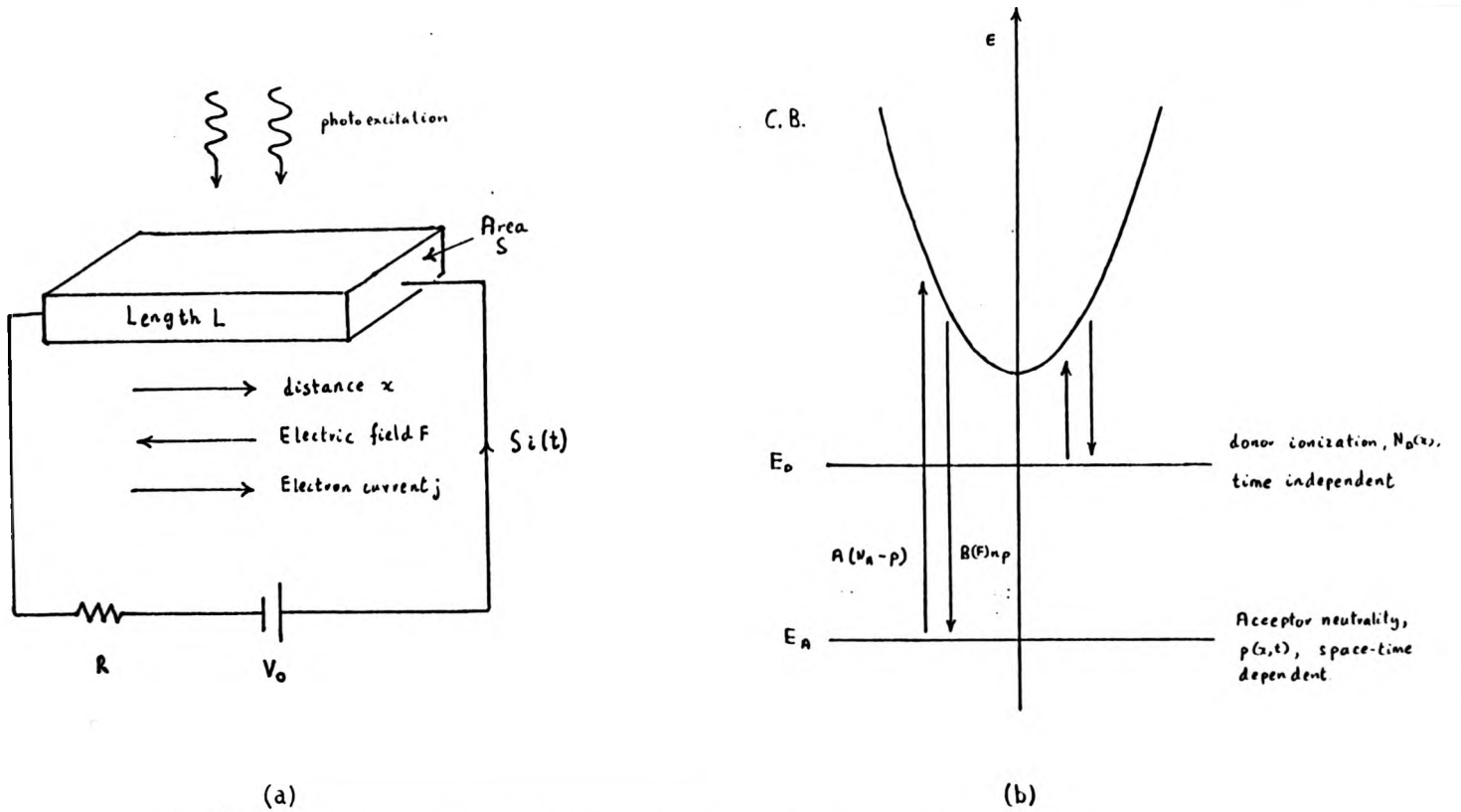

Fig. 4.2. An illustration of the model used to study trap modified Gunn domains.

(a) The circuit arrangement and a definition of the symbols used.

(b) The photoconductive transitions involved.

$$n^+(x,t) = N_D(x) - N_A(x) + p(x,t) \tag{4.4}$$

and the electron density involved in equation 4.3 is found from Poisson's equation

$$n(x,t) = \frac{\varepsilon\varepsilon_0}{e} \frac{\partial F}{\partial x} + n^+(x,t) \tag{4.5}$$

We assume that the velocity field characteristic involved in equation 4.1 is the one appropriate to GaAs in the absence of trapping and we neglect the position dependence of v(F) caused by the position dependence of the ionized impurity density. The assumption that trapping effects do not alter the form of v(F) is probably valid for low resistivity GaAs because the trapping rate B(F)p can be no more than $\sim 5 \times 10^{11}$ s^{-1} in our model. This is about an order of magnitude less than the rate of L.O. phonon scattering, which is the dominant type of scattering in GaAs at $\sim 300^0$K. Similarly a high L.O. phonon scattering rate would be expected to mask any position dependence of v(F) due to spatially non-uniform ionized impurity scattering. The assumptions may be of lesser validity for the high resistivity materials in which slow domains are often observed.

We suppose that the field dependence of the capture coefficient arises from enhanced capture from the upper valley, and following Ridley and co-workers (1972) we write

$$B(F) = B_1 \{1 + (\frac{B_2}{B_1} - 1)\, \eta(F)\} \tag{4.6}$$

where B_1 and B_2 are constant capture coefficients for the upper and lower valleys respectively and η is the fraction of electrons in the upper valley. Although Leach and Ridley (1978) have shown that this form of field dependence may be inappropriate we use equation 4.6 because our numerical study had been completed prior to publication of their results. It is unlikely that use of a different form for B(F) would alter qualitatively the conclusions we have reached.

Equations 4.1 to 4.6 form a set of two coupled non-linear partial differential equations whose numerical solution, with appropriate initial and boundary conditions, is described in the section 4.5. In the next section we show how the low threshold field associated with slow domain nucleation can be understood in terms of the model we have just described.

4.4. A small signal analysis of the model.

To investigate slow domain nucleation we examine the small signal response of a system described by equations 4.1 to 4.5; no assumptions are made about the form of B(F) other than that it increases with field. We restrict ourselves to considering periodic boundary conditions and consider first a circuit in which the resistance and battery are replaced by a constant current generator. In addition we assume spatially uniform donor and acceptor densities N_D and N_A. Then one possible solution of equation 4.1 to 4.5 is a uniform steady state in which the field F_o and acceptor neutrality p_o are related to the constant current density i as follows:

$$e\,(N_D - N_A + p_o)\,v(F_o) = -i \tag{4.7a}$$

$$A\,(N_A - p_o) = B(F_o)(N_D - N_A + p_o)p_o \tag{4.7b}$$

Next we consider the linear space-time evolution of small perturbations to the uniform steady state. First we linearize equations 4.1 to 4.5 about p_o and F_o by making the substitutions $F \to F_o + \delta F$, $p \to p_o + \delta p$, where δF and δp are small perturbations. Then we seek a solution for δF and δp in the form of a Fourier series:

$$\delta F = \sum_k \delta F_k e^{i(\omega t - kx)} \qquad \delta p = \sum_k \delta p_k e^{i(\omega t - kx)} \tag{4.8}$$

$$k = \pm \frac{2\pi m}{L} \qquad m = 0,1,2,\ldots$$

And following the steps outlined in Appendix 4 we arrive at an equation which yields a dispersion relation for $\omega(k)$:

$$\omega^2 - \omega\{kv_o + iDk^2 + i\,(\frac{1}{\tau_d} + \frac{1}{\tau_d})\} - \frac{1}{\tau_g\tau_d}$$

$$+ \frac{1}{\tau_1^2} + i(kv_o + iDk^2)\,(\frac{1}{\tau_g} + \frac{1}{\tau_k}) + i\,\frac{kD}{v_o\tau_1^2} = 0 \qquad (4.9)$$

where

$$\frac{1}{\tau_d} = \frac{e}{\varepsilon\varepsilon_o}(N_D-N_A+p_o)v'(F_o),\ v_o = v(F_o),\ \frac{1}{\tau_R} = p_o\,B(F_o)$$

$$\frac{1}{\tau_g} = A + B(F_o)(2p_o+N_D-N_A),\ \frac{1}{\tau_1^2} = \frac{e}{\varepsilon\varepsilon_o}\,p_o\,v(F_o)B'(F_o)(N_D-N_A+p_o) \qquad (4.10)$$

A dispersion relation similar to ours has previously been obtained by Barker and Hearn (1969; see also Barker 1969) who have studied a system of equations similar to equations 4.1 to 4.5 and have assumed the recombination coefficient to be field independent. We now use the dispersion relation to examine the stability of the uniform steady state with respect to small perturbations in field or acceptor neutrality. The condition for stability of any mode in either of the two branches of the dispersion relation is $\mathrm{Im}[\omega(k)] \geq 0$. With the aid of an argument due to Pimpale (1977), we can show that all modes will be stable if the inequality

$$\frac{1}{\tau_d} - \frac{\tau_g}{\tau_1^2} \geq 0 \qquad (4.11)$$

is satisfied (See Appendix 4). If we use the definitions of the steady state (Equations 4.7) and the time constants (Equations 4.10) we readily find that this is equivalent to the simpler condition $\frac{dJ_o}{dE_o} \geq 0$, where J_o is the steady state current density, $J_o = -e(N_D-N_A+p_o(E_o))v(E_o)$ as a function of electric field, E_o, with E_o measured in the *positive* direction ($E_o = -F_o$).

The low threshold field for slow domain nucleation can easily be understood with the aid of inequality 4.11. In the absence of carrier generation recombination the uniform steady state is unstable if the differential dielectric relaxation time τ_d is negative. In the presence of carrier generation recombination the stability condition 4.11 contains the extra term $\tau_g \tau_1^{-2}$, which is positive because B increases with field. If this term is sufficiently large the left hand side of inequality 4.11 can become negative even if τ_d is positive. It follows that the system could become unstable at fields below the threshold field for the Gunn instability.

Our conclusions so far apply to a constant current circuit. If the circuit is resistive, the stability criterion is unaltered for $k \neq 0$, but for $k = 0$ this dispersion relation has an additional term of $\tau_g^{-1}\tau_c^{-1}$ (this term is a contribution from equation 4.2). Hence, for $k = 0$, the condition for stability becomes:

$$\frac{1}{\tau_d} + \frac{1}{\tau_c} - \frac{\tau_g}{\tau_1^2} \geq 0$$

where τ_c is the time constant of the RC circuit formed by the parallel plate capacity of the sample and the circuit resistance.

4.5. A numerical study of the model.

This section concerns a numerical study of the model described in section 4.2. We start with an explanation of the boundary and initial conditions required for the study. Next we give a brief discussion of the numerical technique and then describe the various parameters associated with the numerical solutions. Finally we present the numerical results.

Fortunately the complications involved in selecting boundary conditions for our oscillatory photoconductivity study do not arise in the present problem. As discussed in section 3.5, we can impose realistic boundary conditions for a Gunn effect simulation by assuming that the semiconductor

The low threshold field for slow domain nucleation can easily be understood with the aid of inequality 4.11. In the absence of carrier generation recombination the uniform steady state is unstable if the differential dielectric relaxation time τ_d is negative. In the presence of carrier generation recombination the stability condition 4.11 contains the extra term $\tau_g \tau_1^{-2}$, which is positive because B increases with field. If this term is sufficiently large the left hand side of inequality 4.11 can become negative even if τ_d is positive. It follows that the system could become unstable at fields below the threshold field for the Gunn instability.

Our conclusions so far apply to a constant current circuit. If the circuit is resistive, the stability criterion is unaltered for $k \neq 0$, but for $k = 0$ this dispersion relation has an additional term of $\tau_g^{-1}\tau_c^{-1}$ (this term is a contribution from equation 4.2). Hence, for $k = 0$, the condition for stability becomes:

$$\frac{1}{\tau_d} + \frac{1}{\tau_c} - \frac{\tau_g}{\tau_1^2} \geq 0$$

where τ_c is the time constant of the RC circuit formed by the parallel plate capacity of the sample and the circuit resistance.

4.5. A numerical study of the model.

This section concerns a numerical study of the model described in section 4.2. We start with an explanation of the boundary and initial conditions required for the study. Next we give a brief discussion of the numerical technique and then describe the various parameters associated with the numerical solutions. Finally we present the numerical results.

Fortunately the complications involved in selecting boundary conditions for our oscillatory photoconductivity study do not arise in the present problem. As discussed in section 3.5, we can impose realistic boundary conditions for a Gunn effect simulation by assuming that the semiconductor

The low threshold field for slow domain nucleation can easily be understood with the aid of inequality 4.11. In the absence of carrier generation recombination the uniform steady state is unstable if the differential dielectric relaxation time τ_d is negative. In the presence of carrier generation recombination the stability condition 4.11 contains the extra term $\tau_g \tau_1^{-2}$, which is positive because B increases with field. If this term is sufficiently large the left hand side of inequality 4.11 can become negative even if τ_d is positive. It follows that the system could become unstable at fields below the threshold field for the Gunn instability.

Our conclusions so far apply to a constant current circuit. If the circuit is resistive, the stability criterion is unaltered for $k \neq 0$, but for $k = 0$ this dispersion relation has an additional term of $\tau_g^{-1}\tau_c^{-1}$ (this term is a contribution from equation 4.2). Hence, for $k = 0$, the condition for stability becomes:

$$\frac{1}{\tau_d} + \frac{1}{\tau_c} - \frac{\tau_g}{\tau_1^2} \geq 0$$

where τ_c is the time constant of the RC circuit formed by the parallel plate capacity of the sample and the circuit resistance.

4.5. A numerical study of the model.

This section concerns a numerical study of the model described in section 4.2. We start with an explanation of the boundary and initial conditions required for the study. Next we give a brief discussion of the numerical technique and then describe the various parameters associated with the numerical solutions. Finally we present the numerical results.

Fortunately the complications involved in selecting boundary conditions for our oscillatory photoconductivity study do not arise in the present problem. As discussed in section 3.5, we can impose realistic boundary conditions for a Gunn effect simulation by assuming that the semiconductor

has heavily doped contact regions and requiring the field to obey the condition $\left.\frac{\partial F}{\partial x}\right|_{x=0} = \left.\frac{\partial F}{\partial x}\right|_{x=L} = 0$.

To obtain an initial condition we assume that at the moment of switch on the capacitor formed by the sample and its connecting leads is uncharged. Also we neglect any internal electric fields generated as a result of diffusion of electrons out of the contact regions. Then the initial condition is

$$F(x,0) = 0$$
$$p(x,0) = p_o(0)$$

where $p_o(0)$ is the zero field solution of equation 4.7b.

The boundary and initial conditions ensure that after switch-on the bulk field rises rapidly, while the contact field remains low. If V_o is sufficiently high the bulk field eventually becomes large enough to violate condition 4.11. Once this happens an instability is nucleated if a perturbing influence exists. This is provided by a doping notch as discussed in section 3.6.

The form of $N_D(x)$ used in the computations is shown in Fig. 3.9b. The acceptor density was taken to be uniform and equal to the bulk donor density at a distance midway along the sample.

For the velocity field characteristic we employed a piecewise linear approximation to that measured by Ruch and Kino (1966) as shown in Fig. 4.3. The fraction of electrons in the upper valley was approximated using a form given by Kroemer (1966)

$$\eta(F) = \frac{(F/F_o)^2}{1 + (F/F_o)^2}, \quad F_o = 4.7 \times 10^5 \text{ Vm}^{-1}$$

The capture coefficient B_1 was taken to be 10^{-14} m^3 s^{-1}, which is similar to the value of 5×10^{-15} m^3 s^{-1} given by Harutunian and Varosian (1977). The other data used in our calculations are shown in Table 4.2. The value

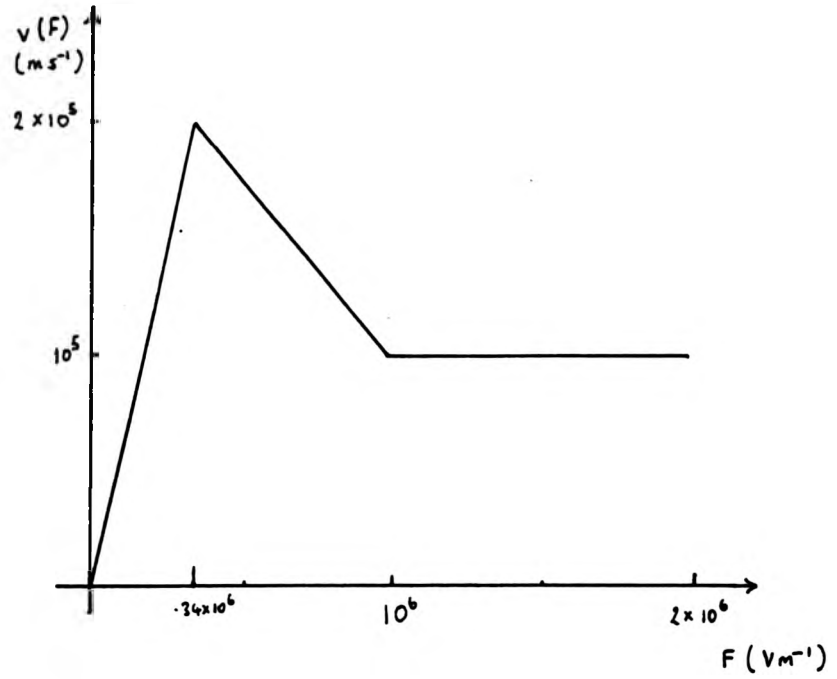

Fig. 4.3. The velocity field characteristic used in the numerical study of trap modified Gunn domains. This is a piecewise linear approximation to the velocity field characteristic of GaAs (Ruch and Kino, 1966).

Quantity	Symbol	Value	Unit
Donor density scaling factor	N	1.014×10^{21}	m^{-3}
Dielectric constant	ε	12.0	-
Diffusion coefficient	D	3×10^{-2}	$m^2\ s^{-1}$
Sample length	L	5×10^{-5}	m
Sample area	S	10^{-6}	m^2
Resistance	R	50	Ω
Battery e.m.f.	V_o	40	V

Table 4.2: The parameters used in the computational study of trap modified Gunn domains.
The donor density scaling factor N is defined such that the donor density is $N\ n_o'(x)$ where $n_o'(x)$ is shown in Fig. 3.9b (See also Appendix 3).

for the dielectric constant of GaAs given in the table is 12.0 in place of the accepted value of 12.91 (Rode, 1975). This figure was chosen for numerical convenience and is unlikely to alter the qualitative conclusions we have reached.

Our numerical solutions were obtained using an explicit finite difference scheme. The field equation (4.1) was treated as in our study of oscillatory photoconductivity, (Appendix 3) and the time derivative in the rate equation (4.3) was approximated by means of a forward difference. We did not attempt an extensive analysis of the numerical properties of the difference method used to solve these two coupled differential equations, however it is clear that if solutions of the difference analogue to the rate equation converge, in the limit of vanishing mesh size, then the solution to the analogue of the field equation will also converge provided that inequalities 3.15 are satisfied. It is plausible that restrictions on mesh size would also result from the need to ensure that solutions to the difference analogue to the rate equation are also convergent.However, no problems with numerical stability arose in our computations which were all carried out using a mesh which satisfied inequalities 3.15. Hence any restrictions arising from the analogue to the rate equation are likely to be less severe than those arising from the analogue to the field equation.

The limits on mesh size that we have given in chapter 2 are not in agreement with those quoted by Maksym and Hearn (1978) for a finite difference approximation to equations 4.1 to 4.6. Their limits are slightly too restrictive and should be replaced by inequalities 3.15.

In practice we found that application of our difference method required a large amount of computer time. The reason for this is that the large drift velocities encountered in GaAs forced us to use a small space step, which in turn required use of a small time step. As a result we were only

able to follow the evolution of instabilities in a short sample, for a short period following switch-on. In addition we were unable to obtain solutions to the model for as wide range of parameters as we would have wished.

The computations have all been performed using a modified version of the program which had previously been used for our study of oscillatory photoconductivity. This gives solutions to the field equation in the system of units described in Appendix 2 and solutions to the rate equation with p measured in units of YL^{-3}, Y being the total number of electrons in a volume L^3. These units are used to present all the numerical solutions described in this chapter. The actual values of the units are listed in Table 4.3.

In our first calculation we solved the field equation, without including the coupling to the rate equation. The solution took the form of a typical Gunn domain, which was used as a standard against which all subsequent calculations were compared. Our next set of computations was performed in order to find values for the ionization coefficient A and the trapping ratio B_2/B_1 for which the domain differed from the standard either in shape or velocity. We found that for values of $A \leq 10^6$ and $B_2/B_1 \leq 500$ the instabilities took the form of accumulation layers. Dipole domains were nucleated if similar values of B_2/B_1 were used in conjunction with ionization coefficients in the range $10^7 \leq A \leq 10^{11}$. Coupled motion of the field and acceptor neutrality within a domain was significantly in evidence only if $B_2/B_1 = 500$ and $A = 10^{11}$ or if $B_2/B_1 = 5000$. The domain velocities were found to be significantly reduced only if $B_2/B_1 = 5000$ and $A \leq 10^9$.

The trapping ratios for which the instability differs from the standard Gunn domain are unacceptably large. $B_2/B_1 = 500$ would imply a lifetime of 2×10^{-10}s, for electrons in the upper valley if the acceptor neutrality was 10^{21} m^{-3}. It is therefore probable that equations 4.3 and

Quantity	Symbol	Unit
Electric field	F	10^{6} Vm^{-1}
Distance	x	5×10^{-5} m
Current	i	0.3537A
Time	t	3×10^{-12} s
Acceptor neutrality	P	2×10^{21} m^{-2}

Table 4.3: The system of units used to present the results of the computational study of trap modified Gunn domains. (Figs. 4.4 to 4.7).

4.6 form an unrealistic model for the carrier generation recombination process. However some of our numerical solutions, show good qualitative agreement with experiment. We describe these solutions in the remainder of this section.

We were able to simulate damped current oscillations by choosing $B_2 = 500\ B_1$ and $A = 10^8\ s^{-1}$. The time evolution of the current is shown in Fig. 4.4. In addition to being damped the oscillations have a decreasing period which is qualitatively consistent with the data of Teszner and Boccon-Gibod. Quantitative comparison was not possible because they used samples with lengths in the range 300 to 1000 um, which are longer than the maximum length for which we could obtain a solution. Fig. 4.5 illustrates the evolution of the instability over a period of 200.0 time units after switch-on and consists of 'snapshots' taken at intervals of 25.0 $\text{time}_{\text{units}}$. The instability responsible for the first of the current pulses shown in Fig.4.4. is similar to a triangular Gunn domain, except that the negative charge layer is followed by a long tail in which the acceptor neutrality recovers to its equilibrium value. It is likely that the sample is of insufficient length to accommodate this tail entirely. Thus when the domain enters the anode contact a non-uniform distribution of traps is left in the bulk. The next domain nucleates at the point of minimum acceptor neutrality which is closer to the anode than the notch. This results in a reduced transit time. The process repeats leading to damped oscillations of decreasing period. By increasing A we could reduce the damping and length of tail. For $A > 10^{10}\ s^{-1}$ the oscillations are virtually undamped and renucleation occurs at the notch. For all values of A the velocity of the domain was close to the outside drift velocity (as measured in front of the positive charge layer).

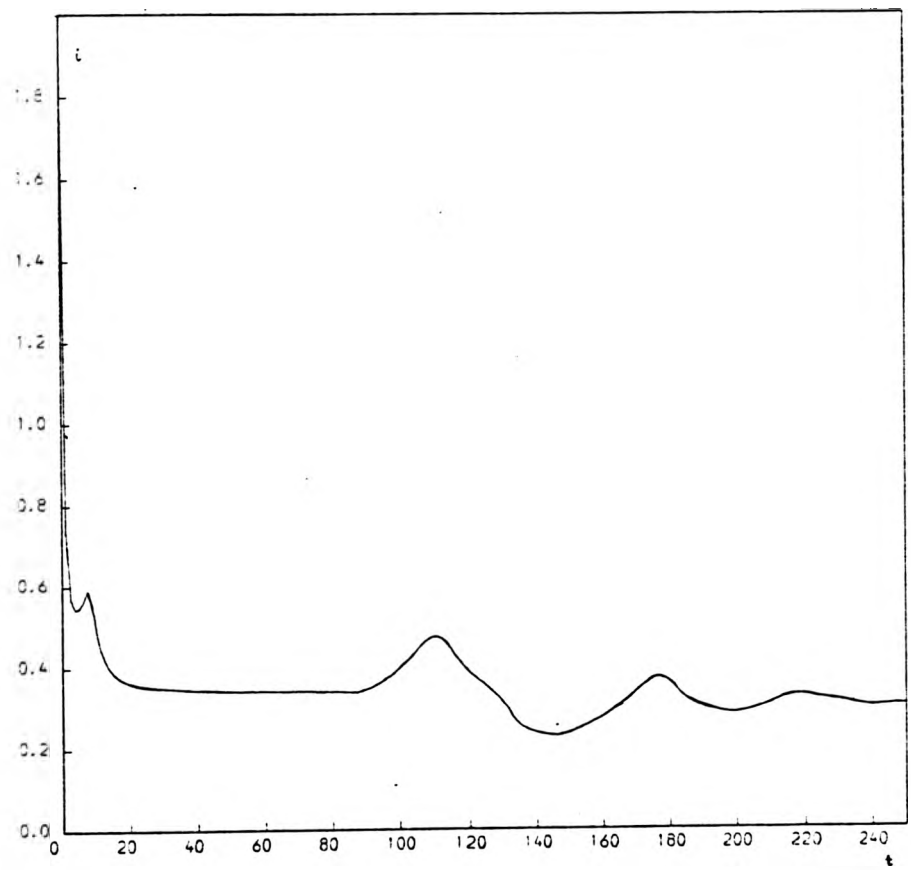

Fig.4.4. The time evolution of the current, showing damped oscillations. $A = 10^8$; $B/B_1 = 500$.

The current and time units are given in Table 4.3.

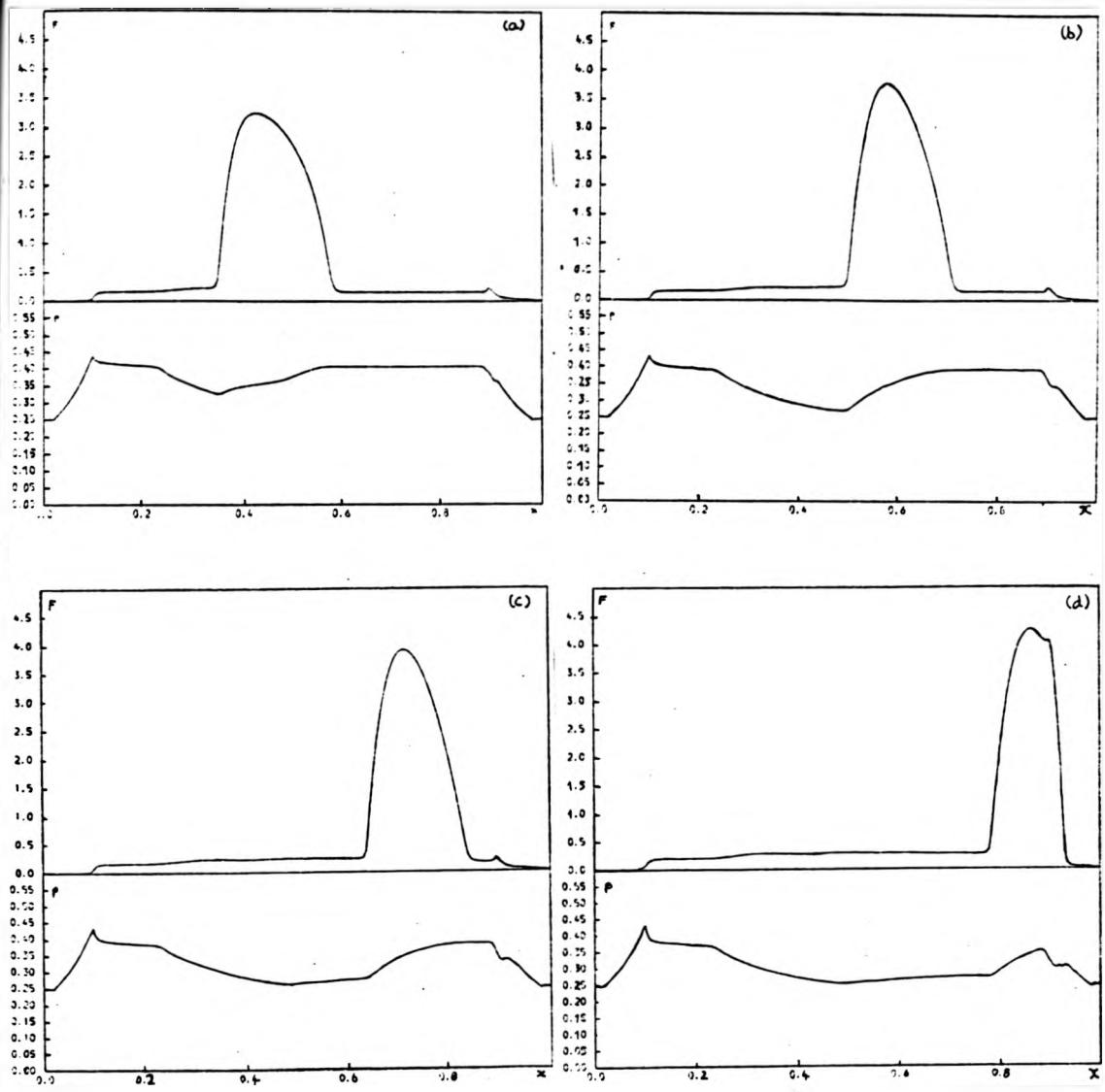

Figs. 4.5a to d. A sequence of 'snapshots' showing the domain instabilities responsible for the damped current oscillations shown in Figure 4.4. Each 'snapshot' shows $p(x,t)$ and $F(x,t)$ at a specific time. The interval between the snapshot' is 25.0, and the first (Fig. 4.5a) refers to a time of 25.0 . The units of p, F, x and t are given in Table 4.3.

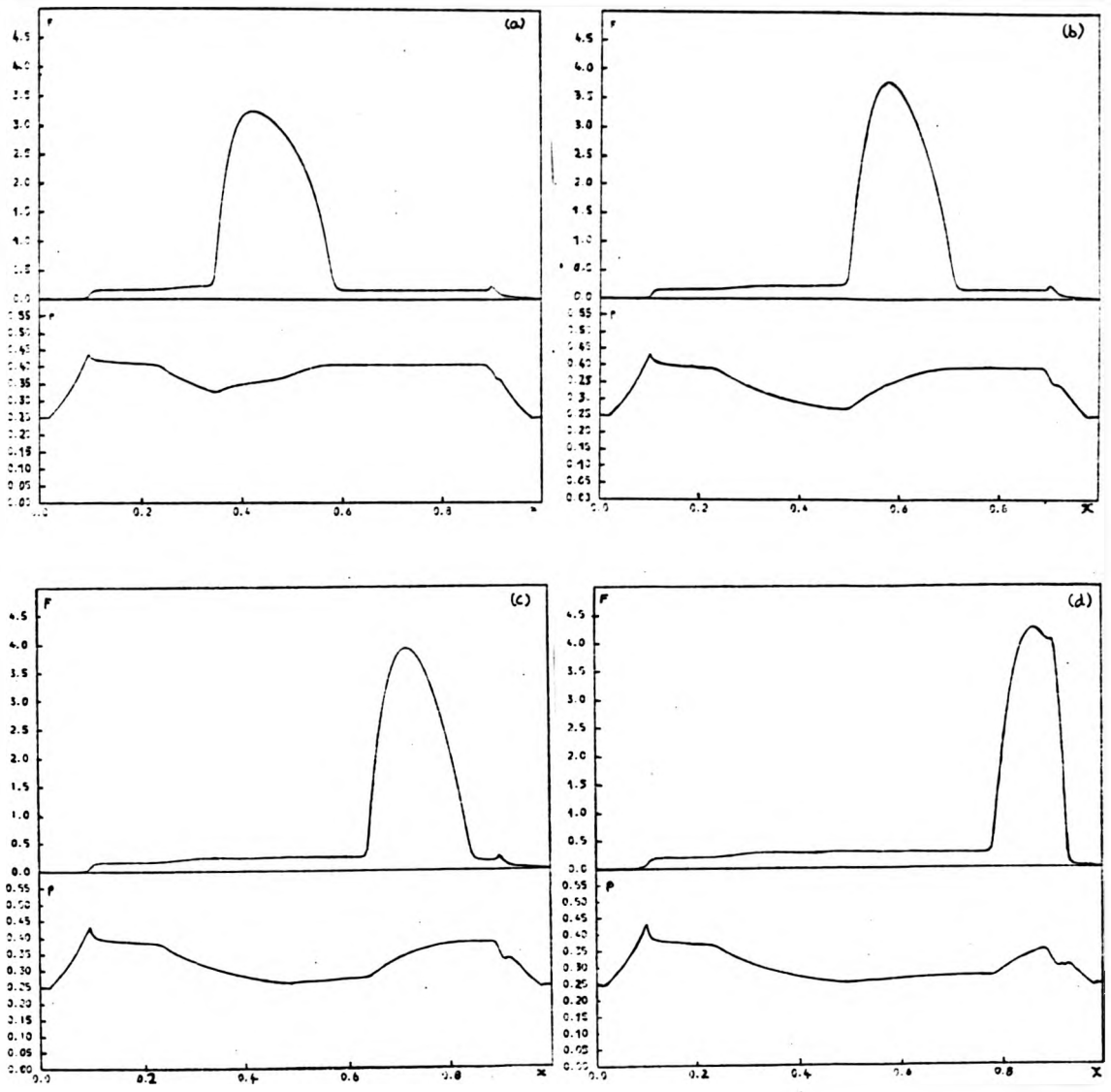

Figs. 4.5a to d. A sequence of 'snapshots' showing the domain instabilities responsible for the damped current oscillations shown in Figure 4.4. Each 'snapshot' shows $p(x,t)$ and $F(x,t)$ at a specific time. The interval between the 'snapshot' is 25.0, and the first (Fig. 4.5a) refers to a time of 25.0 . The units of p, F, x and t are given in Table 4.3.

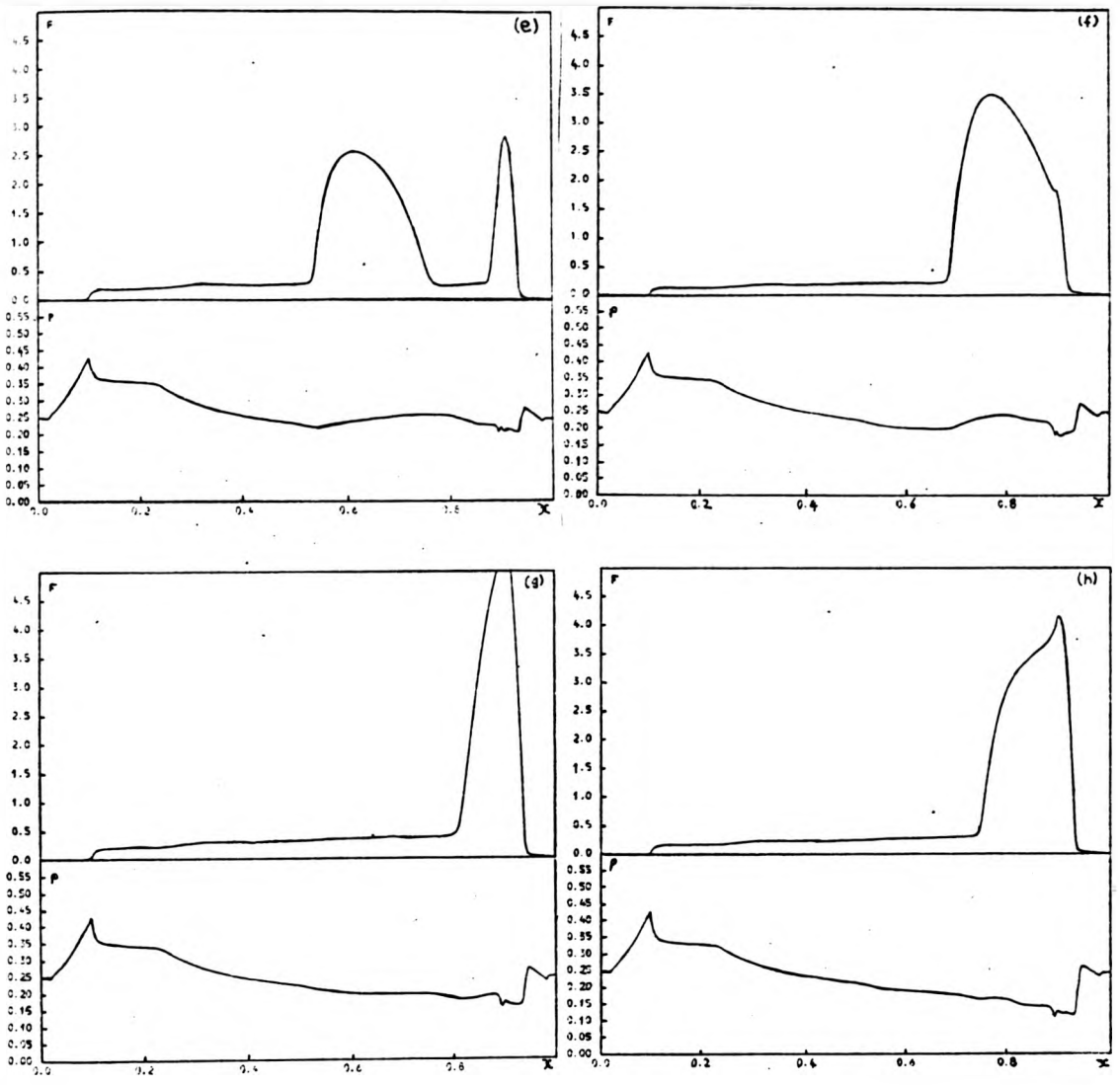

Figs. 4.5e to h. A sequence of 'snapshots' showing the domain instabilities responsible for damped current oscillations shown in Fig. 4.4.
Each 'snapshot' shows p(x,t) & F(x,t) at a specific time. The interval between the 'snapshots' is 25.0, and the first (Fig. 4.5e) refers to a time of 125.0.

In Figs. 4.6 and 4.7 we show the time evolution of a reduced velocity domain and the associated current, obtained with the choice of parameters: $A = 10^9\ s^{-1}$, $B_2/B_1 = 5000$. The period and interval are as in Figs. 4.4 and 4.5. It can be seen that the domain is much broader than the fast domains and has a more pronounced tail. Inside its body the acceptors are almost completely full. The domain velocity was found to increase with increasing A, corresponding to the experimental observation of increasing velocity with increasing illumination in density. Our results for the variation of velocity with A are summarized in Table 4.4. It is interesting that for small values of A the domain velocity is close to half the drift velocity measured just in front of the domain. The velocities given in the table are two orders of magnitude greater than the largest slow domain velocities reported in the literature. (Tokumaru, 1969). For the numerical reasons already mentioned we were unable to investigate whether an alternative choice of parameters, would enable our model to predict smaller domain velocities.

4.6. Conclusion.

We have investigated a model for the trap modified Gunn instability and have found that it has many features qualitatively in accord with experiment. Small signal analysis has been used to show that with a suitable field dependent recombination coefficient the model could account for the low threshold fields associated with slow domain acceleration.

Numerical studies have been used to show that if the recombination rate at high fields is not too large the model predicts domain velocities which are equal to the outside drift velocity. Trapping effects merely damp the Gunn oscillations and reduce their period. If the high field recombination rate is sufficiently large the domains are broadened and their velocity is reduced. A deficiency of the model is that unrealistically large high

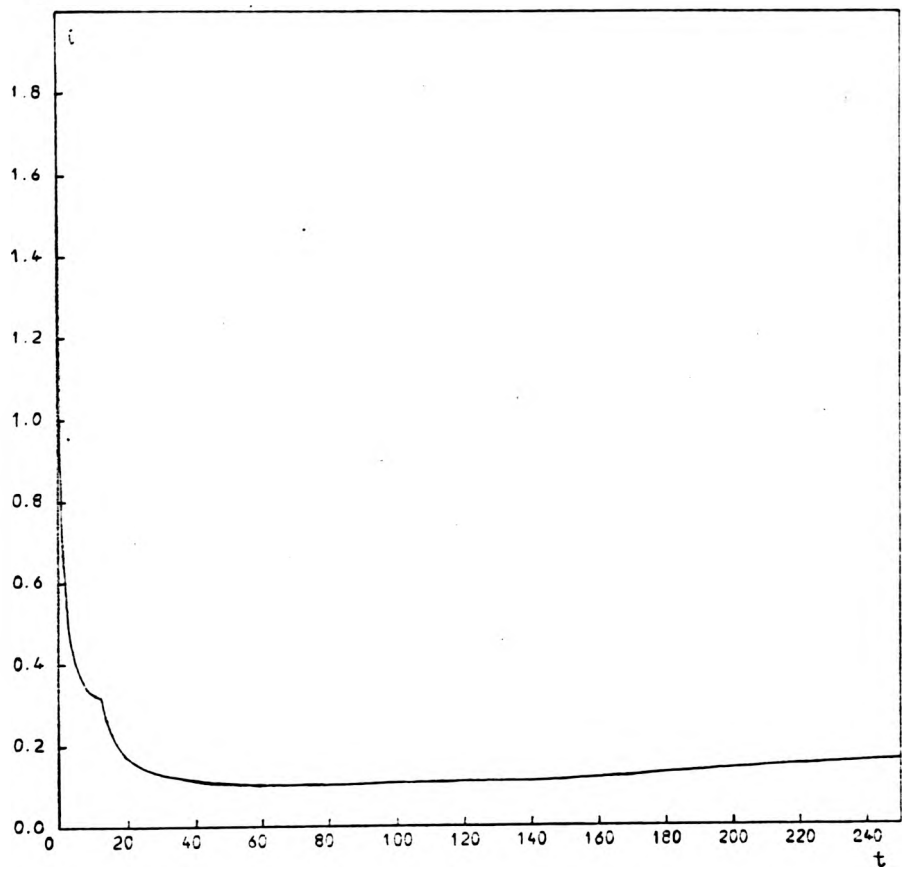

Fig. 4.6. The time evolution of the current associated with a reduced velocity domain, $A = 10^9$, $B_2/B_1 = 5000$.

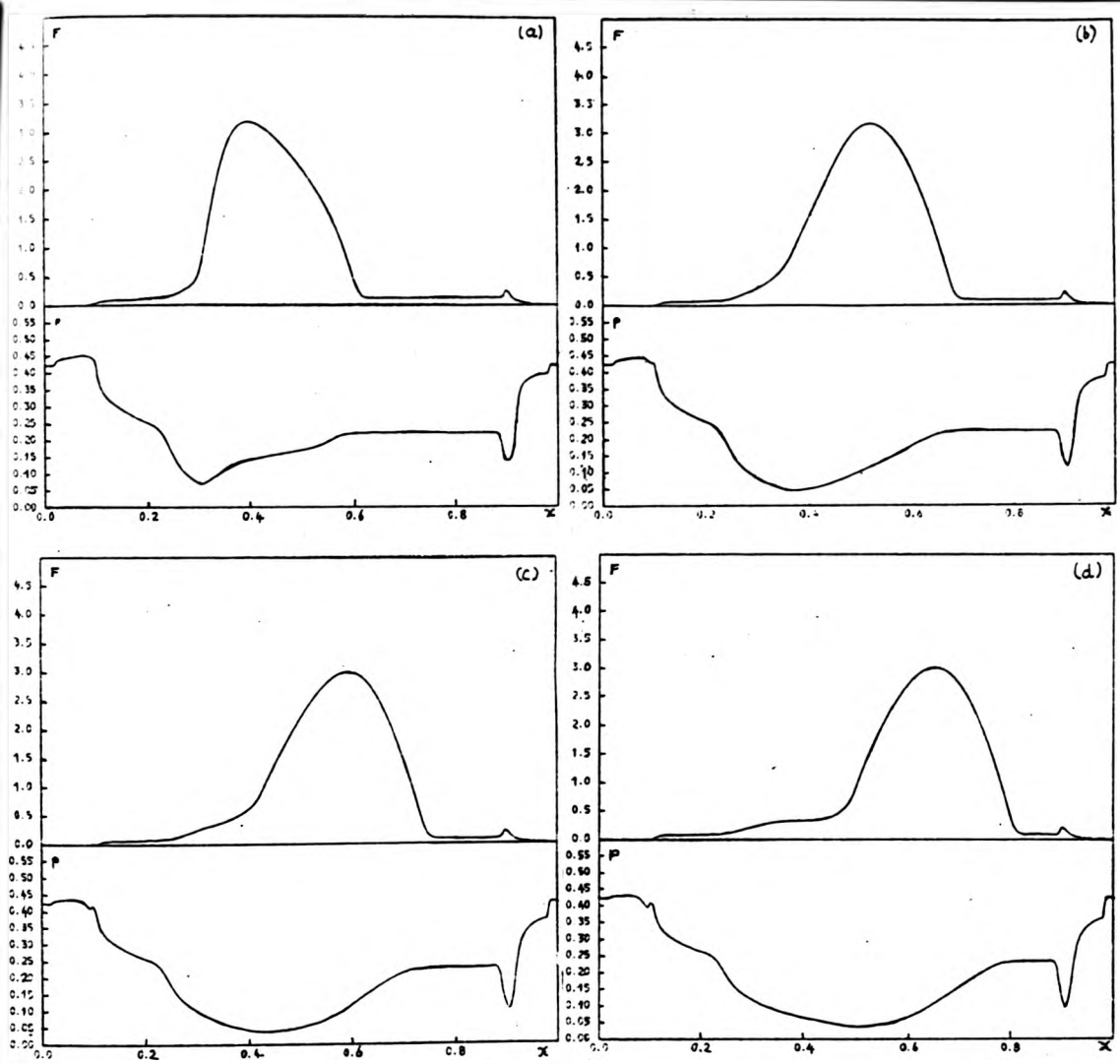

Figs. 4.7a to d. A sequence of 'snapshots' showing the evolution of the reduced velocity domain, corresponding to i(t) as shown in Fig. 4.6. Each 'snapshot' shows p(x,t)&F(x,t) at a specific time. The interval between the 'snapshots' is 25.0, and the first (Fig. 4.7a) refers to a time of 25.0. The units of p, x, F and t are given in Table 4.3.

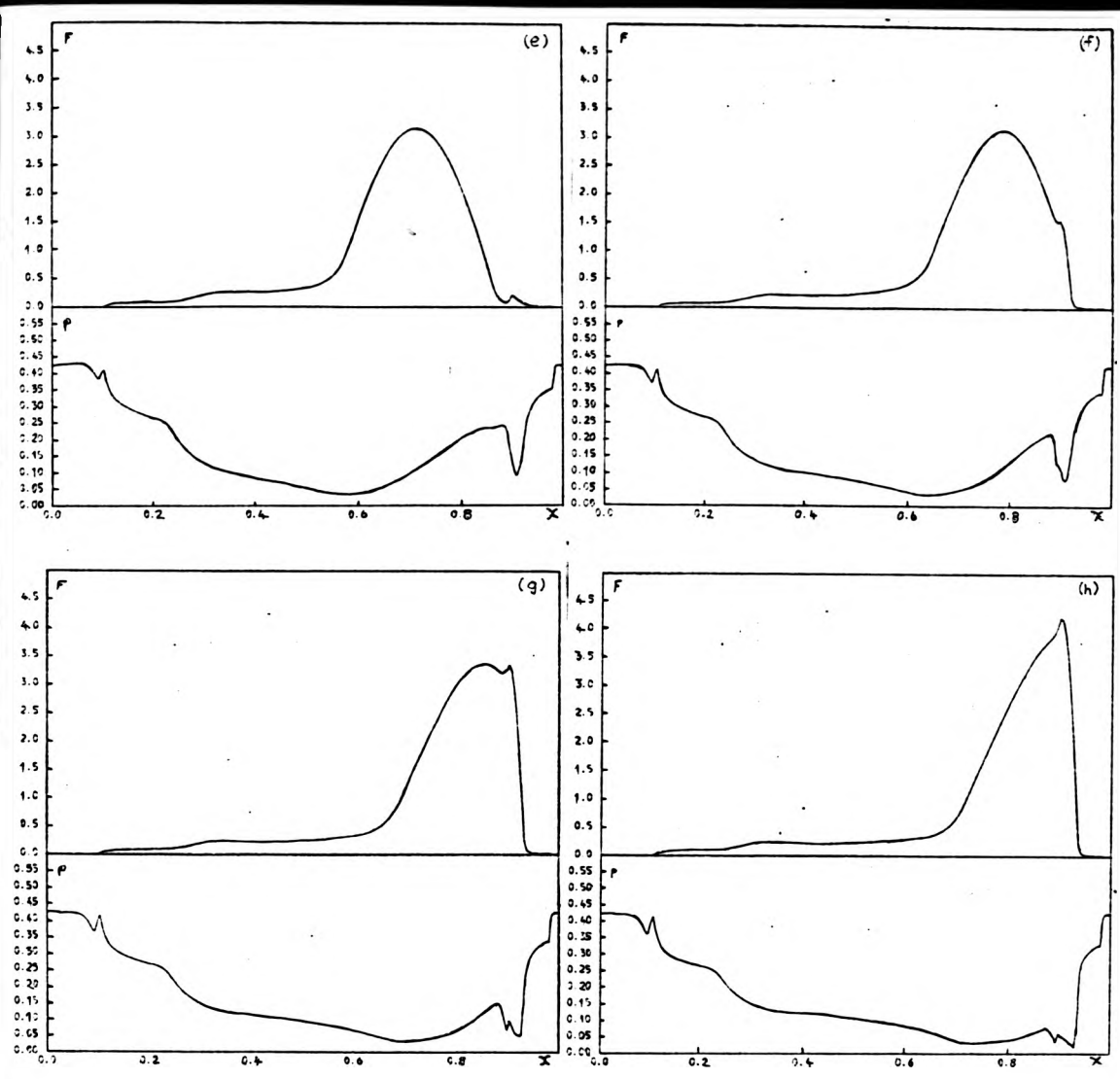

Figs. 4.7e to h. A sequence of 'snapshots' showing the evolution of the reduced velocity domain corresponding to i(t) as shown in Fig. 4.6. Each 'snapshot' shows p(x,t)&F(x,t) at a specific time. The interval between the 'snapshot' is 25.0 and the first (Fig. 4.7e) refers to a time of 125.0.

$A(s^{-1})$	Domain velocity (ms^{-1})	Drift velocity of electrons in the uniform field region just in front of the domain (ms^{-1})
10^{12}	1.0×10^5	1.05×10^5
10^{11}	1.08×10^5	0.89×10^5
10^{10}	0.66×10^5	0.68×10^5
10^{9}	0.25×10^5	0.51×10^5
10^{8}	0.17×10^5	0.36×10^5

Table 4.4: Numerical results for the dependence of the domain velocity on the ionization coefficient A. The value of B_2/B_1 is 5,000.

field recombination rates have to be employed to obtain these results.

The numerical studies required a prohibitive amount of computer time and it proved impossible to investigate whether the model would predict very slow broad domains in a long sample. In addition it was not feasible to systematically calculate numerical solutions for a wide range of parameters.

field recombination rates have to be employed to obtain these results.

The numerical studies required a prohibitive amount of computer time and it proved impossible to investigate whether the model would predict very slow broad domains in a long sample. In addition it was not feasible to systematically calculate numerical solutions for a wide range of parameters.

CHAPTER 5 - DISCUSSION

5.1. Introduction

In this chapter we summarize the main results of our work and suggest some areas where scope for future study exists. In each of Chapter 2 to 4 we have been concerned with a distinct aspect of photo-excited carriers in semiconductors. Our work on distribution functions for photoexcited electrons in GaAs (Chapter 2) has involved a study of the scattering events undergone by these electrons. In our study of oscillatory photoconductivity (Chapter 3) we have considered one macroscopic consequence of these events, namely the space-time dependence of the electric field in a semiconductor under conditions of photoexcitation. Our work on trap modified Gunn domains (Chapter 4) has also been concerned with the space-time dependence of the electric field in such a semiconductor but emphasis was placed on features attributable to the carrier generation recombination process. In reality the phenomena described in Chapters 2 to 4 may be less distinct than we have supposed. Our discussions in this chapter (Sections 5.2 to 5.3) stress the need to study these phenomena from a unified point of view. We consider only phenomena which can be treated within the framework of Boltzmann transport theory. However, we mention here that there are other phenomena, such as excitons and plasmons, whose effect on photoexcited carriers are not fully understood. These effects could usefully be investigated in future.

5.2. Distribution functions for photoexcited electrons in GaAs.

In Chapter 2 we have described a computational study of some distribution functions for photoexcited electrons in GaAs. The distribution functions have been obtained within a one band, Boltzmann equation model and are appropriate to conditions of continuous monochromatic photoexcitation and lattice temperatures in the liquid helium range. Three important conclusions follow from the results of this work.

The first conclusion concerns the steady state distribution function for photoexcited electrons under conditions such that the effect of inter-electron scattering is insignificant. A formal iterative solution of the Boltzmann equation has been used to show how such distribution functions are characteristic of the phonon scattering events undergone by the photo-excited electrons (Section 2.4). The actual form of some steady state distribution functions has been computed using a numerical implementation of the iterative technique (Section 2.5) and the time evolution of some of these distribution functions has been studied using an extension of the same technique (Section 2.6). Piezoelectric scattering and deformation potential scattering by acoustic phonons and polar scattering by L.O. phonons have been taken into account in the computations. If the electron injection spectrum has the form of a δ function in energy, the distribution function always consists the sum of a singular and non-singular part. If the electron injection energy is 3.989 meV the non-singular part of the steady state distribution function has a lattice temperature, Maxwellian form at energies within $\sim$ 1 meV of the band minimum but has a non-Maxwellian plateau at higher energies. A shoulder is present just below the injection energy (or the energy at which electrons are reinjected after undergoing any possible L.O. phonon emissions). Above this energy the distribution again has a lattice temperature, Maxwellian form. In addition the steady state distribution function has some fine structure which is characteristic of those electrons which have undergone $\sim$1 or 2 collisions.

The second conclusion concerns electron-electron scattering. We have shown how this mechanism can be taken into account in calculations of the distribution function: either a large screening model (Sections 2.7, 2.8) or a series expansion model (Section 2.9) can be used. However, the calculations require a large amount of computer time. One preliminary

result is that at electron densities $\gtrsim 3 \times 10^{16}\ m^{-3}$ electron-electron scattering would be expected to cause significant heating of those electrons which have energies greater than the injection energy.

The third conclusion concerns electron-acceptor luminescence under photoexcitation conditions such that the effect of inter-electron collisions is insignificant. (Section 2.10). Electron-acceptor luminescence spectra for C doped GaAs at a lattice temperature of $1.2^{o}K$, have been computed within the one band, Boltzmann equation model. The computed spectra have a fair comparison with spectra obtained in recent photoluminescence experiments.

Extensive further work with the one band, Boltzmann equation model is possible. In the following four paragraphs we list some ways in which the model could be developed. In paragraphs A and B we describe how the model can be applied to existing experimental results (Most of these results are summarized in Section 2.2). The former paragraph is concerned with situations in which intercarrier scattering is unlikely to be significant, the latter with situations in which intercarrier scattering is likely to be important. In paragraph C we suggest some new experiments to which the model could readily be applied. All future studies of the model would benefit from improvements in computational techniques. It is especially important to investigate any improvement which would allow distribution functions to be computed more rapidly than do existing techniques. Some ways in which this could be done are mentioned in paragraph D.

A. Low intensity photoexcitation.

Further studies of electron-acceptor luminescence should be undertaken. In general all the features listed at the end of Section 2.10 (Except those involving intercarrier scattering) should be taken into account in such work. In particular it is important to investigate the

result is that at electron densities $\gtrsim 3 \times 10^{16}\ m^{-3}$ electron-electron scattering would be expected to cause significant heating of those electrons which have energies greater than the injection energy.

The third conclusion concerns electron-acceptor luminescence under photoexcitation conditions such that the effect of inter-electron collisions is insignificant. (Section 2.10). Electron-acceptor luminescence spectra for C doped GaAs at a lattice temperature of $1.2^{o}K$, have been computed within the one band, Boltzmann equation model. The computed spectra have a fair comparison with spectra obtained in recent photoluminescence experiments.

Extensive further work with the one band, Boltzmann equation model is possible. In the following four paragraphs we list some ways in which the model could be developed. In paragraphs A and B we describe how the model can be applied to existing experimental results (Most of these results are summarized in Section 2.2). The former paragraph is concerned with situations in which intercarrier scattering is unlikely to be significant, the latter with situations in which intercarrier scattering is likely to be important. In paragraph C we suggest some new experiments to which the model could readily be applied. All future studies of the model would benefit from improvements in computational techniques. It is especially important to investigate any improvement which would allow distribution functions to be computed more rapidly than do existing techniques. Some ways in which this could be done are mentioned in paragraph D.

A. Low intensity photoexcitation.

Further studies of electron-acceptor luminescence should be undertaken. In general all the features listed at the end of Section 2.10 (Except those involving intercarrier scattering) should be taken into account in such work. In particular it is important to investigate the

effect of non-equilibrium phonons on the photoexcited electron distribution. This may explain why experimental luminescence spectra are broader than the computed spectra described in Section 2.10.

B. High intensity photoexcitation.

The effects of all the features listed in Section 2.10 should be explored. Theoretical investigations of the following phenomena would be of interest:

1. The non-Maxwellian form of the electron distribution function under conditions of very high intensity photoexcitation ($\gtrsim 2 \times 10^5$ W cm^{-2} ; Shah, 1978).
2. The oscillatory form of the electron temperature as a function of injection energy (Weisbuch, 1978a).
3. The time evolution of the electron temperature in experiments involving transient photoexcitation (Ulbrich, 1973).
4. Electric field induced heating of photoexcited electrons. (Ulbrich, 1978).

The existence of non-Maxwellian carrier distributions under conditions of very high intensity photoexcitation (as mentioned above and first reported by Shah) has been confirmed in very recent experiments due to Leheny and co-workers (1979). The experiments involve pulse photoexcitation followed by optical transmission spectroscopy on a picosecond time scale. It is deduced from the spectra that the photoexcited carrier distributions are non-Maxwellian if the carrier density exceeds $\sim 10^{24}$ m^{-3}. Leheny and co-workers suggest that their results may be explicable if, at such high carrier densities, screening reduces the effectiveness of intercarrier and L.O. phonon scattering. However, the detailed reasons for the non-Maxwellian form of the carrier distributions are not fully understood and theoretical studies of the distribution function are required. The large screening

model of electron-electron scattering (Section 2.7) could be used for this purpose. The other three phenomena mentioned above could be studied using the series expansion model (Section 2.9). However, a more suitable expansion than the Taylor series may need to be devised for this purpose. It is suggested that the Hermite polynomial expansion mentioned in Section 2.9 may be appropriate.

C. Experiments.

The following comments apply to photoexcitation experiments whose results could readily be compared with the predictions of the model:

1. Excitation from an impurity level would eliminate the uncertainty as to the fractions of electrons injected from each of the two valence bands.

2. The predicted fine structure (Chapter 2) should be investigated. Excitation from an impurity level would be best for this purpose.

3. Time resolved luminescence spectroscopy could be carried out under conditions of low intensity photoexcitation. This would show how the steady state photoexcited electron distributions is established as a result of the phonon scattering events undergone by the photoexcited electrons. (See Section 2.6).

4. Electric field induced heating of the photoexcited electrons could be studied under conditions such that the effect of inter-electron scattering is not significant. Such heating would be expected to depend on the orientation of the electric field because of the anisotropy of piezoelectric scattering.

5. If the photoexcitation were sufficiently monochromatic the distribution function would be expected to have a pulse like form at the injection energy (or energies). The sum of the recombination and scattering rates at the injection energy could be estimated if the magnitude of this pulse

could be measured.

6. Photoluminescence experiments could be used to investigate oscillatory photoconductivity. (See Section 5.3).

D. Computation.

Methods which allow distribution functions to be computed in a small amount of computer time should be sought. The following possibilities are suggested:

1. Young (1971; see also Appendix 2.4), describes techniques for accelerating the convergence of matrix iterative computations. These techniques may improve the rate of convergence of the matrix iterative method (the Jacobi method) used to compute the distribution functions described in Section 2.5.

2. It should be investigated whether similar acceleration techniques could be used to improve the convergence rate of the iterative solution of the non-linear integral equations which describe the effects of electron-electron scattering.

3. The phonon scattering integrals need to be performed on a mesh in k whereas a mesh in k^2 is most suitable for computation of the electron-electron scattering integrals. Savings in computer time may result if the distribution function is computed on a mesh in k, but interpolated to a mesh in k^2 for the electron-electron parts of the computation.

Our studies of electron-acceptor luminescence (Section 2.10) confirm the suggestion that optical techniques can be used to investigate electron scattering in semiconductors (Ulbrich, 1978a). In particular such techniques could help to increase our knowledge of the parameters of the electron-phonon interaction. They may also yield information on electron-electron scattering - a scattering mechanism which is at present less well understood than electron-phonon scattering. Both photoluminescence

spectroscopy (Section 2.2) and transmission spectroscopy (Bauer 1974, 1978) are expected to provide data suitable for these purposes. Electron scattering would be investigated in three stages. Firstly the carrier distribution functions would be computed according to a specific scattering model. Secondly, optical spectra would be derived from the computed distributions. Finally, the model would be tested by comparing the computed spectra with experimental data. However, one obstacle remains to be overcome before this type of work becomes routine: the inherent precision of optical techniques cannot be fully exploited either unless full account is taken of the effects of spatially non-uniform photoexcitation or unless it is known with certainty that the experimental conditions used are such that the optical spectra are well approximated by those due to a spatially uniform distribution of carriers.

Qualitatively, a steady state, spatially non-uniform distribution of photoexcited carriers would be expected to be established as follows. Due to attenuation effects the intensity of the optical excitation would be expected to be spatially non-uniform. As a result the carriers would be injected in a spatially non-uniform manner. The various types of carrier would be expected to diffuse at different rates and so the diffusion processes would cause space-charge formation. Hence an electric field would be established. In a steady state the magnitude of this field would be such that drift currents exactly counter-balance the diffusion currents. Theoretical studies of the carrier distribution functions appropriate to this situation will be difficult. The simplest viable model would require that the following equations be solved simultaneously:

1. a set of Boltzmann equations for the carrier distribution functions.
2. a set of rate equations which describe the occupancy of the impurity levels.
3. Poisson's equation for the electric field. ~~The dependence of the~~

~~electric field~~. The dependence of the electric field on more than one spatial dimension may need to be considered.

In a more realistic model the effects of non-equilibrium phonons and surface recombination should also be taken into account and the screening of the carrier interactions should be calculated self consistently. The problems involved in these studies are likely to be similar to those encountered in work on semiconductor devices. It is possible that the simulation (Jones and Rees, 1973) and Monte Carlo (Warriner, 1977) methods used in device physics could be applied to studies of photoexcited carriers.

An alternative to large scale computation of spatially non-uniform carrier distributions would be to eliminate experimentally the effects of non-uniform photoexcitation. Possibly, this could be achieved through time resolved measurements of optical spectra. If such measurements are carried out on a time scale shorter than that of the carrier diffusion processes a theoretical analysis based on the assumption of uniform photo-excitation may be applicable.

5.3. Oscillatory Photoconductivity.

The most important result of Chapter 3 concerns the stability of the negative current state associated with oscillatory photoconductivity. Specifically, a Gunn effect model has been used to investigate the stability of this state with respect to space change formation. This has been done with the aid of numerical studies of the space-time dependence of the electric field in a semiconductor exhibiting oscillatory photoconductivity under conditions of 'sub-threshold' injection. A stable, negative current inhomogenous steady state has been predicted to occur if the semiconductor is connected in a resistive circuit and the circuit resistance is sufficiently high. If the circuit is similar but the resistance is low,domain instabilities are expected to nucleate. Cyclic propagation of these

instabilities would cause the current to oscillate. Depending on the e.m.f. active in the circuit and the conditions of photoexcitation, the current during one cycle of the oscillation is expected either to remain positive or negative or to alternate in sign. Neither the negative current state nor the instabilities have yet been observed in practice. Indeed only a few experimental investigations of oscillatory photoconductivity under conditions of 'sub-threshold' injection have been reported. Clearly further experimental and theoretical work is necessary before oscillatory photoconductivity under such conditions is fully understood.

Improved calculations of the oscillatory photoconductivity velocity field characteristic are required. Existing calculations are based on a one band, Boltzmann equation approach and involve the assumption that the phonon system is in thermal equilibrium. However, for 'sub-threshold' injection the rate of L.O. phonon emission would be comparable to the electron injection rate. Under such conditions the assumption of thermal equilibrium phonons may be suspect. The effect of non-equilibrium phonons should be taken into account in future calculations of the velocity field characteristic. Such calculations should also include a comparative study of the velocity field characteristic for all the materials in which oscillatory photoconductivity has been observed to occur (At present only characteristics for InSb are available). This would enable selection of the most suitable material for future experimental work on the negative current state.

Further theoretical work on the instabilities and inhomogeneous steady statesassociated with oscillatory photoconductivity is essential. These phenomena can only be properly understood if full account is taken of the dynamics of the carrier generation-recombination processes, the space-time dependence of the electron and phonon distributions, the space-time

instabilities would cause the current to oscillate. Depending on the e.m.f. active in the circuit and the conditions of photoexcitation, the current during one cycle of the oscillation is expected either to remain positive or negative or to alternate in sign. Neither the negative current state nor the instabilities have yet been observed in practice. Indeed only a few experimental investigations of oscillatory photoconductivity under conditions of 'sub-threshold' injection have been reported. Clearly further experimental and theoretical work is necessary before oscillatory photoconductivity under such conditions is fully understood.

Improved calculations of the oscillatory photoconductivity velocity field characteristic are required. Existing calculations are based on a one band, Boltzmann equation approach and involve the assumption that the phonon system is in thermal equilibrium. However, for 'sub-threshold' injection the rate of L.O. phonon emission would be comparable to the electron injection rate. Under such conditions the assumption of thermal equilibrium phonons may be suspect. The effect of non-equilibrium phonons should be taken into account in future calculations of the velocity field characteristic. Such calculations should also include a comparative study of the velocity field characteristic for all the materials in which oscillatory photoconductivity has been observed to occur (At present only characteristics for InSb are available). This would enable selection of the most suitable material for future experimental work on the negative current state.

Further theoretical work on the instabilities and inhomogeneous steady statesassociated with oscillatory photoconductivity is essential. These phenomena can only be properly understood if full account is taken of the dynamics of the carrier generation-recombination processes, the space-time dependence of the electron and phonon distributions, the space-time

dependence of the electric field and the interaction of the semiconductor with the external circuit. This could be done using the methods developed in semiconductor device physics (as mentioned in Section 5.2). The results of numerical simulations, using such methods, indicate that a number of spatial and temporal overshoot effects are important in hot electron devices (Kroemer, 1978). It would be especially interesting to study these effects within the context of oscillatory photoconductivity.

Future experiments on oscillatory photoconductivity should include a investigation of the steady state photoconductive response under conditions of 'sub-threshold' injection. Recently tunable dye lasers have become available (Weisbuch 1978c) and such lasers could serve well as a source of monochromatic excitation for the experiments. However, the instability phenomena mentioned in Chapter 3 may complicate the interpretation of the experimental results. It is suggested that an experiment involving transient photoexcitation may be free of these complications. In addition such an experiment may allow the mechanism of oscillatory photoconductivity to be directly probed. A single optical pulse would be used to inject electrons into the conduction band at an energy just below the L.O. phonon threshold. If the electron density were $\sim 10^{15}$ m^{-3} the differential dielectric relaxation time would be expected to $\sim$ 10nS. Thus measurements of the photocurrent on a nanosecond timescale could allow the negative current state to be investigated, before any instabilities developed. In addition time resolved luminescence spectroscopy could be used to obtain information on the electron distribution function. In the suggested experiment the initial photocurrent would be expected to be positive, but the photocurrent should change sign at a time when those electrons which had been injected with a velocity component anti-parallel to the field had been accelerated to the L.O. phonon theshold and had emitted an L.O. phonon. At the same time there should be an increase in the intensity of the

luminescence from the electrons at the band minimum. After a further time the photocurrent would become positive again, because these electrons which had undergone L.O. phonon emission would be accelerated and would then make a large, positive contribution to the total current. The one band, Boltzmann equation model and the iterative method (as described in Chapter 2) could readily be adapted to give a quantitative prediction of the distribution function and photocurrent in this type of experiment.

5.4. Trap modified Gunn domains.

In Chapter 4 we have shown that a simple model, which involves electric field dependent recombination of electrons, can be used to account qualitatively for many of the properties of trap modified Gunn domains in GaAs. However, this qualitative agreement is obtained at the expense of having to assume an unrealistically large high field recombination rate. One feature which we are unable to explain is the incubation time associated with slow domain nucleation. In principle the incubation time could be understood in terms of the dispersion relation described in Section 4.4. At the threshold field F_{th} for slow domain nucleation there is at least one mode of frequency ω for which the condition $\mathrm{Im}[\omega(k)] < 0$ is satisfied. And the magnitude of a small perturbation to F_{th} grows with a time constant τ, given by $\tau = |\mathrm{Im}[\omega(k)]|^{-1}$. The time constant is itself a function of electric field and a long incubation time would be expected if τ were small over a sufficiently large range of fields above threshold. This could be possible with a suitable form for the field dependent capture coefficient. It is clear that a thorough understanding of the electron capture process is required before the model described in Chapter 4 can be used forfurther studies of trap modified Gunn domains. Also the model can be used to simulate slow domains only if numerical solutions for the electric field trapped electron density can be obtained in a small amount of computer time. It is possible that an implicit finite difference scheme could

allow faster computations than does the explicit difference scheme mentioned in Chapter 4. The spatial and temporal overshoot effects mentioned in the previous section should be taken into account if the model described in Chapter 4 is to be improved. It is especially important to consider these effects in detailed studies of the role of trapping in the propagation of fast Gunn domains.

References

ARLT, G. and QUADFLIEG, P. 1968. Phys. Stat. Sol. 25 323

BARKER, J.R., 1969 Ph.D. Thesis, University of Warwick.

BARKER, J.R. and HEARN, C.J. 1969. J. Phys. C. 2 2128

BARKER, J.R. and HEARN, C.J. 1970. Phys. Lett. 31A 51

BARKER, J.R. and HEARN, C.J. 1973. J. Phys. C. 6 3097

BARKER, J.R. 1979 in The Physics of Non-linear Transport in Semiconductors. (Proceeding of a NATO advanced Study Institute, Sogesta, Italy, 1979).

BARRY-BEBB,H. and WILLIAMS, E.W. 1972 in semiconductors and semimetals 8 ed. Willardson R.K. and Beer, A.C., Academic Press, New York.

BAUER, G. 1974 Springer Tracts in Modern Physics 74, Springer Verlag, Berlin.

BAUER, G. 1978 Solid State Electron. 21 17

BELL, W.W. 1968Special Functions for Scientists and Engineers, D. Van Nostrand, London.

BÖER,K.W. and WARD, J.J. (1967). Solid State Commun. 5 467.

BONCH-BRUEVICH, V.L., ZVYAGIN, I.P. and MIRONOV, A.G. 1972. Domain Electrical Instabilities in Semiconductors, Nauka Press, Moscow (English translation 1975, New York, Consultants' Bureau)

BUTCHER, P.N. 1967 Repts. Prog. Phys. 30 97

CHAMBERLAIN, J.M., ERGUN, H.B., GEHRING K.A. and STRADLING, R.A. 1971 Solid State Commun. 9 1563

DIMMOCK, J. 1967 in Semiconductors and Semimetals 3 259 Ed. Willardson R.K. and Beer A.C., Academic Press, New York.

DYKMAN, I.M. and TOMCHUK, P.M. 1960 Fiz. Tverd. Tela 2 2228 (English Translation: 1960 Sov. Phys. Solid State 2 1988)

EAVES, L. 1979 Private communication.

ELESIN, V.F. and MANYKIN, E.A. 1965 Zh. Eksp. Teor. Fiz 50 1381 (English Translation: 1966 Soviet Physics JETP 23 917).

EHRENREICH, H. 1959 J. Phys. Chem. Sol. 8 130

EHRENREICH, H. and COHEN, M.H. 1959 Phys. Rev. 115 786

FOLLAND, N.O. 1970 Phys. Rev. B2 418

GARLAND, C.W. and PARK, K.C. 1962 J. Appl. Phys. 33 759

GILBERT, F. and HOFFMANN, H.J. 1975 Phys. Stat. Sol. a31 543

GOEBEL, E.O. and HILDEBRAND, O. 1978 Phys. Stat. Sol. b88 645.

GOEBEL, E.O., HILDEBRAND, O. and ROMANEK, K.M. 1979 in Proc. 14th Int. Conf. on the Physics of Semiconductors (Ed. B.L.H. Wilson) p. 157, Inst. Phys. Conf. Ser. 43, Inst. Phys. London

HAMBLETON, K.G. 1965 Phys. Lett. 16 241

HARPER, P.G., HODBY, J.W. and STRADLING, R.A. 1973 Rep. Prog. Phys. 36 1

HARUTUNIAN, V.M. and VAROSIAN, A.G. 1977 J. Phys. C. 10 2633

HAUG, A. and ECKART, W. 1975 Solid State Commun. 17 267

HEARN, C.J. 1966 Proc. Phys. Soc. 88 407

HEARN, C.J. 1979 in Non-linear Transport in Semiconductors. (Proc. Nato Summer Institute, Sogesta, Italy).

HILDEBRAND, O., GOEBEL, E.O., ROMANEK, K.M., WEBER, H. and MÄHLER, G. 1978 Phys. Rev. B17 4775

HOLZHÜTTER, H.G. and MOCKER, M. 1976 Phys. Stat. Sol. 77 203

HUTSON, A.R. and WHITE, D.L. 1962 J. Appl. Phys. 33 40

INOUE, M., TAKENAKA, N., SHIRAFUJI, J. and INUISHI, Y.

1978a Solid State Electron. 21 29

1978b Solid State Electron. 21 1527

1978c J. Phys. Soc. Japan 45 1630

ISAACSON, E. and KELLER, H.B. 1966 Analysis of Numerical Methods, Wiley, New York.

JOHNSON, E.J. and FAN, H.Y. 1963 Phys. Rev. 139A 1991

JONES, B.L. and BEAUDET, P.R. 1967 Can. J. Phys. 45 4091

JONES, D. and REES, H.D. 1973 J. Phys. C. 6 1781

KITTEL, C. 1963 Quantum Theory of Solids, Wiley, New York.

KOMOLOV, V.L. and YASSIEVICH, I.N. 1974 Fiz. Tekh Poluprovdn 8 1125 (English Translation: 1974 Sov. Phys. Semiconductors 8 732)

KROEMER, H. 1972 J. Appl. Phys. 43 5124

KROEMER, H. 1978 Solid State Electron. 21 61

LANDAU, L.D. 1937 Zh. Eksp. Teor. Fiz 7 203

LANDSBERG, P.T. 1966 in Lectures in Theoretical Physics, University of Colorado, Boulder 8A 313 Ed. W.E. Brittin, Gordon and Breach, New York.

LAWAETZ, P. 1971 Phys. Rev. B4 3468

LAX, M. 1960 Phys. Rev. 119 1502

LEACH, M.F. and RIDLEY, B.K. 1978 J. Phys. C. 11 2265

LEBWOHL, P.A. and PRICE, P.J. 1971 Appl. Phys. Lett. 19 530.

LEHENY, R.F., SHAH, J., FORK, R.L., SHANK, C.V. and MIGUS, A. 1979 Solid State Commun. 31 809.

MAKSYM, P.A. and HEARN, C.J. 1978 Solid State Electron. 21 1531

MATHEWS, J. and WALKER, R.L. 1970. Mathematical Methods of Physics, Benjamin, New York.

McGILLEM, C.D. and COOPER, G.R. 1974 Continuous and Discrete System and Signal Analysis. Holt, Reinhart and Winston, New York.

MINORSKY, N. 1962 Non-linear Oscillations, D. Van Nostrand Co. Inc., Princeton, N.J.

MINORSKY, N. 1964 The Mathematics of Physics and Chemistry, Vol. 2., Ch.6., ed. H. Margenau and G.M. Murphy, D. Van Nostrand Co. Inc., Princeton, N.J.

MOORADIAN, A.L. and WRIGHT, G.B. 1966 Solid State Commun. 4 431

NARAYANAMURTI, V. LOGAN, B.A., CHIN, M.A. and LAX, M. 1978. Solid State Electron. 21 1295.

NOGUERRA, B.A. Ph.D. Thesis University of Warwick, 1978.

NOGUERRA, B.A. and HEARN, C.J. 1978 Solid State Electron. 21 171

NORTHROP, D.C., THORNTON, P.R., TREZISE, K.E. 1964 Solid State Electron. 7 17

PIMPALE, A. 1977 Ph.D. Thesis University of Southampton.

REES, H.D. 1969 J. Phys. Chem. Solids. 30 643

1978 J. Phys. C. 6 641

RIDLEY, B.K. and PRATT, R.G. 1965 J. Phys. Chem. Solids 26 21

RIDLEY, B.K. and WISBEY, P.H. 1967 Brit. J. Appl. Phys. 18 761

RIDLEY, B.K., CRISP, J.J., SHISHIYANU, F. 1972 J. Phys. C. 5 187.

RIDLEY, B.K. and HARRIS, J.J. 1976 J. Phys. C. 9 991

RODE, D.L. 1970 Phys. Rev. B2 1012

RODE, D.L. 1975 in semiconductors and semimetals 10 ed. Willardson R.K. and Beer, A.C. Academic Press New York.

RUCH, J.G. and KINO, G.S. 1966 Appl. Phys. Lett. 9 283

SACKS, H.K. and MILNES, A.G. 1970 Int. J. Electronics 28 565

SHAH, J. and LEITE, R.C. 1969 Phys. Rev. Lett. 22 1304

SHAH, J. 1974 Phys. Rev. B10 3697

SHAH, J. 1978 Solid State Electron. 21 43

STILLMAN, G.E., LARSEN, E.M., WOLFE, C.M. and BRANDT, R.C. 1971 Solid State Commun. 9 2245

STOCKER, H.J. and KAPLAN, H. 1966 Phys. Rev. 150 619

STOCKER, H.J., LEVINSTEIN, H. and STANNARD, C.R. 1966 Phys. Rev. 150 613.

STOCKER, H.J. 1967 Phys. Rev. Lett. 18 1197

STURGE, M.D. 1962 Phys. Rev. 127 768

TESZNER, J.L. and BOCCON-GIBOD, D. 1973 J. Appl. Phys. 44 2765.

TOKUMARU, Y. 1969 Appl. Phys. Lett. 14 212

ULBRICH, R.G. 1971 Phys. Rev. Lett. 24 1512

ULBRICH, R.G. 1973 Phys. Rev. B8 5719

ULBRICH, R.G. 1976 in Proc. of the 13th Int. Conf. on the Physics of Semiconductors (Ed. F.G. Fumi) p.1226, Tipografia Marves, Rome.

ULBRICH, R.G. 1978a in Proc. of the 14th Int. Conf. on the Physics of Semiconductors (Ed. B.L.H. Wilson) p.11, Inst. Phys. Conf. Sev. 43, Inst. Phys. London.

ULBRICH, R.G. 1978b Solid State Electron. 21 51

WARRINER, R.A. 1977 I.E.E. Journal on Solid State and Electron Devices 1 92.

WEISBUCH, C. 1978a Solid State Electron. 21 179

WEISBUCH, C. 1978b Private Communication.

WEISBUCH, C. 1978c in Proc. of the 14th Int. Conf. on the Physics of Semiconductors (Ed. B.L.H. Wilson) p.93, Inst. Phys. Conf. Ser. 43, Inst. Phys. London.

YOUNG, D.M. 1971 Iterative Solution of large linear systems, Academic Press, New York.

ZAWADZKI, W. and SZYMAŃSKA, W. 1971 Phys. Stat. Sol. b 45 415

ZIMAN, J.M. 1960 Electrons and Phonons. Oxford University Press, London.

ZOOK, J.D. 1964 Phys. Rev. 136A 869.

APPENDIX 2

SOME FURTHER DETAILS RELEVANT TO CHAPTER 2

A2.1. The spherical averaging procedure.

In this appendix we discuss the spherical averaging procedure mentioned in Section 2.3.1. We consider the form of the distribution function in the case that there are many scattering mechanisms. Of these mechanisms at least one is assumed to be isotropic and it is assumed that there is another which is both elastic and isotropic. We show that if the elastic, isotropic scattering rate is large compared to the anisotropic rate then the isotropic part of f is large compared to the anisotropic part.

Within our one band model the distribution function is given by the solution to equation 2.3:

$$\frac{\partial f}{\partial t} = \int f(\underline{k}')\, S(\underline{k}' \rightarrow \underline{k})\, d\underline{k}' - f(\underline{k})\lambda(\underline{k}) - R(k)f(\underline{k}) + G(k)\theta(t) \qquad (2.3)$$

where $\lambda(\underline{k}) = \int S(\underline{k} \rightarrow \underline{k}')\, d\underline{k}'$

In general we can write the scattering Kernel S as the sum of three terms: $S = S^a + S^i + S^e$. S^a is a kernel for anisotropic scattering and depends on the orientation of $\underline{k}$ and $\underline{k}'$ with respect to the crystal axes and also on the magnitudes of these vectors. S^i is a kernel for isotropic scattering and depends on the angle γ between $\underline{k}$ and $\underline{k}'$ and also on the magnitudes of these vectors: $S^i = S^i(k', k, \gamma)$. S^e is a kernel for scattering which is both isotropic and elastic. It has the form $S^e = S^e(K', k, \gamma)\delta(\epsilon(k') - \epsilon(k))$. Both S^i and S^e can be written in the form of a Legendre polynomial expansion:

$$S^{i(e)}(k', k, \gamma) = \sum_{\alpha} P_{\alpha}(\cos(\gamma))\, S_{\alpha}^{i(e)}(k' \rightarrow k). \qquad (A2.1)$$

where $S^{i(e)}$ denotes S^i or S^e as appropriate.

To solve equation 2.3 we introduce a spherical polar co-ordinate system which has one of the crystal axes as its polar axis (Fig. A2.1). Then we use the following spherical harmonic expansions of S^a, S^i, S^e and f:

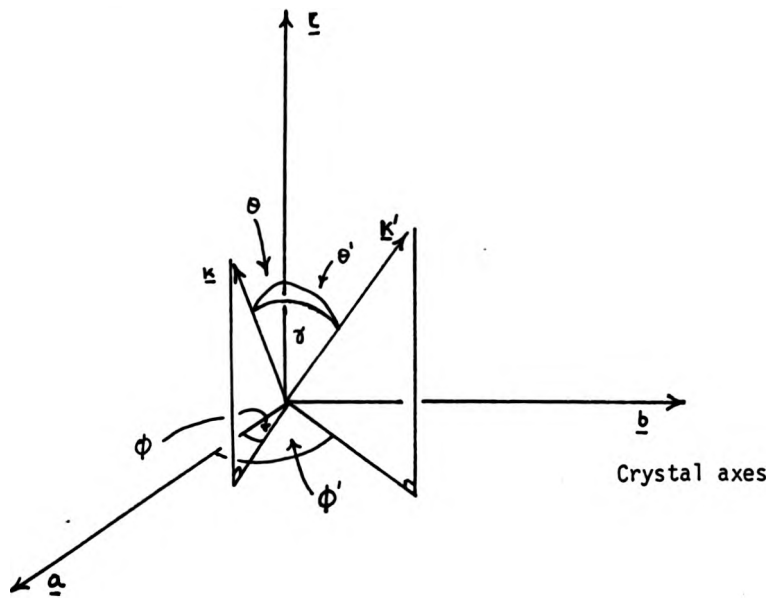

Fig. A2.1. The co-ordinate system used for the spherical harmonic expansion of the distribution function.

$$S(\underline{k}' \to \underline{k}) = \sum_{\substack{\ell m \\ \alpha\beta}} \{S^a_{\substack{\ell m \\ \alpha\beta}}(k' \to k) + S^i_{\substack{\ell m \\ \alpha\beta}}(k' \to k) + S^e_{\substack{\ell m \\ \alpha\beta}}(k' \to k)\} Y_{\alpha\beta}(\theta',\phi') Y^*_{\ell m}(\theta,\phi)$$

$$f(\underline{k},t) = \sum_{\alpha\beta} f_{\alpha\beta}(k,t) Y_{\alpha\beta}(\theta,\phi)$$

where $S^a_{\substack{\ell m \\ \alpha\beta}} = \int S^a(\underline{k}' \to \underline{k}) Y_{\alpha\beta}(\theta',\phi') Y^*_{\ell m}(\theta,\phi) d\Omega'\, d\Omega$

$$S^{i(e)}_{\substack{\ell m \\ \alpha\beta}} = \frac{4\pi}{2\alpha+1} S_\alpha(k' \to k)\, \delta_{\alpha\ell}\, \delta_{pm} .$$

To obtain the spherical harmonic expansions of S^i and S^e we have used the composition theorem for Legendre polynomials (Mathews and Walker, 1970) to substitute for P_α in equation A2.1:

$$P_\alpha(\cos\gamma) = \frac{4\pi}{2\alpha+1} \sum_\beta Y^*_{\alpha\beta}(\theta',\phi')\, Y_{\alpha\beta}(\theta,\phi)$$

Upon substituting the expansions of S and f into equation 2.3 we find that the isotropic part of f (f_{00}) is coupled to the anisotropic parts ($f_{\alpha\beta}$; $\alpha\beta \neq 00$) via the following system of equations:

$$\frac{\partial f_{00}}{\partial t} = \sum_{\alpha\beta} \int f_{\alpha\beta}\, S^a_{\substack{00 \\ \alpha\beta}}(k' \to k) k'^2 dk' - \sum_{\alpha\beta} f_{\alpha\beta}\, \lambda^a_{\substack{00 \\ \alpha\beta}} - R(k)\, f_{00} + G_{00}\theta(t)$$

$$+ 4\pi \int f_{00}\, S^i_0(k' \to k) k'^2\, dk' - \lambda^i(k)\, f_{00} \qquad \text{(A2.2)}$$

$$\frac{\partial f_{pq}}{\partial t} = \sum_{\alpha\beta} \int f_{\alpha\beta}\, S^a_{\substack{pq \\ \alpha\beta}}(k' \to k) k'^2 dk' - \sum_{\alpha\beta} f_{\alpha\beta}\, \lambda^a_{\substack{pq \\ \alpha\beta}} - R(k)\, f_{pq}$$

$$+ \frac{4\pi}{2p+1} \int f_{pq}\, S^i_p(k' \to k) k'^2 dk' - \lambda^i(k) f_{pq} - 4\pi[S^e_0(k) - \frac{1}{2p+1} S^e_p(k)] f_{pq} .$$

(A2.3)

where

$$\lambda^a_{\substack{pq \\ \alpha\beta}} = \int Y^*_{pq}(\theta,\phi) Y_{\alpha\beta}(\theta,\phi) \lambda^a(\underline{k}) d\Omega, \quad \lambda^a(\underline{k}) = \int S^a(\underline{k} \to \underline{k}') d\underline{k}'$$

$$S^e_p(k) = \frac{2p+1}{2} \int S^e P_p(\cos\gamma) \sin\gamma d\gamma \, k'^2 dk'$$

$$\lambda^i(k) = \int S^i(k,k',\gamma) d\underline{k}'$$

$$G_{00} = \int Y^*_{00}(\theta,\phi) G(k) d\Omega$$

From the definition of S^e_p it is clear that the term in square brackets in equation A2.2 (the elastic scattering term) is positive. If this term is large compared to the inelastic scattering terms then the steady state value of f_{pq} will be small. Also no elastic scattering term contributes to the equation for the isotropic part of f (Equation A2.2). Hence the isotropic part of f is unaffected by elastic scattering. Therefore if the elastic scattering rate is sufficiently large the isotropic part of f will be large compared to the anisotropic parts. In this case we can write $f(\underline{k})$ in the form $f(k) + \delta f(\underline{k})$ where $f(k)$ is the large isotropic part and δf the sum of the anisotropic parts. If we substitute this form into equation A2.2 and neglect the contribution of δf we find that $f(k)$ satisfies the equation

$$\frac{\partial f}{\partial t} = \frac{1}{4\pi} \int f(k') S(\underline{k}' \to \underline{k}) d\underline{k}' \, d\Omega - f(k) \frac{1}{4\pi} \int S(\underline{k} \to \underline{k}') d\underline{k}' d\Omega - R(k) f(k) + G(k)\theta(t)$$

which is the Boltzmann equation (equation 2.3) with the scattering rates replaced by their spherical averages. We now estimate the magnitude of the elastic scattering term for ionized impurity scattering. For this mechanism $S^e(\underline{k}' \to \underline{k})$ has the form (Rode, 1975):

$$S^e(\underline{k}' \rightarrow \underline{k}) = \frac{4\ Ne^4}{\hbar(4\pi\epsilon\epsilon_0)^2} \quad \frac{\delta(\epsilon(k')-\epsilon(k))}{(|\underline{k}-\underline{k}'|^2 + \mu^2)^2}$$

where N is the ionized impurity and μ is an inverse screening length.

Taking p = 2 (for odd values of p f_{pq} vanishes because f is a symmetric function of $\underline{k}$). We find that

$$4\pi[S_0^e - \frac{S_2^e}{5}] = \frac{6\pi N\, m^* e^4}{(4\pi\epsilon\epsilon_0)^2\hbar^3} \frac{1}{k^3} \{2\alpha \ln \frac{\alpha+1}{\alpha-1} - 4\}, \quad \alpha = 1 + \frac{\mu^2}{2k^2}$$

And for $k = 10^8\ m^{-1}$, $\mu = 10^6\ m^{-1}$ and $N = 10^{19}\ m^{-3}$ we estimate that the above elastic scattering term is $\sim 10^{11}\ s^{-1}$ and this is greater than the acoustic phonon scattering rates (which are at most $\sim 10^9\ s^{-1}$).

A2.2. <u>The form of the distribution functions corresponding to δ function injection</u>.

We now explain how the singular and non-singular parts of the distribution function are related. We start with equation 2.8 for the isotropic part of f:

$$\frac{\partial f}{\partial t} = \int f(k') < S(\underline{k}' \rightarrow \underline{k}) > d\underline{k}' - f(k)\ \lambda(k) - R(k)\ f(k) + G(k)\ \theta(t) \quad (2.8)$$

and take G(k) to be the monoenergetic injection spectrum given by equation 2.6:

$$G(k) = \frac{Q}{\rho(\epsilon_i)} \quad \delta(\epsilon(k_i) - \epsilon(k)) \quad (2.6)$$

We seek a solution of equation 2.8 which has the form of the sum of a non-singular function $\bar{f}$ and a ladder of δ functions (as discussed in Section 2.3.2 - equation 2.11):

$$f(k) = \bar{f}(k) + \sum_{n=0}^{N_0} a_n(t)\ \delta(\epsilon(k) - \epsilon_i + n\hbar\omega_0) \quad (A2.4)$$

To obtain a system of equations for $\bar{f}$ and the a_n we need to use an explicit form for the k dependence of the L.O. phonon scattering rates. This form is given in Appendix 2.3. Referring to the appendix we find that

$$\left.\frac{\partial f}{\partial t}\right|_{\substack{\text{scat}\\ \text{L.O.}}} = f([k^2 + k_o^2]^{\frac{1}{2}})\gamma_o(k) - f(k)\,\chi_o(k) \tag{A2.5}$$

where $k_o^2 = 2m^* \omega_o/\hbar$.

And upon substituting the form of f given by equation A2.4, the L.O. phonon scattering rate given by equation A2.5 and the injection spectrum given by equation 2.6 into equation 2.8 we obtain the following system of equations for $\bar{f}$ and the a_n:

$$\frac{\partial \bar{f}}{\partial t} = \int \bar{f}(k',t) < S_1(\underline{k}' \to \underline{k}) > d\underline{k}' - \bar{f}(k,t)\,\lambda_1(k) - R(k)\,\bar{f}(k) + \theta(t) \times \sum_{n=0}^{N_o} a_n(t)\,\pi^2\,\rho(\epsilon_i - n\hbar\omega_o) \int < S_1(\underline{k}' \to \underline{k}) > d\Omega' \Big|_{k'=k_n} \tag{A2.6}$$

$$\frac{da_n}{dt} = a_{n-1}\,\gamma_o(k_n) - a_n\,[\lambda_1(k_n) + R(k_n) + \chi_o(k_n)] \qquad 0 < n \le N_o \tag{A2.7}$$

$$\frac{da_0}{dt} = \frac{Q}{\rho(\epsilon_i)} - a_0[\lambda_1(k_i) + R(k_i) + \chi_o(k_i)] \tag{A2.8}$$

where $k_n^2 = k_i^2 - nk_o^2$ and S_1 and λ_1 are respectively the scattering kernel and scattering out rate for all scattering mechanisms other than L.O. phonon scattering. Equations A2.6 to A2.8 give $\bar{f}$ and the a_n in their most general form. We are especially interested in the form of these quantities in the steady state and we consider two cases:

Case 1. No electron-electron scattering

If e.e. scattering is not taken into account, then the collision term of equations 2.8 and 2.9 is linear in f and so the a_n are independent of $\bar{f}$. The are found from the following system of equations:

$$a_0 = \frac{1}{\lambda_1(k_i)+R(k_i)+\lambda(k_i)} \quad \frac{Q}{\rho(\epsilon_i)} \tag{A2.9}$$

$$a_n = \prod_{m=1}^{n} \frac{Y_o(k_m)}{\lambda_1(k_m)+R(k_m)+\lambda(k_m)} \; a_o \qquad 0 < n \leq N_o \tag{A2.10}$$

And $\bar{f}$ can be found from equation 2.9 provided that the true generation rate G is replaced by an effective generation rate $\bar{G}$ defined as:

$$\bar{G}(k) = \sum_{n=0}^{N_o} \pi^2 a_n \rho(\epsilon_i - n\hbar\omega_o) \int < S_1(\underline{k}' \rightarrow \underline{k}) > d\Omega' \Big|_{k'=k_n} \tag{A2.11}$$

i.e. $\bar{f}$ obeys the equation:

$$\int \bar{f}(k') < S_1(\underline{k}' \rightarrow \underline{k}) > d\underline{k}' - \bar{f}(k)[\lambda_1(k) + R(k)] + \bar{G}(k) = 0 \tag{A2.12}$$

The explicit forms of $\bar{G}$ for acoustic phonon scattering are given in Appendix 2.3

Case 2. Electron-electron scattering taken into account.

If e.e. scattering is taken into account then the kernel S_1 is functionally dependent on f, and so $\bar{f}$ and the a_n are interdependent. However, provided that effective scattering and generation rates are suitably defined $\bar{f}$ and the a_n can be found from a coupled system of equations which are structurally similar to equations A2.9, A2.10 and A2.12. In general the kernel S_1 can be written as the sum of a phonon (other than L.O.) scattering kernel which we denote as S_p, and an e.e. scattering kernel S_e which is defined by equation 2.33. An effective scattering kernel $\bar{S}_1$ is then obtained by substituting the form of f given by equation A2.4 into the form of S_e given by equation 2.33:

$$\bar{S}_1(\underline{k}' \to \underline{k}) = S_p(\underline{k}' \to \underline{k}) + S_e(\bar{f}:\underline{k}' \to \underline{k}) +$$

$$\left(\frac{V}{8\pi^3}\right)^2 \frac{4\pi}{\hbar} p_s \sum_{n=0}^{N_o} a_n \int \delta(\epsilon_b - \epsilon_i + n\hbar\omega_o) M^2(\underline{k}_b - \underline{k}) \delta(\epsilon(\underline{k}' + \underline{k}_b - \underline{k}) + \epsilon(\underline{k}) - \epsilon(\underline{k}') - \epsilon(\underline{k}_b)) \, d\underline{k}_b \tag{A2.13}$$

where $\underline{k}_1 = \underline{k}' - \underline{k}$, $\underline{k}_2 = \underline{k}_b - \underline{k}$ and the kernel S_e is to be evaluated using $\bar{f}$ in place of f. And equation A2.12 can be used to find $\bar{f}$ provided that the kernel S_1 is replaced by $\bar{S}_1$, the scattering out rate λ_1 is replaced by an effective scattering out rate $\bar{\lambda}_1$ (defined as $\bar{\lambda}_1 = \int \langle \bar{S}_1(\underline{k} \to \underline{k}') \rangle d\underline{k}'$) and an appropriate form is used for the effective generation rate. This form is similar to that given by equation A2.11 except that the kernel S_1 in that equation is replaced by $\bar{S}_1$. Also the a_n can be found from equations A2.9 and A2.10 provided that λ_1 is replaced by $\bar{\lambda}_1$. Notice that making these replacements results in a coupled system of equations for $\bar{f}$ and the a_n. The coupling arises because $\bar{S}_1$ and $\bar{\lambda}$ depend on both $\bar{f}$ and the a_n. The explicit forms of $\bar{S}_1$ and $\bar{G}$ corresponding to the large screening model are given in Appendix 2.3.

A2.3. The scattering rates

A2.3.1. Electron-phonon scattering

The electron-phonon scattering rates, which we have used in computing our distribution functions, are listed in Table A2.1. In addition the corresponding effective generation rates are listed in Table A2.2. All these rates are based on the Hamiltions listed in Table A2.3. The symbols used in Tables A2.1 to A2.3 are defined in Table A2.4.

The Hamiltonians listed in Table A2.2 have been derived in a fairly standard way (see the references listed in the Table). The electrons are assumed to be in Bloch states and are supposed to make transitions between these states because of the deformation potential and piezoelectric interactions with acoustic phonons and the polar interaction with L.O. phonons. Umklapp processes are neglected and the integrals of the overlap between the modulating functions of the Bloch states are assumed to be unity.

Type of Rate	Mech-anism	Rate k = 0	Rate $0 < k < k_\alpha$	Rate $k \geq k_\alpha$
$\left.\frac{\partial f}{\partial t}\right\|_{in}$	D.P.	$64B_D k_{oL}^5 \dfrac{f(2k_{oL})}{1-\exp(-\beta\epsilon_{oL})}$ (E)	$B_D \int_{2k_{oL}-k}^{2k_{oL}+k} \dfrac{f(k')}{\lvert k-2k_{oL}\rvert} \dfrac{A_D(k',k)}{1-\exp[\beta(\epsilon-\epsilon')]} \dfrac{k'}{k}\,dk'$ (E)	$B_D \int_k^k \dfrac{f(k')}{\lvert k-2k_{oL}\rvert} \dfrac{A_D(k,k')}{\exp[\beta(\epsilon-\epsilon')]-1} \dfrac{k'}{k}\,dk'$ (A) $+ B_D \int_k^{k+2k_{oL}} f(k') \dfrac{A_D(k,k)}{1-\exp[\beta(\epsilon-\epsilon')]} \dfrac{k'}{k}\,dk'$ (E)
	T.P.	$\dfrac{64B_T k_{oT}^5}{[4k_{oT}^2+\mu^2]^2} \dfrac{f(2k_{oT})}{1-\exp(-\beta\epsilon_{oT})}$ (E)	$B_T \int_{2k_{oT}-k}^{2k_{oT}+k} \dfrac{f(k')}{\lvert k-2k_{oT}\rvert} \dfrac{A_T(k',k)}{1-\exp[\beta(\epsilon-\epsilon')]} \dfrac{k'}{k}\,dk'$ (E)	$B_T \int_k^k \dfrac{f(k')}{\lvert k-2k_{oT}\rvert} \dfrac{A_T(k,k')}{\exp[\beta(\epsilon-\epsilon')]-1} \dfrac{k'}{k}\,dk'$ (A) $+ B_T \int_k^{k+2k_{oT}} f(k') \dfrac{A_T(k',k)}{1+\exp[\beta(\epsilon-\epsilon')]} \dfrac{k'}{k}\,dk'$ (E)
	L.O.	$f(k_o)\, Y_o(0)$	$f[(k^2+k_o^2)^{1/2}]\, Y_o(k)$	$f[(k^2+k_o^2)^{1/2}]\, Y_o(k)$
$\lambda(k)$	D.P.	$\dfrac{64B_D k_{oL}^3}{\exp(\beta\epsilon_{oL})-1}$ (A)	$B_D \int_{2k_{oL}-k}^{2k_{oL}+k} \dfrac{A_D(k',k)}{\exp[\beta(\epsilon'-\epsilon)]-1} \dfrac{k'}{k}\,dk'$ (A)	$B_D \int_k^k \dfrac{A_D(k,k')}{1-\exp[\beta(\epsilon-\epsilon')]} \dfrac{k'}{k}\,dk'$ (E) $+ B_D \int_k^{k+2k_{oL}} \dfrac{A_D(k',k)}{\exp[\beta(\epsilon'-\epsilon)]-1} \dfrac{k'}{k}\,dk'$ (A)
	T.P.	$\dfrac{64\, B_T k_{oT}^5}{[4k_{oT}^2+\mu^2]^2} \dfrac{1}{\exp(\beta\epsilon_{oT})-1}$ (A)	$B_T \int_{2k_{oT}-k}^{2k_{oT}+k} \dfrac{A_D(k',k)}{\exp[\beta(\epsilon'-\epsilon)]-1} \dfrac{k'}{k}\,dk'$ (A)	$B_T \int_k^k \dfrac{A_T(k,k')}{1-\exp[\beta(\epsilon-\epsilon')]} \dfrac{k'}{k}\,dk'$ (E) $+ B_T \int_k^{k+2k_{oT}} \dfrac{A_T(k',k)}{\exp[\beta(\epsilon'-\epsilon)]-1} \dfrac{k'}{k}\,dk'$ (A)
	L.O.	$X_o(0)$	$X_o(k)$	$X_o(k)$

Table A2.1. The electron-phonon scattering rates used in computing the distribution functions described in Chapter 2.

Notes:
1. The symbols used above are defined in Table A2.4.
2. Phonon absorption and emission rates are identified by (A) and(E)respectively
3. The L.P. scattering rates are not shown above. These rates can be obtained from the above T.P. rates by replacing B_T, $k_{\alpha T}$ and A_T by B_L, $K_{\alpha L}$ and A_L respectively (See Table A2.4).
4. The quantity $\epsilon_\alpha = \hbar^2 k_\alpha^2/2m^*$.

Mechanism	Effective Generation rate $0 \le k \le k_\alpha$	Effective Generate rate $k \ge k_\alpha$
D.P.	$\frac{B_D A_D(k,k_n)}{\exp[\beta(\epsilon-\epsilon_n)]-1} \frac{\rho(\epsilon_n)}{k\,k_n} \{\theta(k+k_n-2k_{\alpha L})-\theta(k-k_n+2k_{\alpha L})\}$ (A)	$\frac{B_D A_D(k_n,k)}{1-\exp[\beta(\epsilon-\epsilon_n)]} \frac{\rho(\epsilon_n)}{k\,k_n} \{\theta(k-k_n-2k_{\alpha L})-\theta(k-k_n)\}$ (E) $+\frac{B_D A_D(k,k_n)}{\exp[\beta(\epsilon-\epsilon_n)]-1} \frac{\rho(\epsilon_n)}{k\,k_n} \{\theta(k-k_n)-\theta(k-k_n-2k_{\alpha L})\}$ (A)
T.P.	$\frac{B_T A_T(k,k_n)}{\exp[\beta(\epsilon-\epsilon_n)]-1} \frac{\rho(\epsilon_n)}{k\,k_n} \{\theta(k+k_n-2k_{\alpha T})-\theta(k-k_n+2k_{\alpha T})\}$ (A)	$\frac{B_T A_T(k_n,k)}{1-\exp[\beta(\epsilon-\epsilon_n)]} \frac{\rho(\epsilon_n)}{k\,k_n} \{\theta(k-k_n-2k_{\alpha T})-\theta(k-k_n)\}$ (E) $+\frac{B_T A_T(k,k_n)}{\exp[\beta(\epsilon-\epsilon_n)]-1} \frac{\rho(\epsilon_n)}{k\,k_n} \{\theta(k-k_n)-\theta(k-k_n-2k_{\alpha T})\}$ (A)

Table A2.2. The effective generation rates used in computing the distribution functions described in Chapter 2.

Notes 1. The symbols used above are defined in Table A2.4.

2. The quantities shown above are defined as $\rho(\epsilon_n) \int \langle S_1(\underline{k}' \to \underline{k}) > d\Omega' \Big|_{k'=k_n}$

where $\epsilon_n = \epsilon_i - n\hbar\omega_o$. To obtain the effective generation rate for a particular k_n they quantities shown must be multiplied by $\pi^2 a_n$ (see equation A2.11)

3. The effective generation rates due to L.P. scattering are not shown above. These rates are obtained from the above T.P. rates by replacing B_T, $k_{\alpha T}$ and A_T by B_L, $k_{\alpha L}$ and A_L respectively (see Table A2.4).

4. Absorption and emission rates are identified by (A) and (E) respectively.

Mechanism	Hamiltonian	Reference
Deformation Potential	$i C_D \sum_{\underline{k}\,\underline{q}} \left(\frac{\hbar}{2V\rho\omega_{\underline{q}}^{L}}\right)^{1/2} q(a_{\underline{q}L} - a^{+}_{\underline{q}L})\, C^{+}_{\underline{k}+\underline{q}}\, C_{\underline{k}}$	Kittel, 1963
Piezoelectric	$-\frac{e}{\varepsilon\varepsilon_o} \sum_{\underline{k}\,\underline{q}\,\nu} \left(\frac{\hbar}{2V\rho\omega_{\underline{q}}^{\nu}}\right)^{1/2} \frac{4e_{14}}{q^2+\mu^2} (\sigma^{\nu}(\underline{q})_1\, a_2\, a_3 + \sigma^{\nu}(\underline{q})_2\, q_1\, q_3 + \sigma^{\nu}(\underline{q})_3\, q_1 a_2) \times (a_{\underline{q}\nu}\, C^{+}_{\underline{k}+\underline{q}}\, C_{\underline{k}} + a^{+}_{\underline{q}\nu}\, C^{+}_{\underline{k}-\underline{q}}\, C_{\underline{k}})$	Zawdzki and Sz manska, 1971; Ehrenreich and Cohen, 1959 (Screening)
longitudinal optical	$ie\omega_o \left[\frac{\hbar}{2V} \frac{1}{\varepsilon_o} \left(\frac{1}{\varepsilon_\infty} - \frac{1}{\varepsilon}\right)\right]^{1/2} \sum_{\underline{k}\,\underline{q}} \frac{1}{\omega_{\underline{q}}^{1/2}} \frac{q}{q^2 + \frac{\varepsilon}{\varepsilon_o}\mu^2} (a_{\underline{q}}\, C^{+}_{\underline{k}+\underline{q}}\, C_{\underline{k}} - a^{+}_{\underline{q}}\, C^{+}_{\underline{k}-\underline{q}}\, C_{\underline{k}})$	Kittel, 1963; Ehrenreich, 1959 (Screening)

Table A2.3. The Hamiltonians used to derive the scattering rates given in Table A2.1 and the effective generation rates given in Table A2.2. The symbols used above are defined in Table A2.4.

Symbol	Definition
B_D	$\frac{\hbar}{16\pi\rho}\ \frac{C_D^2}{m^{*2}\cdot^4 v_{SL}}$
$A_D(k',k)$	$(k'^2-k^2)^2$
B_T	$\frac{4}{35}\ \frac{m^*}{\pi\hbar^2\rho v_{ST}}\ \frac{e_{14}^2}{\varepsilon\varepsilon_o}\ \frac{e^2}{\varepsilon\varepsilon_o}$
$A_T(k',k)$	$\frac{(k'^2-k^2)^4}{[(k'^2-k^2)^2+4k_{\alpha T}^2\mu^2]^2}$
B_L	$\frac{3}{35}\ \frac{m^*}{\pi\hbar^2\rho v_{SL}}\ \frac{e_{14}^2}{\varepsilon\varepsilon_o}\ \frac{e^2}{\varepsilon\varepsilon_o}$
$A_L(k',k)$	$\frac{(k'^2-k^2)^4}{[(k'^2-k^2)^2+4k_{\alpha L}^2\mu^2]^2}$
β	$(k_B T_L)^{-1}$
$Y_o(k)$	$B_o\{\frac{1}{2k}\ln\left[\frac{[(k^2+k_o^2)^{\frac{1}{2}}+k]^2+\mu_o^2}{[(k^2+k_o^2)^{\frac{1}{2}}-k]^2+\mu_o^2}\right]-\frac{2\mu_o^2(k^2+k_o^2)^{\frac{1}{2}}}{(k_o^2+\mu_o^2)^2+4\mu_o^2k^2}\}$
$X_o(k)$	$B_o\{\frac{1}{2k}\ln\left[\frac{[k+(k^2-k_o^2)^{\frac{1}{2}}]^2+\mu_o^2}{[k-(k^2-k_o^2)^{\frac{1}{2}}]^2+\mu_o^2}\right]-\frac{2\mu_o^2(k^2-k_o^2)^{\frac{1}{2}}}{(k_o^2-\mu_o^2)^2 4\mu_o^2k^2}\}\ \theta(k-k_o)$
B_o	$\frac{m^*\omega_o}{\hbar^2}\ \frac{e^2}{4\pi\varepsilon_o}\left(\frac{1}{\varepsilon_\infty}-\frac{1}{\varepsilon}\right)$
μ_o	$\varepsilon\mu^2/\varepsilon_\infty$

Table A2.4a: A key to the symbols used in Tables A2.1 and A2.2. Any symbols not defined above are explained in Chapter 2. (see especially Table 2.4.)

Symbol	Definition
$a^{+}_{\underline{q}\nu}$, $a_{\underline{q}\nu}$	Phonon creation and destruction operators corresponding to a wave vector $\underline{q}$ and a polarisation of type ν
$\underline{\sigma}^{\nu}(\underline{q})$	Polarization vector for a phonon of wave vector $\underline{q}$ and polarization type ν
$\omega^{\nu}_{\underline{q}}$	Frequency associated with a phonon of wave vector $\underline{q}$ and of polarization type ν
σ^{ν}_{i}, q_i	Components of $\underline{\sigma}^{\nu}$ and $\underline{q}$
$C^{+}_{\underline{k}}$, $C_{\underline{k}}$	Electron creation and destruction operators.

Table A2.4b: A key to the symbols used in Table A2.3. Any symbols not defined above are explained in Chapter 2 (See especially Table 2.4.)

These assumptions allow the D.P. interaction Hamiltonian to be written in the form given in Table A2.2. To obtain the Hamiltonians for the piezoelectric and polar interactions it is in addition necessary to take account of screening. The standard derivations of these two Hamiltonians involve solving Poisson's equation in the form $\nabla \underline{D} = \rho_s$ where $\underline{D}$ is the electric field associated with the piezoelectric or polar interaction potential denoted by ϕ and ρ_s is the screening charge induced by ϕ. For screening by a distribution of electrons moving relative to fixed background of positive charges $\rho_s = e\,\delta n$ where δ_n is the change in electron density induced by ϕ. In the standard derivations of the Hamiltonians it is assumed that the distribution of electrons is Maxwellian, whereas we had to evaluate δn for a non-Maxwellian distribution. In general δn can be found with the aid of a self consistent field approximation due to Ehrenreich and Cohen (1959). Thus the Fourier components of δn and ϕ are related by the equation

$$\delta n(\omega,\underline{q}) = \lim_{\alpha\to 0} V\sum_{\underline{k}\,l,m} |\langle \underline{k},l|\underline{k}+\underline{q},m\rangle|^2 \frac{f(\epsilon_m(\underline{k}+\underline{q}))-f(\epsilon_l(k))}{\epsilon_m(\underline{k}+\underline{q}) - \epsilon_l(\underline{k})-\hbar\omega+i\hbar\alpha} e\phi(\omega,\underline{q}) \quad \text{(A2.14)}$$

where f is the distribution function in the absence of the interaction potential, l and m are band indices and V is the volume of the crystal. The distribution function is assumed to be spherically symmetric. To estimate δn we use equation A2.14 but we make the Debye approximation, i.e. we assume that the screening is quasi-static. This approximation enables δn to be evaluated by taking the zero frequency limit of the sum in equation A2.14.We also assume that only the term appropriate to the conduction band makes a significant contribution to the sum in equation A2.14 and that the overlap integrals for this band are unity. Then we find that δn and ϕ have the simple relation:

$$\delta n(\omega,\underline{q}) = \frac{\varepsilon\varepsilon_o}{e}\mu^2 \quad \phi(\omega,\underline{q}) \tag{A2.15}$$

where the inverse screening length μ is defined as:

$$\mu^2 = \frac{e^2}{\varepsilon\varepsilon_o} \quad \frac{m^*}{\hbar^2\pi^2} \int_o^\infty f(k)dk. \tag{A2.16}$$

In deriving equation A2.15 from equation A2.14 the approximations

$$f(\epsilon(\underline{k}+\underline{q})) - f(\epsilon(\underline{k})) \sim \underline{q}.\ \underline{\nabla}_k f \text{ and } \epsilon(\underline{k}+\underline{q})-\epsilon(\underline{k}) \sim \underline{q}.\underline{\nabla}_k\epsilon$$

have been made. The Hamiltonians for the piezoelectric and polar interactions, as given in Table A2.2, have both been derived by substituting the form of δn given by equations A2.15 and A2.16, into Poisson's equation. Note that in the Hamiltonian for the polar interaction μ^2 is premultiplied by a factor of $\varepsilon\varepsilon_\infty^{-1}$. This is consequence of the form of the relation between D and $\dot{\phi}$ for the polar interaction (See the references listed in Table A2.2).

The scattering rates given in Table A2.1 have all been derived using the golden rule of first order time dependent perturbation theory. In accordance with the comments made in Section 2.3 the electron distribution is assumed to be non-degenerate. Thus for each of the Hamiltonians listed in Table A2.3 (and denoted by $H_{e.p.}$ below) the scattering in and out rates for a state of wave vector $\underline{k}$ and a particular spin, are found to be:

$$\left.\frac{\partial f}{\partial t}\right|_{in} = \frac{2\pi}{\hbar} \sum_{\underline{q}\ (A)} |\langle n_{\underline{q}}-1,\underline{k}|H_{e.p.}|\ n_{\underline{q}},\underline{k}-\underline{q}\rangle|^2\ \delta(\epsilon(\underline{k})-\epsilon(\underline{k}-\underline{q})-\hbar\omega(\underline{q}))f(\underline{k}-\underline{q})$$

$$+ \frac{2\pi}{\hbar} \sum_{\underline{q}\ (E)} |\langle n_{\underline{q}}+1,\underline{k}|H_{e.p.}|\ n_{\underline{q}},\underline{k}+\underline{q}\rangle|^2\ \delta(\epsilon(\underline{k})-\epsilon(\underline{k}+\underline{q})+\hbar\omega(\underline{q}))f(\underline{k}+\underline{q})$$

$$\delta n(\omega,\underline{q}) = \frac{\varepsilon\varepsilon_o}{e}\mu^2 \quad \phi(\omega,\underline{q}) \tag{A2.15}$$

where the inverse screening length μ is defined as:

$$\mu^2 = \frac{e^2}{\varepsilon\varepsilon_o} \quad \frac{m^*}{\hbar^2\pi^2} \int_o^\infty f(k)dk. \tag{A2.16}$$

In deriving equation A2.15 from equation A2.14 the approximations

$$f(\epsilon(\underline{k}+\underline{q})) - f(\epsilon(\underline{k})) \sim \underline{q}.\ \underline{\nabla}_k f \text{ and } \epsilon(\underline{k}+\underline{q})-\epsilon(\underline{k}) \sim \underline{q}.\underline{\nabla}_k \epsilon$$

have been made. The Hamiltonians for the piezoelectric and polar interactions, as given in Table A2.2, have both been derived by substituting the form of δn given by equations A2.15 and A2.16, into Poisson's equation. Note that in the Hamiltonian for the polar interaction μ^2 is premultiplied by a factor of $\varepsilon\varepsilon_\infty^{-1}$. This is consequence of the form of the relation between D and ϕ for the polar interaction (See the references listed in Table A2.2).

The scattering rates given in Table A2.1 have all been derived using the golden rule of first order time dependent perturbation theory. In accordance with the comments made in Section 2.3 the electron distribution is assumed to be non-degenerate. Thus for each of the Hamiltonians listed in Table A2.3 (and denoted by $H_{e.p.}$ below the scattering in and out rates for a state of wave vector $\underline{k}$ and a particular spin, are found to be:

$$\left.\frac{\partial f}{\partial t}\right|_{in} = \frac{2\pi}{\hbar} \sum_{\underline{q}} |\langle n_{\underline{q}}-1,\underline{k}|H_{e.p.}|\ n_{\underline{q}},\underline{k}-\underline{q}\rangle|^2\ \delta(\epsilon(\underline{k})-\epsilon(\underline{k}-\underline{q})-\hbar\omega(\underline{q}))f(\underline{k}-\underline{q})$$
$$(A)$$

$$+ \frac{2\pi}{\hbar} \sum_{\underline{q}} |\langle n_{\underline{q}}+1,\underline{k}|H_{e.p.}|\ n_{\underline{q}},\underline{k}+\underline{q}\rangle|^2\ \delta(\epsilon(\underline{k})-\epsilon(\underline{k}+\underline{q})+\hbar\omega(\underline{q}))f(\underline{k}+\underline{q})$$
$$(E)$$

$$\left.\frac{\partial f}{\partial t}\right|_{out} = f(\underline{k})\,\frac{2\pi}{\hbar}\sum_{\underline{q}\ (A)} |\langle n_{\underline{q}}-1,\underline{k}+\underline{q}|H_{e.p.}|\,n_{\underline{q}},\underline{k}\rangle|^2\,\delta(\epsilon(\underline{k}+\underline{q})-\epsilon(\underline{k})-\hbar\omega(\underline{q}))$$

$$+\ f(\underline{k})\,\frac{2\pi}{\hbar}\sum_{\underline{q}\ (E)} |\langle n_{\underline{q}}+1,\underline{k}+\underline{q}|H_{e.p.}|\,n_{\underline{q}},\underline{k}\rangle|^2\,\delta(\epsilon(\underline{k}-\underline{q})-\epsilon(\underline{k})+\hbar\omega(\underline{q})) \qquad \text{(A2.7)}$$

In these equations the state vectors are labelled by the wave vectors of the electron and phonon states whose occupation numbers change in a transition, e.g. $|n_{\underline{q}},\underline{k}\rangle$ is the initial state vector corresponding to $n_{\underline{q}}$ phonons of wave etc. and one electron of wave vector $\underline{k}$. Also $\hbar\omega(\underline{q})$ is the energy of a phonon with wave vector $\underline{q}$. Both the scattering in and scattering out rates have the form of two summations over $\underline{q}$. These summations (labelled A and E in equations 2.17) correspond respectively to scattering by absorption and emission of phonons. In obtaining equations A2.17 the golden rule has been used in a form involving a δ function. This implies that the summation over $\underline{q}$ is to be evaluated as an integral.To do this it is convenient to make the substitutions $\underline{k}'=\underline{k}\pm\underline{q}$ as appropriate. Then the deformation potential and L.O. phonon scattering rates given in Table A2.1 are obtained, provided that the phonons are assumed to be in thermal equilibrium and provided that the phonon dispersion relations and polarizations are taken to be as explained in Section 2.3. To obtain the piezoelectric scattering rates given in the table it is, in addition, necessary to perform the spherical averaging discussed in Section 2.3 and Appendix 2.1. The acoustic phonon scattering rates given in Table A2.1 have been derived using Bose-Einstein statistics to obtain the phonon occupation number: in this respect no approximations to $n_{\underline{q}}$ are involved. The L.O. phonon scattering rates are based on the assumption that the L.O. phonon occupation numbers are all negligibly

$$\delta n(\omega,\underline{q}) = \frac{\varepsilon\varepsilon_o}{e}\mu^2 \quad \phi(\omega,\underline{q}) \tag{A2.15}$$

where the inverse screening length μ is defined as:

$$\mu^2 = \frac{e^2}{\varepsilon\varepsilon_o} \quad \frac{m^*}{\hbar^2\pi^2} \quad \int_o^\infty f(k)dk. \tag{A2.16}$$

In deriving equation A2.15 from equation A2.14 the approximations

$$f(\epsilon(\underline{k}+\underline{q})) - f(\epsilon(\underline{k})) \sim \underline{q}.\ \underline{\nabla}_k f \text{ and } \epsilon(\underline{k}+\underline{q})-\epsilon(\underline{k}) \sim \underline{q}.\underline{\nabla}_k\epsilon$$

have been made. The Hamiltonians for the piezoelectric and polar interactions, as given in Table A2.2, have both been derived by substituting the form of δn given by equations A2.15 and A2.16, into Poisson's equation. Note that in the Hamiltonian for the polar interaction μ^2 is premultiplied by a factor of $\varepsilon\varepsilon_\infty^{-1}$. This is consequence of the form of the relation between D and ϕ for the polar interaction (See the references listed in Table A2.2).

The scattering rates given in Table A2.1 have all been derived using the golden rule of first order time dependent perturbation theory. In accordance with the comments made in Section 2.3 the electron distribution is assumed to be non-degenerate. Thus for each of the Hamiltonians listed in Table A2.3 (and denoted by $H_{e.p.}$ below) the scattering in and out rates for a state of wave vector $\underline{k}$ and a particular spin, are found to be:

$$\left.\frac{\partial f}{\partial t}\right|_{in} = \frac{2\pi}{\hbar} \sum_{\underline{q}} |\langle n_{\underline{q}}-1,\underline{k}|H_{e.p.}|\ n_{\underline{q}},\underline{k}-\underline{q}\rangle|^2\ \delta(\epsilon(\underline{k})-\epsilon(\underline{k}-\underline{q})-\hbar\omega(\underline{q}))f(\underline{k}-\underline{q})$$
$$(A)$$

$$+ \frac{2\pi}{\hbar} \sum_{\underline{q}} |\langle n_{\underline{q}}+1,\underline{k}|H_{e.p.}|\ n_{\underline{q}},\underline{k}+\underline{q}\rangle|^2\ \delta(\epsilon(\underline{k})-\epsilon(\underline{k}+\underline{q})+\hbar\omega(\underline{q}))f(\underline{k}+\underline{q})$$
$$(E)$$

$$\delta n(\omega,\underline{q}) = \frac{\varepsilon\varepsilon_o}{e}\mu^2 \quad \phi(\omega,\underline{q}) \tag{A2.15}$$

where the inverse screening length μ is defined as:

$$\mu^2 = \frac{e^2}{\varepsilon\varepsilon_o} \quad \frac{m^*}{\hbar^2\pi^2} \int_o^\infty f(k)dk. \tag{A2.16}$$

In deriving equation A2.15 from equation A2.14 the approximations

$$f(\epsilon(\underline{k}+\underline{q})) - f(\epsilon(\underline{k})) \sim \underline{q}.\ \underline{\nabla}_{\underline{k}} f \text{ and } \epsilon(\underline{k}+\underline{q})-\epsilon(\underline{k}) \sim \underline{q}.\underline{\nabla}_{\underline{k}}\epsilon$$

have been made. The Hamiltonians for the piezoelectric and polar interactions, as given in Table A2.2, have both been derived by substituting the form of δn given by equations A2.15 and A2.16, into Poisson's equation. Note that in the Hamiltonian for the polar interaction μ^2 is premultiplied by a factor of $\varepsilon\varepsilon_\infty^{-1}$. This is consequence of the form of the relation between D and ϕ for the polar interaction (See the references listed in Table A2.2).

The scattering rates given in Table A2.1 have all been derived using the golden rule of first order time dependent perturbation theory. In accordance with the comments made in Section 2.3 the electron distribution is assumed to be non-degenerate. Thus for each of the Hamiltonians listed in Table A2.3 (and denoted by $H_{e.p.}$ below the scattering in and out rates for a state of wave vector $\underline{k}$ and a particular spin, are found to be:

$$\left.\frac{\partial f}{\partial t}\right|_{in} = \frac{2\pi}{\hbar} \sum_{\underline{q}\ (A)} |\langle n_{\underline{q}}-1,\underline{k}|H_{e.p.}|\ n_{\underline{q}},\underline{k}-\underline{q}\rangle|^2\ \delta(\epsilon(\underline{k})-\epsilon(\underline{k}-\underline{q})-\hbar\omega(\underline{q}))f(\underline{k}-\underline{q})$$

$$+ \frac{2\pi}{\hbar} \sum_{\underline{q}\ (E)} |\langle n_{\underline{q}}+1,\underline{k}|H_{e.p.}|\ n_{\underline{q}},\underline{k}+\underline{q}\rangle|^2\ \delta(\epsilon(\underline{k})-\epsilon(\underline{k}+\underline{q})+\hbar\omega(\underline{q}))f(\underline{k}+\underline{q})$$

$$\left.\frac{\partial f}{\partial t}\right|_{out} = f(\underline{k})\,\frac{2\pi}{\hbar}\sum_{\underline{q}\ (A)} |\langle n_{\underline{q}}-1,\underline{k}+\underline{q}|H_{e.p.}|\, n_{\underline{q}},\underline{k}\rangle|^2\ \delta(\epsilon(\underline{k}+\underline{q})-\epsilon(\underline{k})-\hbar\omega(\underline{q}))$$

$$+\ f(\underline{k})\,\frac{2\pi}{\hbar}\sum_{\underline{q}\ (E)} |\langle n_{\underline{q}}+1,\underline{k}+\underline{q}|H_{e.p.}|\, n_{\underline{q}},\underline{k}\rangle|^2\ \delta(\epsilon(\underline{k}-\underline{q})-\epsilon(\underline{k})+\hbar\omega(\underline{q})) \qquad \text{(A2.7)}$$

In these equations the state vectors are labelled by the wave vectors of the electron and phonon states whose occupation numbers change in a transition, e.g. $|n_{\underline{q}},\underline{k}\rangle$ is the initial state vector corresponding to $n_{\underline{q}}$ phonons of wave etc. and one electron of wave vector $\underline{k}$. Also $\hbar\omega(\underline{q})$ is the energy of a phonon with wave vector $\underline{q}$. Both the scattering in and scattering out rates have the form of two summations over $\underline{q}$. These summations (labelled A and E in equations 2.17) correspond respectively to scattering by absorption and emission of phonons. In obtaining equations A2.17 the golden rule has been used in a form involving a δ function. This implies that the summation over $\underline{q}$ is to be evaluated as an integral.To do this it is convenient to make the substitutions $\underline{k}'=\underline{k}\pm\underline{q}$ as appropriate. Then the deformation potential and L.O. phonon scattering rates given in Table A2.1 are obtained, provided that the phonons are assumed to be in thermal equilibrium and provided that the phonon dispersion relations and polarizations are taken to be as explained in Section 2.3. To obtain the piezoelectric scattering rates given in the table it is, in addition, necessary to perform the spherical averaging discussed in Section 2.3 and Appendix 2.1. The acoustic phonon scattering rates given in Table A2.1 have been derived using Bose-Einstein statistics to obtain the phonon occupation number: in this respect no approximations to $n_{\underline{q}}$ are involved. The L.O. phonon scattering rates are based on the assumption that the L.O. phonon occupation numbers are all negligibly

small i.e. $n_{\underline{q}} = 0$ for all $\underline{q}$. The resulting approximation to the L.O. phonon scattering rates is very good for the range of lattice temperatures with which we have been concerned.

A2.3.2. Electron-electron scattering

In this part of the Appendix we first explain some details of the derivation of the exact form of the e.e. scattering rates, as quoted in Section 2.7. Following this we outline the derivations of the e.e. scattering kernels appropriate to the large screening and series expansion models. We also give the effective scattering and generation rates appropriate to the large screening model.

To obtain the e.e. scattering rates we assume that the electrons interact via a screened Coulomb potential and that they make transitions between Bloch states. The transition rate is estimated using the golden rule of first order time dependent perturbation theory, and, following the discussion of Section 2.3, the electron distribution is assumed to be non-degenerate. Thus the scattering in and out rates for a state of spin s and wave vector $\underline{k}$ are found to be:

$$\left.\frac{\partial f}{\partial t}\right|_{in} = \frac{2\pi}{\hbar} \sum_{\substack{\underline{k}_a \underline{k}_b \underline{k}_c \\ s_a s_b s_c}} |\langle s_c\, s\, \underline{k}_c \underline{k}|H_{ee}|s_a s_b \underline{k}_a \underline{k}_b\rangle|^2 \delta(\epsilon(\underline{k}_c)+\epsilon(\underline{k}\,)-\epsilon(\underline{k}_a)-\epsilon(\underline{k}_b)) f(\underline{k}_a) f(\underline{k}_b)$$

$$\left.\frac{\partial f}{\partial t}\right|_{out} = f(\underline{k}) \frac{2\pi}{\hbar} \sum_{\substack{\underline{k}_a \underline{k}_b \underline{k}_c \\ s_a s_b s_c}} |\langle s_a s_c \underline{k}_a \underline{k}_c|H_{ee}|s_b s \underline{k}_b \underline{k}\rangle|^2 \delta(\epsilon(\underline{k}_c)+\epsilon(\underline{k}_a)-\epsilon(\underline{k}\,)-\epsilon(\underline{k}_b)) f(\underline{k}_b)$$

Here $H_{e.e.}$ is the Hamiltonian for the screened Coulomb interaction and the state vectors have been labelled by the wave vectors and spins of the states whose occupancy changes in a transition. The matrix elements and spin summations involved in equations A2.18 are evaluated as discussed by Landsberg (1966; See also Hearn 1966). Hence, assuming the overlap integrals to be unity we find that:

$$\sum_{s_a s_b s_c} |\langle s_c s, \underline{k}_c k | H_{ee} | s_a s_b, \underline{k}_a \underline{k}_b \rangle|^2$$

$$= [\, M^2(\underline{k}-\underline{k}_b) + M^2(\underline{k}_a-\underline{k}) + \{M(\underline{k}-\underline{k}_b) - M(\underline{k}_a-\underline{k})\}^2]\, \delta_{\underline{k}_a+\underline{k}_b, \underline{k}_c+\underline{k}} \qquad \text{(A2.19)}$$

where M is defined as

$$M(\underline{k}-\underline{k}_b) = \frac{e^2}{\epsilon\epsilon_o V} \frac{1}{\mu^2+|\underline{k}-\underline{k}_b|^2}$$

The three terms within the square brackets of equation A2.19 are the magnitudes of the squared matrix elements for the following types of interelectron collision: direct collisions between electrons of unlike spin ($M^2(\underline{k}-\underline{k}_b)$), exchange collisions between electrons of unlike spin ($M^2(\underline{k}_a-\underline{k})$) and collisions between electrons of like spin ($\{M^2(\underline{k}-\underline{k}_b) - M(\underline{k}_a-\underline{k})\}^2$). Figure A2.2 illustrates the spin configurations associated with these types of collision. In deriving equation A2.19 it has been assumed that the direct and exchange parts of the scattering are screened in the same way. However, there is some uncertainty concerning the validity of this assumption. (Haug and Eckart, 1975). The scattering rates given by equations 2.31 follow from equations A2.18 and A2.19 if the sums over $\underline{k}_a$, $\underline{k}_b$ and $\underline{k}_c$ are replaced by integrals. And then by introducing the spin uncertainty factor p_s (see Section 2.7), the scattering rates can be obtained in the form given by equation 2.33:

$$\left.\frac{\partial f}{\partial t}\right|_{e.e.} = \int f(\underline{k}_a) S_e(f:\underline{k}_a \to \underline{k})\, d\underline{k}_a - f(\underline{k}) \int S_e(f:\underline{k} \to \underline{k}_a)\, d\underline{k}_a$$

where (A2.20)

$$S_e(f:\underline{k}_a \to \underline{k}) = \left(\frac{V}{8\pi^3}\right)^2 \frac{4\pi}{\hbar} p_s \int M^2(\underline{k}-\underline{k}_b) f(\underline{k}_b) \delta(\epsilon(\underline{k}_a+\underline{k}_b-\underline{k}) + \epsilon(\underline{k}) - \epsilon(\underline{k}_a) - \epsilon(\underline{k}_b))\, d\underline{k}_b$$

Because we compute spherically symmetric distribution functions we need

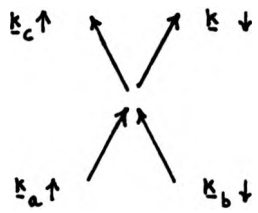

Direct collision between electrons of unlike spin

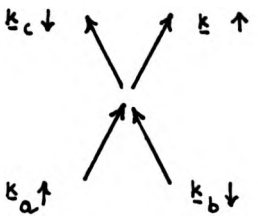

Exchange collision between electrons of unlike spin

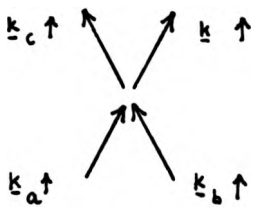

Collision between electrons of like spin

Fig. A2.2, An illustration of the possible spin configurations in an electron-electron collision.

to consider the form of $\int S_e(f:\underline{k}_a \rightarrow \underline{k})d\Omega_a$. This quantity can readily be simplified by integrating out the δ function in S_e. To do this we make the substitution $\underline{k}_2 = \underline{k}_b - \underline{k}$ and integrate over $\underline{k}_2$, using a spherical polar co-ordinate system with $\underline{k}_a - \underline{k}$ as the polar axis. Thus we have:

$$\int S_e(f:\underline{k}_a \rightarrow \underline{k})d\Omega_a = 2\pi \int_o^\pi S_e(f:\underline{k}_a \rightarrow \underline{k}) \sin\theta_a d\theta_a =$$

$$\frac{m^*}{\hbar^2}\left(\frac{V}{8\pi^3}\right)^2 \frac{8\pi^2}{\hbar} P_s \int_o^\pi \int_o^\infty \int_o^{2\pi} M^2(k_2) f([k_2^2+k^2+2k_2 k \sin\alpha \cos\phi]^{\frac{1}{2}}) \frac{k_2}{|\underline{k}_a-\underline{k}|} d\phi dk_2 \sin\theta_a d\theta_a \quad (A2.21)$$

where the angles θ, α and ϕ are as defined in Figure A2.3. The forms of $\int S_e \, d\Omega_a$ appropriate to the large screening and series expansion models are both based on equation A2.21. We now explain how these forms are derived.

1. The large screening model

In the large screening model equation A2.21 reduces to

$$\int S_e(f:\underline{k}_a \rightarrow \underline{k})d\Omega_a =$$

$$\frac{B_{1ee}}{4\pi} \int_o^\pi \int_o^\infty \int_o^{2\pi} f([k_2^2+k^2+2k_2 k \sin\alpha\cos\phi]^{\frac{1}{2}}) \frac{k_2}{|\underline{k}_a-\underline{k}|} \, d\phi \, dk_2 \sin\theta_a d\theta_a$$

where $B_{1ee} = \frac{1}{4\pi^3} \frac{2m^*}{\hbar^3} \left(\frac{e^2}{\varepsilon\varepsilon_o}\right)^2 \frac{1}{\mu^4}$.

To do the integral over ϕ and k_2 we change variables to ψ and z where $z^2 = k_2^2 + k^2 + 2k_2 k \sin\alpha \cos\phi$ and the angle ψ is defined in Figure A2.3.

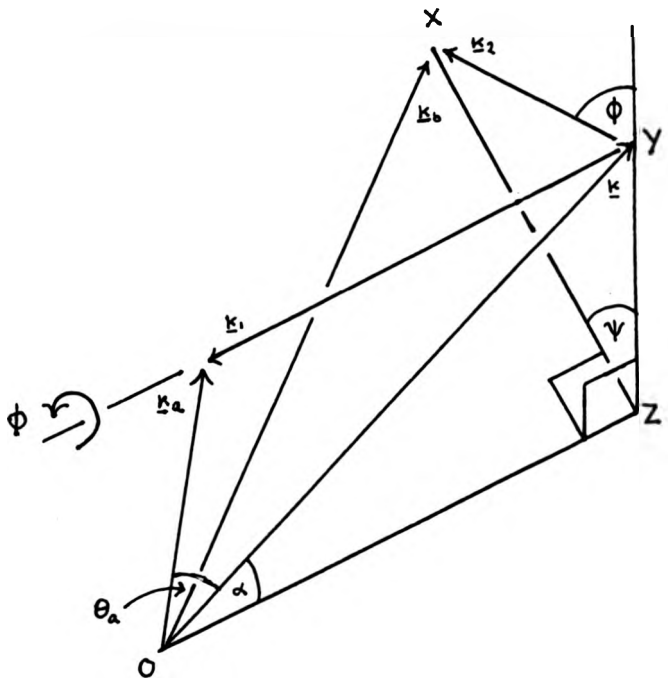

Fig.A2.3. The co-ordinate system used to evaluate the electron-electron scattering integrals. The delta function restricts the integral over $\underline{k}_b$ to the plane containing the triangle XYZ. This plane is perpendicular to the plane containing the vectors $\underline{k}$ and $\underline{k}_a$.

This gives

$$\int S_e(f:\underline{k}_a \rightarrow \underline{k})d\Omega_a$$

$$= \frac{B_{1ee}}{2} \int_{-1}^{1} \frac{1}{(k_a^2 + k^2 - 2k_a k \cos\theta_a)^{1/2}} \int_{k\cos\alpha}^{\infty} f(z)\, z\,dz\, d\cos\theta_a$$

And upon interchanging the order of integration we obtain the form of $\int S_e\, d\Omega_a$ as given by equation 2.34 of Chapter 2.

Within the large screening model the effective scattering rates (see Section 2.3 and Appendix 2.2) are derived from the sum of two kernels:

$$\bar{S}_e = \int S_e(\bar{f}:\underline{k}_a \rightarrow \underline{k})d\Omega_a + \int Q(\underline{k}_a \rightarrow \underline{k})d\Omega_a$$

The kernel $\int Q(\underline{k}_a \rightarrow \underline{k})d\Omega_a$ has the form:

$$\int Q(\underline{k}_a \rightarrow \underline{k})d\Omega_a = B_{1ee} \frac{m^*}{\hbar^2} \sum_{n=0}^{N_o} a_n R_n(\underline{k}_a,k)$$

where $R_n = R_>(\underline{k}_a,k)$ if $k_n \geq k$ and $R_n = R_<(k_a,k,k_n)$ if $k_n \leq k$

and $R_>$ and $R_<$ are defined as follows:

$$R_>(k_a,k) = \frac{1}{k_a} \quad \text{for } k_a \geq k$$

$$= \frac{1}{k} \quad \text{for } k_a \leq k$$

$$R_<(k_a,k,k_n) = \frac{k_n}{k_a k} \quad \text{for } k_a \geq k$$

$$= \frac{1}{k_a k}\{k_a^2 - k^2 + k_n^2\}^{1/2} \quad \text{for } (k^2-k_n^2)^{1/2} \leq k_a \leq k$$

$$= 0 \quad \text{for } k_a \leq (k^2-k_n^2)^{1/2}$$

Also the e.e. effective generation rates appropriate to the large screening model has the form:

$$\bar{G}(k) = \pi^2 \sum_{n=0}^{N_o} a_n \rho(\epsilon_i - n\hbar\omega_o) \int S_e(\bar{f}:\underline{k}_a \rightarrow \underline{k}) d\Omega_a \Big|_{k_a=k_n}$$

$$+ \pi^2 \sum_{n=0}^{N_o} a_n \rho(\epsilon_i - n\hbar\omega_o) \int Q(\underline{k}_a \rightarrow \underline{k}) d\Omega_a \Big|_{k_a=k_n}$$

2. The series expansion model

Within the series expansion model the form of $f(\underline{k})$ is assumed to be the product of a Maxwellian function and a modulation function $g(k)$: $f(k) = e^{-\gamma k^2} g(k)$. We now show that if f has this form and if a suitable power series expansion of $g(k)$ is available then only integrals of one dimension need be computed to calculate the e.e. scattering rates. We discuss two types of series expansion namely a power series in k and a Taylor series in $|\underline{k}_b - \underline{k}|$. First we consider the Taylor series. Expanding $g(k)$ about $\underline{k} = \underline{k}_b$ and taking the Taylor series to second order we have

$$g(|\underline{k}_b - \underline{k}|) \sim g(k) + |\underline{k}_b - \underline{k}|\, g'(k)\sin\alpha\cos\phi + \tfrac{1}{2}|\underline{k}_b - \underline{k}|^2 \{g'(k)\sin^2\alpha\cos^2\phi + \frac{g'(k)}{k}(1-\sin^2\alpha\cos^2\phi)\}$$

And using this form of g to substitute for f in equation A2.21 gives the approximation:

$$\int S_e(f:\underline{k}_a \rightarrow \underline{k}) d\Omega_a \sim$$

$$g(k)\, e^{-\gamma k^2} \int_o^\pi \frac{1}{|\underline{k}_a - \underline{k}|} P(k,\alpha,\gamma)\sin\theta_a d\theta_a - g'(k) \frac{e^{-\gamma k^2}}{2\gamma} \int_o^\pi \frac{1}{|\underline{k}_a - \underline{k}|} \frac{\partial}{\partial k} P(k,\alpha,\gamma)\sin\theta_a d$$

$$+ \frac{1}{2}\{g''(k) - \frac{g'(k)}{k}\} \frac{e^{-\gamma k^2}}{4\gamma^2} \int_o^\pi \frac{1}{|\underline{k}_a - \underline{k}|} \frac{\partial^2}{\partial k^2} P(k,\alpha,\gamma)\sin\theta_a d\theta_a$$

$$+ \frac{1}{2} \frac{g'(k)}{k} e^{-\gamma k^2} \int_o^\pi \frac{1}{|\underline{k}_a - \underline{k}|} P_1(k,\alpha,\gamma)\sin\theta_a d\theta_a$$

where we have defined P and P_1 to be the integrals:

$$P(k,\alpha,\gamma) = B_{2ee} \int_0^\infty \int_0^{2\pi} \frac{e^{-\gamma(k_2^2+2k_2 k \sin\alpha \cos\phi)}}{(\mu^2+k_2^2)^2} \, d\phi \; k_2 \; dk_2$$

$$P_1(k,\alpha,\gamma) = B_{2ee} \int_0^\infty \int_0^{2\pi} \frac{k_2^2 \, e^{-\gamma(k_2^2+2k_2 k \sin\alpha\cos\phi)}}{(\mu^2+k_2^2)^2} \, d\phi \; k_2 \; dk_2$$

and the constant B_{2ee} is defined as $B_{2ee} = \frac{1}{8\pi^4} \left(\frac{e^2}{\varepsilon\varepsilon_o}\right)^2 \frac{m^*}{\hbar^3} p_s$

To do the above integrals we first make use of a standard result involving Bessel functions (Bell, 1968):

$$\int_0^{2\pi} e^{-x \cos\phi} \, d\phi = 2\pi \, I_o(x)$$

where $I_o(x)$ is a modified Bessel function of the first kind. This enables us to integrate with respect to ϕ but the resulting integrals over k_2 involve the Bessel function $I_o(2\gamma k k_2 \sin\alpha)$. These integrals can be done by expanding I_o as a power series and integrating term by term. Thus:

$$P(k,\alpha,\gamma) = B_{2ee} \sum_{r=0} b_r \frac{(\gamma k)^{2r}}{r!} [\sin\alpha]^{2r} \qquad \text{(A2.23)}$$

$$P_1(k,\alpha,\gamma) = B_{2ee} \sum_{r=1} b_{r+1} \frac{(\gamma k)^{2r}}{r!} [\sin\alpha]^{2r}$$

where $b_r = \pi \int_0^\infty \frac{u^r \, e^{-\gamma u}}{(\mu^2+u^2)^2} \, du$. For $r > 0$, the b_r can be found from the recurrence relation $b_r = r\,C_{r-1} - \gamma C_r$ with $C_r = (r-1)!\,\gamma^{-r} - \mu^2 C_{r-1}$ and for $r = 0, b_o = \pi\mu^{-2} - \gamma C_o$ with $C_o = \pi e^{\gamma\mu^2} E_1(\gamma\mu^2)$. E_1 is the exponential integral $E_1(\gamma\mu^2) = \int_{\gamma\mu^2}^\infty t^{-1} e^{-t} \, dt$.

To obtain the from of S_e given as equation 2.25 of Section 2.9 we substitute the forms of P and P_1 given by equation A2.23 into equation A2.28. Equation 2.35 then follows upon performing the integration with respect to θ. This involves integrals of the form:

$$\int_0^\pi \frac{1}{|\underline{k}_a - \underline{k}|} (\sin\alpha)^{2r} \sin\theta_a d\theta_a = \int_0^\pi K_a^{2r} \frac{(1-\cos^2\theta_a)^r}{(k_a^2+k^2-2k_a k\cos\theta_a)^{r+\frac{1}{2}}} d\cos\theta_a.$$

And these integrals can be done with the aid of the identity:

$$(1 - 2xt + t^2)^{-\lambda} = \sum_{n=0} C_n^\lambda(x) t^n \qquad |t| < 1, \quad x \leq 1, \quad \lambda > -\tfrac{1}{2}$$

where C_n^λ is a Gegenbauer polynomial of degree n and order λ (Bell, 1968). And then equation 2.35 results from using the following orthogonality property of the Gegenbauer polynomials:

$$\int_{-1}^{1} (1-x^2)^{\lambda-\frac{1}{2}} C_n^\lambda(x)\, C_m^\lambda(x) dx = 2^{1-2\lambda} \pi \frac{\Gamma(n+2\lambda)}{(n+\lambda)\,\Gamma^2(\lambda)\Gamma(n+1)} \delta mn$$

where $\Gamma(y)$ is the gamma function: $\Gamma(y) = \int_0^\infty e^t\, t^{y-1}\, dt$.

Equation 2.35 gives the kernel S_e in a form suitable for computation of the approximate e.e. scattering rates: only integrals with respect to k_a need be computed to obtain these rates.

Now we consider the form of S_e appropriate to a power series expansion of g(k). Because f(k) can be taken to be a symmetric function of k we need only consider power series in k^2. Suppose that g(k) has the form $g(k) \sim \sum_{q=0} a_q k^{2q}$. Then substituting $e^{-\gamma k^2} g$ for f in equation A2.21 gives

$$\int S_e(f:\underline{k}_a \to \underline{k}) d\Omega_a \sim \sum_{q=0} a_q (-1)^q \frac{d^q}{d\gamma^q} \int_0^\pi \frac{1}{|\underline{k}_a - \underline{k}|} P(k,\alpha,\gamma) \sin\theta_a d\theta_a$$

And in this equation the integrals with respect to ϕ, k_2 and θ can be done in a similar manner to those involved in the Tayler series approximation. Thus again only integrals with respect to k_a need be computed to obtain the approximate e.e. scattering rates. The power series approximation to g(k) could be obtained using Hermite polynomials (See Section 2.9.1).

A2.4. Some comments on the iterative method

A2.4.1. The normalization condition and the sum rule

In general the integral with respect to $\underline{k}$ of the collision term, $\left.\frac{\partial f}{\partial t}\right|_{scat}$, of the Boltzmann equation has a value of zero. A direct consequence of this result is that the steady state distribution functions, given by the solution to equation 2.3, must satisfy the following normalization condition (equation 2.15):

$$\int G(k)\, d\underline{k} - \int R(k)\, f(\underline{k}) d\underline{k} = 0.$$

We show here that this normalization condition does not hold if $\left.\frac{\partial f}{\partial t}\right|_{scat}$ is evaluated numerically and if the resulting quantity is then numerically integrated with respect to $\underline{k}$. In addition we explain the sum rule quoted in Section 2.5.

To show that the normalization condition does not hold if $\left.\frac{\partial f}{\partial t}\right|_{scat}$ is evaluated numerically, we need to consider separately the following scattering mechanisms: acoustic phonon scattering, L.O. phonon scattering and e.e. scattering. To evaluate the acoustic phonon scattering integrals numerically we use Simpson's rule or the trapezium rule together with a k space mesh as described in Section 2.5. Because these scattering integrals have limits of the form $|k \pm 2\underline{k}_\alpha|$ (See Table A2.1) it is necessary to choose the point $k' = k$ as the starting point for assigning

the Simpson's rule or trapezium rule weight coefficients. Thus the acoustic phonon scattering rates are estimated by replacing the integrals over $\underline{k}'$ with the following sums over the k space mesh:

$$\left.\frac{\partial f}{\partial t}\right|_{scat} = \int f(k')\langle S(\underline{k}' \to \underline{k})\rangle d\underline{k}' - f(k) \int \langle S(\underline{k}' \to \underline{k})\rangle \, d\underline{k}'$$

$$\to \left.\frac{\partial f}{\partial t}\right|_{scat} \sim 4\pi \sum_{j=1}^{N_p} \gamma_{ji} \, f_j \, S_{ji} \, k_j^2 - 4\pi \, f_i \sum_{j=1}^{N_p} \gamma_{ij} \, S_{ij} \, k_j^2 \qquad \text{(A2.24)}$$

where $f_j = f(k_j)$ and $S_{ji} = \langle S(\underline{k}_j \to \underline{k}_i)\rangle$ if k_j and k_i are both in the mesh but is defined to be zero if either or both of k_j and k_i are outside of the mesh. The γ_{ji} are the weight coefficients for the numerical integration over k' with k held fixed at k_i. They are defined to be zero if k_j has outside the limits $|k \pm 2k_\alpha|$. We emphasize that for both Simpson's rule and the trapezium rule, as implemented in our program, the γ_{ij} are symmetric i.e. $\gamma_{ij} = \gamma_{ji}$. Now we consider the numerical integration of $\left.\frac{\partial f}{\partial t}\right|_{scat}$. Replacing the integral over k with a sum over the mesh we have

$$\int \left.\frac{\partial f}{\partial t}\right|_{scat} d\underline{k} \to 16\pi^2 \sum_{j=1}^{N_p} \sum_{i=1}^{N_p} \gamma_i' \gamma_{ji} f_j S_{ji} k_j^2 k_i^2 - 16\pi^2 \sum_{j=1}^{N_p} \sum_{i=1}^{N_p} \gamma_i' \gamma_{ij} f_i S_{ij} k_j^2 k_i^2 \qquad \text{(A2.25)}$$

where the γ_i' are the weight coefficients used to numerically evaluate the integral over $\underline{k}$. (The starting point for assigning these coefficients is k = 0). It is clear from A2.25 that the numerical integral of the acoustic phonon and scattering rates is non-vanishing. (interchange i and j in the second sum). The e.e. collision integrals (large screening model) do not have finite limits and the point k' = k = 0 can be used as the starting point for assigning the weight coefficients for the integrations over k' and over k. Therefore, in principle, the numerical integral of $\left.\frac{\partial f}{\partial t}\right|_{e.e.}$ can be zero. However, truncation errors are involved in the

evaluation of the kernel S_e so that in practice the integral of $\left.\frac{\partial f}{\partial t}\right|_{e.e.}$ is non-vanishing. The integral of $\left.\frac{\partial f}{\partial t}\right|_{scat}$ for L.O. phonon scattering does not have a value of zero because these scattering rates involve f at values of k which are incommensurate with the mesh points. (See Section 2.5 and Table A2.1).

The sum rule quoted in Section 2.5 (equation 2.28) is valid for numerical solutions of equation 2.9 provided that only scattering by acoustic phonons is taken into account. If the acoustic phonon scattering rates are evaluated numerically according to equation A2.24 then equation 2.9 becomes

$$4\pi \sum_{j=1}^{N_p} \gamma_{ji} f_j S_{ji} k_j^2 - 4\pi f_i \sum_{j=1}^{N_p} \gamma_{ij} S_{ij} k_j^2 - R_j f_i + G_i = 0 \qquad \text{(A2.26)}$$

where $R_i = R(k_i)$ and $G_i = G(k_i)$. And upon multiplying equation A2.26 by k_i^2, summing over i and using the symmetry of the γ_{ji} (see previous paragraph) we obtain the sum rule:

$$\sum_{i=1}^{N_p} k_i^2 R_i f_i - \sum_{i=1}^{N_p} k_i^2 G_i = 0$$

which is as quoted in Section 2.5.

A2.4.2. Matrix Iterative methods

We now explain how the iterative procedure described in Section 2.4 is similar to the Jacobi method for solving linear algebraic equations. We suppose that e.e. scattering is not taken into account and first we show that our numerical implementation of the iterative procedure is equivalent to numerically solving a system of linear algebraic equations. Following this we outline some of the matrix iterative methods used for solving such equations and finally we show that our numerical implementation of the iterative procedure is equivalent to the Jacobi method.

If the collision term of the Boltzmann equation is evaluated numerically (see equation A2.26) then the quantities f_j which approximate f at the jth mesh point obey a system of equations which can be written as

$$\underline{A}\underline{f} + \underline{G} = \underline{0} \tag{A2.27}$$

where $(\underline{f})_j = f_j$, $(\underline{G})_j = G(k_j)$ and the elements of the matrix A have the form

$$A_{ij} = 4\pi \gamma_{ji} \; S_{ji} \; k_j^2 - \delta_{ij}(\lambda_i + R(k_i))$$

with λ_i being given by a sum of the form:

$$\lambda_i = 4\pi \sum_j \gamma_{ij} S_{ij} k_j^2 .$$

It is to be understood that both the acoustic and L.O. phonon scattering rates contribute to the elements of the matrix A.

A class of iterative procedures for solving linear equations of the form A2.27 can be obtained by writing the matrix A as the sum A = N + P, where, in principle, N and P can be arbitrary. This enables an iterative solution to be attempted as follows:

$$\underline{f}_m = -N^{-1}P \; \underline{f}_{m-1} - N^{-1}\underline{G} \tag{A2.28}$$

The iterative procedures of the type defined by equation A2.28 are only useful if $\underline{f}_m$ converges to $\underline{f}$ and if $\underline{f}_m$ can be easily computed. Three matrix iterative procedures which are known to satisfy these conditions are the backward and forward Gauss Seidel methods and the Jacobi method. They are defined as follows:

$$\begin{aligned}
\underline{f}_m &= -(L + D)^{-1} U \; \underline{f}_{m-1} - (L+D)^{-1}\underline{G} \quad \text{(forward Gauss Seidel)} \\
\underline{f}m &= -(U+D)^{-1} \; L \; \underline{f}_{m-1} - (U+D)^{-1}\underline{G} \quad \text{(backward Gauss Seidel)} \\
\underline{f}_m &= -D^{-1}(L+U) \; \underline{f}_{m-1} - D^{-1}\underline{G} \qquad \text{(Jacobi)}
\end{aligned} \tag{A2.29}$$

where A = L + D + U and L is lower triangular, D is diagonal and U is upper triangular. The three iterative procedures given by equation A2.29 can all be modified to increase their rate of convergence (Young, 1971). In terms of a relaxation parameter, α, the modified procedures are defined as:

$$\underline{f}_m = (1+\alpha D^{-1}L)^{-1}[(1-\alpha)E-D^{-1}U]\underline{f}_{m-1} - (1+\alpha D^{-1}L)^{-1}\,\alpha D^{-1}\underline{G} \quad \text{(accelerated forward Gauss Seidel)}$$

$$\underline{f}_m = (1+\alpha D^{-1}U)^{-1}[(1-\alpha)E-D^{-1}L]\underline{f}_{m-1} - (1+\alpha D^{-1}U)^{-1}\,\alpha D^{-1}\underline{G} \quad \text{(accelerated backward Gauss Seidel)}$$

$$\underline{f}_m = (1-\alpha)\underline{f}_{m-1} - \alpha D^{-1}(L+U)\underline{f}_{m-1} - \alpha D^{-1}\underline{G} \quad \text{(accelerated Jacobi)}$$

where E is the unit matrix. The rate of convergence of the accelerated methods depends on the value of α. In general, the optimum value of α is determined by performing trial computations.

The equivalence of the numerical implementation of the iterative procedure and the Jacobi iteration method can be shown as follows. First we note that for acoustic and L.O. phonon scattering $S_{ii} = 0$, and hence the matrix D^{-1} has elements of the form $(D^{-1})_{ij} = (\lambda_i + R(k_i))^{-1}\,\delta_{ij}$. Therefore the jth element of $\underline{f}_m$ is related to the elements of $\underline{f}_{m-1}$ by the equation:

$$(\underline{f}_m)_j = \frac{1}{\lambda_i+R(k_i)}\left[4\pi \sum_{j=1}^{N_p} \gamma_{ji}(\underline{f}_{m-1})_j\, S_{ji}\, k_j^2 + G(k_i)\right] \qquad \text{(A2.29)}$$

And on comparing equation 2.14 with equation A2.29 it can be seen that equation A2.29 can also be obtained from equation 2.14 by numerically evaluating the integral over $\underline{k}'$.

APPENDIX 3

FINITE DIFFERENCE METHODS AND THE NUMERICAL STUDY OF OSCILLATORY PHOTOCONDUCTIVITY

Our aim in what follows is to outline the steps involved in numerically solving equations 3.6 and 3.7. In Section A2.2 we give the dimensionless form of the equations and in the following section explain the difference scheme we have used for performing our calculations. Section A2.4 is concerned with the restrictions on mesh size necessary to ensure a satisfactory numerical solution. We start with a discussion of some techniques for the solution of partial differential equations by finite difference methods. Our discussion is novel because we make use of z transform techniques.

A3.1. Finite difference methods for partial differential equations.

Suppose that we have a partial differential equation for a function u, of several independent variables. And suppose that we wish to solve the equation numerically. To do this we represent the independent variables by a discrete mesh and replace the partial derivatives by their finite difference equivalents. The unknown function u is thus approximated by a mesh function U, which obeys a partial difference equation. Usually several alternative difference schemes can be devised and it is not a priori certain that they all have solutions which are in some sense close to those of the differential equation they are designed to solve. To establish rigorously the conditions under which any particular scheme is useful we would need to consider the concepts of consistency, convergence and stability for partial difference operators. (Isaacson and Keller, 1966). However our prime purpose in this section is to explain how difference schemes are applied in practice and we find it sufficient to accept that a convergent difference scheme is one for which solutions to the difference equation converge to solutions of the differential equation, in the limit of vanishing mesh size.

Before we can make use of any difference scheme to solve a partial differential equation we need to know the conditions under which it is

convergent. To explain the importance of these conditions and to show how they are deduced we investigate a simple problem in which both the difference and the differential equations can be solved analytically. We consider a difference scheme which is convergent only if restrictions are imposed on the mesh size and we show that the solution to the difference equation can become unbounded, in the limit of vanishing mesh size, if these restrictions are not obeyed.

Specifically we consider the following linear equation with constant coefficients:

$$\frac{\partial u}{\partial t} = a \frac{\partial^2 u}{\partial x^2} + b \frac{\partial u}{\partial x} + cu \qquad a \geq 0 \qquad \text{(A3.1)}$$

together with the initial condition $u(x,0)$ given and the periodic boundary conditions

$$u(0,t) = u(L,t).$$

To solve the differential equation we first Laplace transform with respect to time and, denoting the Laplace transform of u by $\bar{u}$, we obtain the ordinary differential equation,

$$s\bar{u} - u(x,0) = a \frac{d^2\bar{u}}{dx^2} + b \frac{d\bar{u}}{dx} + c\bar{u}$$

for which we can easily find a solution in the form of a Fourier series $\bar{u} = \sum_k \alpha_k(s)\, e^{ikx}$, $k = \frac{2\pi n}{L}$, $n = 0, \pm 1 \ldots$ Inverting the Laplace transform we find the solution

$$u(x,t) = \sum_k \beta_k e^{-(ak^2 - c)t}\, e^{ikbt}\, e^{ikx} \qquad \text{(A3.2)}$$

where the β_k are the coefficients of a Fourier series expansion of $u(x,0)$

$$\beta_k = \frac{1}{L} \int_0^L u(x,0) e^{-ikx} dx. \qquad \text{(A3.3)}$$

An explicit finite difference scheme for equation A3.1 can be constructed by representing the space derivatives by central differences and the time derivative by forward differences. First we introduce a discrete mesh which has a space step Δx and a time step Δt. There are N space steps and $L=N\Delta x$.

Then denoting $u(m\Delta x, j\Delta t)$ by u_{mj}, $m = 0,1,\ldots,N$, $j = 0,1\ldots$ and introducing differences in the standard way we have

$$\frac{\partial u}{\partial x} = \frac{u_{m+1j} - u_{m-1j}}{2\Delta x} + O(\Delta x^2)$$

$$\frac{\partial^2 u}{\partial x^2} = \frac{u_{m+1j} - 2u_{mj} + u_{m-1j}}{\Delta x^2} + O(\Delta x^2) \qquad (A3.4)$$

$$\frac{\partial u}{\partial t} = \frac{u_{mj+1} - u_{mj}}{\Delta t} + O(\Delta t)$$

By the symbol $O(\Delta x^n)$ we mean that if, for any small quantities A and Δx, $A = O(\Delta x^n)$, then for some $M > 0$ independent of Δx, $|A| \leq M\Delta x^n$. Upon carrying out the substitutions we arrive at the equation

$$u_{mj+1} = A\, u_{m+1,j} + B\, u_{mj} + C\, u_{m-1,j} + O(\Delta t^2) + O(\Delta t \Delta x^2) \qquad (A3.5)$$

where we have defined

$$A = qa + pb$$

$$B = 1 - 2qa + c$$

$$C = qa - pb$$

$$p = \frac{\Delta t}{2\Delta x}, \quad q = \frac{\Delta t}{\Delta x^2}.$$

The numerical solution to the differential equation can be obtained by solving the partial difference equation:

$$U_{mj+1} = AU_{m+1,j} + B\, U_{mj} + CU_{m-1,j} \qquad (A2.5)$$

with the initial condition U_{mo} given, and the boundary conditions

$U_{oj} = u_{Nj}$. To illustrate the problems which can arise in obtaining such a solution we solve the difference equation analytically using techniques totally analogous to those used for solving the differential equation. First we z transform with respect to j. (The z transform may be thought of as a discrete analogue to the Laplace transform and, for any sequence y_j is defined by the sum: $y(z) = \sum_{j=0}^{\infty} y_j z^{-j}$. The inversion formula is $y_j = \frac{1}{2\pi i} \oint y(z) z^{j-1} dz$, the integral being evaluated anticlockwise around a closed contour within the radius of convergence of the sum, however, as with Laplace transforms inversion can often be carried out by inspection. z transform techniques are used extensively in digital systems analysis (McGillem and Cooper, 1974)). Carrying out the z transformation we arrive at the ordinary difference equation:

$$z\, U_m(z) - zU_{mo} = A\, U_{m+1}(z) + BU_m(z) + CU_{m-1}(z) \qquad \text{(A3.6)}$$

And taking N to be even we can solve this difference equation with the aid of a discrete Fourier series in the form

$$U_m(z) = \sum_{\ell = -N/2}^{\ell = N/2} \alpha_k(z)\, e^{imk} \qquad \text{(A3.7)}$$

where $k = 2\pi\ell/N$ and ℓ is an integer. Upon substituting the Fourier series into the difference equation A3.6 we find that α_k obey the equation

$$\alpha_k(z) = \beta_k[1 - z^{-1}\{2qa \cos(2\pi\ell/N) + 2ipb \sin(2\pi\ell/N) + 1 - 2qa + c\Delta t\}]^{-1} \qquad \text{(A3.8)}$$

where $\beta_k = \frac{1}{N} \sum_{m=0}^{m=N} U_{mo} e^{-imk}$.

The z transform of U_{mj} (given equations A3.7 and A3.8) can be inverted by inspection. To do this we use the result that the z transform of the sequence $y_j \equiv h^j$ (h is independent of j) is $(1 - hz^{-1})^{-1}$. Whereupon the solution to the partial difference equation, A3.5, becomes

$$U_{mj} = \sum_{k'=-\frac{N\pi}{L}}^{k'=\frac{N\pi}{L}} \beta_{k'} \{2qa \cos(k'\Delta x)+2ipb \sin(k'\Delta x)+1-2qa+c\Delta t\}^{t/\Delta t} e^{ik'x} \quad (A3.9)$$

where $j = t/\Delta t$; $\beta_{k'} \equiv \beta_k$; and $k' = 2\pi\ell/L$.

Now we wish to examine the conditions under which the solution of the difference equation approximates that of the differential equation. Because of the presence of the quantities $p = \frac{\Delta t}{2\Delta x}$, $q = \frac{\Delta t}{\Delta_x 2}$ within the curly brackets it is clear that U_{mj} could become unbounded if we let Δx and $\Delta t \to 0$ in some arbitrary manner. If, however, we specify the conditions $p|b| \leq qa$, $1 - 2qa + c\Delta t \geq 0$ we can easily establish the inequality

$$|\{2qa \cos(k'\Delta x) + 2ipb \sin(k'\Delta x) + 1 - 2qa + c\Delta t\}| \leq 1 + c\Delta t$$

Furthermore under the conditions specified $(1 + c\Delta t)^{t/\Delta t} \leq e^{ct}$ for all values of c. Therefore for all values of k' the coefficients of $e^{ik'x}$ in equation A3.6 are bounded in the limit of vanishing mesh size. Taking this limit we find that $U_{mj} \to u(x,t)$ as given by equation A3.2 and A3.3.

We established the convergence criteria for our difference scheme by explicitly considering the solutions of equation A3.5. This was done in order to show how the solution to a difference equation can become unbounded. In general a simpler procedure can be used to establish the convergence criteria of a difference scheme. This procedure involves considering a difference equation for the error $e_{mj} = u_{mj} - U_{mj}$. We now apply the procedure to our problem. Subtracting equation A3.5 from equation A3.4 gives the equation

$$e_{mj+1} = Ae_{m+1j} + Be_{mj} + Ce_{m-1} + O(\Delta t^2) + O(\Delta t \Delta x^2)$$

And it follows that provided the conditions (A3.6) are satisfied the maximum absolute error satisfies the inequality:

$$\max_m |e_{mj+1}| \leq (1+c\Delta t)\max_m |e_{mj}| + O(\Delta t^2) + O(\Delta t \Delta x^2) \qquad (A3.10)$$

Applying the above inequality recursively we find an upper bound for the error.

$$\max_m |e_{mj+1}| \leq Te^{cT}\{O(\Delta t) + O(\Delta x^2)\} + \max_m |e_{mo}|\, e^{cT} \qquad (A3.11)$$

where $T = (j+1)\Delta t$. Supposing that $e_{mo} = 0$ for all m we find that the error is vanishing in the limit of vanishing mesh size. Therefore convergence is assured.

In our example problem we obtained the difference equation by using forward differences for the time derivatives. This enabled us to solve for U_{mj+1} explicitly in terms of the U_{mj}, however we found it necessary to specify conditions on the mesh size to obtain convergence. If we had chosen to use backward differences for the time derivative we would have found that U_{mj+1} would have been given implicitly by a set of linear equations. Such implicit schemes are often unconditionally convergent but have the disadvantage that more complicated computational procedures are required for their solution.

A3.2. <u>The dimensionless form of the equations used in the numerical study.</u>

In terms of dimensional quantities equations 3.6 and 3.7 are:

$$\frac{\partial F}{\partial t} - D\frac{\partial^2 F}{\partial x^2} + v(F)\frac{\partial F}{\partial x} + \frac{e}{\varepsilon\varepsilon_o}\{n_o v(F) - D\frac{dn_o}{dx}\} = -\frac{1}{\varepsilon\varepsilon_o RS}\left(\int_0^L F dx - V_o\right) \qquad (A3.12)$$

We now introduce dimensionless quantities, by making the transformation

$$F = fF' \qquad x = Lx' \qquad t = Tt' \qquad (A3.13)$$
$$n_o = Nn_o'(x') \qquad x(F) = v_o\, v'(F') \qquad D = D_o D'$$

In equations A3.12 the primed quantities are dimensionless and the unprimed quantities are suitable units. Next we substitute equations A3.13 into A3.12 and choose the time unit T as D_o/v_o^2. Thus we obtain equations 3.6 and 3.7 in a dimensionless form:

$$\frac{\partial F'}{\partial t'} - \frac{D'}{\lambda^2}\frac{\partial^2 F'}{\partial x'^2} + \frac{1}{\lambda} v'(F')\frac{\partial F'}{\partial x'} + \alpha[\frac{1}{\lambda} v'(F')n_o'(x') - \frac{D'}{\lambda^2}\frac{d}{dx'} n_o'(x')] =$$

$$- \mu \int_0^1 F' \, dx' - \nu) \qquad \text{(A3.14)}$$

where the dimensionless constants α, λ, μ and the dimensionless emf ν are defined as

$$\alpha = \frac{NeL}{\varepsilon\varepsilon_o f} \qquad \lambda = \frac{Lv_o}{D_o} \qquad \mu = \frac{TL}{\varepsilon\varepsilon_o RS} \qquad \nu = \frac{V_o}{Lf} .$$

Equation A3.14 is the one we have solved numerically. In practice we have found i convenient to choose N as $YL^{-1}S^{-1}$ where Y is the total number of donors in the sample. With this choice it follows that the dimensionless donor density n_o' is normalized such that $\int_0^1 n_o'(x')\,dx' = 1$, This form of the donor density is given in Fig. 3.9.

A3.3. <u>The explicit finite difference scheme used in the numerical study.</u>

We now explain the difference scheme we have used to solve equation A3.14. First we drop the primes and state that from now on all quantities are to be understood as being dimensionless unless otherwise stated. Then proceeding as in the example problem of section A3.1 we introduce a mesh of space step Δx and time step Δt and represent the derivatives by their finite difference equivalents (see equation A3.4). In addition we can perform the integration by any suitable numerical rule by making the replacement:

$$\int_0^1 F dx \rightarrow \sum_{m=0}^{N} \gamma_m F_{mj}.$$

In practice Simpson's rule is used. Then N must be even; the γ_m are defined such that for $m \neq 0$ and $m \neq N$, $\gamma_m = 4\Delta x/3$ if m is odd and $2\Delta x/3$ if m is even, and $\gamma_0 = \gamma_N = \Delta x/3$. For Simpson's rule the truncation error is $O(\Delta x^4)$.

After performing the necessary substitutions we obtain at the non-linear difference equation:

$$F_{mj+1} = A_{mj} F_{m+1j} + B F_{mj} + C_{mj} F_{m-1j} - \Delta t N_{mj} - \mu\Delta t(\Sigma_m \gamma_m F_{mj} - \nu) \qquad (A3.15)$$

where F_{mj} denotes the mesh function, which represents $F(x,t)$, and the other quantities present in equation A3.15 are defined as follows:

$$A_{mj} = qD - pv(F_{mj})$$

$$C_{mj} = qD + pv(F_{mj})$$

$$B = 1 - 2qD$$

$$N_{mj} = \alpha\left[\frac{1}{\lambda} v(F_{mj})\, n_o(m\Delta x) - \frac{D}{\lambda^2} \left.\frac{dn_o}{dx}\right|_{m\Delta x}\right]$$

together with $p = \dfrac{\Delta t}{2\lambda\Delta x}$ $q = \dfrac{\Delta t}{\lambda^2 \Delta x^2}$

With field boundary conditions imposed F_{oj} and F_{Nj} obey the equation

$$F_{oj} = F_{Nj} = \nu$$

And to impose slope boundary conditions we use the convention that

$$F_{-1j} = F_{1j}, \; F_{N+1,j} = F_{N-1j}.$$

All the numerical work described in Chapter 3 has involved use of equation A3.15. In the next section we explain the convergence criteria for this equation.

A3.4. The convergence properties of the difference scheme.

We will establish the convergence criteria for our difference scheme directly by considering the difference equation for the error e_{mj} (defined as $e_{mj} = f_{mj} - F_{mj}$ where f_{mj} is the solution of the differential equation evaluated at the mesh point $(m\Delta x, j\Delta t)$; see section A3.1)

We subtract the difference equations obeyed by f and F, and then linearize the resulting equation by using the mean value theorem. Thus we arrive at the linearized error equation:

$$e_{mj+1} = A^{\ell}_{mj}\, e_{m+1j} + B^{\ell}\, e_{mj} + C^{\ell}_{mj}\, e_{m-1j} - \mu\Delta t \sum_m \nu_m e_{mj} + O(\Delta t^2) + O(\Delta t \Delta x^2) + O(\Delta t \Delta x^4)$$

where the coefficients involved in this equation are given by

$$A^{\ell}_{mj} = qD - pv(F_{mj})$$

$$B^{\ell}_{mj} = 1 - 2qD - [p(f_{m+1j} - f_{m-1j}) - \Delta t \frac{\alpha}{\lambda} n_o(m\Delta x)]v'(\xi_{mj})$$

$$\equiv 1 - 2qD + a_{mj}\Delta t$$

$$C^{\ell}_{mj} = qD + pV(F_{mj})$$

ξ_{mj} is defined by our use of the mean value theorem: $v'(\xi_{mj})\, e_{mj} = v(f_{mj}) - v(F_{mj})$. Provided that we can select a mesh such that for all m,j the following conditions are satisfied,

$$p|v(F_{mj})| \leq qD,\ 1 - 2qD + a_{mj}\Delta t \geq 0 \qquad \text{(A3.16)}$$

an inequality analogous to A3.11 holds:

$$\max_m |e_{mj+1}| \leq \max_m (1 + (\mu + a_{mj})\Delta t) \max_m |e_{mj}| + O(\Delta t^2) + O(\Delta t \Delta x^2) + O(\Delta t \Delta x^4)$$

Therefore assuming that the a_{mj} are bounded we can estimate the error as follows:

$$\max_m |e_{mj+1}| \leq Te^{AT}\{O(\Delta t) + O(\Delta x^2) + O(\Delta x^4)\} + e^{AT} \max_m |e_{mo}| \qquad \text{(A3.15)}$$

where $T = (j+1)\Delta t$ and $A = \max_{mj} |\mu + a_{mj}|$.

Converting back to dimensional quantities we find that a_{mj} takes the form of an inverse differential dielectric relaxation time:

$$a_{mj} \rightarrow -\frac{e}{\varepsilon\varepsilon_o}\left\{n_o(x) + \frac{F_{m+1j} - F_{m-1j}}{2\Delta x}\right\} \quad v'_{mj} \equiv -\frac{1}{\tau'_{dmj}} \qquad \text{(A3.16)}$$

For all the velocity field characteristics we are concerned with v' is bounded and for physically acceptable solutions $|F_{mj}|$ is bounded. Therefore, provided that $|e_{mo}| = 0$ for all m, we can use inequality A3.15 to assert that the error vanishes in the limit of vanishing mesh size. And then we can expect that our difference scheme will yield convergent solutions provided that inequalities A3.16 are satisfied. Converting these inequalities back to a dimensional form we obtain the conditions

$$x \leq \frac{2D}{|v(F_{mj})|} \; ; \; 1 - \frac{2D\Delta t}{\Delta x^2} - \frac{1}{\tau'_{d_{mj}}} \quad \Delta t \geq 0 \qquad \text{(A3.17)}$$

These conditions were quoted in section 3.6, (using the notation $v(F_{mj}) = v_{mj}$). They must be satisfied at all mesh points, but in practice the quantities v'_{mj} and $\tau'_{d\,mj}$ are unknown at the beginning of computation. To ensure a satisfactory solution we make the best estimate we can and then make periodic tests to ensure that inequalities A3.17 are satisfied.

APPENDIX 4

SMALL SIGNAL ANALYSIS FOR THE TRAP MODIFIED GUNN EFFECT

Here we outline the derivations of the dispersion relation and stability criteria which have been quoted in Chapter 4. Starting with equations 4.1 and 4.3 to 4.5, but assuming a constant current circuit, we substitute the Fourier series 4.8 and, in the resulting equations we retain only terms linear in δF or δp. We then find that the Fourier coefficients δF_k and δp_k are given by the following pair of homogeneous linear equations:

$$(i\omega + Dk^2 + ikv_o + \tau_d^{-1})\delta F_k + \frac{e}{\varepsilon\varepsilon_o}(v_o - ikD)\delta p_k = 0 \qquad \text{(A4.1)}$$

$$\left[(-i\frac{\varepsilon\varepsilon_o}{e}kp_o B(F_o) + p_o B'(F_o)(N_D - N_A + p_o)\right]\delta F_k + \left[i\omega + A + B_o(N_D - N_A + 2p_o)\right]\delta p_k = 0$$

A non-trivial solution for δF_k and δp_k exists if and only if the determinant of the coefficients of equation A4.1 is vanishing, and this condition gives the equation for $\omega(k)$ quoted in chapter 4 (equation 4.9). Equation 4.9 has two solutions which correspond to the two branches of the dispersion relation. These solutions are as follows:

$$\begin{aligned} \mathrm{Re}[\omega] &= kv_o \pm \frac{b}{\sqrt{2}}\,(a^2 + b^2)^{-\frac{1}{2}} - a)^{-\frac{1}{2}} \\ \mathrm{Im}[\omega] &= Dk^2 + \frac{1}{\tau_d} + \frac{1}{\tau_g} \pm \frac{1}{\sqrt{2}}\left((a^2 + b^2)^{\frac{1}{2}} - a\right)^{\frac{1}{2}} \end{aligned} \qquad \text{(A4.2)}$$

where a and b are functions of k defined by the relations

$$a = k^2 v_o^2 - \left[Dk^2 + \frac{1}{\tau_g} + \frac{1}{\tau_d}\right]^2 - 4\left[\frac{1}{\tau_1^2} - \frac{1}{\tau_d \tau_g} - Dk^2\left(\frac{1}{\tau_g} + \frac{1}{\tau_R}\right)\right]$$

$$b = 2kv_o\left[Dk^2 + \frac{1}{\tau_d} - \frac{1}{\tau_g} - \frac{2}{\tau_R}\right] - \frac{4kD}{v_o \tau_1^2}$$

Any mode of frequency ω is stable if $\mathrm{Im}[\omega] \geq 0$ and this is certainly true for all modes in both branches of the dispersion relation if the following condition is satisfied:

$$Dk^2 + \frac{1}{\tau_d} + \frac{1}{\tau_g} - \frac{1}{\sqrt{2}}\left((a^2 + b^2)^{\frac{1}{2}} - a\right)^{\frac{1}{2}} \geq 0 \qquad \text{(A4.3)}$$

Upon multiplying out the square roots occurring in this inequality we find the equivalent condition

$$a_3k^6 + a_2k^4 + a_1k^2 + a_o \geq 0 \qquad \text{(A4.4)}$$

where $a_3 = 4D^3\left(\frac{1}{\tau_g} + \frac{1}{\tau_R}\right)$

$$a_2 = 16Dv_o\left(\frac{v_o}{\tau_g} + \frac{v_o}{\tau_R} + \frac{2D}{v_o\tau_1^2}\right) + 8D^2\left(\frac{1}{\tau_d} + \frac{1}{\tau_g}\right)\left(\frac{1}{\tau_g} + \frac{1}{\tau_g}\right) + 4D^2\left(\frac{1}{\tau_d\tau_g} - \frac{1}{\tau_1^2}\right)$$

$$a_1 = 16\left(\frac{v_o}{\tau_g} + \frac{v_o}{\tau_R} + \frac{2D}{v_o\tau_1^2}\right)\left(\frac{1}{\tau_d} + \frac{1}{\tau_g}\right) + \left(\frac{v_o}{\tau_g} + \frac{v_o}{\tau_R} + \frac{2D}{v_o\tau_1^2}\right)^2$$

$$+ 4D\left(\frac{1}{\tau_g} + \frac{1}{\tau_d}\right)^2\left(\frac{1}{\tau_g} + \frac{1}{\tau_R}\right) + 8D\left(\frac{1}{\tau_d} + \frac{1}{\tau_g}\right)\left(\frac{1}{\tau_d\tau_g} - \frac{1}{\tau_1^2}\right)$$

$$a_o = 4\left(\frac{1}{\tau_g} + \frac{1}{\tau_d}\right)^2\left(\frac{1}{\tau_d\tau_g} - \frac{1}{\tau_1^2}\right)$$

Following unpublished work due to Pimpale (1977) we consider the equality in A4.4 as a cubic equation in k^2 giving the value of k at which the imaginary part of ω becomes negative. Stability is assured if there are no real positive roots. To investigate the stability conditions we first note that all the coefficients in equation A4.4 are real. Then we need to consider two cases.

Case 1. $\tau_d^{-1} > 0$.

In this case $a_o < 0$. The product of the roots is $-a_o/a_3$ and a_3 is positive. Therefore $-a_o/a_3 > 0$ hence at least one positive real root exists. Therefore the system is unstable.

Case 2. $\tau_d^{-1} \geq 0$.

In this case $\tau_d^{-1}\,\tau_g^{-1} - \tau_1^{-2}$ is either < 0 or ≥ 0. If the former inequality holds then the system is unstable as in case 1. If the latter holds the coefficients in equation A4.4 are all ≥ 0 hence no real positive roots exist. Therefore the system is stable.

Combining the results of cases 1 and 2 we find that the criterion for stability is

$$\frac{1}{\tau_d} - \frac{\tau_g}{\tau_1^2} \geq 0$$

which is the condition quoted in chapter 4, (inequality 4.11).